UNIVERSITY OF THE
WITWATERSRAND,
JOHANNESBURG

TECHNO-ECONOMIC ANALYSIS AND OPTIMIZATION OF A FISCHER-TROPSCH MICRO REACTOR FOR SYNFUELS PRODUCTION FROM UNCONVENTIONAL FEEDSTOCKS

Botang Mamabolo

A thesis submitted to the Faculty of Engineering and the Built Environment, University of the Witwatersrand, in fulfilment of the requirements for the degree of Doctor of Philosophy in Engineering.

Supervised by

Dr. Saeideh Babaee

December, 2024

Declaration

I, Botang Mamabolo, declare that this thesis is my own unaided work. It is being submitted for the Degree of Doctor of Philosophy in Engineering to the University of the Witwatersrand, Johannesburg. It has not been submitted before for any degree or examination to any other university.

Signature

02/12/2024

Date

Publications arising from this study

Mamabolo, B. A., Nkazi, D. *The use of large-scale Fischer-Tropsch Slurry Bubble Column Reactor modelling techniques on microchannel reactors – Adaptability and hydrodynamic effects*. Submitted for publication in the Chemical Engineering and Processing - Process Intensification Journal. Impact factor 4.237, cite score 5.1.

Mamabolo, B. A., Nkazi, D. *A review of the application of microchannel reactor technology in Fischer-Tropsch Synthesis for liquid fuels production*. Submitted for publication in the Energy and Fuels Journal. Impact factor 3.605, cite score 6.1.

Mamabolo, B. A., Babaee, S. *Understanding Fischer-Tropsch Synthesis in Micro Reactors – A Three-phase One-dimensional Microchannel FT reactor Model*. Abstract submitted and accepted for presentation at the Global Congress of Chemical Engineering (GCCE) 2024.

Abstract

The Fischer-Tropsch (FT) process has been applied in the petrochemical industry since its initial development in the early 20th century – allowing for the conversion of carbon-rich resources into liquid fuels and chemicals. Micro-FT (Fischer-Tropsch) reactor systems are an adaptation of the FT process for application in the micro-scale. Micro-FT reactors have the potential to unlock natural resources that have thus far been overlooked. Given this, a thorough comprehension of the governing mechanisms in these systems is important. This has been lacking mostly because of the relative novelty of the concept in FT reactor applications. FT microreactor models represent the operation of FT synthesis at a microscale, where the reactor's dimensions are typically in the range of micrometers to a few millimeters. This small scale can significantly enhance mass and heat transfer rates, leading to more efficient reactions. Reliable micro-FT reactor physical models, able to describe the physical characteristics and behaviour within the micro-reactor, are not openly available in literature and those that are accessible are not comprehensive. While these FT microreactor models offer some insight into micro-FT physico-chemical processes such as hydrodynamics and kinetics, they often depend heavily on simplistic assumptions and this loses the complexity of the real process and renders the model inaccurate. In addition to the technical challenges, the economics related to the commercial viability of a micro-FT driven GTL plant are crucial. The economics associated with micro-FT reactor application must be favourable if this technology is to be adopted. The challenge is the lack of economic models to enable the determination of this viability. The problems around the micro-FT reactor are therefore two-fold, including the technical issues around the reactor model and optimal manifold design and economic issues regarding the methodology applicable in determining the economic feasibility of a mini-GTL plant using micro-FT technology. To solve the current problems outlined above, a holistic approach to the study of the micro-FT system was adopted where the technical and economic aspects were explored to improve the understanding of micro-FT reactors through a comprehensive study and analysis of the reactor and its economic implications. The FT microreactor offers several advantages over conventional FT reactors including enhanced heat and mass transport rates because of the miniature size of the channels and these ultimately lead to a more efficient reactor system. The principles governing the behaviour of a three-phase one-

dimensional 2-bubble-class microchannel system were analysed based on those of a similar, albeit larger FT reactor in the form of a slurry bubble column reactor (SBCR). An FT microchannel reactor mathematical model was developed from 1st principles based on the mass conservation law which was applied to three distinct compartments including the large bubble, small bubble and liquid phases. The model was found to be capable of describing the fate and behaviour of the reactants, more specifically the CO across the length of the microchannel. It was determined that two key parameters primarily influence the performance of the microchannel reactor including the total superficial gas velocity and the axial dispersion, particularly in the gas phase. An increase in the superficial gas velocity from 0.0018 to 0.309 m/s, was found to enhance axial dispersion in both liquid and gas phases by 99.9% and 78.7% respectively and increase large bubble hold-up from 0.015 to 0.158 resulting in the net effect of a reduced syngas conversion from 70% to 40%. It was also determined that an increase in the microchannel diameter from 2.6 $x10^{-3}$ to 3.4$x10^{-3}$ m resulted in an increase in overall syngas conversion from 30% to 70% conversion through its obvious effect on residence time but also indirectly through its influence on the dispersion in the large bubble compartment. The solids concentration (0.38 – 0.3825 v/v) was found to enhance the syngas conversion up to a point (C_V=0.3825), beyond which the effect of the decreasing small bubble hold-up (75% decrease) outweighs the improved reactant consumption rate. Increasing the temperature between 470 K and 515 K was found to improve the reaction kinetics and reduce the large bubble axial dispersion which had the net result of improving syngas conversion by 46.6%. The model results were compared with the results from literature experiments conducted under similar conditions. It was found that the two sets of results are reasonably similar. The capital cost estimate of a mini-GTL plant, using an FT microchannel reactor, was found to be 95% lower than that from a conventional size GTL plant. More importantly, the cost/bbl estimate for the mini-GTL case was found to be 33% lower than in the conventional size case as a result of the improved efficiency brought about in large part by the FT microreactor unit.

Acknowledgements

I would like to thank my family who have shown a great deal of patience and support throughout the completion of this work. I would not have been able complete this project without your unwavering support and encouragement. Thank you for showing faith in me.

A special acknowledgement to my former supervisor, Prof. Diakanua Nkazi, for his guidance throughout this work. His ‘can do’ attitude has contributed immensely to how I approached this work and to the success of this thesis and for that, I will always be grateful. I pay tribute to his selflessness. May his soul rest in peace.

A thank you to my current supervisor, Dr. Saeideh Babaee, for agreeing to take this project on and assisting with completing the thesis. Thank you for the advice and guidance.

I also acknowledge the school of Chemical and Metallurgical Engineering for providing me with the platform and necessary resources to successfully carry out this study.

Contents

List of Figures

List of Tables

Nomenclature

$C^*_{i,L}$	Equilibrium liquid side interfacial concentration of species i (mol/m^3)
k_{FT}	FT reaction rate constant (mol/g_{cat}.s)
P_{CO_2}	Partial pressure of CO_2 (Pa)
P_{H_2}	Partial pressure of H_2 (Pa)
P_{H_2O}	Partial pressure of H_2O (Pa)
P_{CO}	Partial pressure of CO (Pa)
A'	Empirical constant
A_f	Bulk fluid cross-sectional area (m^2)
A_s	Channel wall cross-sectional area (m^2)
A_{wet}	Contact area between the channel wall and the wetted surface area (m^2)
C^*	Total equilibrium liquid side interfacial concentration of species i (mol/m^3)
C_V	Solids concentration (v/v)
$C_{i,L}$	Concentration of species i in the liquid phase (mol/m^3)
D_C	Diameter of reactor column (m)
D_{gL}	Gas-liquid diffusivity (m^2/s)
D_m	Molecular diffusion coefficient (m^2/s)
D_{ref}	Reference diffusivity (m^2/s)
E_G	Gas phase dispersion coefficient (m^2/s)
E_l	Liquid phase dispersion coefficient (m^2/s)
H_i	Henry's constant of component i (m^3.Pa/mol)
K_A	Equilibrium adsorption constant for species A

$K_{La,LB}$	Liquid-side mass transfer coefficient in the large bubbles compartment (s^{-1})
$K_{La,SB}$	Liquid-side mass transfer coefficient in the small bubbles compartment (s^{-1})
K_d	Gas sparger type constant
Mw_g	Molecular weight of gas (g/mol)
Mw_i	Molecular weight of component i (g/mol)
N_0	Number of orifices on sparger
P_T, P_S	Total pressure (Pa)
P_i	Partial pressure of component i (Pa)
P_m	Specific energy dissipation rate (W/m^3)
P_{vap}	Vapour pressure (Pa)
$R_i(G_i)$	Rate of CO consumption of component i ($mol/g_{cat}.s$)
$U_{g,LB}$	Large bubbles superficial liquid velocity (m/s)
$U_{g,SB}$	Small bubbles superficial velocity (m/s)
U_g, U_G	Gas superficial velocity (m/s)
V_{fluid}	Effective volume of fluid filling a channel (m^3)
X_W	Fraction of primary liquid in mixture (w/w)
Y_n	Molar fraction of hydrocarbons with carbon number 'n' in products
d_0	Sparger orifice diameter (m)
d_h	Hydraulic diameter (m)
d_{LB}	Large bubble diameter (m)
d_{SB}	Small bubble diameter (m)
d_b	Bubble diameter (m)

d_p	Particle diameter (m)
k_3	Desorption rate constant (Pa^{-1})
k_L	Mass transfer coefficient (m/s)
k_{La}	Volumetric mass transfer coefficient (s^{-1})
k_{ads}	Adsorption rate constant (Pa^{-1})
r_p	Rate of carbon chain propagation
r_t	Rate of carbon chain termination
ρ_L	Liquid density (kg/m^3)
ρ_g, ρ_G	Gas density (kg/m^3)
ρ_p	Particle density (kg/m^3)
$[*]_0$	Total concentration of active sites on catalyst surface
$[*]$	Concentration of vacant active sites on catalyst surface
$[A*]$	Concentration of active catalyst sites occupied by adsorbing species A
bbl	Barrel
c	conjugate heat transfer conduction parameter
GHSV	Gas hourly space velocity (h^{-1})
h	heat transfer coefficient (W/m^2K)
D	Diffusivity (m^2/s)
H	Reactor Height (m)
J	Molar flux ($mol/m^2.s$)
K	Liquid axial dispersion proportionality constant
Kn	Knudsen coefficient

T	Temperature (K)
U	Superficial velocity (m/s)
f	Channel geometry constant
k	thermal conductivity (W/mK)
γ	Microreactor shape factor

Greek

α_c	Channel aspect ratio
ε_S	Solids hold-up (v/v)
$\varepsilon_{g,LB}$	Large bubbles hold-up (v/v)
$\varepsilon_{g,SB,ref}$	Reference small bubbles hold-up (v/v)
$\varepsilon_{g,SB}$	Small bubbles hold-up (v/v)
ε_g	Gas hold-up (v/v)
θ_{sf}	Solid-fluid contact angle (º)
μ_L	Liquid viscosity (kg/m.s)
σ_L	Liquid surface tension (N/m)
σ_{lg}	Liquid-gas interfacial tension (N/m)
σ_{sg}	Solid-gas interfacial tension (N/m)
σ_{sl}	Solid-liquid interfacial tension (N/m)
ξ	Dimensionless co-ordinate in the axial direction
α	Product distribution constant
γ	Gas sparger type
δ	Mass transfer liquid film thickness (m)

ε	Hold-up (v/v)
θ	Species coverage on catalyst surface
λ	Molecular mean-free path (m)

Subscripts

n	Carbon number of hydrocarbon molecule
L	Liquid phase
SB	Small bubbles phase
LB	Large bubbles phase
S	Solid phase
i	Arbitrary species
cat	Catalyst particle
f	fluid phase

Dimensionless numbers

Bo	Bond number
Br	Brinkman number
Ca	Capillary number
We	Weber number
Pe	Peclet number
Pr	Prandtl number
Vi	Viscous number

ΔT^*	Dimensionless temperature rise
Nu	Nusselt number

Chapter 1: Introduction

1.1 History of Fischer-Tropsch Synthesis

In this chapter, a background on Fischer-Tropsch Synthesis (FTS) is given so that the importance of microreactors is contextualized. A brief history of FTS will be explained followed by the science underpinning this process and the various technologies that have been developed to commercialize it. This is intended to give the reader an appreciation of the importance of micro-reactors in the commercialization of the process of FTS.

The Fischer-Tropsch (FT) process has been applied in the petrochemical industry since being initially development in the early 20th century by a team of German chemists named Franz Fischer and Hans Tropsch. The scientists realized through experimentation that long chain hydrocarbons could be derived from a CO and H_2 feedstock run over a Ni and Co catalyst (Steynberg and Dry, 2004). This discovery facilitated the emergence of Fischer-Tropsch Synthesis (FTS) as a process that could prove to be an alternative route in the production of liquid fuels as compared to the then-conventional means of refining crude oil. After a successful FT pilot plant study by Ruhrchemie AG, several FT plants were constructed in Germany to move the country away from over-dependence on fuel imports (Steynberg and Dry, 2004). The technology was further developed in Europe, North America, and Africa in the latter part of the 20th century despite a decline in the oil price in the middle of the century (Maitlis and de Klerk, 2013). The South African Coal, Oil and Gas Corporation, Ltd. (SASOL) saw an opportunity for the application of FTS technology in South Africa as the country faced oil export sanctions to South Africa and a resurgent oil price in the 1970's reference. The rising oil price over that period in the 1970's also helped to justify the adoption of this technology given the risks associated with its complexity and its high capital cost. SASOL has gone on to lead in the commercial application of FTS.

Apart from SASOL, other international energy companies have also been central to the development of this technology. The rising oil price in the late 20th century and other factors increased interest in FTS technology up to now where several FTS-based plants are in operation in various countries. These factors include the growing need to meet the energy needs of a growing population. It would be important then to exploit alternatives to crude oil as the primary feedstock for liquid fuel production. FTS, through the gas-to-liquids (GTL) process, is best placed to exploit gas reserves that are in areas too remote to be economically transported to the market. It would be

easier to first convert this natural gas to liquid fuels, which would be more cost-effectively transported to market (Speight, 2008; De Deugd, 2004). The above-mentioned factors and the technological FTS advances made over the years leading to improved capital and operating costs, have contributed to the rise in popularity, or at least increased appreciation and attention of FTS-based processes. The various companies making use of this technology presently is presented in Table 1.1.

The reader will notice that most of the application of FTS is in large-scale XTL plants with up to 160000 bbl/day capacity plant. Regarding the commercial application of FTS in intensified or micro processes, there are much fewer organizations that are involved with some projects pending financial investments. This signals the lack of confidence in this new technology that still permeates within the liquid fuels production industry. There is a clear scarcity of application of FT microreactors in industry with only a handful of companies pioneering the implementation of this new process intensification technology. The work in this study will seek to provide some insights into this new field so that this technology can be more broadly adopted and exploited.

Table 1.1: Application of FTS Technology in Industry

Companies	Plant	Country	Operating Mode	Capacity (bbl/day)	Status	References
Qatar Petroleum/Sasol	GTL	Qatar	Low-Temperature Fischer-Tropsch (LTFT)	34 000	In commercial operation	Oryx GTL (n.d)
Qatar Petroleum/ Shell	GTL	Qatar	LTFT	140 000	In commercial operation	Pearl GTL-Overview (n.d)
Sasol Chevron	GTL	Nigeria	High- Temperature Fischer-Tropsch (HTFT)	34 000	In commercial operation	Sasol Nigeria Operations (n.d)
Shell	GTL	Malaysia	LTFT	14 700	In commercial operation	Hoek (2005)
Sasol	GTL	South Africa (Sasolburg)	LTFT	15 600	In commercial operation	Mohammed and Datt (2013)
Sasol	CTL	South Africa (Secunda)	HTFT	160 000	In commercial operation	Mohammed and Datt (2013)

PetroSA	GTL	South Africa	HTFT	45 000	In commercial operation	PetroSA: Operations and Refinery (n.d)
Sasol	GTL	USA	HTFT	96 000	Investment decision delayed	Djakovic (2014)
CompactGTL	GTL	Brazil	-		demonstrated operation for 3 years	Compact GTL – "Commercial Demonstration Plant" (n.d)
Velocys	BTL	USA	Micro-channel	2283	Pre-FEED stage completed – financial investment pending	"Velocys Projects-Bayou Fuels" (n.d)
Velocys	BTL	UK	Micro-channel	1305	Pending financial investment – 2024 target for financial close	Velocys-Altalto: "Transforming waste into sustainable advanced biofuels" (n.d)
Rocky Mountain GTL	GTL	Canada	-	430	Operation was expected in 3rd quarter of 2021- current status unknown	Carseland Alberta Facility – "RMGTL Carseland, Alberta Canada GTL Plant" (n.d)

Coal-to-liquids (CTL) and gas-to-liquids (GTL) processes are the most common methods for converting coal and natural gas to liquid fuels (Maitlis and de Klerk, 2013). Shell, Sasol and PetroSA have operated these types of plants for several decades and have thus demonstrated their operational sustainability. These processes produce cleaner burning fuel with less impurities as opposed to fuels produced from the conventional crude oil-to-fuels refining processes. In both the GTL and CTL processes, FT reactor technology plays a crucial role where a mixture of CO and

H_2 (synthesis gas) is converted under heterogenous catalysis conditions to hydrocarbons of various chain lengths including wax, diesel, gasoline and other products.

1.2 GTL/CTL Process Overview

In this section a description of the general FT-based liquid fuels production process is given to provide a clear understanding of the flowsheet and configuration of such a system. This should give the reader an appreciation of the role taken up by an FT reactor in the larger overall process plant. A more detailed description of this process can be found in the works of various authors (Steynberg & Dry, 2004; Basha et al., 2015; Mamabolo, 2018). An illustration of the main steps in a GTL/CTL process is given in Figure 1.1. The feedstock (coal and/or natural gas) is first converted to synthesis gas (syngas) in either a gasifier, in the case of coal, or in a methane reformer in the case of natural gas. The syngas is then cooled and cleaned to remove sulphur and other contaminants before being converted to useful hydrocarbon products (including liquid fuels) in the FT reactor.

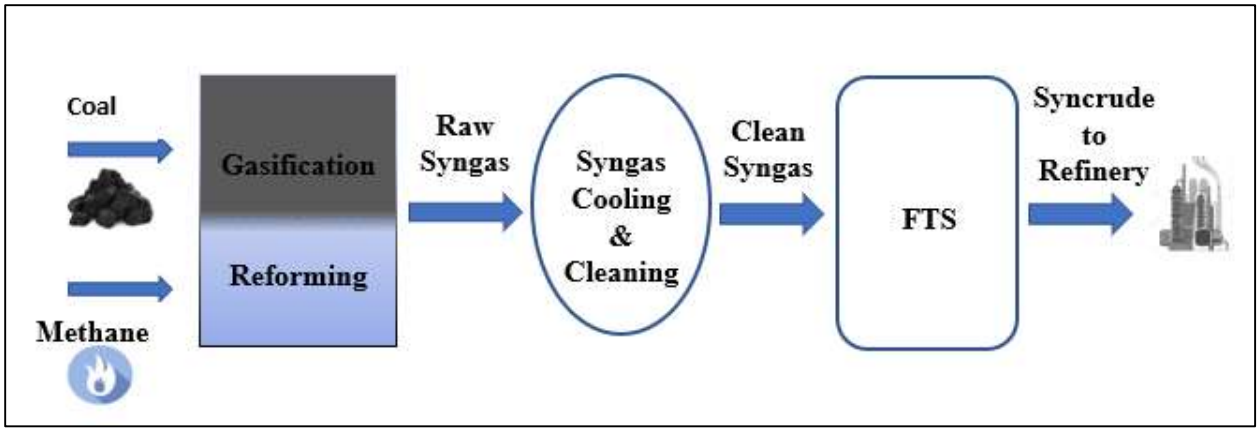

Figure 1.1: GTL/CTL Process

FTS involves multiple reactions in both series and parallel producing a variety of different products. The most dominant reactions include those of paraffin and olefin formation shown in R1 and R2 respectively, the water-gas shift reaction (R3) and alcohol formation (R4) reactions and the Boudouard reaction (R5) (see Table 1.2). The large number of products means it is easier to group them according to their chain lengths. To this end, a product distribution is used to qualify the products. The Anderson-Schulz-Flory (ASF) product distribution model is the most conventional way of doing this, where an α value is assigned to the product stream to indicate the

relative concentrations of products that have specific carbon numbers (Steynberg & Dry, 2004). This model fails to consistently predict the spectrum of various chain-length products accurately and this inconsistency has been studied and discussed by a few authors (Tau et al., 1990; Herington, 1946).

Table 1.2: Dominant FTS reactions

Name	Reaction	Designation
Paraffin Formation	$(2n+1)H_2 + nCO \rightarrow C_nH_{2n+2} + nH_2O$	**R1**
Olefin Formation	$2nH_2 + nCO \rightarrow C_nH_{2n} + nH_2O$	**R2**
Water Gas Shift	$H_2O + CO \leftrightarrows H_2 + CO_2$	**R3**
Alcohol Formation	$2nH_2 + nCO \rightarrow C_nH_{2n+2}O + (n-1)H_2O$	**R4**
Boudouard Reaction	$2CO \leftrightarrows CO_2 + C$	**R5**

1.3 Conversion of carbonaceous material to liquid fuels (XTL)

GTL and CTL processes are only a few of the ways in which the FT process can be used to produce liquid fuels using carbonaceous energy sources. Theoretically, any carbon-containing, combustible material can be processed to the point where liquid fuel is produced. The differentiator between the sources will be the quality and amount of fuel that can be produced, i.e., certain sources such as natural gas and coal are better suited to produce quality fuel at more economically acceptable throughputs than others. It is the process economics therefore that ultimately affects the viability of the use of a particular feedstock in FT synfuel production.

There are other feedstocks that have shown potential for use in FT processes outside coal and natural gas including biomass, stranded gas and associated gas. Even gases from landfill sites could potentially be used for liquid fuels production. The flaring of gas is a particularly worrying phenomenon given the relatively large volumes of energy released when the methane laden gas is combusted. To offer some perspective, the amount of energy wasted in this way is equivalent to the combined annual gas consumption of Central and South America (Murphy-McGreevey, 2019). Table 1.3 shows the total amount of gas flared worldwide. The data shows a slow but steady growth between 2014 and 2018 with a 1% increase in worldwide gas flaring activities. Whilst flaring helps

avoid the release of a more harmful greenhouse gas in CH_4, the volumes of CO_2 that are instead released contribute significantly to climate change.

Liquid fuels production processes considering all these sources are generally referred to as XTL where the 'X' represents a carbon-based feedstock. Because of the relatively high capital cost of conventional GTL and CTL plants, the scale of such plants must be large with relatively high production throughputs to justify their cost. The larger the plant is, the better, as economies of scale take effect. This presents a problem with the other feedstocks as their available volumes don't justify the construction of large plants thus nullifying any potential advantage of economies of scale. It would be economically unfavourable and prohibitive to scale down, at least in the conventional sense, the size of conventional FT reactors in an attempt to accommodate the low available volumes and so a different strategy is required - one that drastically improves the efficiency of the reactor. This would allow for the intensification of the process where the large gains in efficiency could potentially offset some of the losses in economies of scale.

Table 1.3: Total gas flared worldwide in 2018 (World Bank, 2019)

							2017- 2018	2014 -2018
		2014	2015	2016	2017	2018	Change	Change
1	**Russia**	18.3	19.6	22.4	19.9	21.3	1.4	3.0
2	**Iraq**	14.0	16.2	17.7	17.8	17.8	0.0	3.8
3	**Iran**	12.2	12.1	16.4	17.7	17.3	-0.4	5.1
4	**United States**	11.3	11.9	8.9	9.5	14.1	4.6	2.7
5	**Algeria**	8.7	9.1	9.1	8.8	9.0	0.2	0.3
6	**Venezuela**	10.0	9.3	9.3	7.0	8.2	1.2	-1.7
7	**Nigeria**	8.4	7.7	7.3	7.6	7.4	-0.2	-1.0
8	**Libya**	2.9	2.6	2.4	3.9	4.7	0.8	1.8
9	**Mexico**	4.9	5.0	4.8	3.8	3.9	0.1	-1.0
10	**Angola**	3.5	4.2	4.5	3.8	2.8	-1.0	-0.7
11	**Oman**	2.6	2.4	2.8	2.6	2.5	-0.1	-0.1
12	**Saudi Arabia**	1.9	2.2	2.4	2.3	2.3	0.0	0.3
13	**Egypt**	2.8	2.8	2.8	2.3	2.3	-0.1	-0.5
14	**Malaysia**	3.4	3.7	3.2	2.8	2.2	-0.6	-1.1

15	**Indonesia**	3.1	2.9	2.8	2.3	2.1	-0.3	-1.0
16	**Kazakhstan**	3.9	3.7	2.7	2.4	2.0	-0.4	-1.9
17	**China**	2.1	2.1	2.0	1.6	1.8	0.3	-0.3
18	**Congo**	1.3	1.2	1.1	1.1	1.6	0.4	0.3
19	**Turkmenistan**	2.0	1.8	1.8	1.7	1.5	-0.2	-0.5
20	**Gabon**	1.5	1.6	1.6	1.5	1.4	-0.1	-0.1
21	**India**	1.9	2.2	2.1	1.5	1.3	-0.2	-0.5
22	**Canada**	2.1	1.8	1.3	1.3	1.3	0.0	-0.7
23	**United Kingdom**	1.3	1.3	1.3	1.4	1.2	-0.1	-0.1
24	**UAE**	0.9	1.0	0.8	1.0	1.2	0.2	0.2
25	**Cameroon**	0.9	1.1	1.1	1.0	1.1	0.0	0.2
26	**Brazil**	1.5	1.3	1.4	1.1	1.0	-0.1	-0.5
27	**Qatar**	1.3	1.1	1.1	1.0	1.0	0.0	-0.3
28	**Ecuador**	1.0	1.1	1.2	1.1	0.9	-0.2	-0.1
29	**Kuwait**	1.4	0.9	1.1	0.8	0.9	0.1	-0.5
30	**Australia**	1.1	1.1	0.7	0.7	0.9	0.2	-0.3
	Rest of world	11.7	10.7	9.6	9.2	8.1	-1.1	1.1
	Global total	143.9	145.6	147.6	140.6	145.0	4.4	5.9

1.4 FT Micro-reactors in the XTL process

Process intensification is a growing field of interest in process design for several reasons including improved economics, smaller plant footprint, safer processes and reduced environmental impact (Holmen et al., 2013). Process intensification can promote significant efficiency gains through targeted process optimization, for example, and it can also completely transform a process to a point beyond the ordinary scope of optimization where efficiency gains are at least in the region of 3 orders of magnitude so that the throughput is likewise increased or the working volume is reduced accordingly (Jarosch et al., 2005; Leviness et al., 2014). Considering low volume feedstocks, process intensification is of particular interest as the miniaturised system would be more suited to process the relatively lower flows. As the focus here is on the FT reactor as an integral part of the XTL process, miniaturization of the reactor is particularly interesting. Micro-

structured reactors (MSR) are a branch of micro-structured processes (MSP) which are in turn a branch of process intensification focusing on miniaturization at the micron scale and lower. Micro-structured FT reactors will be the focus in this study.

Micro FT reactors, with hydraulic diameters in the sub-millimeter scale, have various advantages over conventional large-scale reactors, with scales in order of several meters in diameter and height, over and above the smaller footprint. The small nature of the reactor means that mass transfer is enhanced as the characteristic transfer time is reduced due to the much shorter diffusion paths (Kockmann, 2008; Kshetrimayum et al., 2016). Heat transfer is likewise improved given the higher surface area per unit volume of the smaller reactor (Pohar & Pazl, 2009; Bakhtiary-Davijany et al., 2011). The improved transport processes drive the process to a more kinetically controlled regime where the optimum possible reaction rates can be realized. In addition, it makes it possible to use more active catalysts where the large amount of heat produced by the exothermic FT reactions can be efficiently removed through the improved heat transfer capabilities of the micro reactor (Na et al., 2017; Leviness et al., 2014; Cao et al., 2009). The increased temperature control also improves product selectivity which is critical in FT syncrude production.

There are different kinds of micro reactors that have the potential to be applied in FT synthesis including micro packed bed, catalytic wall and monolithic reactors. See Figure 1.2 and Figure 1.3 for illustrations of the different types of micro-reactors. The most popular microreactor for FT applications seems to be the microchannel reactor with a coated catalytic wall because of the lower pressure drop and better flow distribution (Kashid et al., 2009). There are issues with regards to microchannel reactors that are yet to be fully addressed including the problem of scaling down from large process piping to the micro scale reactor channels. Flow maldistribution is invariably encountered which is detrimental to performance. This is an area that is ripe for study so that solutions can be found.

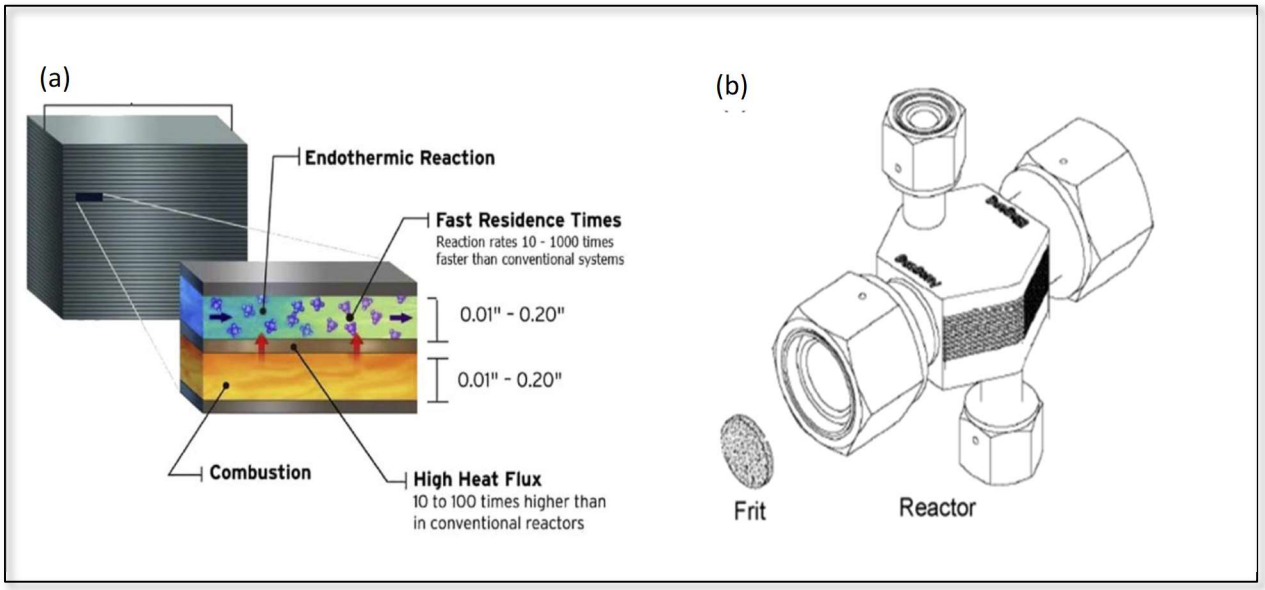

Figure 1.2: An illustration of an FT microchannel reactor: (a) FT microchannel reactor schematic diagram (Lerou et al., 2010) and (b) Illustration of an assembled microchannel reactor (Bakhtiary-Davijany et al., 2011)

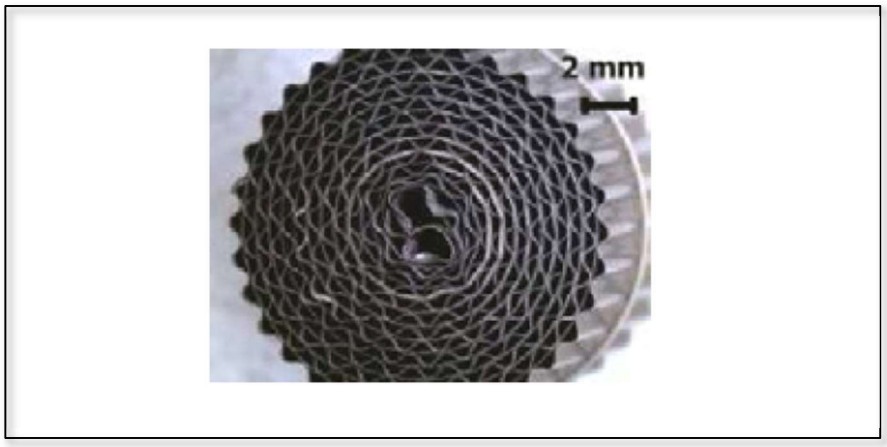

Figure 1.3: A micro monolith reactor for FTS application (Almeida et al., 2011)

Despite the potential benefits of micro-FT reactors, very little literature exists dedicated to their study and as a result the understanding of the process is limited. Consequently, there is a lack of detailed models describing micro-FT systems. It may be possible to extend the application of conventional FT reactor models to micro systems, by using slurry bubble column reactor (SBCR) models for example, but this has to be studied and the suitability of such models understood. The micro-scale nature of micro-FT systems may mean that the behaviour of these systems deviates from conventional ones. Factors such as the effects of fluid properties including surface roughness

and surface tension on performance may be more pronounced (Gunther & Kreutzer, 2009). Viscous dissipation (Fletcher et al., 2009) and conjugate heat transfer (Trachsel & von Rohr, 2009) may be a few of the parameters that would also have to be carefully considered.

1.5 Problem Statement

Given the potential ability of micro-FT systems to unlock natural resources that have thus far been overlooked, a thorough comprehension of the governing mechanisms in these systems is important. This has been lacking mostly because of the relative novelty of the concept in FT reactor applications. Reliable micro-FT reactor models are not openly available in literature and those that are accessible are not comprehensive. These models, although offering some insights into micro-FT processes, often rely on overly simplistic assumptions which have the effect of losing the complexity of the real process and rendering the model inaccurate.

In addition to the technical challenges, the economics related to the commercial viability of a micro-FT driven GTL plant are crucial. The economics associated with micro-FT reactor application must be favourable if this technology is to be adopted. The challenge is the lack of economic models to enable the determination of this viability. The problems around the micro-FT reactor are therefore two-fold, including the technical issues around the reactor model and optimal manifold design and economic issues regarding the methodology applicable in determining the economic feasibility of a mini-GTL plant using micro-FT technology.

1.6 Research Aim and Objectives

To solve the current problems outlined above, a holistic approach to the study of the micro-FT system will be adopted where the technical and economic aspects will be explored. The aim then, is to improve the understanding of micro-FT reactors through a comprehensive study and analysis of the reactor and its economic implications. To this end, the objectives of the study are outlined below:

- Investigation of the physical and chemical phenomena prevalent in the micro-FT reactor.
- Analysis of the hydrodynamics inside an FT micro-reactor.
- Analysis of the economic parameters influential in the costing of a mini-GTL plant incorporating micro-FT reactor technology.

- Development of a comprehensive model to describe the micro-FT reactor and its experimental validation.
- An economic analysis to aid in the economic appraisal of a micro-FT mini-GTL plant.

1.7 Statement of Novelty

Given the above problem statement, the author has identified a method for developing a robust and comprehensive FT microreactor model using a slurry bubble column reactor model as leverage. Ordinarily, mathematical models are derived from 1st principles based on the underlying physical properties of a system. This is done in this thesis albeit with a clear distinction – translating and adapting a model from a large-scale FT reactor to a microchannel reactor where the scale is orders of magnitude smaller. While the idea of using the large-scale model as a basis is not itself novel, the novelty presents itself in the way in which scale-dependant parameters are translated – this requires a great level of understanding around the fundamental physical and chemical processes inherent in both the large-scale and microchannel FT reactors.

The author will present the work by outlining the important scale-dependant parameters and then developing, adapting and translating such parameters to form a cohesive mathematical model for the FT microchannel reactor. The study of FT microchannel reactors and indeed their industrial application, is still relatively new and the study of the principles governing its operations stands to contribute significantly to the field of micro structured chemical processes. The model developed in this thesis will aid researchers and engineers in the field gain a better understanding of the physical processes with these reactors which should help in the development of better models, micro reactor design and microreactor performance optimization in the case of already operational reactors. Furthermore, this work directs particular focus to the hydrodynamics within a FT microchannel reactor. The author is cognisant of the importance of fluid dynamics in micro structured process equipment and this is studied, modelled and discussed in detail in this thesis. The author submits that the work carried out in this thesis in the manner described in the above three paragraphs, qualifies as novel and contributing to the current body of knowledge in the FT reactor field.

1.8 Thesis Outline

The thesis contains a literature review in Chapter 2 where important literature on the underlying concepts in FT micro reactors is analysed and discussed to offer insights into the workings of such reactors. Chapter 3 focuses on the physical and chemical parameters and variables that are important in the development of a FT microchannel reactor, with a particular focus on the hydrodynamic parameters. This chapter also focuses on the sub-models constituting the overall, unified model and how these interface and affect each other. Chapter 4 covers how the model was developed including the methodology and tools used. In chapter 5, the results from the model simulation are presented and discussed in detail to give the reader an appreciation of the inter-dependencies inherent in a microchannel reactor between the hydrodynamics, mass transfer and kinetics. This chapter also covers the validation of the simulation results by comparing the results with results from experiments in literature, conducted under conditions similar to those in this thesis. Also in Chapter 5, an economic evaluation from a capital expenditure point of view is conducted for a mini-GTL plant that would make use of a FT microchannel reactor. This is given to contextualize the economic benefits of micro reactor technology because of their increased efficiency. Lastly, Chapter 6 provides conclusions drawn from the study on the mathematical modelling, simulation, results interpretation and the economic model developed.

1.9 Conclusion

In Chapter 1, the background and history of FT synthesis (FTS) is briefly discussed to contextualize the position and role of FT microreactors in the field. FTS and its reliance on different carbonaceous feed sources from CTL, GTL and more pertinently, XTL process routes. Process intensification in the form of FT microreactors is introduced and discussed along with some its technical advantages. It is noted that FT microreactor models are scarcely available, necessitating the development of such a model to further the current understanding of their design and operation. It is further noted that economic analysis models of FT microreactor-based XTL processes are similarly scarce, so that it is important to develop a comprehensive techno-economic model.

Chapter 2: Literature Review

2.1 Introduction

In this chapter, literature pertinent to the understanding of FT micro reactors is detailed and analysed. The literature review focuses on the advantages offered by micro reactors with particular focus on heat and mass transfer phenomena. The different flow regimes possible in micro reactors are also discussed to aid in the understanding of the flow structures that develop in micro reactors under various flow rate conditions. The interfacial forces prevalent in micro reactors are then discussed to understand the importance of interfacial forces and tension within these reactors, particularly under 3-phase conditions. The importance of micro reactor channel geometry is then analysed to give the reader an appreciation of the effect that various geometric configurations has on flow dynamics in microchannel reactors. Finally, other important considerations for microreactor operation including reactor types, pressure drop across the channel length, residence time distribution and the important considerations to make when charging a reactor with catalyst during are discussed in detail.

Before an overview is provided on the principles of micro-reactors, it is important to contextualize the importance and novelty of such reactors, particularly as applied in FT synthesis, through a brief discussion of its advantages.

2.2 Advantages of Micro Reactors

Micro process technology has significant advantages over conventional systems that arise because of their appreciably smaller operating volume. It is this smaller volume that enables this technology to take advantage of decreased diffusion lengths resulting in greater mass transfer. This is significant in FT systems where mass transfer is sometimes rate limiting (Deckwer, 1991) such that an improved mass transfer rate translates to proportionally improved reaction rates. Heat transfer is also enhanced by a reduction in volume through an increased surface area to volume ratio, i.e., there is more available heat transfer area. This too leads to a de-bottlenecking of the overall reaction rate in reaction systems that are limited by heat transport. It becomes possible then to operate the reactor in a kinetically controlled regime, allowing greater freedom to enhance reaction kinetics without much consideration for heat transfer limitations that would otherwise promote undesirable hot spots or runaway reactions. By drastically reducing mass and heat transfer effects, a micro-reactor can operate more efficiently with higher conversions and throughputs

(Almeida et al., 2013). This is important in FT reactions that are extremely exothermic and often take place in reactors governed by heat transfer limitations.

In a microchannel reactor, a laminar, well defined and predictable flow generally develops (Hessel et al., 2004) ensuring a stable and predictable performance. The greater heat transfer ensures greater temperature control which in turn enhances selectivity (Arzamendi et al., 2010). The control over selectivity is beneficial as it saves on raw material consumption and reduces the load on downstream separation processes. The small nature of micro-reactors ensures that parameter changes are quicker, enabling even tighter control of the reactor conditions (Hessel & Lob, 2009). FT reaction products, as described by a distribution factor, are sensitive to temperature and other reactor conditions so that greater control of these conditions would allow for increased control over the extremely important product distribution.

The necessarily small scale of micro-reactors means that there is no need for scale-up procedures to get the reactor from lab to industrial scale. The micro-reactor channel, as developed in a lab, can simply be replicated such that the channels are stacked to form a compact array of parallel reactors. This process is referred to as scaling out instead of the conventional scaling up. Scaling out capabilities should greatly reduce the time to market of the reactor as well as the costs associated with pilot testing which is generally required for reactor scale-up (Hessel & Lob, 2009). The smaller volume of the reactor makes it inherently safer and this is similarly the case for stacked micro-reactors. This could make the process of meeting any applicable safety regulations easier, further improving the reactor's time to market. There is also the possible advantage that research and development houses could carry out the entire process from lab development up to industrial manufacturing and reactor delivery (Hessel & Lob, 2009). This is an interesting prospect particularly with regards to the ultimate cost of the reactor as a huge share of the cost associated with the use of traditional engineering and manufacturing houses to deliver the final reactor would be averted so that the cost of the micro-reactor should be markedly reduced.

In the following sections the main physical principles governing the operation of micro-reactors are considered and discussed. In chapter 3, which focuses on micro-FT reactor modelling, these principles will be further analysed in greater detail that is sufficient to develop a workable model.

2.3 Heat transfer

One of the main advantages of micro-scale reactors is the high heat transfer rates between the flowing medium and the wall. In standard size heat exchange units, for example, typical heat transfer rates are in the order of 850 kW/m^2 whereas in micro-sized reactors/heat exchangers heat transfer rates of up to 7900 kW/m^2 have been reported (Tuckerman & Pease, 1981). This represents a 9-fold increase in the capability of the system to remove heat and maintain a safe operating regime. Such a capability means that the heat transfer limitation normally present in conventional reactors is relaxed significantly so that the system should now have more flexibility of operation in as far as heat transfer limits are concerned. It would be possible then to employ catalysts with higher activities without the risk of poor temperature control which could lead to runaway reactions, poor product selectivity and safety incidents.

The increased heat transfer rates in micro-reactors are due to its increased surface area-to-volume (S/V) ratio. In conventional systems, S/V values range from 50 to 800 m^2m^{-3} for smaller compact heat exchangers versus a S/V of up to 10000 m^2m^{-3} for micro heat exchangers (Trachsel & von Rohr, 2009). This represents an order of magnitude increase in the surface area available per unit volume for heat transfer. As a rule, particularly in homogenous systems, the heat transfer coefficient is inversely proportional to the characteristic size of the vessel or channel, i.e., smaller microreactor channels will exhibit increased heat transfer coefficients.

2.4 Mass transfer

In heterogeneously catalyzed systems, which are the focus of this work, there exists internal and external mass transfer processes which explain the transfer of matter within the solid catalyst and outside the catalyst, respectively. All things being equal in terms of the catalyst make-up and configuration, the main factor influencing the mass transfer rates within the catalyst particle will be its size. Catalysts with smaller characteristic dimensions will tend to have reduced mass transfer limitations. This is even more so if we consider catalysts that are used in the form of a coating on the inner wall of micro-reactor channels. These catalysts are, by necessity given the already small size of the micro-channel, much smaller than conventional FT catalysts and should therefore exhibit pronounced internal mass transfer rates.

External mass transfer is enhanced by the smaller characteristic size of the micro channel reactor. This is because the path length between the bulk fluid phase and the solid catalyst phase is much

smaller than would be the case in conventional large reactor systems (Fletcher et al., 2009). It can be expected then that the characteristic mass transfer time will be significantly decreased, and the mass transfer gradients similarly reduced. As a result, microchannel reactors will have even lower overall mass transfer limitations than is observed in larger conventional systems. This immediately removes an obstacle to achieving a kinetically controlled system.

2.5 Flow regimes

Flow regimes in microchannels are important in the characterization of the hydrodynamics of the system and as a result the overall performance of the system. It can be appreciated that hydrodynamics affects multiple processes that are directly linked to the performance of a system including the mass, momentum and energy transfer. Determining the structure of flow prevalent within the microchannel reactor is therefore key in characterizing the flow environment under which the aforementioned processes will take place. The flow regimes generally encountered in two-phase flow in capillaries can be generally described by four patterns including bubbly, segmented, annular and churn-turbulent as observed experimentally by Serizawa et al. (2002). These are distinguishable by the relative velocities of the wetting/continuous and non-wetting/dispersed phases. In the study by authors Serizawa et al. (2002), high speed camera images were taken of the evolution of the different flow regimes in a 600 × 600 μm square microchannel. The study was aimed at investigating the effects of inlet mixing on flow dynamics. The images recorded during the authors' investigations are used for illustrative purposes in the discussions below.

2.5.1 Bubbly flow

Bubbly flow occurs when the non-wetting phase velocity is much lower than that of the wetting phase. Under such conditions the non-wetting phase will form bubbles or droplets depending on the two phases in question. These bubbles/droplets will be smaller in diameter than the microchannel size (Gunther and Kreutzer 2009). Bubble coalescence must be considered as it can lead to a change in the flow regime – from bubbly to segmented flow for example. The mechanism of bubble/droplet coalescence and break-up in microchannels has not been thoroughly investigated in the available literature. A visual depiction of bubbly flow in a microchannel is shown in Figure 2.1.

2.5.2 Segmented flow

When the relative velocities of the dispersed and continuous phases are more similar, i.e., their ratio approaches unity, a segmented flow regime is exhibited. In this regime, the dispersed phase takes up more space and forms elongated compartments separated by continuous media. There still remains a thin layer of the continuous phase at the wall of the microchannel. Coalescence of bubbles in an initially bubbly flow system can result in bubbles/droplets large enough to change the system from a bubbly flow to a segmented flow regime. It is important therefore to understand the threshold for bubble coalescence when aiming to control the flow regime. Segmented flow has been suggested to be advantageous in terms of its facilitation of increased mixing and mass transfer and reduced dispersion (Song et al., 2003). A visual depiction of this phenomenon is shown in Figure 2.1.

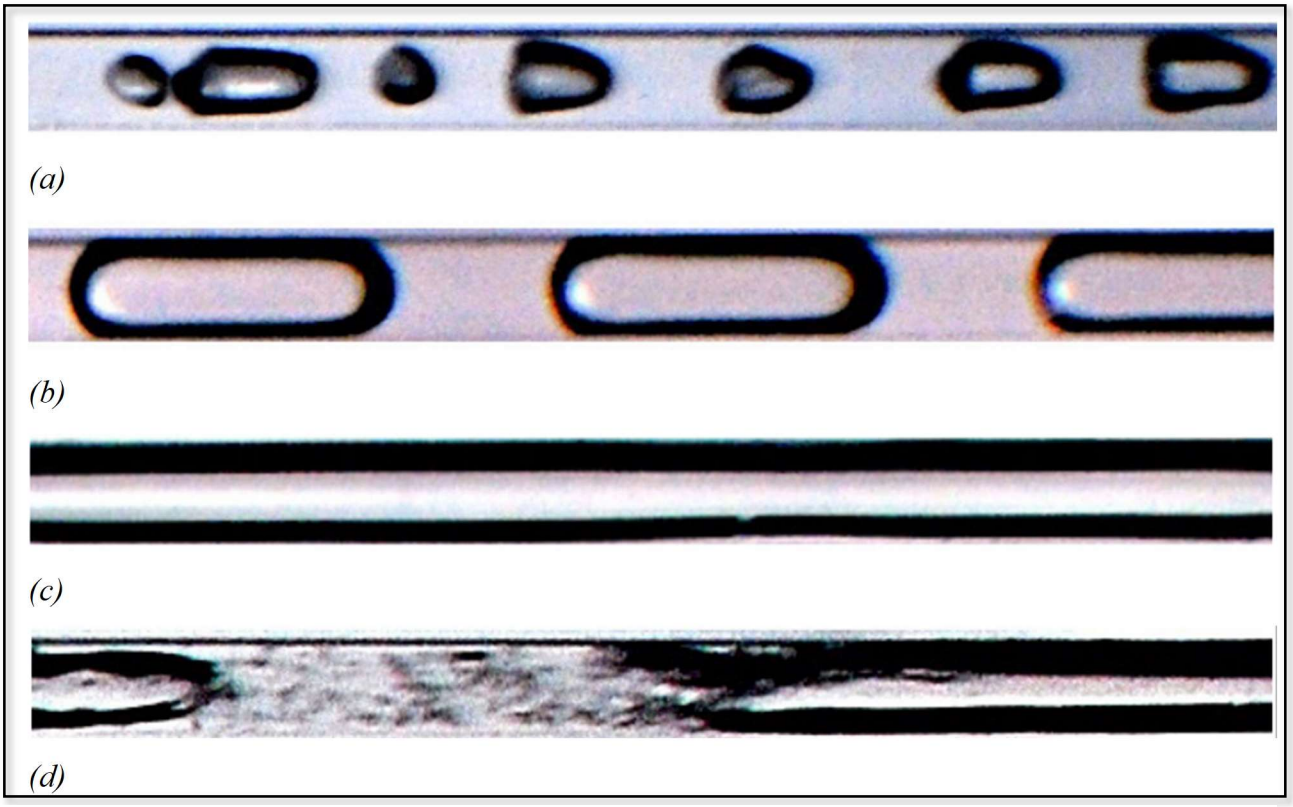

Figure 2.1: High speed camera images showing (a) bubbly, (b) segmented, (c) annular and (d) churn-turbulent flow in a square microchannel (Serizawa et al., 2002)

2.5.3 Annular flow

When the velocity of the dispersed phase is further increased beyond that of the continuous phase, the bubbles/droplets dominate the volume in the microchannel such that this phase covers the entire cross section of the channel, with only a thin layer of the continuous phase at the wall of the channel (see Figure 2.1). The continuous phase therefore flows only in the annular region of the channel. The thickness of the continuous layer is affected by the velocity of the dispersed phase as well as the shape of the channel. In rectangular channels, more liquid will collect around the corners of the channel and in that way facilitate the variation of the thickness of the layer based on its position in the channel. The thickness of the continuous layer is an important consideration, specifically relating to mass and heat transfer from the bulk non-wetting phase through the wetting phase layer and to the channel wall.

2.5.4 Churn-turbulent flow

A further increase of the velocity of the dispersed phase beyond the continuous phase velocity leads to a turbulent flow regime where bubble/droplet sizes vary in a chaotic manner. Regular patterns are no longer noticeable, and the phases make contact with the wall interchangeably. It is more difficult to control the system if operated in this regime. See for an illustration of churn-turbulent flow in a microchannel.

2.6 Interfacial Forces

Because of the characteristic size of microchannels and the dominance of laminar flow as a result, interfacial forces are one of the key dominating forces in microchannel multiphase flow. It can be appreciated that at larger scales, interfacial effects are generally not as influential as inertial and and/or viscous forces but in the case of flow through micro-size channels they seem to be as important if not more important. The relative effects of inertial, gravitational and viscous forces relative to interfacial forces can be characterized through the use of dimensionless numbers. The Weber (We), Bond (Bo) and Capillary (Ca) dimensional numbers (Equations 2.1-2.3) provide a convenient means of comparing the various forces in question relative to interfacial forces.

$$We = \frac{\rho {U_d}^2 d_h}{\sigma} \qquad \text{Eq. 2.1}$$

$$Bo = \frac{\Delta \rho g {d_h}^2}{\sigma} \qquad \text{Eq. 2.2}$$

$$Ca = \frac{\mu^2 U_d}{\mu_d \sigma} \qquad \text{Eq. 2.3}$$

where ρ = density (kg/m^3)

U_d = velocity of the dispersed phase (m/s)

d_h = hydraulic diameter (m)

σ = Interfacial tension (N/m)

μ = viscosity of the continuous phase (Pa.s)

μ_d = viscosity of the dispersed phase (Pa.s)

Gunther & Jensen (2006) reported an increasing interfacial force domination over the other body forces of concern as the characteristic size of the channel decreases. This is illustrated in Figure 2.2 for organic-gaseous and aqueous-organic systems under a changing microchannel hydraulic diameter in ambient pressure and temperature conditions. The authors further studied the effects of the dispersed phase fluid velocity on the dimensionless groups in question and while Bo is not materially affected, Ca and more so We are affected by the change in velocity and increasingly dominate the interfacial forces and relatively high velocities. It remains evident that at lower velocities and smaller channel sizes, which are typical of microfluidic systems, interfacial forces dominate the flow structure.

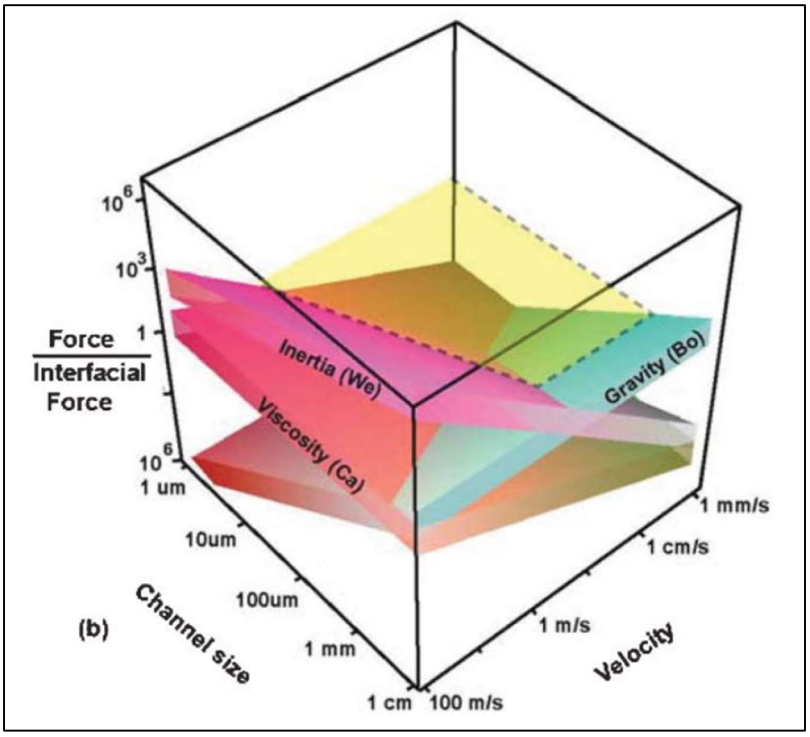

Figure 2.2: The effects of channel size and dispersed phase fluid velocity on the We, Ca and Bo numbers (Gunther & Jensen, 2006)

2.6.1 Interfacial effects in multiphase systems

In multiphase systems, fluid-fluid and/or fluid-solid interfacial tensions must be considered together with their impact on flow stability and dynamics. In a heterogeneously catalyzed multiphase flow microreactor, as is the focus of this study, interfacial forces between the three solid-liquid-gas phases may have to be carefully considered and in order to establish an understanding of the hydrodynamics therein.

The interfacial forces present between the solid-gas, liquid-gas and solid-liquid boundaries can be denoted as σ_{sg}, σ_{lg} and σ_{sl} and each of these affect the system specifically with regards to bubble formation and shapes and the wettability and liquid adsorption to the microchannel wall. If we consider a point in the microchannel where liquid, gas and solid phases are all in contact with one another as shown in Figure 2.3, the curvature of σ_{lg} plays the important role of defining the wettability of the solid surface. This curvature can also be fairly represented by a contact angle θ_{sf} as illustrated in Figure 2.3. θ_{sf} is itself influenced by all three prevailing interfacial forces as in Young's equation shown below in Equation 2.4.

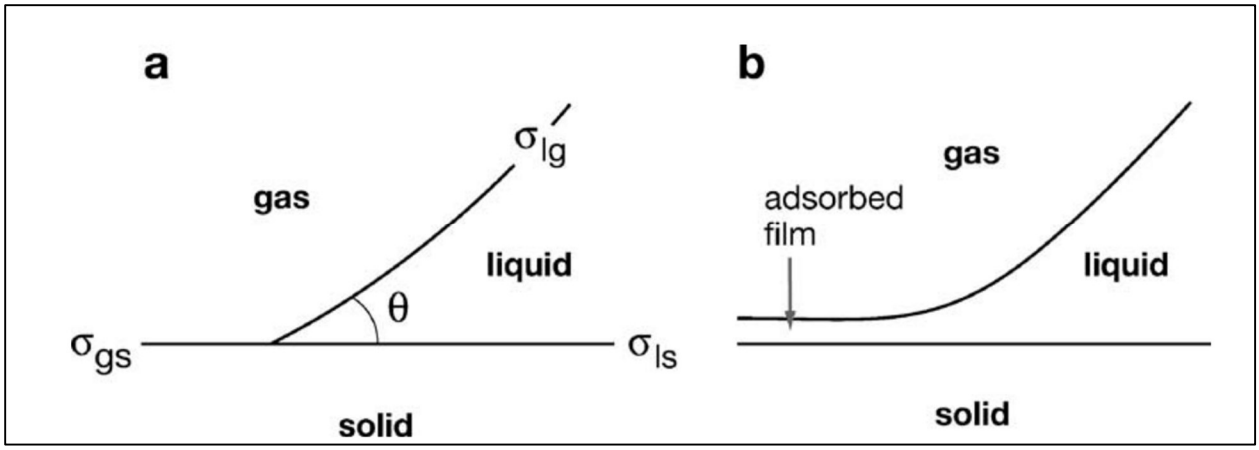

*Figure 2.3: Interfacial forces between liquid, solid and gas phases in a three-phase system under (a) non-wetting and (b) wetting conditions (*Ajaev and Homsy, 2006*).*

$$\sigma_{lg} cos\theta_{sf} = \sigma_{sg} - \sigma_{ls} \qquad \text{Eq. 2.4}$$

The importance of interfacial forces in multiphase microfluidic systems is apparent. Depending on the interfacial tension between the phases, the flow dynamics will take on a particular behavior based on the bubble/droplet morphology and surface-fluid effects including fluid adsorption and surface wettability. This should ultimately affect the mass transfer between the phases which is a key consideration in the design of microchannel reactors.

2.7 Channel Geometry

Conventionally, chemical reactors are designed with a circular cross-section. Microreactors do not necessarily conform to this convention and can take on a variety of shapes depending on the means of manufacture. The manufacturing process of microchannels is specialized and requires one of etching, patterning or even more recently, jet machining processes (Belloy et al., 2002; Ghobeity et al., 2008) which tend to produce channels with a rectangular cross-section. It is evident then, that 2D reactor models which are applicable in cylindrical systems, may not be completely sufficient for rectangular/non-round systems depending on the hydrodynamics prevalent in the particular system.

For segmented bubble flow, Wong et al. (1995) studied the liquid film morphology and its impact on the momentum balance in a polygonal capillary. The authors theorized a variable liquid film thickness adsorbed to the walls of a polygonal tube (Figure 2.4) in contrast to a uniform liquid film

thickness as would be expected in circular capillaries. In the corner regions of a rectangular capillary, the thickness of the liquid film thickness would be at a maximum and a minimum in the central region of the straight sides of the channel where the contact angle approaches zero.

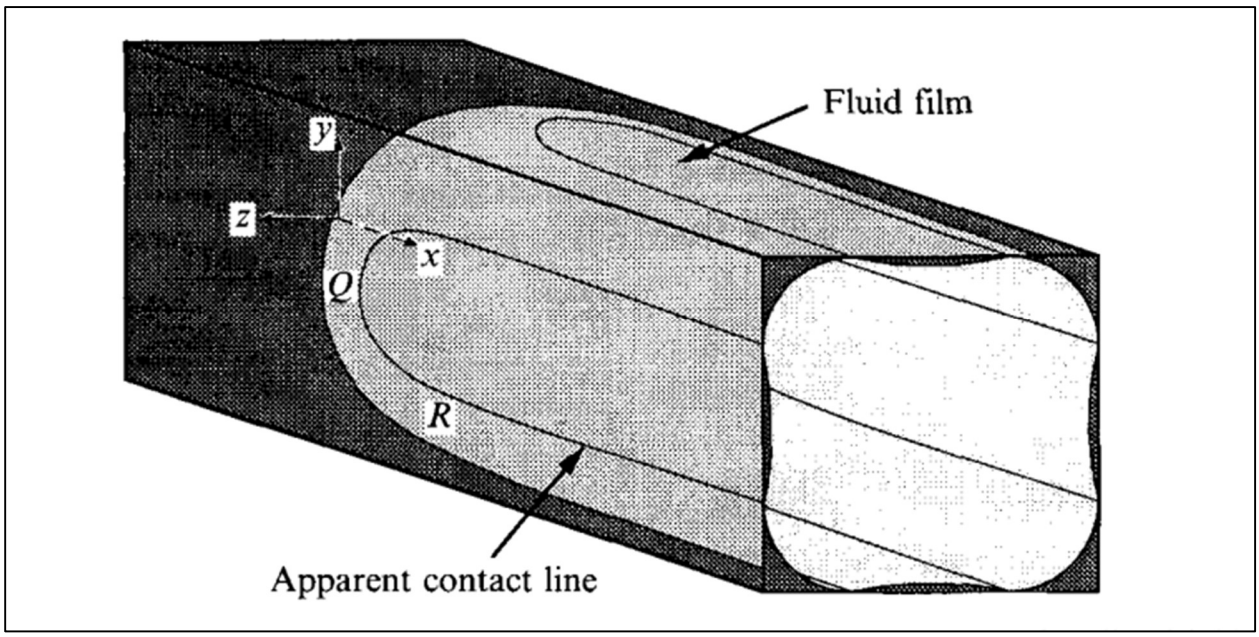

*Figure 2.4: Illustration of segmented 2-phase bubble flow in a rectangular capillary with variable film thickness (*Wong et al., 1995)

The variable film thickness requires a reconsideration of the pressure-velocity effects as analyzed in standard cylindrical systems given the different set of hydrodynamic parameters, i.e., the drag coefficients. It is expected therefore, that the pressure drop model will not follow a classical 2-phase approach but will have to be adapted specifically for micro-sized polygonal structures as encountered in microchannel reactors.

2.8 Reactors

The microreactors available for heterogeneously catalyzed systems can be characterized through identification of the manner in which the catalyst is deposited in the reactor**.** Table 2.1 outlines the different reactor types and their advantages and disadvantages. The selection of a specific reactor will depend on the design temperature and pressure conditions within the reactor. The performance of the reactor measured through product selectivity, yield, and reagent conversion will also inform

the type of reactor to be chosen. The above-mentioned reactor parameters are dependent on the configuration of the reactor-catalyst system and these are outlined in this section.

Table 2.1: Types of 3-phase catalyzed microchannel reactors (Fletcher et al., 2009)

Microreactor Type	Description	Advantages	Disadvantages
Packed Bed	Prepared by filling the microchannel with catalyst particles.	Relatively easy to add the catalyst. Conventional and/or optimized catalysts can be used.	Has a relatively high pressure drop and is prone to flow maldistribution and channeling.
Catalytic Wall	Catalyst coated on the inner wall of the microchannel. Most commonly used.	Produces a relatively lower pressure drop.	Specific area of the catalyst layer has to be enhanced through complex treatment of the surface onto which the catalyst is layered.
Catalytic Bed	Catalyst is applied on a structure such as a filament or wire and incorporated into the reactor. Supposed to be a compromise between catalytic wall and packed bed microreactors.	Low pressure drop. Narrow residence time.	Complex treatment of the wire or filament surface is required to enhance the specific area available for reaction.

2.9 Pressure drop

In micro-structured reactors, the pressure drop is an important parameter to consider given the small size of the reactors. Depending on how the catalysts are arranged, the pressure drop can be significant. The relatively high pressure drop in a packed-bed micro-reactor can be avoided by selecting a catalytic wall reactor which has significantly less flow restriction but has its own disadvantages in other respects, including a reduced contact time between the bulk fluid and the catalyst (see Table 2.1).The catalytic bed microreactor may provide a compromise between pressure drop and residence time given its use of a mesh structure coated with a catalyst and embedded within the reactor. Ajmera, et al. (2002) proposed the use of a cross flow configuration that would make use of multiple feed streams per reactor entering in a normal direction to the channel (Figure 2.5). Each feed stream would be exposed to a reduced bed thickness and thus a reduced pressure drop. Additionally, the authors observed an increased flow distribution within the channel. The main drawback to this cross-flow configuration could be scalability of the channels. Microreactors require scaling out, by packing multiple channels together and distributing the bulk flow evenly through each channel, to achieve high enough throughputs. Cross-flow microreactors may prevent the packing of multiple channels together in a compact manner and may require a much larger footprint which would be potentially prohibitive.

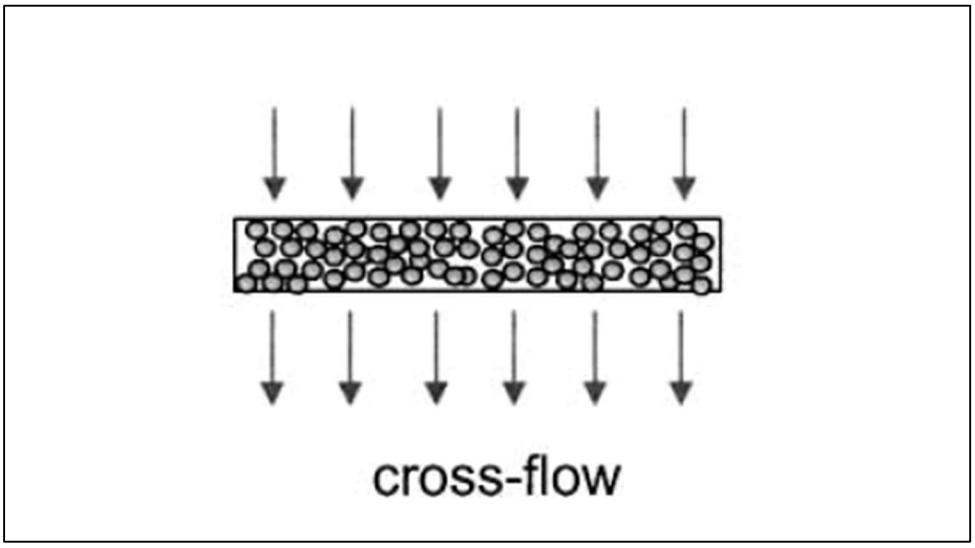

*Figure 2.5: An illustration of a packed bed reactor with multiple cross flow streams (*Ajmera et al., 2002*)*

2.10 Residence time

The residence time is a function of the configuration of the microreactor in as far as providing enough contact time with the catalyst in a heterogeneously catalyzed system. The catalytic wall reactor will provide the least contact time which may be undesirable particularly for systems with lower reaction kinetics. The packed bed microreactor would provide the longest residence time as the flowing fluid would have to pass through a series of closely packed catalyst particles.

2.11 Catalyst deposition

The deposition of catalyst material in a heterogeneously catalyzed system is an important consideration in selecting any specific reactor configuration. There are various deposition methods for metallic microreactors including suspension, sol-gel, impregnation, electrochemical, vapour and flame spray deposition techniques and the use of zeolites on top of microstructures (Belloy et al., 2002; Wong et al., 1995; Hazel & Heil, 2002a; Hazel & Heil, 2002b). Of these, the sol-gel deposition technique is the more commonly used (Gunter et al., 2009) but any of the above methods could be applied. In packed bed microreactors, catalyst deposition will probably be more convenient than would be the case in catalytic wall microreactors given that conventional catalysts with well-established deposition methods can be used in the packed bed. Catalyst deposition may be more complex in catalytic microreactors as the catalysts applied are non-conventional and would have to be specially synthesized. It is important then, to carefully consider the type of catalyst and the ease of its applicable deposition method when selecting a microreactor type.

2.12 Models

There have been several attempts at modelling FTS on a micro basis. The question in this regard has been whether conventional large-scale FT reactor models could be used at the much smaller micro scale. There are indeed several considerations to make regarding those assumptions that may not hold for reactor models at the small scale. The surface properties, e.g., the surface roughness, of the reactor material may be of more concern given the small characteristic diameter of the micro-reactor (Valdes et al., 2007). While surface effects in large diameter reactors are often negligible because the bulk reacting volume is significantly greater than the material layer at the wall surface, they may be significant in micro size reactors in which the material layer at the surface wall is much more comparable to the bulk volume. Surface roughness may, for example, have amplified effects in micro-reactors as compared to its effect in large diameter reactors.

Another consideration is whether fluids in micro-reactors still behave on a continuum basis. The small characteristic size of micro-reactors makes this question relevant as there may be disturbances in the fluid's continuity (Fletcher et al., 2009). Viscous dissipation may also be a real issue at this scale given the very large velocity distributions present within the reactor channel. The energy released may then have to be characterised and considered in the modelling of micro-reactors. Other effects including liquid surface tension, axial heat conduction, wall slip and entrance region effects may also need to be reconsidered for micro-reactor modelling (Hetsroni et al., 2005).

2.12.1 Physical Models

Derevich et al. (2012) studied the hydrodynamic effects in a microchannel FT reactor by employing material and momentum balance equations in a 2-dimensional 2-phase model considering the downward flow of gases and liquids in a cylindrical microchannel with catalyst-coated walls. The authors considered the uneven, rough surface of the microchannel and incorporated this into the model to account for its effect on the flow dynamics of the 2-phase fluid. The authors were able to produce results detailing the effect of space velocities on the liquid film thickness at the wall of the microchannel and on the pressure profile within the reactor. The kinetics of the reactor were not explicitly modelled but a linear reactant conversion profile along the reactor length was assumed. Whilst the focus of the work was on hydrodynamic effects, the effects of kinetics on the fluid dynamics cannot be underestimated and need to be considered more explicitly. It must be appreciated that the reactants conversion will most likely not follow a linear pattern and that a more realistic appraisal of the kinetics is important. The hydrodynamics effects considered must therefore be interpreted carefully.

Gumuslu & Avci (2012) used a 2-phase gas-solid heterogenous approach, modelling the reactor using momentum, material and energy conservation laws. The authors used a wash-coated catalytic wall reactor as a basis for the model in which the effects of wall material and thickness, coolant channel side length and wall texture on heat transfer performance were studied. HTFT conditions were considered and Langmuir-Hishelwood type kinetics were used to model the reactant consumption and product distribution. The authors concluded that coolant flowrate and wall thickness have a significant effect on the heat transfer performance of the microreactor and perhaps more notably, determined that the application of a baffled reactor channel wall improves

heat transfer. This is attributed to the increased local mixing resulting in higher rates of heat transfer. Whilst this observation is promising, the effects of such a configuration should be considered more thoroughly to understand its complete impact on the flow dynamics and by extension the mass transfer. The model provides a useful overview of the parameter relationships in a HTFT microchannel reactor and a validation of the results would have added more value in this regard. A validation exercise, preferably using experimentation would have confirmed the accuracy of the model. This highlights the importance of experiments to test the validity of purely theoretical models so that such models can be adopted and applied confidently.

Park et al. (2015) modelled a large-scale reactor with packed parallel microchannels using channel decomposition and cell-coupling methods. This method is supposed to help reduce the computational expense associated with using more common computational fluid dynamics (CFD) methods for such large scale microreactors. Energy and material balances were used, and the model results validated against literature data. It is noted though, that the validation exercise was limited since the authors relied on results from experiments conducted elsewhere and as a result had no control over the design of that experiment. This brings the validation and the model accuracy into question. The authors also neglected viscous forces and shear stresses in the microreactor arguing that they were insignificant. The authors do not provide any more justification for this and these parameters may as well be important as previously stated because of the unique features of microreactors. A similar exercise was undertaken by Jung et al. (2016) wherein the cell-coupling method was used together with multi-objective optimization to model a large-scale reactor with multiple parallel reaction and cooling channels.

2.12.2 CFD models

There have also been focused attempts to model the hydrodynamics in microchannel reactors. CFD is the best placed tool to model and visualise fluid dynamics and it has been applied extensively in microchannels flow modelling. Shin et al. (2013) used a CFD approach in modelling a packed bed microchannel FT reactor under LTFT conditions. The dimensions of the microchannel modelled are not strictly in the micron scale but are small enough to be considered adequate for understanding hydrodynamics in microchannels. In the study COMSOL Multiphysics was used and the results validated experimentally. COMSOL Multiphysics is a finite element analysis, solver, and simulation software package that's used in a variety of physics and engineering

applications. In defining the gas component properties within the reactor, the authors used Octane as the representative hydrocarbon molecule. This raises questions as to the validity of such a generalization given the extensive array of hydrocarbons of different chain lengths and configurations in FT reactor products particularly considering the longer chain products prevalent in LTFT conditions. The generalization was made to counter the computational limitations experienced by the authors. In a similar manner, CO, H_2 and C_4H_{10} where the chosen representatives for the permeability calculation within the porous catalytic material. Whilst CFD software has great capability in modelling complex systems such as microchannel FTS, care and consideration should be afforded to avoid the simplifications made for the sake of computational convenience so that the system does not become oversimplified. Extra effort should be taken then, to prepare adequate resources before a computational exercise of this nature is undertaken so that oversimplification can be avoided as far as possible. The authors were able to produce results showing the effects of coolant flow and feed temperature on CO conversion and reactor bed temperature.

Using ANSYS CFX, Arzamendi et al. (2010) studied the hydrodynamics in a catalytic wall FT microchannel reactor. ANSYS CFX is a computational fluid dynamics software that's used to model the fluid dynamics in physical systems. A LTFT system was modelled under a cross-current coolant and reactor channel configuration. The study focused on the heat transfer effects and profiles within the reactor under high GHSV conditions between 0.075 and 0.4s. Considerations were given to the effects of buoyancy on the reactor coolant side given a 2-phase liquid-vapour mixture that develops in the coolant channels. The authors determined that heat exchange effectiveness could be improved by reducing the steam content in the coolant channels when considering the buoyancy forces within these channels. Similarly, Kshetrimayum et al. (2016) modelled the fluid dynamics in a microchannel FT reactor using ANSYS Fluent. Various coolants were simulated in the study including oil and saturated water and subcooled water where saturated water was found to provide more heat transfer capacity. These studies are particularly important as few other modelling attempts have considered the coolant side and its possible impacts on the overall performance of the reactor. Since the reactor has to produce high heat transfer across the reaction and coolant channels to sustain the required kinetics, the coolant side should be considered as it is a vital part of the heat transfer process. The flow dynamics also need to be considered on the cooling side as well.

2.13 Conclusion

A survey of pertinent literature has been undertaken. It has been shown that microreactors have several advantages over large scale reactors including improved heat and mass transfer, improved selectivity control and more efficient scale-up programs. The prominent flow regimes in microchannel reactors were analyzed and four distinct flow structures were identified including bubbly, segmented, annular and churn-turbulent flow depending on the flow through the channel. Microchannel reactors are generally operated in the laminar flow range where interfacial forces dominate. Microreactors present unique physicho-chemical interactions which should be thoroughly considered to enable an understanding of their operation. Reactor geometry is an important consideration with cylindrical channels more suited for even flow distribution but for ease of manufacturing, rectangular channels are the more favorable. The sol-gel catalytic deposition method is more common than other methods for catalytic wall microreactor catalyst deposition while the use of conventional catalysts would make a packed bed type of microreactor more convenient for catalyst deposition and handling.

An analysis of current FT reactor modelling work has been given, detailing the relatively scarce works that are available in literature. The modelling efforts include the development of 3-phase mathematical models that consider conservation equations, heat transfer, mass transfer, kinetics and fluid dynamics to varying degrees. The adoption of a wide variety of reactor configurations is also a prominent feature in the literature analysed. CFD modelling, which forms an alternative modelling pathway specifically for hydrodynamic considerations, was attempted by a few authors. It is noted that CFD simulations are computationally intensive and should be conducted with care, with particular attention needed around parameter minimization and numerical solver efficiency.

Chapter 3: Materials & Methods

3.1 Model Principles

3.1.1 Introduction

The microreactor, specifically when considered in Fischer-Tropsch synthesis, provides an opportunity for process intensification and indeed the unlocking of new, previously untapped energy sources. It is important therefore to understand and quantify the working principles, limitations and optimal operating regimes within this reactor. In this chapter, the physical and chemical principles required to comprehensively model an FT microreactor are explored and discussed. These will form the basis of the model, the development of which is also discussed in detail in this chapter.

3.1.2 Continuum Assumption

In conventional systems, the assumption of a continuum in any involved fluid is justified. Bulk fluids in these systems behave as a single medium without any discontinuities in the fluid's physical properties including density, temperature, pressure, viscosity, etc. Whilst on a molecular basis, physical parameters may have some variations, a large number of collisions in conventional systems allows for transfer of these physical phenomena between molecules at a rate that is sufficient for treating the fluid as a single continuous medium where the physical properties can be averaged. Additionally, a continuum model of a fluid suggests the following:

- A linear relationship between stress and strain
- A no-slip boundary condition at the wall
- A linear relationship between the heat flux and temperature
- No temperature discontinuity at the fluid solid interface

The same assumption may not be readily made for fluids under microscale conditions as in FT microreactors. The micro size channels may affect the continuity of the fluid which may lead to the necessity of considering physical property variations on a molecular scale. Under such conditions, the classical Navier-Stokes equations may not hold. The Knudsen number (Equation Eq. 3.1) is a convenient means of determining the continuum nature of fluid flow in a channel. By

taking into account the molecular mean free path (λ) of the fluid and the characteristic dimension of the channel (L) it is possible to predict the continuum nature of the fluid.

$$Kn = \frac{\lambda}{L} \qquad \text{Eq. 3.1}$$

A high Kn indicates a larger molecular mean free path and/or a smaller channel size which will tend to a less continuous fluid medium. The reverse is also true where a smaller molecular mean free path and/or a larger channel size will tend to a more continuous fluid medium. In light of this, continuum effects can be assumed for a Kn<0.1 (Fletcher et al, 2009), otherwise non-continuum effects would have to be considered. This criterion will be different for various systems as evidenced by a more conservative criteria put forward by Dongari et al. (2009) where continuum effects can be considered for Kn<0.001. The authors provide a more general profile of fluid medium continuity based on Kn (Figure 3.1).

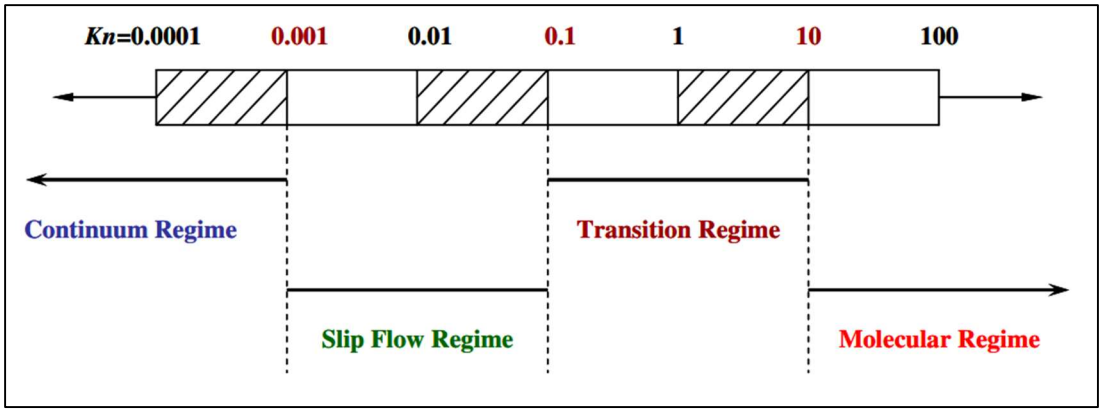

*Figure 3.1: Fluid continuity profile under different Knudsen numbers (*Dongari et al., 2009*)*

In Figure 3.1, the molecular regime is predominant under Kn >10 below which is the slip flow regime and the transition regime between the continuum and molecular regimes. The slip flow regime encompasses the range of conditions where slip flow, particularly at the wall would be predominant. In this study, the slip flow regime will be taken as the cut-off point before non-continuum effects are considered, i.e., the continuum assumption will hold for Kn <0.1 which is in agreement with Fletcher et al. (2009).

Under typical FT microreactor operating conditions (Table 3.6), Kn for both H_2 and CO are at least 500x below the threshold limit for non-continuum effects, even when considering the more

conservative limit of 0.001. This means that the continuum assumption holds for the range of conditions envisioned in this thesis.

3.1.3 Hydrodynamic model

In addition to the contacting pattern within the reactor, it is also important to characterise the phases present in the microreactor. In the current study, a low temperature Fischer-Tropsch (LTFT) system will be studied which produces long chain hydrocarbon products that are liquids at the prevailing temperatures. This means a three-phase gas-liquid-solid system will be present including the gaseous reactants, gas and liquid products and the solid catalyst. It is important then to understand how each of these phases behave individually and how they interact with one another. In conventional large-scale systems, the slurry bubble column reactor (SBCR) is a good example of a three-phase LTFT reactor where the gas and liquid along with the reactor catalyst interact intimately.

The approach taken in this study will be to adapt the hydrodynamic models used in conventional SBCRs to FT microreactors taking into account the effects of the micro size of the reactor on respective hydrodynamic parameters. The work by Mamabolo & Nkazi (2019) which details the hydrodynamic models for SBCRs will be used as a basis.

3.1.3.1 System Conditions

Before the hydrodynamics in micro-FT reactors can be explored, it is important to set out the system conditions detailing the operating and physical conditions in the system. A three-phase system is being considered where CO and H_2 are fed into a rectangular microchannel. The syngas mixture flows through the microchannel, making contact with the loosely packed catalyst bed to produce gaseous and liquid hydrocarbon products. The gas and liquid phases interact and depending on their relative velocities, form a bubble laden flow. This flow may contain bubbles of different shapes particularly under turbulent flow conditions. It will be assumed that the bubbles formed vary in size and their treatment will be simplified by assuming two distinct bubble classes including large and small bubbles. This is important given the different behaviours, e.g. bubble velocity and bubble hold-up, of bubbles depending on their size. This is similar to their treatment in a conventional FT SBCR although the average bubble size would be larger in the larger scale system. This is certainly a safer assumption than if a uniform bubble size was assumed given the potentially dynamic flow structures within the microreactor. The modelling then, will be divided

between 4 compartments including the large and small bubble compartments, liquid compartment and the stationary solid catalyst compartment.

3.1.3.2 Flow models

Given the conceptualization of four different compartments, the flow dynamics in each of these compartments has to be understood and modelled. Characterization of the hydrodynamics in most systems is generally fairly represented by the nature of the mixing in that system and this is the case in the current system under study. This mixing is represented by axial dispersion which can be explained as the spatial gradient of matter and energy that exists in the direction of the theoretical axis of the microreactor. Compared to conventional large scale FT reactors, the axial dispersion models for microchannel systems are extremely scarce with very few authors having developed such models. In this section, the available axial dispersion models for the gas and liquid compartments applicable to the microchannel system will be analyzed by studying the models used in conventional and to some extent microreactors.

In a microreactor, the axial dispersion will be along the height of the reactor. Dispersion in a microreactor is important in quantifying the extent of mixing in the reactor. Greater mixing would represent conditions closer to those in CSTRs whereas less mixing would represent conditions that reflect a more plug-flow system. In an ideal plug flow reactor, an infinitesimally small unit volume of reagents at a point z in a channel will have no interaction with another infinitesimally small unit volume of reagents at a point $z+\Delta z$ downstream in the column. This means that the unit volume that is at a more advanced position will not mix with and dilute the unit volume that precedes it. The consequence of this is a system in which the axial concentration gradients are pronounced along the reactor length/height. This would normally lead to a higher reactant conversion than can be achieved in an ideal CSTR where the perfect mixing assumed in the model would result in no concentration gradients within the reactor.

Radial dispersion will be excluded from the model as its contribution can be considered negligible. This can be justified by considering that it only forms a tenth of the axial dispersion values typically found in more conventional larger three-phase FT reactors (Deckwer, 1991). It can be expected therefore, that the radial dispersion/axial dispersion in microchannels will at least be similar if not lower than that in large-scale FT reactors. This would suggest that radial dispersion

is an insignificant hydrodynamic parameter whose impact on microreactor performance is unimportant.

3.1.3.2.1 Gas phase dispersion

As stated in earlier sections of this report, the hydrodynamic parameters used in conventional 3-phase FT reactors will be used as a basis to see if they can be applied to the micro-scale reactors. Following this approach, the gas phase dispersion coefficient models utilized in large scale FT reactors and more specifically, the SBCR, will be evaluated for use and possible application in FT microreactor hydrodynamic models. This approach is certainly more efficient and should yield some positive results given the already complex nature of the SBCR hydrodynamic models as evidenced by the work of Mamabolo (2018), and in other works (Sehabiague, 2012; Behkish et al., 2006; Bukur, 1983; Degaleesan et al., 1997) in which a comprehensive hydrodynamics focused model was developed. In other words, there already exists a great deal of comprehensive and detailed work done on conventional 3-phase LTFT reactor modelling and it is worth an attempt to leverage said work for the development of a new and relatively novel FT micro reactor.

Compared to liquid phase axial dispersion, there have been limited studies focused on axial mixing in the gas phase which are discussed here. Mangartz and Pilhofer (1980) studied the gas phase axial dispersion in an FT SBCR and attributed the axial dispersion to the column diameter, superficial gas velocity and gas hold-up. According to Deckwer et al., (1980), the modelling of axial dispersion in the gas phase is only justifiable under conditions of high reactor conversion. This is certainly the case in the Fischer-Tropsch process that is being considered in this thesis. Iliuta et al., (2007) and Rados et al. (2005) also assumed the presence of axial dispersion in the gas phase in developing an SBCR model citing the interaction between bubbles of the same size class as a factor in the extent of axial dispersion.

Table 3.1 lists studies in which axial dispersion in the gas phase was considered and modelled. In a study by Schweitzer and Viguie (2009), the authors determined through the use of a radioactive tracer test that the Peclet number (Pe), which is the ratio of transport by convection to that by diffusion, in the large bubble class was six times more than in the smaller bubble class. It is based on these results that the authors advocated for the negligence of axial dispersion in the gas phase when modelling hydrodynamics in an FT SBCR. To support this, Vermeer and Krishna (1981) reported in their study the observation of a swirling upward movement of large bubbles through

the SBCR with no noticeable dispersion, leading the authors to conclude that a plug flow regime was more likely in the gas phase. These assertions were contradicted by Calderbank and Moo-Young (1961) however, where these authors suggest that axial dispersion in the gas phase is often much higher than that in the liquid phase.

It is clear that there are differing opinions on the importance of axial dispersion in the gas phase. What is clear is that dispersion in this phase is predominantly affected by the reactor diameter, reactant superficial gas velocity and the gas hold-up within the reactor as clearly shown in Table 3.1. There is no clear indication that this dependence would be significantly altered at the micro-reactor scale and should therefore be eligible for consideration in the modelling of said microreactors.

In the microreactor, axial dispersion in the gaseous phase cannot simply be ignored given the greater importance of diffusion versus convection with respect to mass transport. Interfacial force effects play a crucial role in the general hydrodynamics within the reactor and would therefore also be a potential factor in the dispersion within not only the gas phase, but the liquid phase as well. It would therefore be important to model the gas phase axial dispersion in order to accurately account for mixing which should ultimately affect the reactor performance. Additionally, if there is any contention as to the extent of mixing in the gas phase, as is clearly the case in large scale FT SBCR's, it would be more prudent to include it and thus confirm its importance or indeed non-importance. As a result, axial dispersion will be considered and modelled in the gas phase of the microreactor system being considered in the current study.

Table 3.1: Gas phase axial dispersion coefficient correlations

Correlation	Experimental conditions	Reference
$\boldsymbol{E_g = 50{D_C}^{1.5}(\frac{U_g}{\varepsilon_g})^3}$		Mangartz and Pilhofer (1980) (as cited in Deckwer et al., 1980)
$\boldsymbol{E_G = 20{D_C}^{1.5}{U_g}^{0.029}}$	$0.2< D_C <0.5$ $H = 4.5\ m$ $0.029< U_g <0.45$ m/s	Wachi and Nojima (1990)
$\boldsymbol{E_G = 0.2{D_C}^2 U_g}$		Towell and Ackerman (1972)
$\boldsymbol{E_G = 9.36 \times 10^{-5}{D_C}^{1.3}{U_g}^{3.56}}$		Field and Davidson (1980)
$\boldsymbol{E_G = D_m + \frac{\gamma U^2 d}{D_m}}$	$D = 0.005\ m$ $H = 41.52\ m$	Taylor (1953) and Aris (1956)

As stated above, the presence of axial dispersion in the gas phase appears to be a safer assumption so that plug flow as a flow regime is directly discounted (Rados et al., 2005; Deckwer et al., 1980).

3.1.3.2.2 Liquid axial dispersion

The liquid phase dispersion can be attributed to various factors in FT SBCR's including liquid phase turbulence as a result of the entrapment of said liquid in the wakes of bubbles and eddy structure formations (Groen, 2004 and Degaleesan et al., 1997). When a bubble travels through a column of liquid, a wake will form around it and displace the fluid in its vicinity. This will promote dispersion in the liquid phase through convection in the direction of the moving bubble. Eddy currents are also produced behind a moving bubble and this will promote localized turbulence. This is thought to be more enhanced under high velocity churn-turbulent conditions (Deckwer, 1991). All these factors in liquid phase axial dispersion are grouped and defined by a one coefficient, the liquid axial dispersion coefficient, E_L.

As is the case with the gas phase axial dispersion coefficient, the dispersion models used in the larger SBCR models should be sufficient for use in the miniature microscale FT reactor environment with the dispersion depending mainly on the reactor diameter and superficial gas velocity as will be made clear in the sections that follow.

3.1.3.2.2.1 Liquid Axial dispersion coefficient

The liquid axial dispersion coefficient is predominantly dependent on bubble size, superficial gas velocity, liquid phase velocity and reactor diameter amongst others. There are numerous correlations of this dispersion coefficient in literature in stark contrast to the situation for gas phase axial dispersion. It is clear that axial dispersion in the liquid phase is beyond contention. A comprehensive summary of the multiple available correlations in literature is given by Basha et al. (2015) and from this, it is clear that most of the correlations place importance on the contributions of the reactor diameter and superficial gas velocity to the coefficient. The correlations generally t a k e s t h e f o r m i n E q u a t i o n 3 . 2 t h a t m o s t o f t h e c o r r e l a t i o n s w e r e d e v e l o p e d (s e e T a b l e 3 . 2) .

$$E_L = K{D_C}^a {U_g}^b \qquad \text{Eq. 3.2}$$

where the relative effects of D_C and U_g on E_L are represented by a and b respectively with K being a proportionality constant. It is from the form in Equation 3.2 that most of the correlations were developed (see Table 3.2).

Table 3.2: Liquid phase axial dispersion coefficient correlations for conventional and microreactor systems

Correlation	Experimental conditions	Reference
$\boldsymbol{E_l = 0,35{D_c}^{\frac{4}{3}}{U_g}^{\frac{1}{3}}}$	Mechanistic model	Baird and Rice (1975)
$\boldsymbol{E_l = 1.23{D_c}^{1.5}{U_g}^{0.5}}$	gas-liquid system, $0.4 < D_C < 1$ m	Towell and Ackerman (1972)
$\boldsymbol{E_l = 2.7{D_c}^{1.4}{U_g}^{0.3}}$	gas-liquid system, $20 < D_C < 440$ cm	Deckwer and Robert (1991)

$E_l = [0.15 + 0.69{U_G}^{0.77}]{D_c}^{1.5}(\frac{1}{\mu_L})^{0.12}$	gas-liquid system, $0{,}043 < U_g < 0{,}338$ m/s air and solutions of different viscosities used	Hikita and Kikukawa (1974)
$E_l = g^{0.5}{D_c}^{1.5}[0.06 + 0.55(\frac{U_g}{\sqrt{gD_c}})^{0.7}]$	gas-liquid system, various liquids including $NaCl$ solution and methanol gas included air, O_2, He and CO_2	Akita and Yoshida (1973)
$E_l = 0.3{D_c}^2{U_g}^{1.2}$	air/water system $40 < D_C < 160$ mm	Ohki and Inoue (1969)

3.1.3.2.3 Microreactor Axial Dispersion Coefficients

The scarcity of gas phase axial dispersion models is not only confined to FT reactors of the larger scale but is also evident in micro scale FT systems. Taylor (1953) and Aris (1956) proposed a correlation to determine the axial dispersion coefficient as shown in Equation Eq. 3.3 where the coefficient is dependent on the molecular diffusion coefficient (D_m), the shape of the microreactor through the shape factor (γ), velocity (U), and diameter (d) of the microreactor.

$$E = D_m + \frac{\gamma U^2 d}{D_m} \qquad \text{Eq. 3.3}$$

3.1.3.2.3.1 Effect of superficial gas velocity

To understand and quantify the differences between the correlations in Table 3.2, the relations between the superficial gas velocities and the dispersion coefficients from some of the correlations put forward by each author cited in Table 3.2 were analyzed as shown in Figure 3.2. Despite the different experimental conditions, the correlations cited in Table 3.2 all imply that increasing the superficial gas velocity will increase the axial dispersion coefficient to various extents. Some correlations predict a more linear relationship than others, e. g., correlations by Hikita and Kikukawa (1974) and Pilhofer et al. (1978) compared to those of Baird and Rice (1975) and Deckwer et al (1974). The apparent increase in the axial dispersion as a function of superficial gas velocity can be attributed to the resulting increased turbulence which should lead to a greater degree of mixing in the liquid phase.

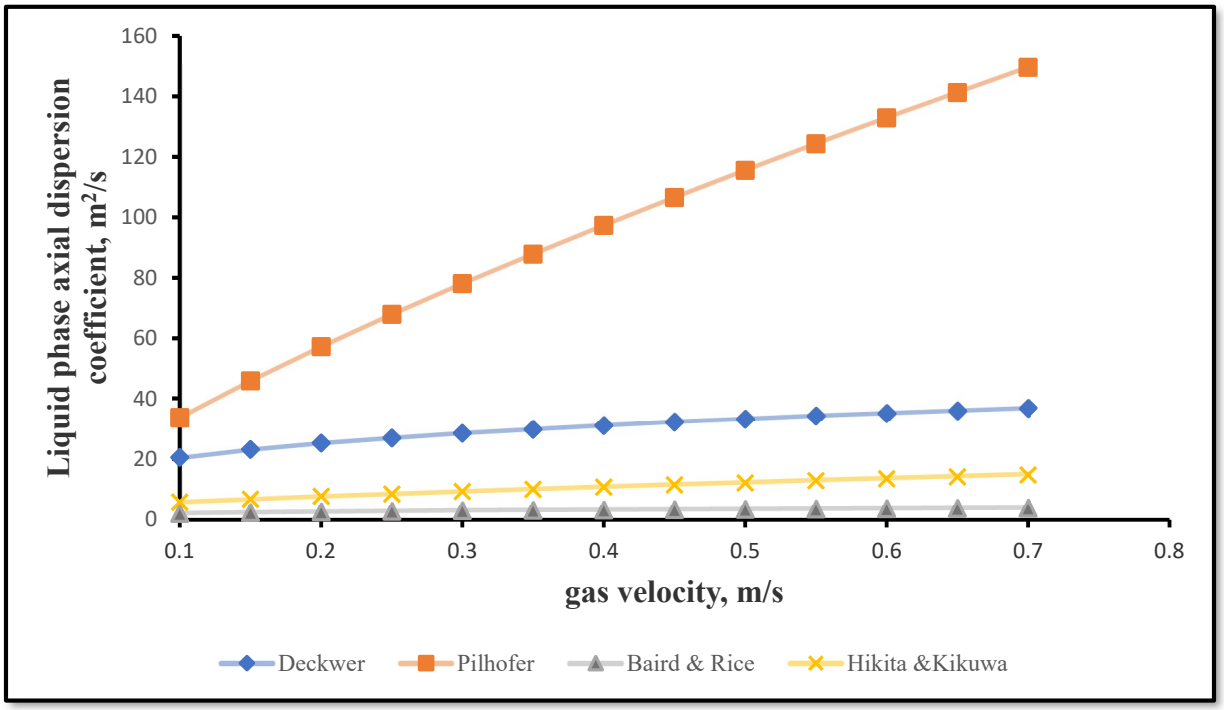

Figure 3.2: Liquid axial dispersion coefficient as a function of superficial gas velocity (Mamabolo, 2018)

3.1.3.2.3.2 Effect of column diameter

As with the effect of the superficial gas velocity, it is widely accepted that the reactor diameter plays a key role in determining the liquid axial dispersion coefficient. As can be seen in Table 3.2, most existing correlations attribute an increasing axial dispersion to an increase in the column diameter. The dispersion coefficient is apparently more sensitive to changes in the column diameter than to those in the superficial gas velocity (Ohki and Inoue, 1969) as evidenced by the higher exponential term associated with the diameter (1.25-1.5) compared to that associated with the superficial gas velocity (0.3-0.5) (Schweitzer and Viguie, 2009). This can be explained through the effect of the diameter on turbulence where a larger column diameter will increase turbulence in the reactor leading to greater dispersion.

3.1.3.2.3.3 Surface tension

A study by Kim et al. (1992) focused on the effects of liquid surface tension on the liquid axial dispersion coefficient and found that increasing the surface tension of the liquid phase had an insignificant effect on the dispersion coefficient with the dispersion coefficient increasing

increasing only minimally when the surface tension was increased between 32 and 72.8 mN/m. Hikita and Kikukawa (1974) similarly determined that the liquid surface tension affected dispersion in a negligible manner when the surface tension was increased from 38.2 to 75.5 mN/m. While these observations may be valid for large scale SBCR FT reactors, they may not necessarily hold for microchannel reactors where viscous effects are more pronounced.

3.1.3.2.3.4 Viscosity

Increasing the viscosity of the bulk continuous phase should reduce turbulence which will have a negative effect on axial dispersion. According to Wu et al. (2013), increasing the liquid viscosity will have a positive impact on axial dispersion where the reduced turbulence will decrease the rate at which bubbles break and therefore produce a bubble size distribution that is dominated by larger bubbles. The net result of these two opposite effects is that of an insignificant change in the dispersion coefficient. There appears to be a consensus that the liquid phase viscosity has minimal effect on axial dispersion in literature (Hikita and Kikukawa, 1974; Towell and Ackerman, 1972; Kim et al., 1992).

3.1.3.2.3.5 Isotropic model

Based on the work by Kolmogorov (1941) and Hinze (1959), Baird and Rice (1975) determined that an already developed isotropic turbulence model can be applied to bubble columns provided that no baffles, internals or packing is present inside the column. This may be applicable in the current microchannel system as instead of closely packing the channel with catalyst, the microchannel will be loosely packed with extremely small catalyst particles. The work of Kolmogorov (1941) assumes equal and uniform turbulence of a fluid in all directions. From this, the author arrived at a correlation for eddy diffusivity/dispersion as shown in EquationEq. 3.4.

$$E = K l^{4/3} P_m{}^{1/3} \qquad \text{Eq. 3.4}$$

E is the eddy dispersion, l is the characteristic length of the tube, P_m is the specific energy dissipation rate and K is a dimensionless constant. Baird and Rice (1975) defined the specific energy dissipation for bubble columns as:

$$P_m = U_g g \qquad \text{Eq. 3.5}$$

Where U_g is the superficial gas velocity and g is the gravitational acceleration constant. Equation Eq. 3.5 could then be re-written as shown in Equation Eq. 3.6 where the characteristic length is the diameter of the column:

$$E_L = K{D_C}^{4/3}(U_g)^{1/3} \quad \text{Eq. 3.6}$$

Where K is has a value of 0.35 (Baird and Rice, 1975; Schweitzer and Viguie, 2009; Groen et al., 1996). The isotropic turbulence model, as adapted for use in bubbly reactors in Equation $E = Kl^{4/3}{P_m}^{1/3}$ Eq. 3.4, compared favorably with other models used to predict the axial dispersion coefficient and can be applied under a wide range of conditions (Baird and Rice, 1975) which makes it versatile and possibly relevant as a correlation for liquid phase axial dispersion in microreactors. It is also noted by Deckwer & Schumpe (1993) that most dispersion coefficient correlations can be reduced to a form similar to the isotropic model which may explain its robustness. The theoretical nature of this model is important as it avoids the limitations, to some extent, faced by the other correlations which were developed empirically and should therefore only be applied under a specific range of conditions. This point is also important when considering the application of such a model in micro systems. Considering the above, the isotropic turbulence model describing dispersion in the liquid phase will be adopted for use in the current FT microchannel modelling study.

3.1.3.3 Hydrodynamic Parameters

3.1.3.3.1 Gas hold-up

Gas hold-up is one of the most important hydrodynamic parameters with regard to bubble column reactor modelling (Maretto and Krishna, 1999). It refers to the volume fraction of gas in the reactor vessel/channel. In general, a high gas hold-up is desirable as this directly translates to more gaseous reactant available for reaction per unit volume of the reactor. Multiple correlations quantifying the gas hold-up in bubble column reactors can be found in literature (Iliuta et al., 2007; Maretto and Krishna, 1999; Behkish, 1997) and it was determined that this hydrodynamic parameter is influenced by a variety of factors including operating conditions such temperature, pressure and superficial gas velocity (Maretto and Krishna, 1999). It is also accepted that liquid phase properties such as density, surface tension, viscosity and vapour pressure affect gas hold-up (Basha et al., 2015). These effects may be more important in micro sized channels as will be discussed in later

sections of this report. Structural properties including the column diameter and sparger type (if the reactants are sparged in) can also have an influence on gas hold-up (Behkish et al., 2006).

Most of the gas hold-up correlations in literature (Table 3.3) were developed in experimental conditions different to those in industrial settings. Bach & Pilhofer (1978) for example, conducted experiments under ambient temperature and pressure conditions with superficial gas velocities up to 0.2 m/s and Jordan & Schumpe (2001) and Fan et al. (1999) attempted to represent real SBCR operating conditions by using pressures and temperatures in the ranges 0.1-5.32 MPa and 293-351 K respectively with superficial gas velocities and reactor column dimensions significantly lower than those observed in industrial reactors.

Table 3.3: Different gas hold-up correlations from literature

Correlation	Reference
$\frac{\varepsilon_g}{1-\varepsilon_g} = 0.115\left(\frac{U_g^{\,3}}{\mu_L g\frac{(\rho_L-\rho_g)}{\rho_L^{\,2}}}\right)^{0.23}$	Bach and Pilhofer (1978)
$\frac{\varepsilon_g}{1-\varepsilon_g} = bBo^{0.16}Ga^{0.04}Fr^{0.7}\left[1+27Fr^{0.52}\left(\frac{\rho_g}{\rho_L}\right)^{0.58}\right]$ $b = sparger\ type\ factor\ (0.109-0.153)$	Jordan & Schumpe (2001)
$\varepsilon_g = \varepsilon_{g,LB} + \varepsilon_{g,SB}\left(1-\varepsilon_{g,LB}\right)$ $\varepsilon_{g,LB} = \frac{0.3}{D_c^{0.18}(U_g-U_{g,SB})^{0.22}}(U_g-U_{g,SB})^{0.8}$ $\varepsilon_{g,SB} = \varepsilon_{g,SB,ref}\left(1-\frac{0.7}{\varepsilon_{SB,ref}}\varepsilon_S\right)$ $\varepsilon_{g,SB,ref}=0.27$	Maretto & Krishna (1999)
$\varepsilon_g = 0.9\left(\frac{U_g^{\,2}d_p\rho_L}{\sigma_L}\right)^{0.11}\left(\frac{U_L}{\sqrt{gd_p}}\right)^{0.22}$	Kito et al. (1978)
$\varepsilon_g = 1.61U_g^{\,0.22}d_p^{\,0.168}D_c^{\,-0.125}$	Begovich & Watson (1978)
$\varepsilon_G = 296U_g^{\,0.44}\rho_L^{\,-0.98}\sigma_L^{\,-0.16}\rho_g^{\,0.19}+0.009$	Reilly et al. (1986)
$\varepsilon_g = \frac{1}{2+\left(\frac{0.35}{U_g}\right)\left(\frac{\rho_L\sigma_L}{72}\right)^{0.3}}$	Hughmark (1967)
$\varepsilon_g = 0.17283\left(\frac{\mu_L^{\,4}g}{\rho_L\sigma_L^{\,3}}\right)^{-0.1844}\left(\frac{P_T+P_{vap}}{P_T}\right)^{1.6105}\left(\frac{U_g\mu_L}{\sigma_L}\right)^{0.5897}$	Zou et al. (1988)

It is also important to note the nature of the gas, liquid and solid phases employed in these experiments as they play a critical role. In the place of the liquid phase which is supposed to represent the wax products formed in the LTFT process, organic solutions are typically used including kerosene, glycol and glycerol with water and some alcohols being used at times. These substances may represent the behaviour of real LTFT FT liquid solutions to some extent but will almost certainly fall short of accurately achieving real reactor conditions which undermines the validity of the resulting correlations. Air, Nitrogen and Helium are typically used to represent the gaseous phase while glass beads and sand are the preferred medium to account for the solid particles. It is clear then that these correlations should be used only when their anticipated error is known and acceptable (Mamabolo, 2018).

The gas hold-up is purported to increase with increasing superficial gas velocity (Sehabiague, 2012), temperature and pressure (Behkish et al, 2006; Wilkinson & Dlerendonck, 1990; Jiang et al., 1995; Therning & Rasmuson, 2001; Sehabiague, 2012). Interestingly, an increasing solids concentration supposedly has a negative effect on the hold-up as put forward by various authors including Behkish et al. (2006), Kara et al. (1982) and Gandhi et al. (1999). This effect is also confirmed by Sehabiague (2012) where the author attributes it to a drop in the small bubble hold-up, which results in a lower overall gas hold-up, as a result of elevated solids concentration levels. The author observed that solids concentrations over 30% (v/v) rendered the small bubble population virtually non-existent - citing an increase in the tendency of the small bubbles to coalesce and form larger bubbles. Large bubbles spend less time in the reactor as they have a higher rise velocity, meaning that for systems with a higher solids concentration the gas hold-up at any one time is lower. In respect of the liquid property influence, gas hold-up should be positively affected by an increase in liquid viscosity and surface tension (Oyevaar et al, 1989). This observation is significant in the context of this study as surface tension effects are expected to be more pronounce in the microchannel system.

Behkish et al. (2006) conducted gas hold-up tests and used the results together with data from various authors to come up with a data set consisting of 3881 data points from which a versatile correlation possibly applicable to a wide range of conditions was developed. The resulting correlation is given in Equation 3.7.

$$\varepsilon_g = 4.94 \times 10^{-3} \left(\frac{{\rho_L}^{0.415} {\rho_g}^{0.177}}{{\mu_L}^{0.174} {\sigma_L}^{0.27}}\right) {U_G}^{0.583} \left(\frac{P_T}{P_T - P_{vap}}\right)^{0.203} \times \left(\frac{D_c}{D_c+1}\right)^{-0.1170.1} \gamma^{0.053} \times e^{(-2.231\varepsilon_s - 0.157\rho_s\varepsilon_s - 0.242X)} \quad \text{Eq. 3.7}$$

Where $$\gamma = K_d N_0 {d_0}^{\alpha_0} \quad \text{Eq. 3.8}$$

Behkish et al. (2006) further developed a correlation for the hold-up of large bubbles specifically in a similar manner by using a total of 1426 data points to arrive at the correlation shown in Equation 3.9.

$$\varepsilon_{g,LB} = {\varepsilon_g}^{0.84} \left(1 - 3.04 \times 10^{-6} \frac{{\rho_L}^{0.97}}{{\mu_L}^{0.16}} e^{4.5X_W - 4.49\varepsilon_s}\right)$$

$$= {\varepsilon_G}^{0.84} F \quad \text{Eq. 3.9}$$

The small bubble hold-up can be determined from the difference between the total gas and large bubble hold-up thus:

$$\varepsilon_{\mathrm{g,SB}} = \varepsilon_g - \varepsilon_{g,LB} \quad \text{Eq. 3.10}$$

A condition for the use of Equations 3.9 is that $\varepsilon_G \leq F^{6.25}$, otherwise the small bubble hold-up would be low enough to neglect so that Equation 3.10 would be re-written as Equation 3.11. A clear disadvantage of the correlations put forward by Behkish et al. (2006) is the large number of parameters that need to be determined beforehand. γ in particular, poses a challenge as the parameters needed in Equation 3.8 are difficult to determine.

$$\varepsilon_g = \varepsilon_{g,LB} \quad \text{Eq. 3.11}$$

3.1.3.3.2 Liquid hold-up

The liquid phase hold-up can be determined from a balance of the total hold-up as shown in Equation 3.12 below.

$$\varepsilon_l = 1 - \varepsilon_G - \varepsilon_s \quad \text{Eq. 3.12}$$

3.1.3.3.3 Superficial gas velocity

The total superficial gas velocity is divided between the small and large bubbles velocities according to Equation 3.13. The superficial velocity of the small bubbles can be determined using the correlation by de Swart (1996) as shown in Equation 3.14. The large bubble superficial gas

velocity can then be determined from the difference between the overall and small bubble superficial gas velocities as in Equation 3.15.

$$U_g = U_{g,SB} + U_{g,LB} \quad \text{Eq. 3.13}$$

$$U_{g,SB} = 2.25 \frac{\sigma_L}{\mu_L} \left(\frac{{\sigma_L}^3 \rho_L}{g {\mu_L}^4}\right)^{-0.273} \left(\frac{\rho_L}{\rho_g}\right)^{0.03} \quad \text{Eq. 3.14}$$

$$U_{g,LB} = U_G - U_{g,SB} \quad \text{Eq. 3.15}$$

3.1.4 Heat transfer Effects

Under the continuum model, heat transfer effects in microreactors can be modelled based on conventional theories and principles. In this section, heat transfer processes in microchannels are explored to determine the applicable heat transfer models in FT microreactors. Various temperature profiles throughout the microreactor are discussed along with their effects on reactor performance.

3.1.4.1 Axial Fluid Heat Conduction

Axial conduction of heat in the fluid is a special case which deviates from conventional heat transfer systems if deemed to be present. In this case, there exists a temperature difference between the downstream and upstream fluid volumes in a channel analogous to axial dispersion in mass transfer problems where a concentration gradient exists. The criterion used to determine the presence of axial conduction makes use of the Peclet number (Pe) which is a product of the Reynolds number (Re) and the Prandtl number (Pr). A Pe>10 (Shah & London, 1978) is generally accepted as the limit below which axial conduction may be an important factor in the fluid temperature profile.

In conventional large-scale systems, axial conduction is normally neglected given the relatively high velocities and large characteristic diameters. These lead to a Pe that is much greater than 10. In microchannels, the characteristic diameters are significantly smaller so that due consideration has to be given to the possibility of axial conduction in the channel. The Pe>10 criterion will be used for this purpose. The above criterion is for fully developed flows and does not account for developing flows around the entrance region. To determine the presence of axial conduction in the entrance region, Equation 3.16 can be used as the criterion (Hetsroni et al, 2005) where x represents the position in the channel and d represents the channel diameter.

$$\frac{x}{d}Pe \leq 20 \qquad \text{Eq. 3.16}$$

3.1.4.2 Transverse Heat Conduction

Heat conduction in the transverse direction can be realized in both the bulk fluid and microchannel wall. Microchannel walls are typically very thin and thus allow sufficient heat flow to maintain a constant temperature across the wall thickness. This is one of the advantages of microreactors where cooling channels can be fitted around the reacting channel to effect a relatively high rate of heat transfer through the very thin and highly conductive walls of the microchannel.

It is expected that the transverse heat transfer in the bulk fluid will be highly pronounced in the microchannel as opposed to that in a conventional large-scale channel. The reduced channel diameter also means there is less fluid thickness through which heat must travel and this improves the heat transfer rates in the microchannel. Given that microchannel flows are typically laminar, conduction can be expected to be more important than convection. In the radial direction, it will be the heat transfer across the fluid layer that is limiting provided the channel wall is thin enough to allow near isothermal conditions across the wall.

In quantifying the heat transfer across the fluid and solid wall, classical Nu correlations typically used in large scale conventional systems can be applied (Shah & London, 1978; Maestri et al, 2005) where the heat transfer coefficients can be determined. The Nu correlations chosen should be appropriate for the conditions being considered. If the reacting system is highly exothermic and thus produces a large amount of heat, the Nu correlation used should have been determined under similarly highly exothermic reactive system experiments. A generalized Nu correlation is shown in Equation 3.17 where h and k refer to the heat transfer coefficient and thermal conductivity respectively. This correlation will take various forms depending on the prevailing reactor system conditions.

$$Nu = \frac{dh}{k} \qquad \text{Eq. 3.17}$$

Various experimental studied have been carried out to quantify the Nu correlations in microchannels by various authors using different study conditions. It is important therefore to select any correlation carefully and to ensure that the system being modelled can be accurately represented by that particular correlation. In the present study an exothermic, heterogeneously catalyzed FT system is being considered so that the Nu correlation chosen should have been

determined under similar conditions. Different microchannel Nu correlations are listed in Table 3.4 under a variety of Re, channel size, channel material of construction and the fluid utilized.

Table 3.4: Microchannel Nu correlations from various authors

Nu Correlation	Experimental conditions	Reference
$\boldsymbol{Nu = 0.293 Re^{0.53} Pr^{0.25}}$	$d_h = 318\ \mu m$ $Pr = 4.56$ $Re < 2000$ Water used as fluid medium Cu material Constant velocity and liquid properties assumed	Mansoor et al. (2012)
$\boldsymbol{Nu = 0.52 (RePrd_h/L)^{0.62}}$ **when** $\boldsymbol{\left(\frac{L}{RePrd_h}\right) < 0.05}$ $\boldsymbol{Nu = 2.02 (RePrd_h/L)^{0.31}}$ **when** $\boldsymbol{\left(\frac{L}{RePrd_h}\right) \geq 0.05}$	$133\ \mu m < d_h < 367\ \mu m$ Water used $Re < 600$ Cu material	Jiang et al. (2001)
$\boldsymbol{Nu = 0.1165 (d_h/P)^{0.81} \alpha_c{}^{0.79} Re^{0.62} Pr^{1/3}}$	$Re < 1000$ $133\ \mu m < d_h < 367\ \mu m$ $0.5 < \alpha_c < 3$ $3.9 < Pr < 7$ $0.5 < P < 3$ Water used Stainless steel material	Peng & Peterson (1996)
$\boldsymbol{Nu = 0.00058 \alpha^{-0.3} Re^{0.621.15} Pr^{1/3} (\mu_{in}/\mu_w)^{2.76}}$	$Re < 3300$ $100\ \mu m < d_h < 134\ \mu m$ $1 < \alpha_c < 2$ $6.3 < Pr < 6.8$ Water used Silicon material	Jung & Kwak (2008)

3.1.4.3 Intra-particle Heat Transfer Effects

Intraparticle heat transfer within catalyst particles in the microreactor can in general be assumed to be without thermal resistance. To avoid prohibitively large pressure drops within the reactor, the size of catalysts used are necessarily small. The small size of these catalyst particles means there is very little distance that heat must travel within the particle such that isothermal conditions can be assumed. This much is confirmed by the works of Ouyang & Besser (2003) and Kaisare et al. (2009). In the current study, the intraparticle heat transfer resistance will be assumed negligible for the reasons discussed above.

3.1.4.4 Viscous Energy Dissipation

Viscous dissipation is an important consideration in microchannel flow modelling, more so than would perhaps be the case in large channel flow. As previously noted, microchannel flow is typically characterized by laminar flow which is in turn characterized by large radial velocity gradients. These velocity gradients can be large enough to effect local rises in temperature as a result of the heat inducing viscous forces prevalent between the fluid layers. It is evident then that the presence of viscous dissipation in a system will affect the inherent temperature profile and will have to be accounted for in the energy balance.

The importance of viscous dissipation was studied by Xu et al and they proposed a dimensionless viscous number (Vi) (Equation 3.18) to serve as a criterion for the applicability of viscous dissipation. In their study, $ViPr^{-1} \geq 0.056$ is the limit above which viscous dissipation must be accounted for. As per Equation 3.18, the velocity and channel diameter in particular play an important role in determining whether viscous dissipation is important or not, i.e., a smaller diameter and /or larger fluid velocity will tend to exhibit pronounced viscous dissipation effects. Any combination of higher fluid dynamic viscosity (μ), longer reactor length or height (L), lower fluid density (ρ) and lower fluid specific heat capacity (Cp) will also increase the viscous dissipation effects. T_{ref} refers to the reference temperature and can be expressed as shown in Equation 3.19 where ΔT is the temperature rise resulting from viscous energy dissipation and ΔT^* is a dimensionless temperature rise.

$$Vi = \frac{\mu UL}{\rho Cp T_{ref} D^2} \qquad \text{Eq. 3.18}$$

$$T_{ref} = \frac{\Delta T}{\Delta T^*} \quad \text{Eq. 3.19}$$

In the case that viscous dissipation is relevant, the Nu correlation for a microchannel flow system will have to consider its effects. To this end, Tso & Mahulikar (1998) developed a specific Nu correlation as shown in Equation 3.20 where A' is an empirical constant and f is a constant dependant on the geometry of the channel. Br is the Brinkman number which takes into account the viscous energy dissipation and is represented by a ratio of energy dissipation and heat conduction as shown in Equation 3.21 where d_h is the hydraulic diameter of the channel.

$$Nu = A' Re^{0.62} Pr^{1/3} f Br^{d} \quad \text{Eq. 3.20}$$

$$Br = \frac{\mu^3 Re^2}{\rho^2 {d_h}^2 k \Delta T} \quad \text{Eq. 3.21}$$

3.1.4.5 Conjugate heat transfer

Conjugate heat transfer refers to the transfer of heat axially along the wall which, in the present case, may have a more pronounced effect given the relatively small fluid volume in the microchannel. Compared with macroscale channels, the wall thickness to channel diameter ratio in microchannel systems is much larger so that the heat transport in the wall is more influential on the channel fluid, i.e., the temperature in the bulk fluid is more strongly dependent on the temperature of the wall. This effect is generally neglected in conventional systems (Shah & London, 1978).

An important consideration would be the determination of the range of conditions under which conjugate heat transfer is important. Chiou (1980) proposed a conduction parameter (Equation 3.22) that would be able to quantify the influence of conjugate heat transfer on the overall system energy balance/heat exchange performance. A stronger dependence would mean that conjugate heat transfer could not be neglected and would have to be taken into account in modelling the heat transfer in the system. Subscripts s and f in Equation 3.22 denote the wall and bulk fluid respectively. A c <0.005 was put froward by the authors as a satisfactory condition to justify the neglect of conjugate heat transfer. This means that a channel with a lower ratio of A_s to A_f, greater length, higher fluid Re and Pr will tend to be less dependent on conjugate heat transfer effects.

$$c = \frac{A_s k_s d_h}{A_f L Re Pr_{\ f}} \quad \text{Eq. 3.22}$$

It can be appreciated that the existence of conjugate heat transfer presents more complexity in terms of modelling the heat transfer in the system as heat transport not only has to be modelled in the bulk fluid but also in the channel wall and in the coupled fluid-wall system. There is some consensus that the bulk fluid Nu is reduced by the presence of conjugate heat transfer (Fedorov & Viskanta, 2000; Guo & Li, 2003) although the exact mechanism behind this effect has not been clearly articulated in literature.

3.1.4.6 Wall-slip

In conventional systems, a non-slip boundary condition at the wall is often justifiably assumed so that the velocity of the fluid at the wall is zero. This may not necessarily be the case in microchannel systems wherein the wall surface property effects are pronounced. One of the effects of surface properties in microchannels is on the slip condition at the wall so that hydrophobic surfaces may have more of an influence on fluid wall-slip than would be the case with the same material in conventional systems.

It can be appreciated that wall-slip will affect the hydrodynamics and heat transfer within the microchannel (Wu & Cheng, 2003). In the event that slip flow is present, the classical N-S equations have to be used in conjunction with additional physics models to account for the effects of the wall-slip.

3.1.4.7 Surface Roughness

In conventional systems, the roughness of a flow channel wall is generally unimportant to the hydrodynamics of the fluid flow given the larger size of these systems compared with the micro scale of the channels being investigated in this study. Any flow disturbances caused by the roughness of the wall do not affect the bulk flow dynamics in any significant way given the much larger fluid cross section versus the smaller fluid layer in contact with the wall.

It can be appreciated that in a system where the bulk fluid cross sectional area and the effective cross-sectional area of the fluid layer in contact with a rough channel wall are more comparable, such as is the case in microchannels, the flow disturbances in the bulk fluid will be more pronounced and thus more important, requiring appropriate fluid dynamics models to be employed. One way to effectively model this disturbance is the use of a hydraulic diameter which

represents the equivalent smooth channel diameter of a rough channel, i.e., the effective diameter of a rough channel represented in terms of a completely smooth channel.

$$d_h = \frac{4V_{fluid}}{A_{wet}} \quad \text{Eq. 3.23}$$

$$A = \frac{V_{fluid}}{L} \quad \text{Eq. 3.24}$$

Valdes et al. (2007) proposed such a method through the use of Equation 3.23 where V_{fluid} is the effective volume of fluid filling a channel and A_{wet} is the surface area of contact between the channel wall and bulk fluid or the wetted surface area. The authors also proposed a similar method to account to account for the effective fluid cross sectional area in a rough channel which will depend on V_{fluid}as shown in Equation 3.24 where L is the channel length. V_{fluid} and A_{wet} have to be determined experimentally and microscopic methods could be used to determine these.

3.1.5 Mass transfer effects

The comprehensive modelling of a micro-FT reactor requires the mass transfer across phases within the microreactor to be adequately accounted for. Two types of mass transfer are encountered in the system including internal and external mass transfer. Internal mass transfer refers to the mass transport within a solid catalyst particle which can be neglected given the necessarily small catalyst particles employed. This will hold provided a catalytic wall type microreactor is being used, which is true in this case as the catalytic wall is the reactor type under investigation. As discussed in an earlier section of this study, the use of a thin catalytic layer on the inner channel wall will require that very small catalyst particles be used – this is the opposite of what would be required in the packed bed type microreactor where larger conventional particles can simply be packed into the channel to create a catalyst bed.

External mass transfer refers to the mass transport processes present outside of the solid catalyst so that only the mass transfer between the fluid phases and the surface of the catalyst particle is considered. The external mass transfer processes are not directly affected by the miniaturization of the channel (Maestri et al., 2005). The mass transfer rates may be positively affected by the small nature of the microchannel but the inherent physics underlying this process will not necessarily be influenced and should remain the same as they are in conventional systems. The external mass transfer rates may further be affected by the other processes within the microchannel

that would have been influenced by the miniaturization including the dominance of interfacial forces and channel wall wettability.

3.1.5.1 Mass transfer Models

The only significant mass transfer resistance in a bubble column microreactor is the gas to liquid mass transfer. The transfer of matter across the gas-liquid boundary is generally assumed to receive the most resistance on the liquid side of the interphase and as a result the total gas-liquid mass transfer phenomenon is based on the liquid side. The mass transfer theory presented in this section is adapted from the work by Mamabolo (2018).

Using the two-film theory, it can be shown that the mass flux from the bulk gas to liquid phase can be written thus:

$$J = k_L(C^*_L - C_L) \qquad \text{Eq. 3.25}$$

Where J represents the mass flux, C_L is the concentration in the bulk liquid phase, C^*_L is the liquid side interfacial concentration and $k_L$is the mass transfer coefficient. The mass transfer coefficient is a function of the gas-liquid diffusivity D_{GL} and liquid film δ thickness thus:

$$k_L = \frac{D_{GL}}{\delta} \qquad \text{Eq. 3.26}$$

To represent the flux in units of mass/time, the volumetric mass transfer coefficient k_{La} is often used where a denotes the interfacial area. The interfacial liquid phase concentration can be related to the partial pressure in the bulk gas phase through Henry's law with the assumption that equilibrium exists between the two phases as shown in Equation 3.27.

$$C^*_{i,L} = \frac{P_i}{H_i} \qquad \text{Eq. 3.27}$$

Where P_i is the partial pressure of species i in the gas phase and H is Henry's constant for species i and $C^*_{i,L}$ is the concentration of species i in the gas phase at the gas-liquid interphase under equilibrium conditions.

3.1.5.1.1 Mass transfer coefficients

The mass transfer coefficient depends strongly on the bubble size in that small bubbles with a greater interfacial area per volume allow more mass transfer than larger bubbles with less interfacial area per unit volume (Basha et al., 2015). Liquid phase axial dispersion can influence

the volumetric mass transfer coefficient (Inga, 1997) meaning that variables that affect dispersion will also affect the mass transfer coefficient. These variables include the reactor diameter and superficial gas velocity. Various correlations for volumetric mass transfer coefficients are given in Table 3.5.

Table 3.5: Various volumetric mass transfer coefficient correlations

Correlation	Experimental conditions	Reference
$K_{La} = 0.5\varepsilon_g$		Vermeer and Krishna (1981)
$K_{La,LB} = 0.5\varepsilon_{g,LB}\sqrt{\frac{D}{D_{ref}}}$ $K_{La,SB} = \varepsilon_{g,SB}\sqrt{\frac{D}{D_{ref}}}$		Vemeer and Krishna (1981)
$K_{La} = cD^{0.5}(\frac{\mu_L}{\rho_L})^{-0.62}D_C{}^{0.17}g^{0.93}\varepsilon_g{}^{1.1}$	$D_C = 15.2\ cm$ $H = 400\ cm$	Akita and Yoshida (1973)
$K_{La} = \frac{6.14\times10^4\rho_L{}^{0.26}\mu_L{}^{0.12}\varepsilon_g{}^{1.21}D^{0.5}\gamma^{0.11}}{\sigma^{0.52}\rho_g{}^{0.06}U_g{}^{0.12}d_b{}^{0.05}T^{0.68}}(\frac{D_C}{1+D_C})^{0.4}$		Lemoine et al. (2008)
$K_{La} = 4.41U_g{}^{0.338}\varepsilon_S{}^{0.595}(1-\frac{\rho_L}{\rho_p})^{0.337}$	$0.0025 < D_C < 0.05\ m/s$ $D_C = 0.06\ m$	Guo et al. (1997)
$K_{La} = 0.4U_g{}^{0.625}U_L{}^{0.26}e^{(1.477\times10^{-5}H)}$	$0.02 < D < 0.04\ m/s$ $D_C = 0.05\ m$	Chen et al (2001)

Vermeer and Krishna (1981) have developed a correlation for the mass transfer coefficient that relates the coefficient only to the total gas hold-up (Equation 3.28) which is simpler than the other correlations being discussed here. Steynberg and Dry (2004) have endorsed this correlation, going as far as recognizing it as a rule of thumb. Following a similar correlation, Vermeer and Krishna (1981) and Letzel et al. (1999) have provided mass transfer coefficient correlations for the large and small bubble classes, making a clear distinction between the coefficients of the two size

classes. Krishna and Sie (2000) modified the correlation put forward by Letzel et al. (1999) by introducing the liquid phase diffusive coefficient.

$$K_{La} = 0.5\varepsilon_g \qquad \text{Eq. 3.28}$$

The mass transfer coefficient correlations by Akita and Yoshida (1973) and Calderbank and Moo-Young (1961) enjoy a lot of popularity but Maretto and Krishna (1999) and Schweitzer and Viguie (2009) note that the correlations are limited in their applicability in reactors operating in the heterogenous regime with a high large bubble hold-up. As per the assertions by Akita and Yoshida (1973), viscosity, liquid phase diffusivity, liquid surface tension, liquid density, column diameter and superficial gas velocity all contribute to the volumetric mass transfer coefficient. The structure of the correlations described here is such that they can be applied in the microchannel reactor model being developed in this study. Care should be taken though in selecting an appropriate mass transfer coefficient model that will help arrive at reasonable and accurate results.

Based on the work by Lemoine et al. (2008), Sehabiague (2012) developed a correlation (Equation 3.29) for the mass transfer coefficients in SBCRs using an experimental pilot plant. The author tested the validity of the correlation by comparing it to that proposed by Lemoine et al. (2008) with regard to modelling the K_{La} values from various sources (1917 in total) and found the correlation to be more accurate.

$$KLa = \frac{7.99\times10^{-9}{\rho_L}^{1.82}{\rho_G}^{0.27}{U_G}^{0.387}}{{U_L}^{0.25}\sigma^{0.976}{Mw_g}^{0.02}}\left(\frac{P_T}{P_T-P_{vap}}\right)^{0.242}\left(\frac{D_c}{D_c+0.3}\right)^{0.1}\gamma^{0.173}e^{\left(-0.0013\rho_p\varepsilon_s+0.8\left(\frac{\rho_S\varepsilon_S}{1000}\right)^2-\left(\frac{\rho_S\varepsilon_S}{1000}\right)^3-167\ .7d_p+0.176X_W\right)}$$

Eq. 3.29

3.1.6 Residence Time Distribution

Residence time distribution (RTD) is an important parameter in any reactor and this applies to microreactors as well. RTD characterizes the residence time profile of the flowing reactants within the reactor and can have two extremes, namely a perfectly mixed profile where all reactants entering the reactor are perfectly mixed so that each unit volume of flowing reactants experience the same residence time and on the opposite extreme is a zero-mixing profile where successive unit volumes of flowing reactants do not mix at all. As one can imagine, it would be crucial to adequately control the RTD such that the product quality is maintained within desired parameters.

The physical design of the reactor plays an important role in this regard as this greatly determines the flow pattern within the reactor. Factors such as the mixing capability of the reactor, whether through baffles or motorized mixers, and the shape of the reactor vessel which may support or impede channelling of flow are all important in determining the RTD.

Mixing is an important determinant of RTD and as a result focus is often placed on the mixing nature of the system and not explicitly the RTD profile. To this extent, the continuously Stirred Tank Reactor (CSTR) and plug flow models are often assumed as simple approximations of the mixing within reactor. While these may be adequate in some situations, they may prove too simplistic for the purposes of studying an FT microreactor where important details may be affected by such simplified assumptions. It is more prudent to assume a mixing model that is a mix between the two extreme assumptions. This is referred to as an axial dispersion model (ADM) and is characterized by a dispersion coefficient.

3.1.6.1 Axial Dispersion Model

Axial dispersion can be described as the spatial gradient of matter and energy that exists in the direction of the theoretical axis of the reactor. In a microreactor the axial dispersion will be along the height of the reactor. Dispersion in a microreactor is important in as far as quantifying the extent of mixing in the reactor. Greater mixing would represent conditions closer to those in CSTRs whereas less mixing would represent conditions that reflect a more plug-flow system. In an ideal plug flow reactor system, a unit volume of reactants at a point z in a column will have no interaction with a unit volume at a point $z+\Delta z$ downstream in the column. This means that the unit volume that is at an advanced position will not mix with or dilute the unit volume that precedes it. The consequence of this is a less homogenous system in which the axial concentration gradients are pronounced. This should lead to a higher reactant conversion rate than can be achieved in an ideal CSTR where the perfect mixing results in no axial concentration gradients.

3.1.7 Multitubular flow distribution

Good flow distribution in large scale FT microchannel reactors is important in as far as ensuring uniform flow conditions in each channel. Uneven distribution has detrimental effects on the selectivity and productivity of the microchannel reactor. The inlet flow distribution system in a FT microchannel reactor must be prioritized and perhaps afforded the same importance as the core reactor channels. The multi-scale conditions prevalent in the inlet section of a large-scale

microchannel reactor present flow distribution problems as the fluid must flow from a larger scale pipe into multiple smaller scale channels that are significantly smaller. The small nature of the channels means that it is easier for the incoming flow to by-pass or at least preferentially flow away from some channels. This is the multi-scale problem associated with microchannel systems not only in FTS but in other industrial applications as well. There have been attempts to solve this problem by optimizing the inlet flow distribution system as is discussed below.

It was Pigford et al. (1983) that studied the flow distribution in piping manifold systems. The study identified the pressure variations within the distribution headers as the main cause of flow maldistribution and they attributed these variations to the friction forces and momentum losses. This is a theory shared by other authors as well (Solovitz & Mainka, 2011; Wang, 2011; Zhou et al., 2018). The study also puts forward an empirically derived fluid distribution theory governing specifically flow distribution in turbulent systems and cylindrical headers. This brings the theory's applicability to other conditions into question. Using a different strategy, Pan et al. (2008) studied flow distribution in microchannels and the effect of various geometries on the distribution. An analytical optimization procedure was suggested to determine the optimum manifold configuration and the procedure was tested on specific manifold systems. The flow distribution was determined to be most sensitive to the microchannel width.

An important summary on the theory of manifold flow distribution is given by Wang (2011) in which several theoretical models are considered. This is important because of the robustness of theoretical models as compared to empirical ones. Various theoretical models were considered and discussed at length for purposes of creating a unified manifold model to aid in the optimal designs of manifolds for different flow applications. In their study, the authors argue for the superiority of analytical models over discreet and CFD models citing the complexity and computational expense of the latter options. This is particularly true when the manifold geometry optimisation limits and parameters are not well defined at the initial stages. The number of CFD computations required for the vast number of test geometries would be prohibitively large. The case would be different if the optimization was to be conducted within a given set of limitations and boundaries although this would call the result into question given the limited scope of that optimization process. The authors selected a single framework through the combination of various existing models including that of Acrivos et al (1959). The developed analytical model is supposed to be simpler and more

robust without the need for numerous iterations and computations, but instead provide the ability to scan a wide range of manifold geometries and their performance through an explicit relation between performance and geometric parameters.

Despite the above assertion by Wang (2011), there are authors who studied optimal manifold geometry using CFD methods including Kim et al. (2011), Hassan et al. (2015), Jung et al (2016) and Tomor & Kristof (2016). Kim et al. (2011) used a numerical CFD method to represent optimal manifold conditions using a dimensionless number. The model was validated using micro particle image velocimetry and is able to determine, through calculation of the dimensionless parameter, the optimal configuration of a flow distribution manifold for uniform flow distribution.

3.1.8 Kinetics

The intrinsic kinetics in FT microreactors are not expected to be different to those in conventional large scale FT reactors given that the same types of catalysts are used, i.e., the governing kinetic rate laws will not be influenced by the miniaturization of the reactor system. It is only the size of the catalyst that may need to be reconsidered as smaller catalyst particles may be required when catalytic wall microreactors are used. This section will cover the background of FT kinetics, specifically in the context of heterogeneously catalysed three-phase systems. The literature is readily available in common FT literature and the background theory given here is based largely on previous work by Mamabolo (2018).

The kinetics on the surface of a catalyst are governed by the processes of adsorption, chemical reaction and desorption. This is illustrated in Figure 3.3. Adsorption refers to the attachment of the reactant molecules to the surface of the catalyst before they can react, and desorption refers to the de-attachment of the resulting products from the surface of the catalyst into the bulk liquid phase. The surface kinetics can be limited by either of the processes and it is thus important to clearly understand each process and the underlying mechanisms.

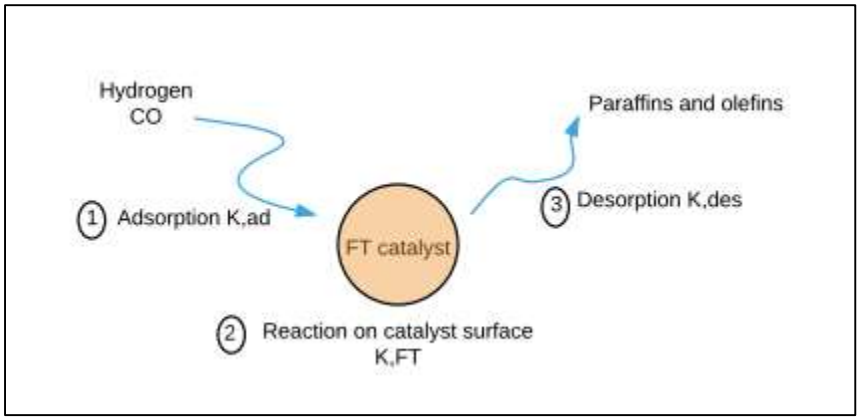

Figure 3.3: Illustration of the processes of adsorption, reaction and desorption of FT species on a catalyst particle (Mamabolo, 2018)

3.1.8.1 Adsorption

When a molecule adsorbs onto a catalyst, the extent to which the molecule covers the surface of the catalyst, referred to as the surface coverage θ, is dependent mainly on the concentration of that particular species in the bulk fluid phase. θ describes the fraction of the surface of the catalyst covered by a reactant species. A higher concentration would result in more surface coverage. Other factors including the adsorption constant affect the surface coverage as well and are an important factor to consider in modelling the adsorption process. The process of species adsorption can follow various mechanisms depending on the prevailing operating conditions.

3.1.8.1.1 Method of adsorption

An adsorbed reactant species will react with either another adsorbed species or with a species from the bulk fluid phase. The former and latter phenomena are referred to as dual and single site mechanisms respectively and ultimately affect the kinetics of the system. Furthermore, the reacting molecules can adsorb competitively or non-competitively. In the case of multiple reactants, the adsorbing molecules may compete for the same active site on the surface of the catalyst or the reactants may react on separate classes of active sites. The surface coverage of a reactant, which is the equivalent of concentration in homogenous reaction systems, is determined with the use of an isotherm. The Langmuir isotherm described in Equation 3.30 relates the concentration of the reactant in the bulk liquid phase with the surface coverage by introducing the adsorption constant. The Langmuir isotherm is predicated on the following few assumptions (Levenspiel, 1999):

1. The adsorption process is in equilibrium.
2. The catalyst surface behaves ideally, i.e., all sites have equal activity.
3. The adsorbed molecules do not interact with each other.

$$\theta_A = \frac{K_A P_A}{1+K_A P_A} \quad \text{Eq. 3.30}$$

Where A is an arbitrary reactant species, K_A is the adsorption equilibrium constant and P_A is the concentration of A in the bulk fluid phase which can also be represented by C_A in the event that the fluid phase is liquid. Equation 3.30 is specifically for a system where A adsorbs onto the active catalyst site without competition. The surface coverage of A would be retarded if more reactants where present to compete for the same site as shown in Equation 3.31.

$$\theta_A = \frac{K_A P_A}{1+K_A P_A+K_B P_B+K_C P_C+\cdots\ldots+K_{m-1} P_{m-1}+K_m P_m} \quad \text{Eq. 3.31}$$

If the adsorption step is rate limiting, then the rate equation will take the form:

$$R = k_{ads}[A][*] \quad \text{Eq. 3.32}$$

Where $[*]$ represents the concentration/number-density of vacant active sites on the catalyst surface and k_{ads} represents the adsorption rate constant. $[*]$ can be determined through a catalyst site balance by understanding that the total available sites are shared between occupied and unoccupied sites thus:

$$[*]_0 = [*] + [A*] \quad \text{Eq. 3.33}$$

Where $[*]_0$ denotes the total concentration of active sites on the catalyst surface and $[A*]$ represents the concentration of sites occupied by a reactant molecule which can in turn be determined by understanding the definition of surface coverage as shown in Equation 3.34.

$$\theta_A = \frac{[A*]}{[*]_0} \quad \text{Eq. 3.34}$$

Equation 3.32 is possible due to the assumption of pseudo-equilibrium for the surface reaction and desorption rates (Sinnot, 2005). It is common and reasonable practice to assume that the other surface processes besides the rate limiting step are in pseudo-equilibrium (Davis and Davis, 2003). Following the same logic and assuming pseudo-equilibrium for the surface reaction and the adsorption step when the desorption step is rate-limiting; the overall rate will take the form:

$$R = \frac{k_3 K_2 K_1 [*]_0 [A]}{1+(K_1+K_2 K_1)[A]} \quad \text{Eq. 3.35}$$

Where k_3 denotes the desorption rate constant, K_1 and K_2 represent the equilibrium adsorption and reaction constants respectively.

3.1.8.2 Chemical reaction

The chemical reaction kinetics will depend on the surface coverage of the reacting species which in turn depend on the adsorption isotherm. In simple homogenous elementary single reactions, the rate law, i.e., the equation that defines the rate of reaction, is easy to determine. The reactions in FTS are multiple and non-elementary, occurring on a catalyst surface. This introduces a level of difficulty in determining a rate law that will satisfactorily model the rate and thus the reactant conversion as a function of the prevailing reactor conditions. In determining a rate law, the reaction constants of the elementary reactions must be known and consolidated to give the resulting rate law for a particular reacting system. This means that for FTS, in which multiple reactions take place and even more elementary reaction steps are present, the task of determining the rate law is made difficult. To deal with this difficulty, FT reactions are lumped together according to the products formed and the total number of reactions is reduced accordingly. In general, the important reactions in FT are those that form paraffins and olefins. The water-gas-shift (WGS) reaction is also important, along with the reactions responsible for alcohol formation and the Boudouard reaction as seen in Table 1.2. In microreactors operating under the typical conditions as set out in Table 3.6, the FT reaction can be represented generally by [R2].

The next step is to determine the reaction rate constants of the elementary steps of the lumped reactions. This requires the understanding of the mechanism through which each of these reaction types occur. This is the most important step and is a point of contention among researchers. FTS is a polymerisation reaction with hydrocarbon molecules coming together to form longer chain products. The difficulty in describing the FTS reaction lies with the mechanism by which these long chain hydrocarbon products are formed. Various mechanisms have been put forward to account for the way the hydrocarbon products are formed and depending on the mechanism chosen, the rate equation will be different. One of the mechanisms proposed is the surface carbide mechanism where methylene acts as the monomer on which the propagation of chain growth is based (Brady & Pettit, 1981; Ojeda et al., 2010; Fischer and Tropsch, 1926). In this mechanism,

CO and H_2 adsorb dissociatively and the chain growth proceeds through the repeated insertion of the monomer (see Figure 3.4). Although this mechanism has received criticism stemming from the model's inconsistency with thermodynamic data relating to the formation of hydrocarbons through hydrogenation at elevated industrial temperatures (Craxford & Rideal, 1939). Davis (2009) used tracer studies in conjunction with available characterisation data as a basis for endorsing the use of the surface carbide mechanism in Co catalysed FTS. The author further suggests use of the oxygenate mechanism for Fe catalysed FTS.

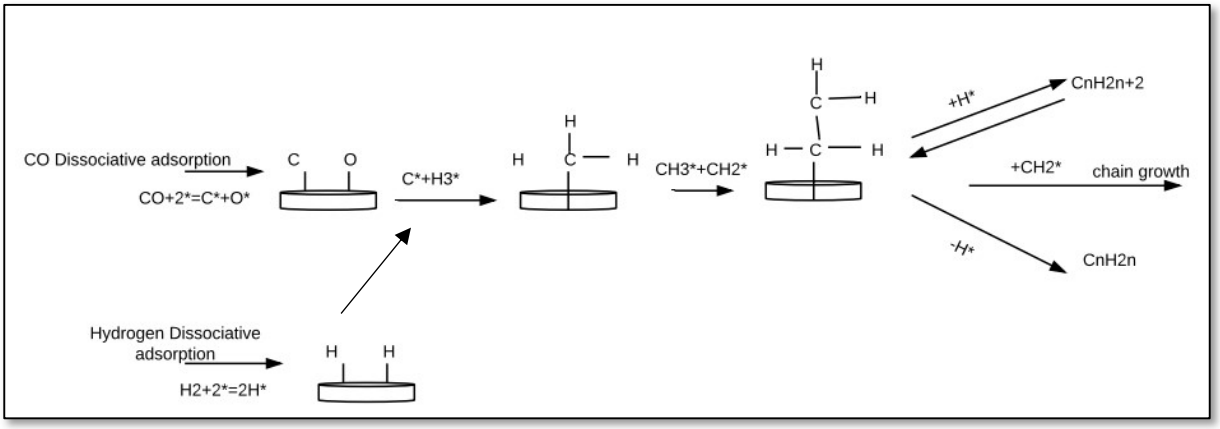

Figure 3.4: Surface carbide mechanism (Mamabolo, 2018)

Various mechanisms can be differentiated based on the type of monomers present and the propagation pathways followed. Chang et al., (2007) describes six different reaction mechanisms based upon these two factors. In the proposed mechanisms, the propagation step was assumed to be rate-limiting so that all other steps were taken to be quasi-equilibrated or in pseudo-equilibrium. The kinetics are also affected by the type of catalyst used with different rate equations resulting from the use of either Fe or Co catalysts. Reaction mechanisms can also be differentiated by the way in which the reactants adsorb onto the catalyst surface. The two main adsorption models are the Langmuir-Hishelwood-Hougen-Watson (LHHW) and the Eiley-Rideal models. These models were formulated to describe the adsorption mechanisms of reactants in heretogenously catalysed reactions. In the LHHW model, all the reactants adsorb onto the catalyst surface at separate active sites before reacting with one another and in the case of Eley-Rideal models only one of the reactants adsorbs onto an active catalyst site before reacting with an unadsorbed reactant (Albright, 2009). Eley-Rideal models are more important under extreme conditions, particularly in the

semiconductor production field whereas LHHW models are more common in catalysed reactions (Davis and Davis, 2003).

Table 3.6: Typical FT microreactor operating conditions

Operating Conditions	**Values**
Reactor Temperature (K)	473 - 530
Reactor Pressure (bar)	20 - 30
Dispersion height (mm)	10
Average residence time	290 ms
Gas superficial velocity, U_G (m/s)	0.05 - 0.5
Liquid superficial velocity (m/s)	$0.1U_G$
Liquid phase properties	
Density (kg/m^3)	640 - 696
Viscosity (Pa.s)	0.00029 - 0.004
Surface tension (N/m)	0.01 - 0.018
CO diffusivity (m^2/s)	17.2×10^{-9}
H_2 diffusivity (m^2/s)	45.5×10^{-9}
Solid phase properties (Co/MgO catalyst supported on SiO_2)	
Catalyst diameter (m)	42×10^{-6} - 50×10^{-6}
Catalyst density (kg/m^3)	647

Once a reaction mechanism is identified, the rate controlling step within that mechanism must be identified to allow for the development of the rate law, provided the surface reaction is rate limiting. Through the use of steady-state approximation, the overall rate law based on the rate limiting step can be determined (Equation 3.36). The steady-state approximation is based on the assumption that the concentration of an intermediate in a multiple elementary reaction system is constant, i.e., its rate of formation is equal to its rate of consumption. The steady-state approximation can greatly simplify the process of determining an overall surface reaction rate when applied to the limiting reaction step and a quasi-equilibrated step. A quasi-equilibrated step is a combination of the rest of the elementary reaction steps which are assumed to be in equilibrium. This in effect reduces a complex system of multiple elementary reactions to a

simplified set of reactions on which the overall surface reaction rate can be derived (Davis and Davis, 2003).

$$R = \frac{r_i - r_{-i}}{\sigma_i} \quad \text{Eq. 3.36}$$

Where R is the overall rate, r_i is the forward reaction rate, r_{-i} is the reverse reaction rate and σ_i is the stoichiometric number of the elementary reaction step. The final equation should take the form shown in Equation 3.37.

$$R = \frac{k_2 K_{ads}[*]_0[A]}{1 + K_{ads}[A]} \quad \text{Eq. 3.37}$$

Where k_2 represents the reaction rate constant. Equation 3.37 exemplifies a typical LHHW rate law given by:

$$Rate = \frac{(kinetic\ term)(potential\ term)}{adsorption\ term} \quad \text{Eq. 3.38}$$

The overall rate law is usually determined empirically by assuming a reaction scheme and determining the reaction and adsorption constants through regression analysis. According to Levenspiel (1999), all possible reaction pathways with all possible rate-limiting steps should be noted at which stage experiments can be used to disprove and exclude those pathways that do not fit the data. The author (Levenspiel, 1999) also cautions against the assumption that a pathway that fits the data perfectly represents the correct reaction mechanism as more than one mechanism may fit the data. It is therefore difficult to determine accurately the mechanism by which FT reactions occur. Nonetheless, several authors have put forward rate laws to describe the kinetics in FTS for both Co and Fe catalysed systems. Espinoza et al. (1999), Pratt (2012) and Sehabiague (2012) provide a summary of these rate laws (see Table 3.7).

Table 3.7: Various FT Kinetic rate laws(Mamabolo, 2018)

Catalyst	Rate law	Reference
Co	$R_{FT} = k_{FT}\frac{P_{H_2}{}^2}{P_{CO}}$	Brotz (1949)
Co	$R_{FT} = k_{FT}\frac{P_{CO}{}^{0.5}P_{H_2}{}^{0.5}}{(1+aP_{CO}{}^{0.5})^2}$	Sarup and Wojciechowski (1989)
Co	$R_{FT} = k_{FT}\frac{kP_{CO}P_{H_2}}{(1+aP_{CO})^2}$	Yates and Satterfield (1991)
Fe	$R_{FT} = k_{FT}\frac{P_{CO}P_{H_2}}{P_{CO}+aP_{CO_2}}$	Nettelhoff et al. (1985)
Co	$R_{FT} = k_{FT}\frac{P_{H_2}{}^2P_{CO}}{P_{COP_{H_2}}+aP_{H_2}O}$	Withers et al. (1990)
Co	$R_{FT} = k_{FT}\frac{P_{H_2}{}^{1.5}P_{CO}}{(aP_{COP_{H_2}}+P_{H_2}O)^2}$	Schweich et al. (2007)
Fe	$R_{FT} = k_{FT}\frac{P_{H_2}{}^{0.5}P_{CO}}{(1+aP_{CO}+bP_{CO_2})^2}$	van der Laan (1999)
Fe	$R_{FT} = k_{FT}\frac{\frac{P_{H_2}{}^{1.5}P_{CO}}{P_{H_2}O}}{(1+a\frac{P_{CO}P_{H_2}}{P_{H_2}O})^2}$	van Steen and schulz (1999)

3.1.8.3 Catalysts

In general, FT processes catalyzed by a Co catalyst are negligibly affected by the presence of water. This is because Co catalysis does not promote the water gas shift reaction which affects the consumption of H_2. The opposite is true for Fe catalysis (Espinoza et al., 1999). Co catalysts generally achieve a higher per pass conversion than Fe catalysts and are thus more favoured in FT systems (Espinoza et al., 1999). Given that they are more expensive than Fe catalysts, tolerance for attrition and/or deactivation of this catalyst is typically low from an economic point of view. Compared to conventional high temperature FT reactors whose high superficial gas velocities and turbulence create a violent environment in which a Co catalyst would quickly degrade, the conditions in a LTFT microchannel reactor will be less violent allowing the Co catalyst to last longer.

Yates and Satterfield (1991) developed a rate law based on Co catalysis in a continuous stirred tank reactor (CSTR). The authors modified the rate laws postulated by Sarup and Wojciechowski (1989) and Wojciekwoski (1988) and tested the resulting rate laws under 220 – 240 °C, 0.5 to 1.5 bar and H_2/CO ratios between 1.5 and 3.5. The rate law that accurately predicted the experimental results was selected (Equation 3.39). Equation 3.39 was tested against data from other sources (Wojciekwoski, 1988) and was found to produce accurate results.

$$-Rco = \frac{kP_{CO}P_{H_2}}{(1+aP_{CO})^2} \qquad \text{Eq. 3.39}$$

Regarding the control of the overall rate between mass transfer and surface kinetics, Inga & Morsi (1996) note that the resistance to the FT process lies significantly with the kinetics so that the surface kinetics would have to improve by a great margin for the gas-solid mass transfer to be rate-limiting. Deckwer et al. (1980) also puts forth an argument to this effect. For the purposes of this study, the rate law as proposed by Yates and Satterfield (1991) will be applied.

3.2 Model Development

In developing a model to describe FTS in a microchannel reactor, the literature and analysis covered in chapter 3 will be applied and incorporated into a single unified mathematical model that should be able to fairly represent the conditions in real FT microreactors. The conditions to be used as a basis for the model are provided in Table 3.6. Additionally, the physical properties of the microreactor to be modelled are provided in Table 3.8 below primarily sourced from typical conditions in literature (Deshmukh et al., 2010; Jarosch et al., 2005). The sizes provided should allow for relatively easy fabrication as demonstrated by various authors (Deshmukh et al., 2010; Leviness et al., 2014) so that their practicality is not in question. The layered wall catalyst will cover the entire length of the channel. The catalyst layer thickness selected is supposed to minimize mass and heat transfer limitations and should be mechanically stable under the prevailing operating conditions (Kolb, 2013).

Table 3.8: Typical FT micro reactor physical conditions

Physical Conditions	Description
Channel shape	Rectangular
Characteristic gap/diameter (mm)	3.49
Reactor length (mm)	10
Reactor width (mm)	3.5
Catalyst loading (v/v)	0.3
Material of Construction	SS 316

3.2.1 Assumptions

A summary of the relevant FT microreactor system assumptions that will be adopted during the model development phase are given below:

- The system is in steady-state
- No internal/intra-particle mass transfer resistance
- External mass transfer resistance is only present across the gas-liquid interphase
- Gas-liquid mass transfer resistance presents on the liquid side of the interphase
- Only H_2 and CO are present in the feed
- No radial dispersion effects are present
- The liquid and small bubble phases are pseudo-homogenous
- Small bubbles hold-up and velocity are independent of axial position
- System is isothermal
- System is isobaric

3.2.2 Material Balances

The development of the microchannel reactor mathematical model will be carried out from 1st principles based on conservation laws. For the micro-FT reactor currently under study, only the material balance will be considered. This is because the conditions within the microchannel produce very high heat transfer between the reactor contents and the cooling medium, given the heat transfer improvements inherent in microchannels, to ensure a stable and constant temperature profile. This is evidenced in the work by Jarosch et al. (2005) where experiments on FT

microchannels in LTFT conditions produced a relatively constant reactor contents temperature over the entire length of the channel (see Figure 5.37). Additionally, the main objectives identified for developing this model is to provide a platform for the study of the hydrodynamics inside a SBCR and as such the material balance should suffice. It is the flow dynamics within the FT microchannel reactor that are of paramount importance. The development of the material balance equations in this section were adopted for use in an FT microchannel reactor from the previous work of Mamabolo (2018) which focused on FT SBCR's.

The material balances from the law of mass conservation will take the following general form:

$$[\,moles\ accumulated] = [\,moles\ trannsported\ in] - [\,moles\ transported\ out] - [\,moles\ consumed\ by\ reaction] \quad \text{Eq. 3.40}$$

In applying the material balance, the microchannel will be discretized along its axis as shown in Figure 3.5. Molar fluxes will be used to represent the axial transport of material in and out of each discrete volume element ΔV. The terms in the general mole balance in Equation 3.40 are specified as follows:

$$[number\ of\ moles\ accumulated] = (C_{i_{t+\Delta t}} - C_{i_t}) \times A_c \times \Delta z \quad \text{Eq. 3.41}$$

$$[number\ of\ moles\ trannsported\ in] = Flux\ in_z \times A_c \times t \quad \text{Eq. 3.42}$$

$$[number\ of\ moles\ trannsported\ out] = Flux\ out_{z+\Delta z} \times A_c \times t \quad \text{Eq. 3.43}$$

$$[number\ of\ moles\ consumed\ by\ reaction] = G \times A_c \times t \times \Delta z \times \rho_{cat} \times \varepsilon_s \times \varepsilon_l \quad \text{Eq. 3.44}$$

The total flux is the sum of the convective and dispersive flux terms. Convective transport of material occurs along the axial direction through the bulk flow of material in and out of the volume element and is given by:

$$Convective\ flux = U_i C_i \quad \text{Eq. 3.45}$$

Dispersive flux is transport of material driven by, amongst other factors, molecular diffusion, turbulent mixing and eddy formations. It is described by Equation 3.46 thus:

$$Dispersive\ flux = -E\varepsilon_n \frac{dC_{i,m}}{dz} \quad \text{Eq. 3.46}$$

The total flux can then be computed as:

$$Total\ flux = U_i C_i - E\varepsilon_n \frac{dC_{i,m}}{dz} \quad \text{Eq. 3.47}$$

Using the specified terms in Equations 45 – 48, Equation 3.40 can be re-written accordingly:

$$(C_{i_{t+\Delta t}} - C_{i_t}) \times A_c \times \Delta z = (Flux\ in_z \times A_c \times t) - (Flux\ out_{z+\Delta z} \times A_c \times t) - (G \times A_c \times t \times \Delta z \times \rho_{cat} \times \varepsilon_s) - (Interphase\ mass\ trasfer \times A_c \times t \times \Delta z) \quad \text{Eq. 3.48}$$

By dividing Equation 41 by $A_c \times t \times \Delta z$ and taking the limits as $z \to 0$ and $t \to 0$, Equation 3.49 is determined:

$$\frac{\partial C_i}{\partial t} = \frac{\partial Flux_i}{\partial z} - Interphase\ mass\ trasfer - (G_i \times \rho_{cat} \times \varepsilon_s \times \varepsilon_l) \quad \text{Eq. 3.49}$$

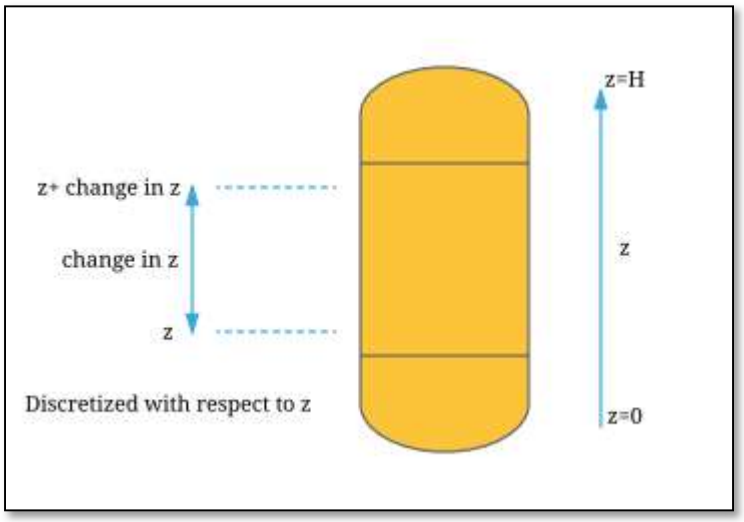

Figure 3.5: Discretization with respect to length of microchannel reactor (Mamabolo, 2018)

In Equation 3.49, the interphase mass transfer term refers to the transfer of material from the gas to liquid phase and is determined according to Equation 3.25 which is based on the two-film theory to give:

$$Interphase\ mass\ transfer = K_{La}({C_{i,L}}^* - C_{i,L}) \quad \text{Eq. 3.50}$$

Substituting Equation 3.47 into Equation 3.49 and considering a steady-state model, a general axial dispersion ordinary differential equation (ode) for microchannel reactors can be determined as in Equation 3.51.

$$0 = \frac{UdC_{i,m}}{dz} - E_m\varepsilon_m \frac{d^2C_{i,m}}{dz^2} + a^*K_{La,i,m}({C_{i,L}}^* - C_{i,L}) - (G_i \times \rho_{cat} \times \varepsilon_s \times \varepsilon_l) \quad \text{Eq. 3.51}$$

Where a^* is either 1 or -1 depending on whether mass is leaving the gas phase or being received by the liquid phase respectively. Using Equation 3.51, the large bubble compartment material balance can be written as shown in Equation 3.52 with the assumption that no reaction takes place in the gas phase. Accordingly, the gas phase material balances for CO and H_2 in the large bubbles compartment are given in Equations 57 and 58 respectively.

$$0 = \frac{U_{LB} dC_{i,LB}}{dz} - E_{LB}\varepsilon_{LB}\frac{d^2C_{i,LB}}{dz^2} + K_{La,i,LB}({C_{i,L}}^* - C_{i,L}) \quad \text{Eq. 3.52}$$

$$\frac{U_{LB} dC_{CO,LB}}{dz} - E_{LB}\varepsilon_{LB}\frac{d^2C_{CO,LB}}{dz^2} = -K_{La,CO,LB}({C_{CO,L}}^* - C_{CO,L}) \quad \text{Eq. 3.53}$$

$$\frac{U_{LB} dC_{H_2,LB}}{dz} - E_{LB}\varepsilon_{LB}\frac{d^2C_{H_2,LB}}{dz^2} = -K_{La,H_2,LB}({C_{H_2,L}}^* - C_{H_2,L}) \quad \text{Eq. 3.54}$$

The small bubbles experience axial dispersion in a similar manner to the liquid phase because of the assumption previously put forward that the liquid and small bubbles compartments can be treated as a single pseudo-homogenous phase. The result of this is the inclusion of the dispersion term in the small bubble compartment material balance. No reaction takes place in the small bubbles so that the balance equation can be written as shown in Equation 3.55. The material balances for CO and H_2 in the small bubble compartment are given in Equations 3.56 and 3.57 respectively.

$$0 = \frac{U_{SB} dC_{i,SB}}{dz} - E_{SB}\varepsilon_{SB}\frac{d^2C_{i,SB}}{dz^2} + K_{La}({C_{i,L}}^* - C_{i,L}) \quad \text{Eq. 3.55}$$

$$\frac{U_{SB} dC_{CO,SB}}{dz} - E_{SB}\varepsilon_{SB}\frac{d^2C_{CO,SB}}{dz^2} = -K_{La,CO,SB}({C_{i,L}}^* - C_{i,L}) \quad \text{Eq. 3.56}$$

$$\frac{U_{SB} dC_{H_2,SB}}{dz} - E_{SB}\varepsilon_{SB}\frac{d^2C_{H_2,SB}}{dz^2} = -K_{La,H_2,SB}({C_{i,L}}^* - C_{i,L}) \quad \text{Eq. 3.57}$$

It is assumed that the liquid phase experiences axial dispersion and that the FT reaction takes place only in the liquid phase. Adopting R2 as a representative reaction for FT synthesis, the consumption rate of H_2, G_{H_2}, is double that of CO, G_{CO}. The resulting material balance equation for the liquid phase is written in Equation 3.58. The CO and H_2 material balances are given in Equations 3.59 and 3.60 respectively. In Equations 3.59 and 3.60, G, which will be represented by

Equation 3.39, is the reaction rate law. As the gas concentration will be treated in mol/m^3 instead of Pa, the partial pressure terms will be converted to concentration terms using the ideal gas law so that Equation 3.39 can be re-written as in Equation 3.61.

$$0 = \frac{U_L dC_{i,L}}{dz} - E_L\varepsilon_L \frac{d^2C_{i,L}}{dz^2} - K_{La,i,SB}({C_{i,L}}^* - C_{i,L}) - K_{La,i,LB}({C_{i,L}}^* - C_{i,L}) - (G_i \times \rho_{cat} \times \varepsilon_s \times \varepsilon_l)$$

Eq. 3.58

$$\frac{U_L dC_{CO,L}}{dz} - E_L\varepsilon_L \frac{d^2C_{CO,L}}{dz^2} = +K_{La,CO,SB}\left({C_{i,L}}^* - C_{i,L}\right) + K_{La,CO,LB}\left({C_{i,L}}^* - C_{i,L}\right) + (G_{CO} \times \rho_{cat} \times \varepsilon_s \times \varepsilon_l)$$

Eq. 3.59

$$\frac{U_L dC_{H_2,L}}{dz} - E_L\varepsilon_L \frac{d^2C_{H_2,L}}{dz^2} = +K_{La,H_2,SB}\left({C_{i,L}}^* - C_{i,L}\right) + K_{La,H_2,LB}\left({C_{i,L}}^* - C_{i,L}\right) + (G_{H_2} \times \rho_{cat} \times \varepsilon_s \times \varepsilon_l)$$

Eq. 3.60

$$\mathrm{R} = \frac{kC_{CO,G}C_{H_2,G}(RT)^2}{(1+bC_{CO,G}RT)^2}$$

Eq. 3.61

3.2.3 Boundary conditions

The solutions to the six odes in Equations 3.53, 3.54, 3.56, 3.57, 3.59 and 3.60 require the definition of boundary conditions. Danckwerts-type boundary conditions will be used in this model. For the odes describing the large bubble compartment, the boundary conditions are applied as shown in Equations 3.62 – 3.64.

$$at\ z = 0, \qquad C_{i,LB} = C_{i,G,0}$$

Eq. 3.62

so that

$$C_{CO,LB} = C_{CO,G,0}$$

Eq. 3.63

$$C_{H_2,LB} = C_{H_2,G,0}$$

Eq. 3.64

Similarly, the boundary conditions applicable to the small bubble compartment are defined in Equations 3.65 –3.67.

$$at\ z = 0, \qquad C_{i,SB} = C_{i,G,0}$$

Eq. 3.65

$$C_{CO,SB} = C_{CO,G,0}$$

Eq. 3.66

$$C_{H_2,LB} = C_{H_2,G,0}$$

Eq. 3.67

The ode's describing the liquid and small bubble compartments are of the 2nd order type, thus requiring the use of two boundary conditions. The Danckwerts-type boundary conditions were again used. For the liquid phase the boundary conditions adopted are shown in Equations 3.68 – 3.70 (Deckwer, 1991).

$$\frac{dC_{i,L}}{dz} = -\frac{HU_L C_{i,L}}{E_L \varepsilon_L} \quad \text{Eq. 3.68}$$

so that

$$\frac{dC_{CO,L}}{dz} = -\frac{HU_L C_{CO,L}}{E_L \varepsilon_L} \quad \text{Eq. 3.69}$$

$$\frac{dC_{H_2,L}}{dz} = -\frac{HU_L C_{H_2,L}}{E_L \varepsilon_L} \quad \text{Eq. 3.70}$$

For the small bubble compartment, Danckwerts-type boundary conditions as suggested by Sehabiague (2012) were applied. These are shown in Equations 75 to 77.

$$U_{SB} C_{i,SB} - E_{SB} \varepsilon_{SB} \frac{dC_{i,SB}}{dz} = U_{SB,0} C_{i,SB,0} \quad \text{Eq. 3.71}$$

For CO:

$$U_{SB} C_{CO,SB} - E_{SB} \varepsilon_{SB} \frac{dC_{CO,SB}}{dz} = U_{SB,0} C_{CO,SB,0} \quad \text{Eq. 3.72}$$

For H_2:

$$U_{SB} C_{H_2,SB} - E_{SB} \varepsilon_{SB} \frac{dC_{H_2,SB}}{dz} = U_{SB,0} C_{H_2,SB,0} \quad \text{Eq. 3.73}$$

Dankwerts type boundary conditions were also adopted for the large bubble compartment as shown below (Sehabiague, 2012):

$$U_{LB} C_{i,LB} - E_{LB} \varepsilon_{LB} \frac{dC_{i,LB}}{dz} = U_{LB,0} C_{i,LB,0} \quad \text{Eq. 3.74}$$

For CO:

$$U_{LB} C_{CO,LB} - E_{LB} \varepsilon_{LB} \frac{dC_{CO,LB}}{dz} = U_{LB,0} C_{CO,LB,0} \quad \text{Eq. 3.75}$$

For H_2:

$$U_{LB} C_{H_2,LB} - E_{LB} \varepsilon_{LB} \frac{dC_{H_2,LB}}{dz} = U_{LB,0} C_{H_2,LB,0} \quad \text{Eq. 3.76}$$

3.2.4 Parameter Estimation

Before the modelling exercise can be carried out, it is necessary to estimate several crucial parameters that are often empirically derived and presented in the form of correlations. It would be ideal to measure these parameters individually under the exact range of operating and physical conditions for which the model is developed, but this will require a significant, concerted and sustained effort on the part of researchers which may not be readily attainable. It may also not always be worthwhile given that some of the available correlations are quite robust and can be applied under an extended range of conditions with relatively good prediction accuracy. In this section, the parameters relevant to the FT microchannel reactor model currently being developed will be carefully analysed and selected to ensure optimal model accuracy.

3.2.4.1 Superficial velocity

The superficial gas velocity in the small bubble class was calculated based on the correlation by Sehabiague (2012) where the assumption is made that this parameter is independent of axial position. Instead, it is predominantly affected by liquid phase properties as shown in Equation 3.14. Under the conditions described in Table 3.6 and Table 3.8, a mainly a wax product composed of long chain hydrocarbons is expected. The study by Sehabiague (2012) considered the liquid properties of a Sasol wax product with an average carbon number of 80 manufactured by Moore and Munger, Inc. which is supposed to closely resemble the wax that Sasol produces in their commercial Fischer-Tropsch reactors. Surface tension, density and viscosity were measured under varying temperatures (290 -500 K) and are given as functions of temperature in Table 3.9. The density of the gas was taken to be 7 kg/m^3 (Krishna and Sie, 2000). As stated earlier, the large bubble superficial gas velocity will then be determined from the difference between the overall and small bubble velocities according to Equation 3.15.

*Table 3.9: SBCR liquid phase properties as functions of temperature (*Sehabiague, 2012*)*

Liquid Property	Correlation
Density (kg/m^3)	$\rho_L = 959.08\text{-}0.513T$
Viscosity (kg/m.s)	$\mu_L = e^{(-4.3284+\frac{2319.4}{T})}$
Surface tension (N/m)	$\sigma_L = 0.001(70.57\text{-}0.175T + (1.04 \times 10^{-4}T^2)$

The overall superficial gas velocity will decrease along the axial direction in the reactor because of a decrease in the moles of total reactants following consumption by the FT reaction. This can be modelled through an overall gas phase material balance as shown in Equation 3.77

$$\frac{dU_G C_G}{dz} = \frac{dU_{SB}C_{CO,SB}}{dz} + \frac{dU_{LB}C_{CO,LB}}{dz} + \frac{dU_{SB}C_{H_2,SB}}{dz} + \frac{dU_{LB}C_{H_2,LB}}{dz} \quad \text{Eq. 3.77}$$

where

$$U_G = U_{G,0} \quad at \quad z = 0 \quad \text{Eq. 3.78}$$

and C_G is the total gas concentration in both large and small bubble compartments:

$$C_G = C_{CO,SB} + C_{CO,LB} + C_{H_2,SB} + C_{H_2,LB} \quad \text{Eq. 3.79}$$

The liquid superficial velocity describes the velocity of liquid product as it is drawn from the microreactor or is pushed out through momentum transfer by the flowing gaseous phase. It is normally an order of magnitude lower than the superficial gas velocity (Dudukovic et al., 1999; Boyer et al., 2016)

3.2.4.2 Hold-up

The small bubbles hold-up correlation given in Equation 3.80 as put forward by Maretto and Krishna (1999) will be used to determine the volume proportion of small bubbles relative to the total reactor bed volume. In Equation 3.80, $\varepsilon_{SB,ref}$ refers to the small bubble hold-up in a liquid phase void of any solid particles and is given as 0.27 for paraffin oil liquid, a sufficiently similar liquid to the real waxy conditions in FT reactors pending the use of a more closely related liquid in further experimental studies. The same author developed a correlation for the large bubble class hold-up which is thought to depend on the geometry of the reactor and the velocity difference between the large and small bubbles as shown in Equation 3.81. Because of its dependence on

superficial gas velocity, the large bubble hold-up will change relative to the axial position in the vessel following the consumption of the gaseous reagents by the FT reaction. The dependence of the large bubble hold-up on reactor diameter in Equation 3.81 only exists for diameters less than 1 m, which is the case for the FT microchannel reactor being considered in the current study, otherwise Equation 3.82 is used. The total gas hold-up will be computed by taking into account the large and small bubble hold-ups and applying them in Equation 3.83 (Maretto and Krishna, 1999).

$$\varepsilon_{SB} = \varepsilon_{SB},ref\ (1 - \frac{0.7}{\varepsilon_{SB,ref}}\ \varepsilon_S) \quad \text{Eq. 3.80}$$

$$\varepsilon_{LB} = 0.3\frac{(U_g - U_{g,SB})^{0.8}}{D_C{}^{0.18}(U_g - U_{g,SB})^{0.22}} \quad \text{Eq. 3.81}$$

$$\varepsilon_{LB} = 0.3\frac{(U_g - U_{g,SB})^{0.8}}{(U_g - U_{g,SB})^{0.22}} \quad \text{Eq. 3.82}$$

$$\varepsilon = \varepsilon_{LB} + \varepsilon_{SB}(1 - \varepsilon_{LB}) \quad \text{Eq. 3.83}$$

The liquid phase hold-up can be determined from the balance of the total gas and solids hold-up as shown in Equation 3.84.

$$\varepsilon_l = 1 - \varepsilon_g - \varepsilon_s \quad \text{Eq. 3.84}$$

3.2.4.3 Dispersion coefficients

3.2.4.3.1 Liquid axial dispersion coefficient

The axial dispersion coefficient for the liquid phase will be determined according to the isotropic turbulence model developed by Baird and Rice (1975) as described in Equation 3.6. The small bubbles dispersion coefficient is assumed to be equal to that in the liquid phase because the small bubbles are trapped in the liquid phase and as a result follow the movement of the liquid phase (Steynberg and Dry, 2004). The small bubble class dispersion coefficient is consequently given by Equation 3.85.

$$E_{SB} = K{d_c}^{4/3}(U_g g)^{1/3} \quad \text{Eq. 3.85}$$

3.2.4.3.2 Gas phase axial dispersion coefficient

Given the importance of gas phase axial dispersion to 3-phase reactor systems with high conversion rates, the correlation by Mangartz and Pilhofer (1980) will be used in this study to represent of back-dispersion in the large bubble class.

3.2.4.4 Mass transfer coefficients

The volumetric mass transfer coefficients through the large and small bubble classes as proposed by Maretto and Krishna (1999) will be adopted in this study. The mass transfer coefficient for the large bubble class can be determined through Equation 3.86 and the coefficients for the specific CO and H_2 species can be calculated using Equations 3.87 and 3.88 respectively.

$$K_{La,i,LB} = 0.5\varepsilon_{LB}\sqrt{\frac{D_i}{D_{ref}}} \quad \text{Eq. 3.86}$$

$$K_{La,CO,LB} = 0.5\varepsilon_{LB}\sqrt{\frac{D_{CO}}{D_{ref}}} \quad \text{Eq. 3.87}$$

$$K_{La,H_2,LB} = 0.5\varepsilon_{LB}\sqrt{\frac{D_{H_2}}{D_{ref}}} \quad \text{Eq. 3.88}$$

Equations 3.89 to 3.91 will be used for determining the mass transfer coefficients of the reacting species in the small bubble class. D and D_{ref} refer to the diffusion coefficient and the reference diffusion coefficient respectively.

$$K_{La,i,SB} = \varepsilon_{SB}\sqrt{\frac{D_i}{D_{ref}}} \quad \text{Eq. 3.89}$$

$$K_{La,CO,SB} = \varepsilon_{SB}\sqrt{\frac{D_{CO}}{D_{ref}}} \quad \text{Eq. 3.90}$$

$$K_{La,H_2,SB} = \varepsilon_{SB}\sqrt{\frac{D_{H_2}}{D_{ref}}} \quad \text{Eq. 3.91}$$

3.2.4.5 Henry's constants

To evaluate the mass transfer between the gas and liquid phases, $C_{i,L}{}^*$ must be converted to $C_{i,g}$ using Henry's constants as shown in Equation 3.27. For gas concentrations in moles/m^3, as in the current study, H_i can be expressed in dimensionless form so that $C_{i,g}$ instead of P_i can be determined from Equation 3.27. As a result, Equation 3.27 can be re-written using $C_{i,g}$ (Equation

3.93) with the application of the ideal gas law (Equation 3.92). Henry's constants are functions of temperature and Soriano's (2005) equations describing Henry's constants as functions of temperature for CO and H_2 were used as shown in Equations 3.94 to 3.96. The parameters in Equations 3.95 and 3.96 are given in Table 3.10.

$$P = RT\frac{n}{V} \quad \text{Eq. 3.92}$$

$$C_{i,L}{}^{*} = RT\frac{C_{i,g}}{H_i} \quad \text{Eq. 3.93}$$

Soriano (2005) Henry's constants correlations are given as:

$$H_i = H_{i,o}e^{(A_i(\frac{1}{T})^2 + B_i(\frac{1}{T}))} \quad \text{Eq. 3.94}$$

$$H_{CO} = H_{CO,o}e^{(A_{CO}(\frac{1}{T})^2 + B_{CO}(\frac{1}{T}))} \quad \text{Eq. 3.95}$$

$$H_{H_2} = H_{H_2,o}e^{(A_{H_2}(\frac{1}{T})^2 + B_{H_2}(\frac{1}{T}))} \quad \text{Eq. 3.96}$$

Table 3.10: Henry's constant correlations parameters (Soriano, 2005)

Species	Ho	A	B
CO	22.8	-365100	1873
H_2	42.18	-192900	1345

3.2.4.6 Kinetic constants

The rate law to be used in this study (Equation 3.39) requires knowledge of reaction rate and adsorption constants, k and a respectively. Both these constants depend on temperature and follow the Arrhenius equation. For the rate constant:

$$k = A_{FT}e^{-\frac{E_{a,FT}}{RT}} \quad \text{Eq. 3.97}$$

Where $E_{a,FT}$ refers to the reaction activation energy.

For the adsorption constant:

$$a = A_{ad} e^{-\frac{E_{a,ad}}{RT}} \quad \text{Eq. 3.98}$$

Where $E_{a,ad}$ referes to the adsorption activation energy.

The parameters in Equations 3.97 and 3.98 are quantified in Table 3.11.

Table 3.11: Reaction rate and adsorption constants for Equations 3.97 and 3.98 (Sehabiague, 2012)

	Pre-exponential Factor		Activation Energy	
Reaction	A_{FT}	8.037×10^{-9}	$E_{a,FT}$	37369.5
Adsorption	A_{ad}	1.243×10^{-12}	$E_{a,ad}$	-68474.1

3.2.5 Reactor feed conditions

The H_2/CO mole ratio of the synthesis gas fed to the microreactor will be 2 as this is the most ideal for Co catalyzed reactions that facilitate no WGS reaction (Dry, 2002). Assuming the syngas feed contains only the reactants and no other components, the feed component concentrations can be determined thus:

$$\frac{m_{syngas,feed}}{molar\ syngas\ unit} = 2\ mol\ H_2\left(MW_{H_2}\right) + 1\ mol\ CO(MW_{CO})$$

$$= 4.04 + 28.01$$

$$= 32.05\ g \quad \text{Eq. 3.99}$$

The inlet concentrations of the reactant species can then be determined as:

$$C_{H_2,0} = \frac{2}{32.05} \times \rho_G \times 10^3$$

$$= 436.82 \frac{mol\ H_2}{m^3 syngas} \quad \text{Eq. 3.100}$$

$$C_{CO,0} = \frac{1}{32.05} \times \rho_G \times 10^3$$

$$= 218.41 \frac{mol\ CO}{m^3 syngas} \quad \text{Eq. 3.101}$$

The operating and physical conditions given in Table 3.6 and Table 3.8 will be adopted in the current study.

3.2.6 Conclusion

In this chapter, the physical properties and models important to FT microreactor systems were identified and analyzed. It was determined that the principle of fluid continuity still holds under the circumstances considered in this thesis, i.e., the fluid within the microchannel reactor will behave as a single continuum. The gas and liquid phase axial dispersion are important parameters to model as they stand to influence the behaviour and performance of a microchannel reactor. Hold-up of the gaseous and liquid phases are important parameters that directly determine the available volume of liquid and gas available in the microchannel reactor. These parameters are primarily influenced by the gas phase superficial velocity and the physical properties of both the gas and liquid phases.

Several, important microchannel reactor heat transfer effects were identified and discussed along with their applicable correlations. These include conjugate heat transfer, transverse and axial heat conduction, intra-particle heat transfer and viscous dissipation, which may be more prominent in micro-structured systems. The effects of interfacial forces were also considered and discussed including the possible presence of slip conditions at the microchannel wall given the prominence of interfacial forces is such systems. Surface roughness was also analyzed in microchannels as its effects could be more pronounced in micro diameter channels.

Mass transfer in microchannel systems was analysed and discussed in detail including the relevant applicable correlations to be used in the thesis model. The axial dispersion model was identified as an appropriate mixing model for microreactors as it allows the flexibility and robustness to describe a wide range of operating conditions. The FT kinetics were discussed in detail to provide a kinetics environment in which the overall model would be placed. This included the analysis of the reaction steps, the kinetic rate laws and the relevant catalysts.

Using available correlations from literature, important parameters were defined and represented for input into the overall model. These included the superficial gas velocity, hold-up, dispersion coefficients, mass transfer coefficients and kinetic constants. These correlations were set-up to

feed into the set of mass balances which form the basis of the overall model. A set of mass balance equations were developed from 1st principles to describe the fate of the reacting species in the microchannel reactor. A set of assumptions for the model were put forward as well as microchannel reactor feed conditions to provide the context under which the model was being developed. These mass balance equations, assumptions, reactor feed conditions and estimated parameters will be used to construct the overall mathematical model.

Chapter 4: Modeling & Simulation

The numerical solutions to the model ordinary differential equations (ODEs) will be carried out in MATLAB's Simulink environment. The mass balance serves as the focal point of the model and the odes describing the complete mass conservation are input into the Simulink environment for numerical solution operations. In this chapter, CO and H_2 material balance odes in the small, large bubble and liquid phases will be translated into Simulink models/blocks. In all the following Simulink models and sub-models, blue blocks will denote model inputs while red blocks will denote outputs from the model. Yellow blocks will be used to represent the scope block whose function is to produce a plot of the change in the variable of interest over the length of the microchannel. Sub-models, in which the models/equations are translated in detail will be given a grey colour. The numbers inside the input and output blocks are assigned automatically by Simulink and have no relationship to the actual model. When interpreting the models, these should be ignored and the block descriptions should be used instead, which indicate the parameter under consideration.

4.1 Large bubble phase

The species mass balance odes in the large bubble compartment, represented by Equations 3.53 and 3.54 for CO and H2 species respectively, were translated into Simulink sub-models as shown in Figure 4.1 and Figure 4.2. These sub-models should provide data concerning the change in CO and H2 concentrations in the large bubble class as a function of the reactor axial length. The boundary conditions for the large bubble class mass balance odes were set-up as shown in Figure 4.3 and Figure 4.4 for the CO and H2 species respectively. A more detailed illustration of the boundary condition sub-model is given in Appendix A.

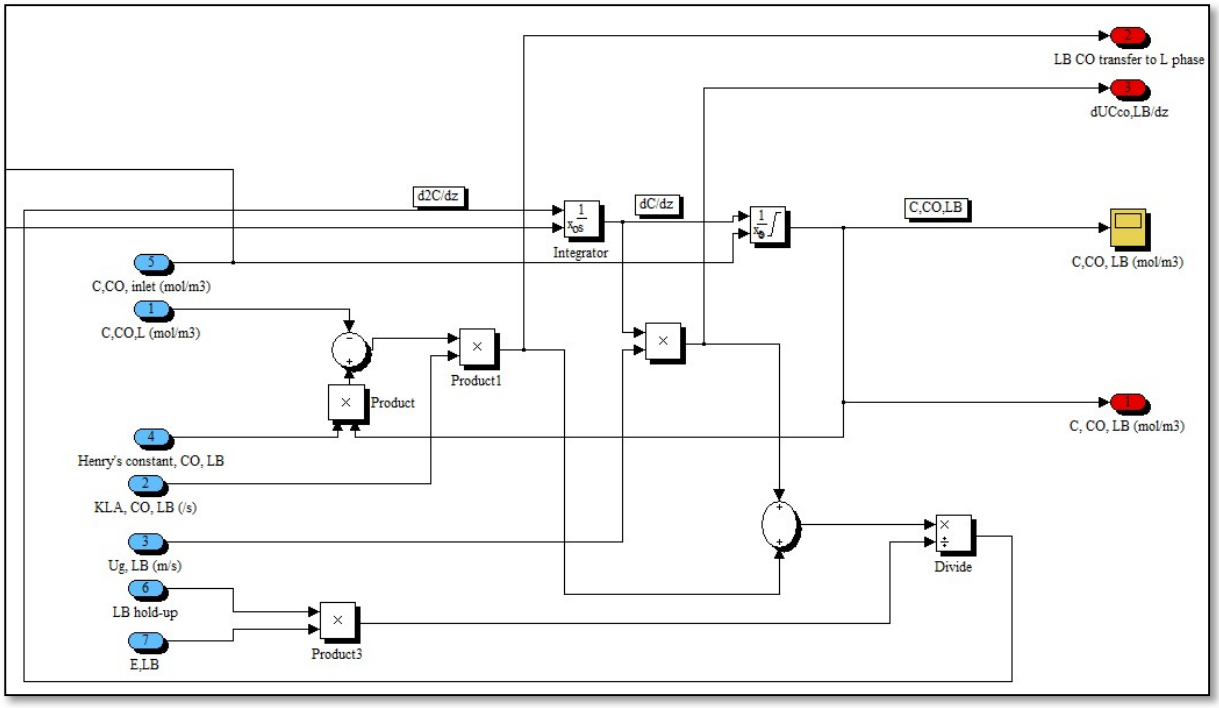

Figure 4.1: Large bubble class CO mass balance sub-model

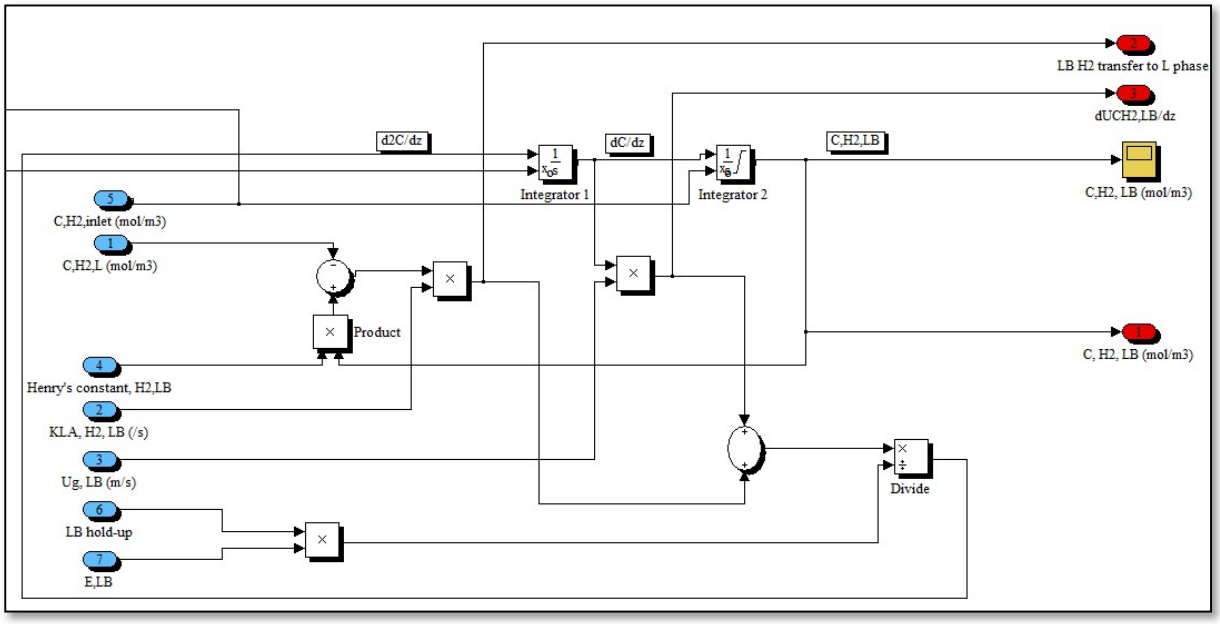

Figure 4.2: Large bubble class H_2 mass balance sub-model

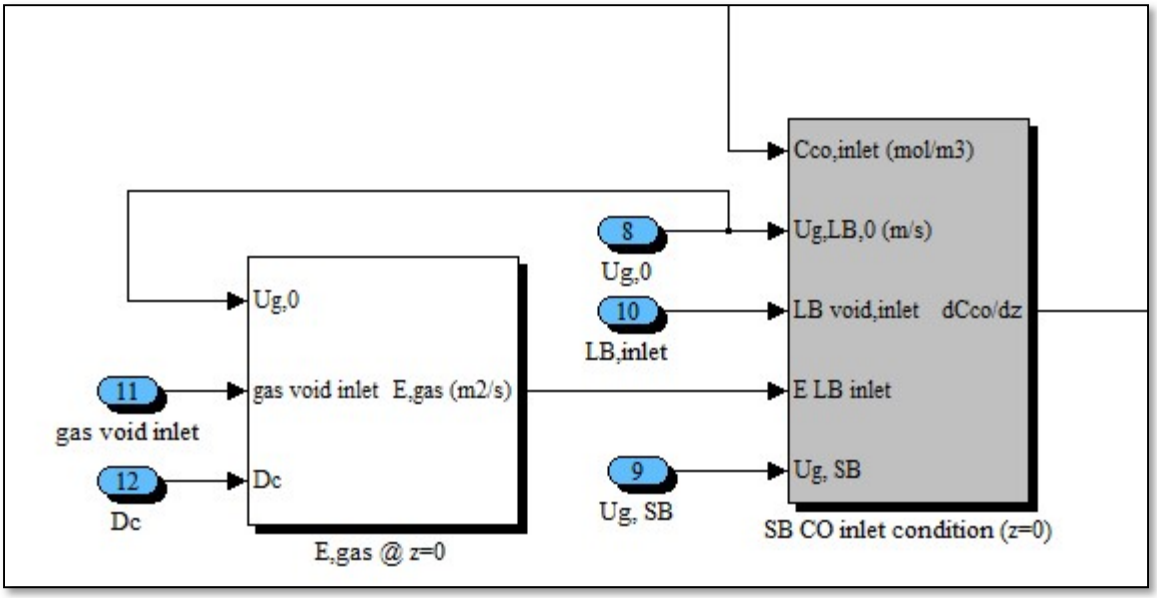

Figure 4.3: Large bubble class CO mass balance boundary condition sub-model

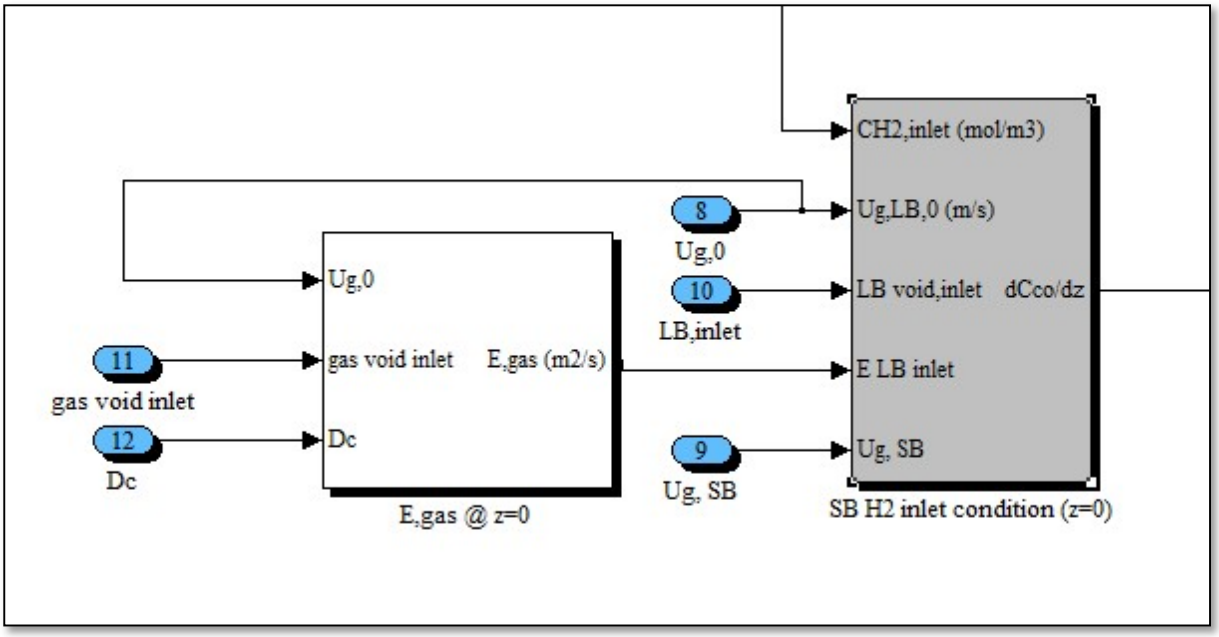

Figure 4.4: Large bubble class H_2 mass balance boundary condition sub-model

4.2 Small bubble phase

The odes in Equations 3.56 and 3.57 representing the small bubble CO and H_2 species material balances respectively were translated into Simulink sub-models as shown in Figure 4.5 and Figure 4.7 respectively. The small bubble CO inlet conditions, as per the Danckwerts type boundary conditions, were modelled as shown in Figure 4.6. The boundary conditions for the H_2 material

balance odes are shown in Figure 4.8. A more detailed illustration of the boundary condition sub-model is given in Appendix A: Simulink Boundary Condition Models.

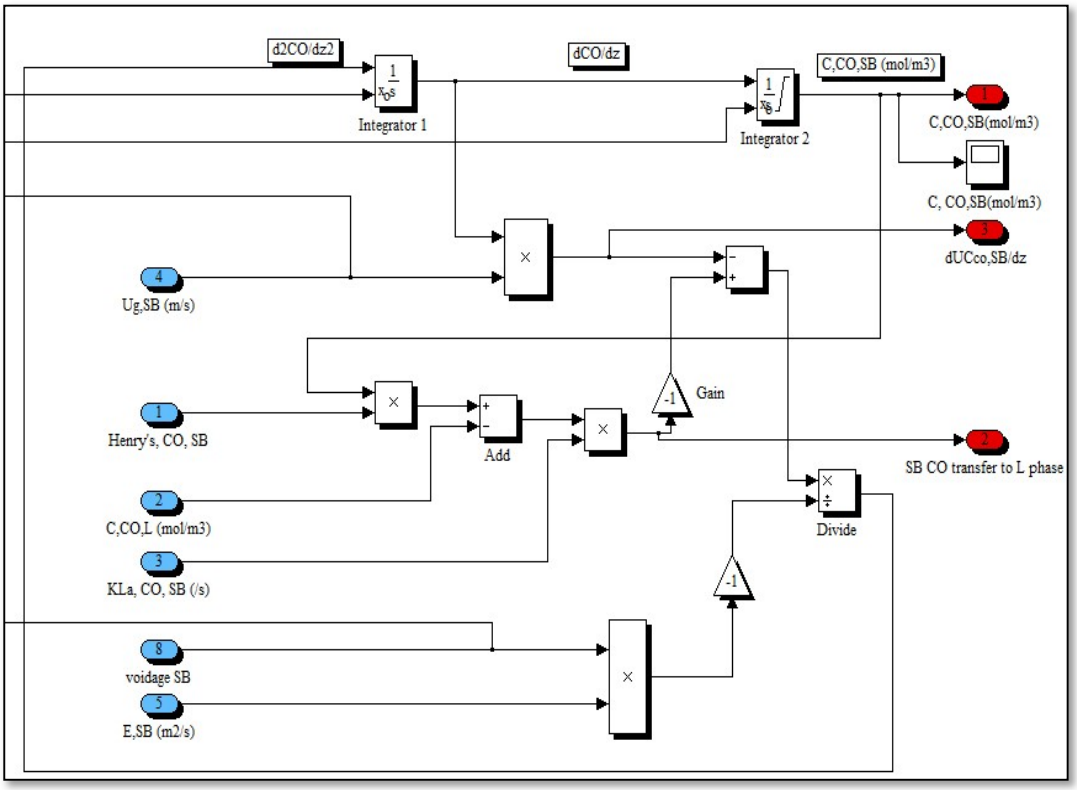

Figure 4.5: Sub-model for CO mass balance in the small bubble class

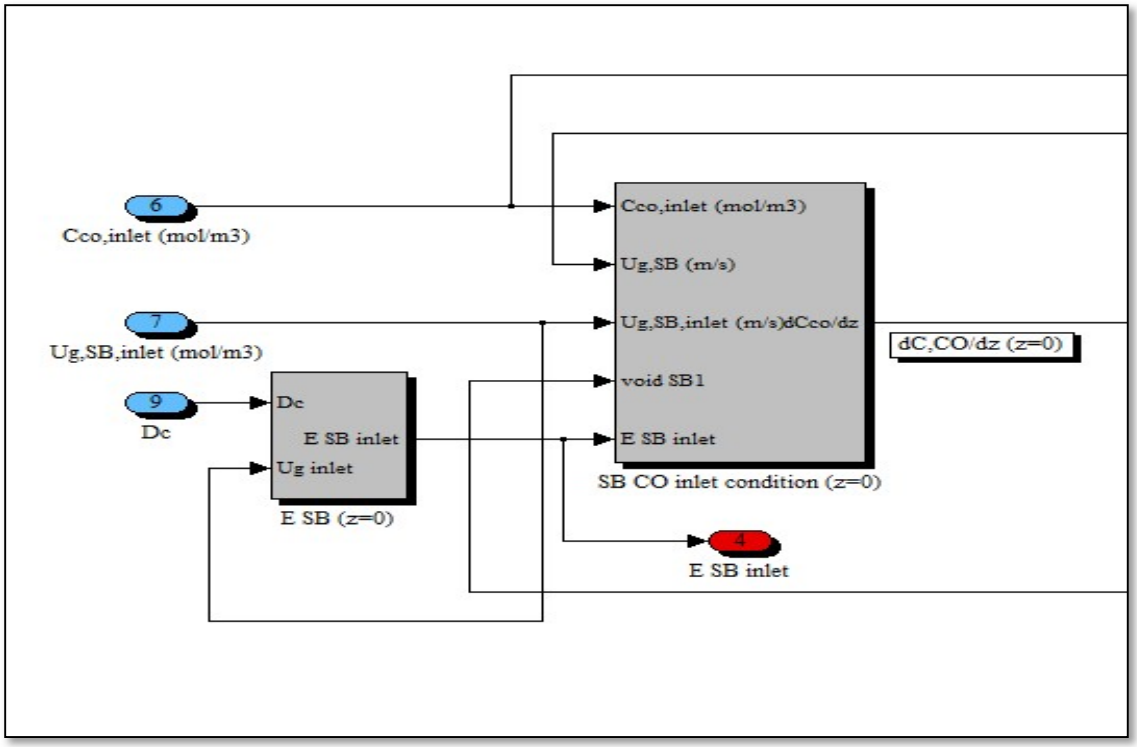

Figure 4.6: Small bubble class CO mass balance boundary condition sub-model

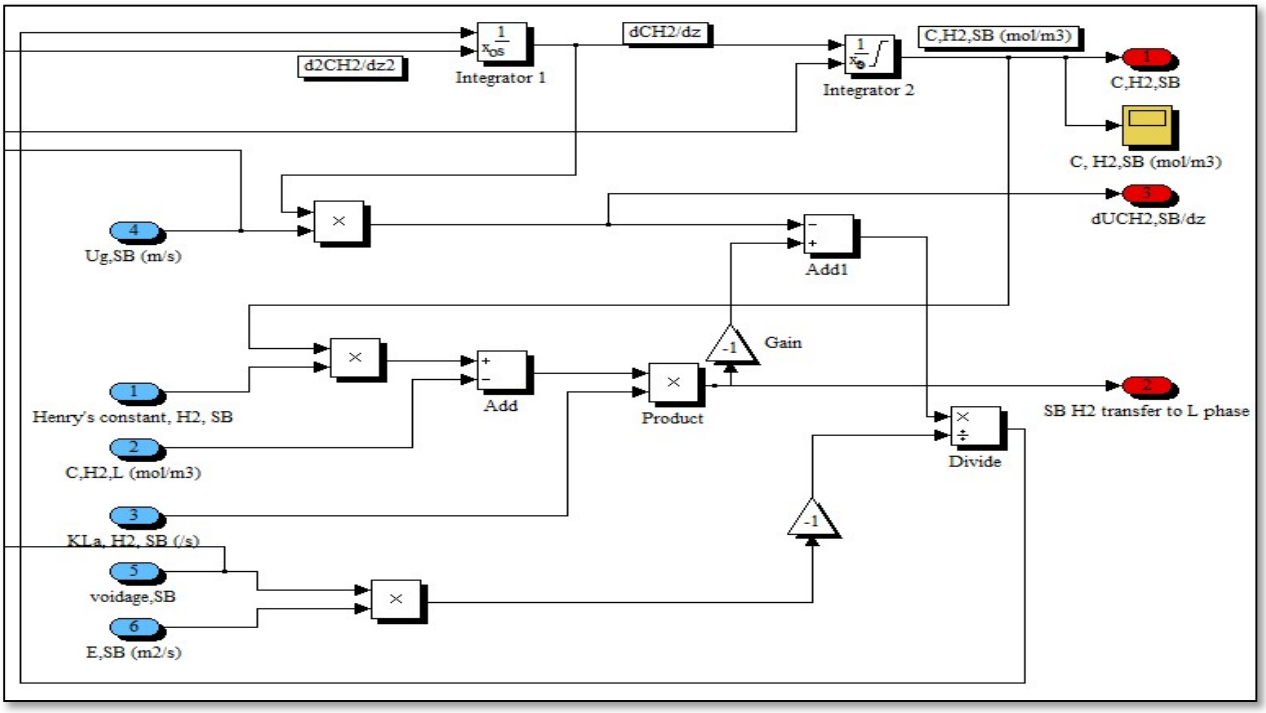

Figure 4.7: Sub-model for H_2 mass balance in the small bubble class

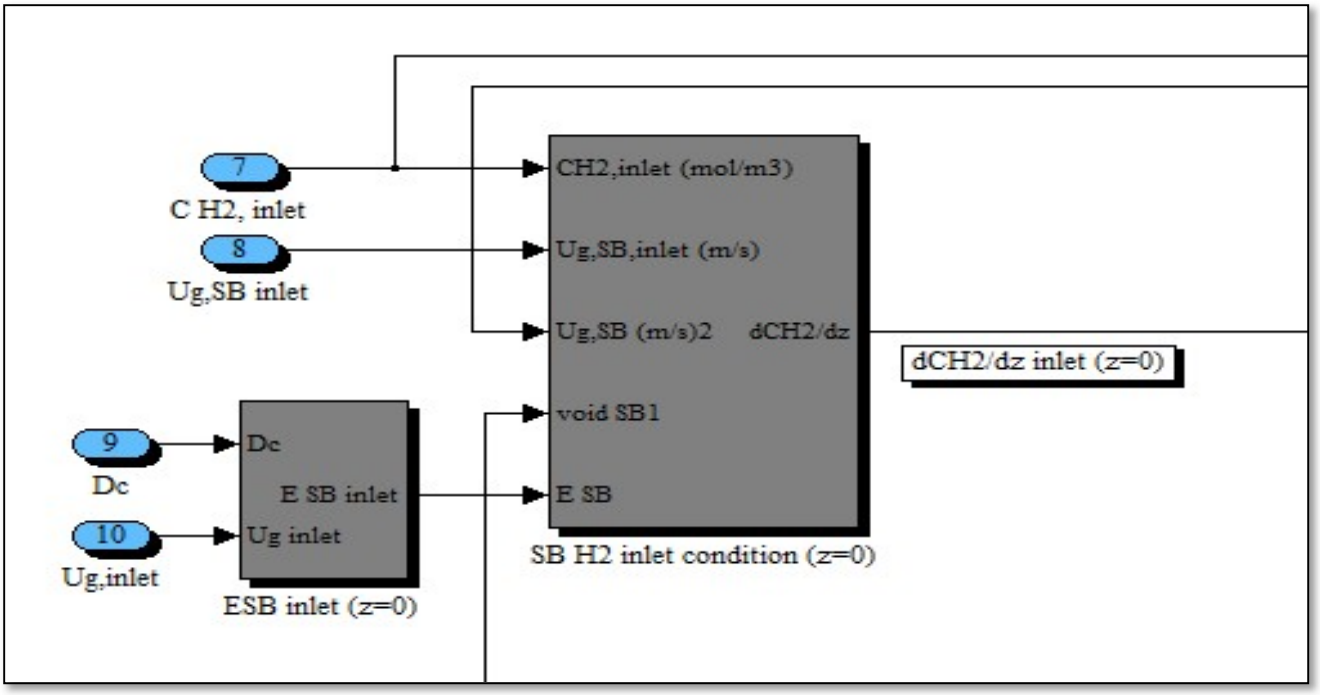

Figure 4.8: Small bubble class H_2 mass balance boundary condition sub-model

4.3 Liquid phase

The liquid phase mass balance was modelled using Equations 3.59 and 3.60 for the CO and H_2 species respectively as is shown in Figure 4.9 and Figure 4.11 as Simulink sub-models. Sub-models for the boundary conditions of the material balance odes for both species are given in Figure 4.10 for CO and Figure 4.12 for H_2.

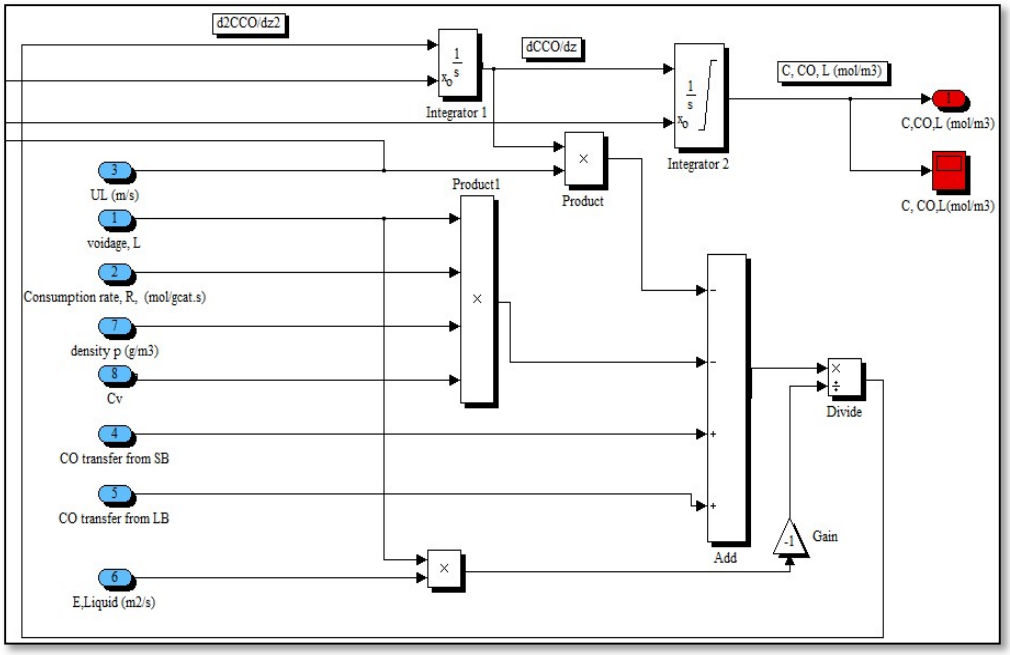

Figure 4.9: Sub-model for CO mass balance in the liquid phase

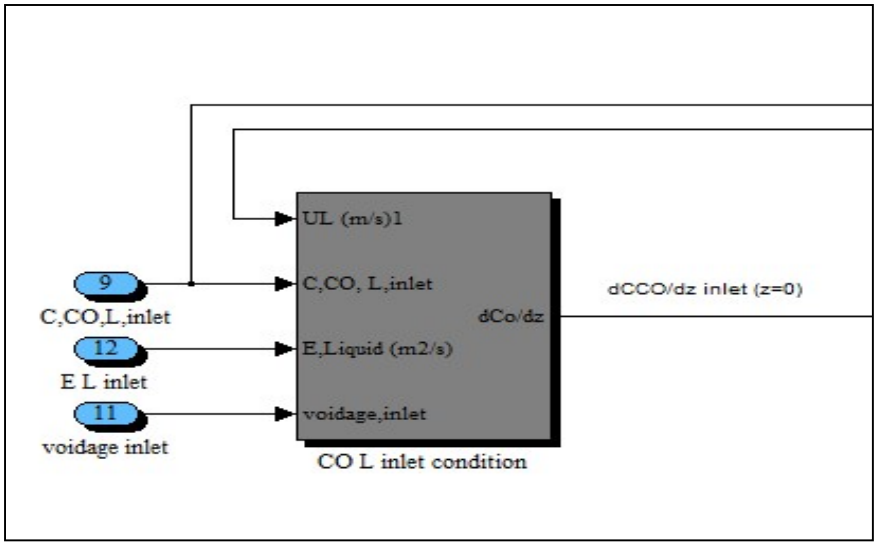

Figure 4.10: Liquid phase CO mass balance boundary condition sub-model

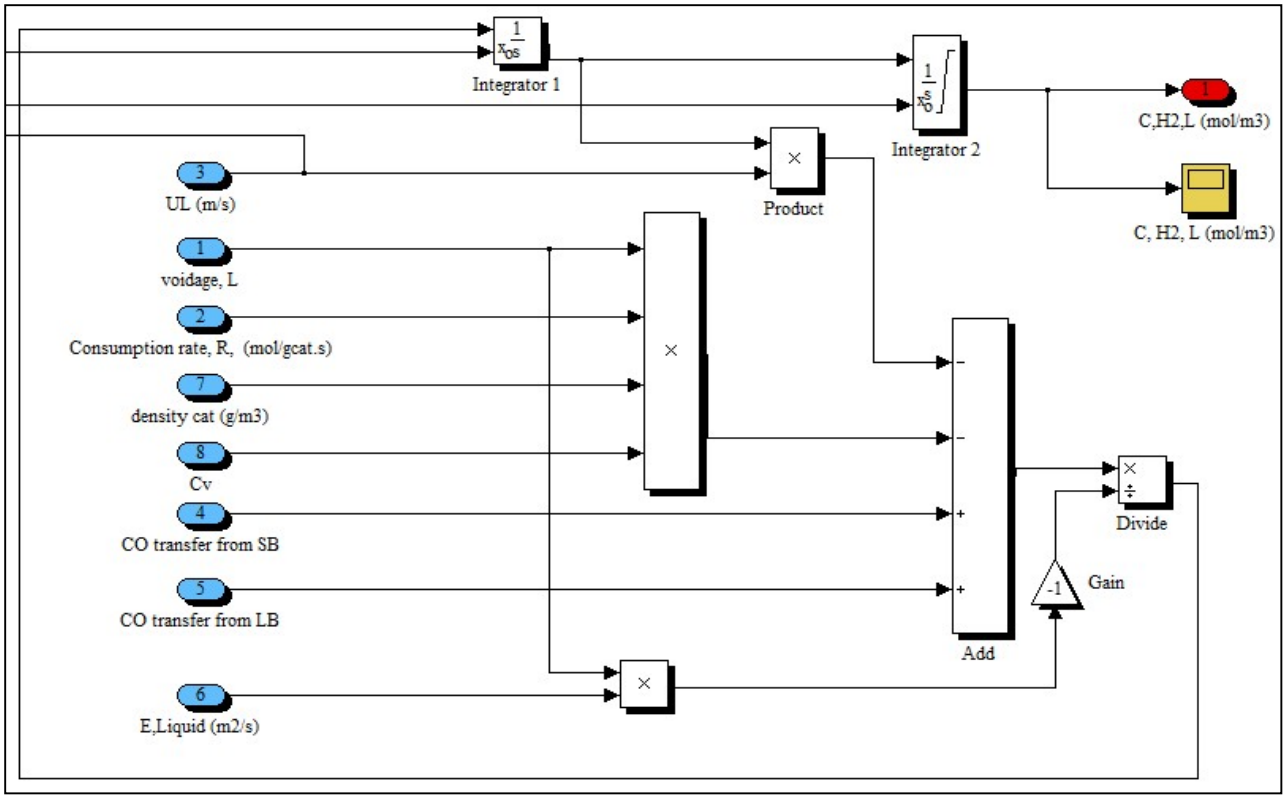

Figure 4.11: Sub-model for H_2 mass balance in the liquid phase

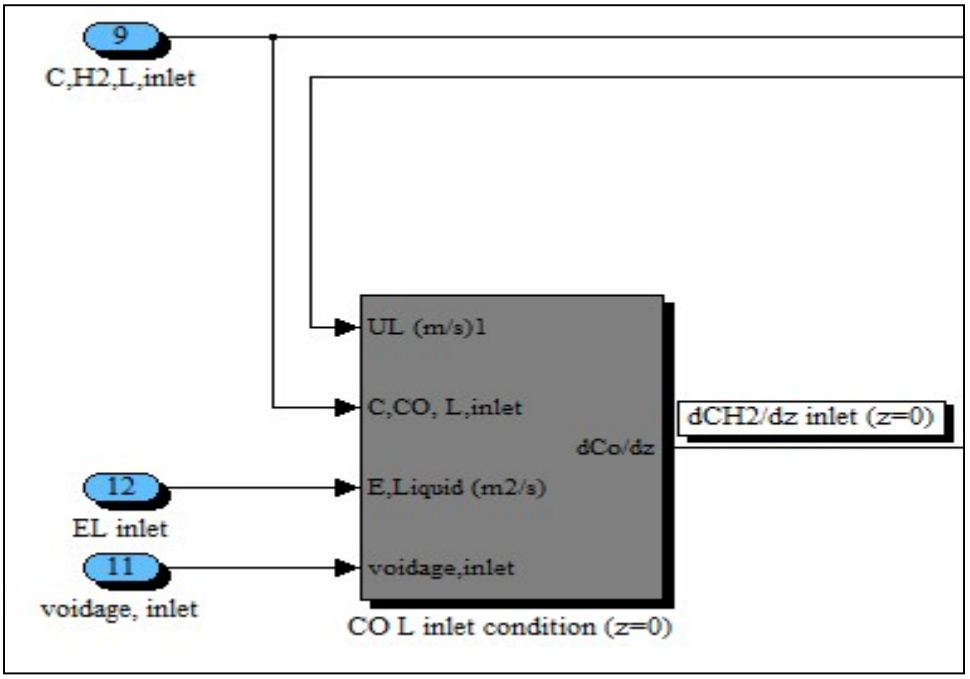

Figure 4.12: Liquid phase H_2 mass balance boundary condition sub-model

4.4 Hydrodynamics

The equations describing the hydrodynamic parameters were next to be translated into Simulink models.

4.4.1 Superficial gas velocity

The small bubbles superficial velocity was modelled as shown in Figure 4.13. The overall superficial gas velocity through the micro-reactor was modelled using Equation 3.77 to account for its decrease because of consumption by the FT reaction. The relevant Simulink sub-model is given in Figure 4.14. In Figure 4.14, the gas concentration input refers to the sum total of CO and H_2 concentrations in the large and small bubble classes which is modelled as shown in Figure 4.15.

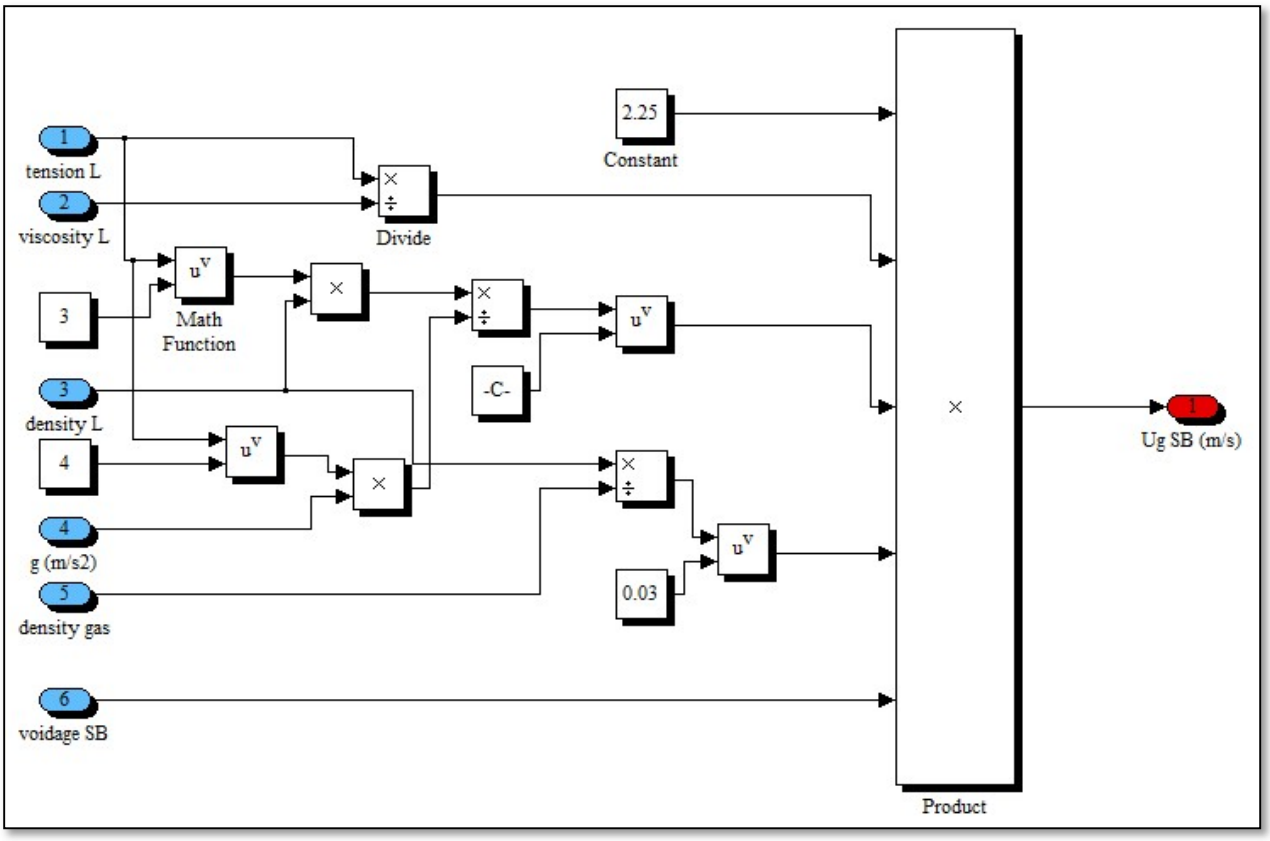

Figure 4.13: Small bubble superficial gas velocity sub-model

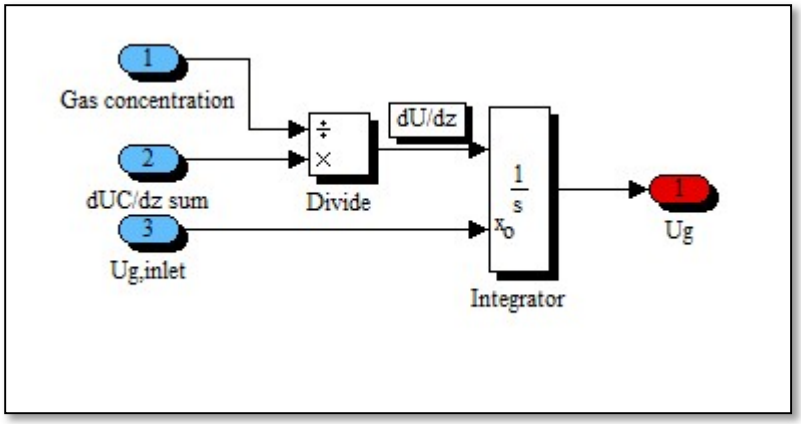

Figure 4.14: Overall superficial gas velocity sub-model

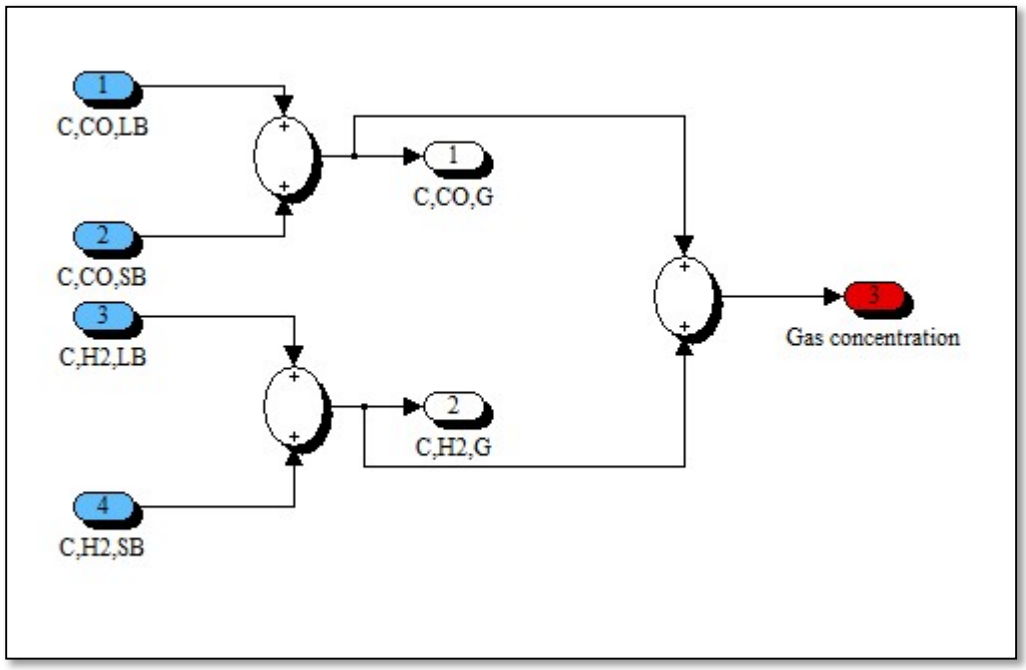

Figure 4.15: Total gas concentration sub-model

4.4.2 Hold-up

The small bubble class gas hold-up sub-model, modelled according to Equation 3.69, is shown in Figure 4.16. The large bubble class sub-model, modelled as per Equation 3.82, is shown in Figure 4.17.

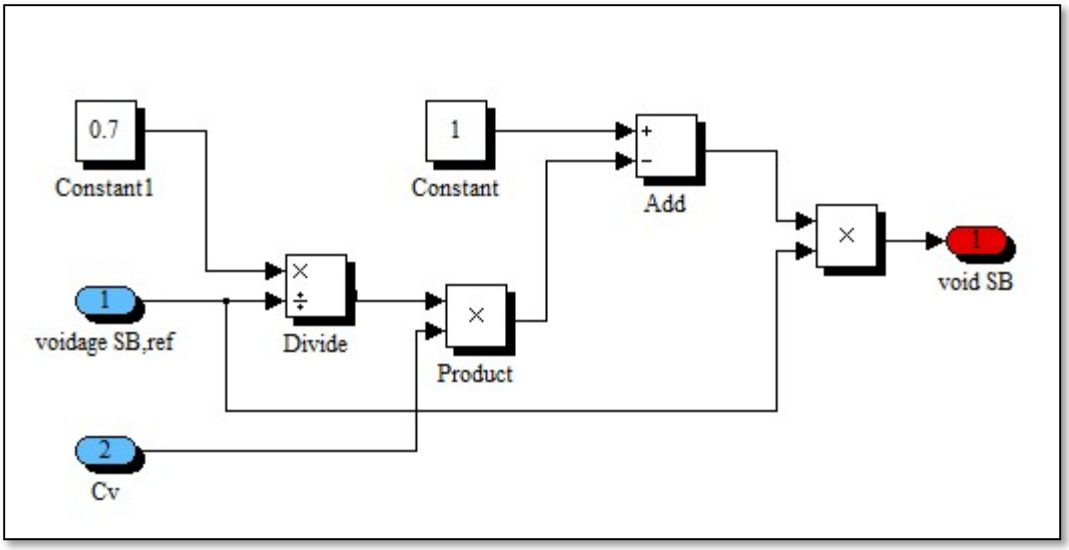

Figure 4.16: Small bubble class hold-up sub-model

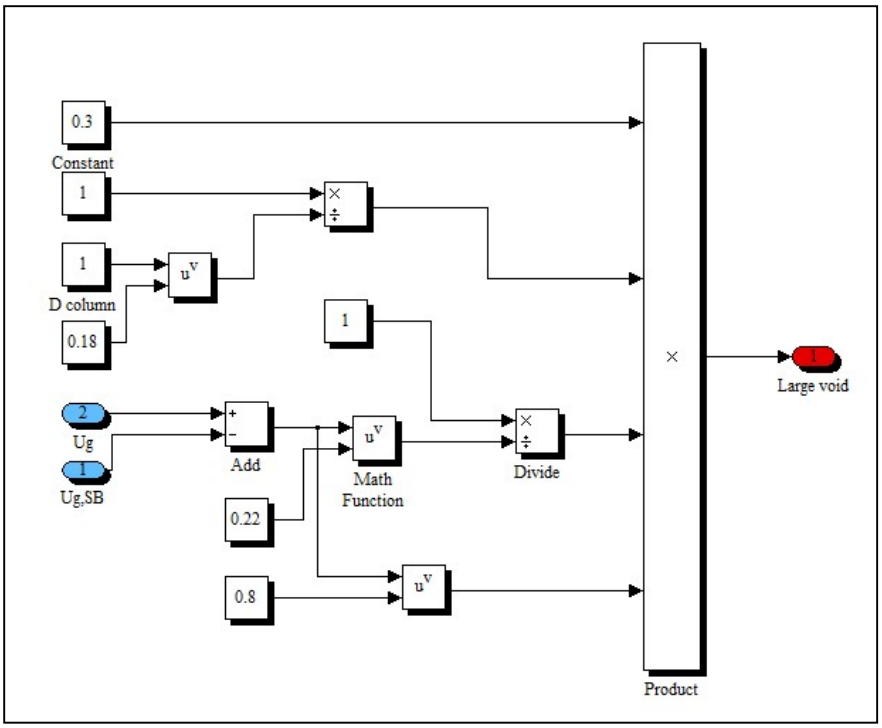

Figure 4.17: Large bubble class hold-up sub-model

4.5 Axial dispersion coefficient

4.5.1 Small bubble and liquid phase

The axial dispersion coefficient correlation sub-model, which has been assumed to be applicable in both the small bubble and liquid compartment, is shown in Figure 4.18.

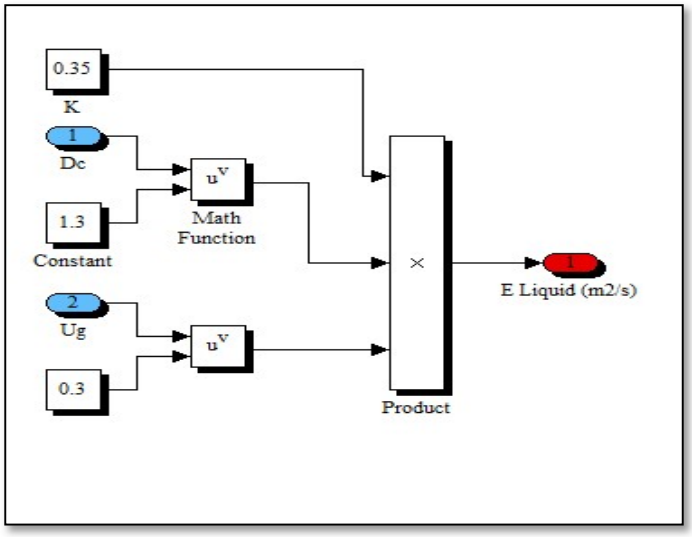

Figure 4.18: Liquid phase axial dispersion coefficient sub-model

4.5.2 Gas phase

The large bubble dispersion coefficient sub-model is shown in Figure 4.19 following the adoption of the correlation put forward by Mangartz and Pilhofer (1980).

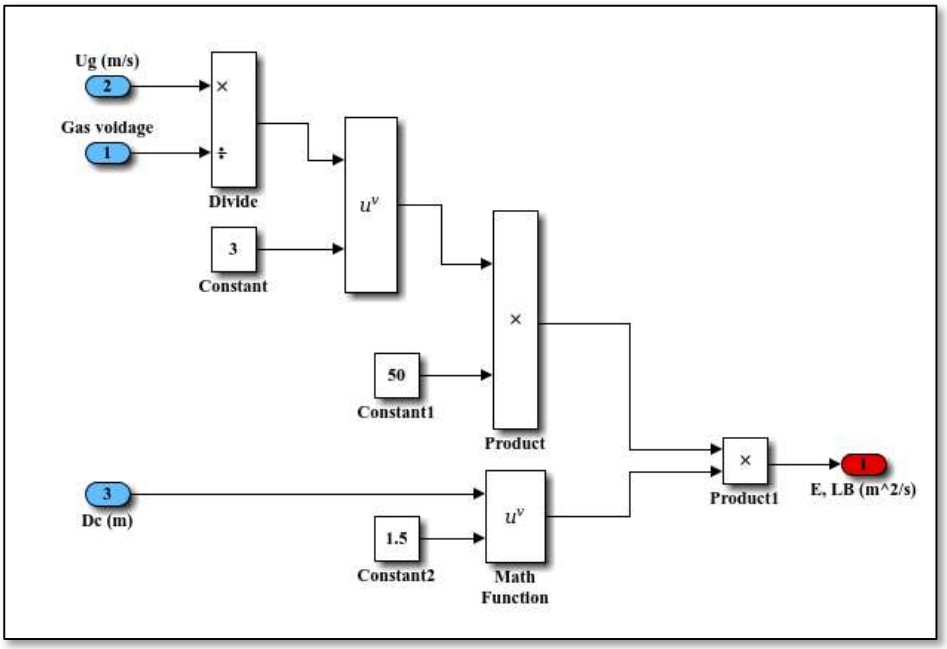

Figure 4.19: Large bubble axial dispersion coefficient sub-model

4.6 Kinetics

The kinetic rate law from Equation 3.39 was translated into a Simulink sub-model shown in Figure 4.20. The rate and adsorption constant inputs in Figure 4.20 were derived from Equations 3.97 and 3.98 respectively with the relevant sub-models shown in Figure 4.21 and Figure 4.22.

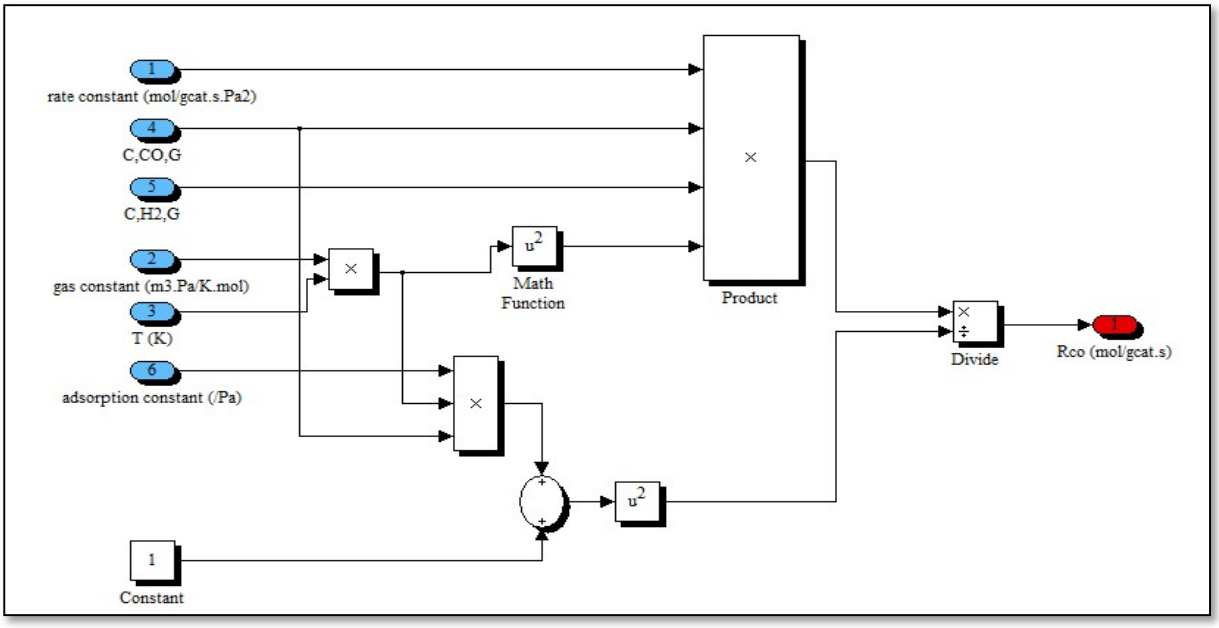

Figure 4.20: FT kinetic rate law in sub-model

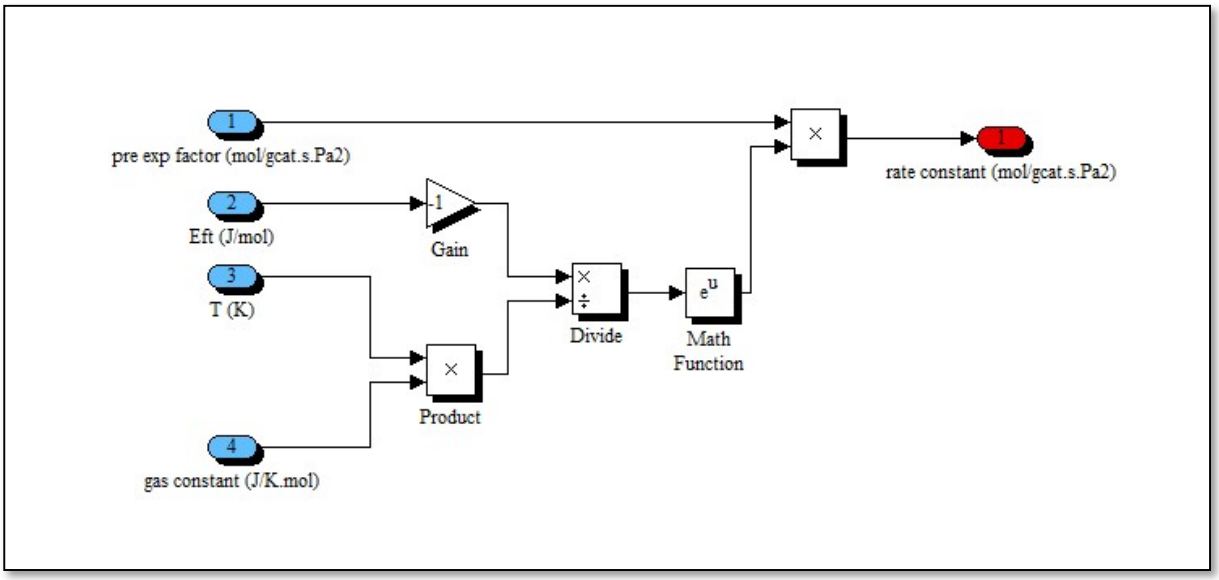

Figure 4.21: FT kinetic rate constant sub-model

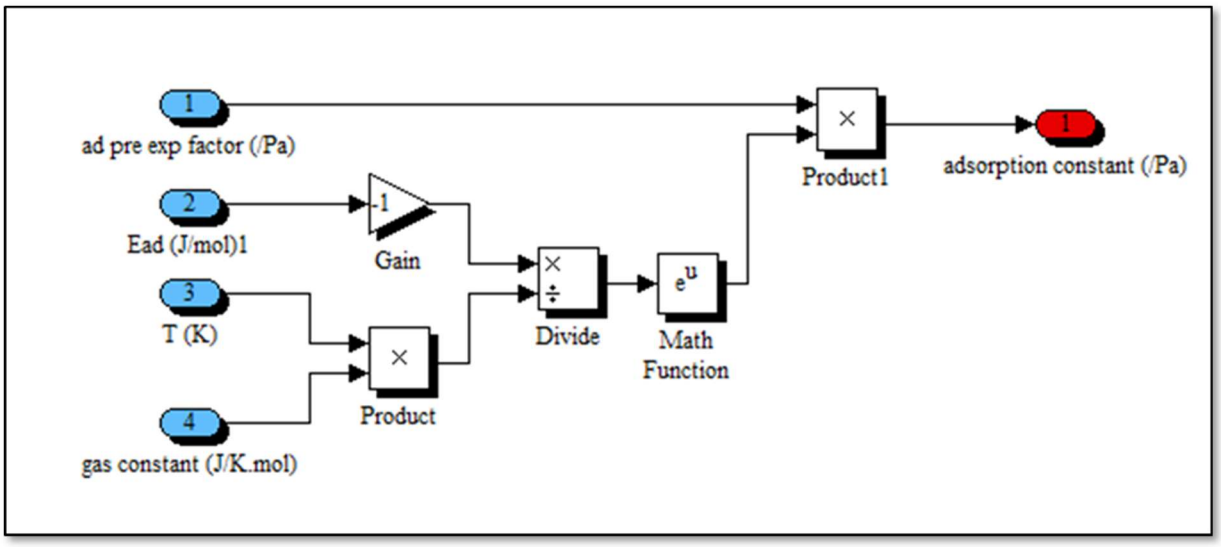

Figure 4.22: FT adsorption rate constant sub-model

4.7 Mass transfer

The volumetric mass transfer coefficients for CO in both the large (Equation 3.87) and small bubble (Equation 3.90) classes were modelled as shown in the sub-models in Figure 4.23 and Figure 4.24 respectively. The H_2 volumetric mass transfer coefficient sub-models in the large and small bubble classes are shown in Figure 4.25 and Figure 4.26 respectively.

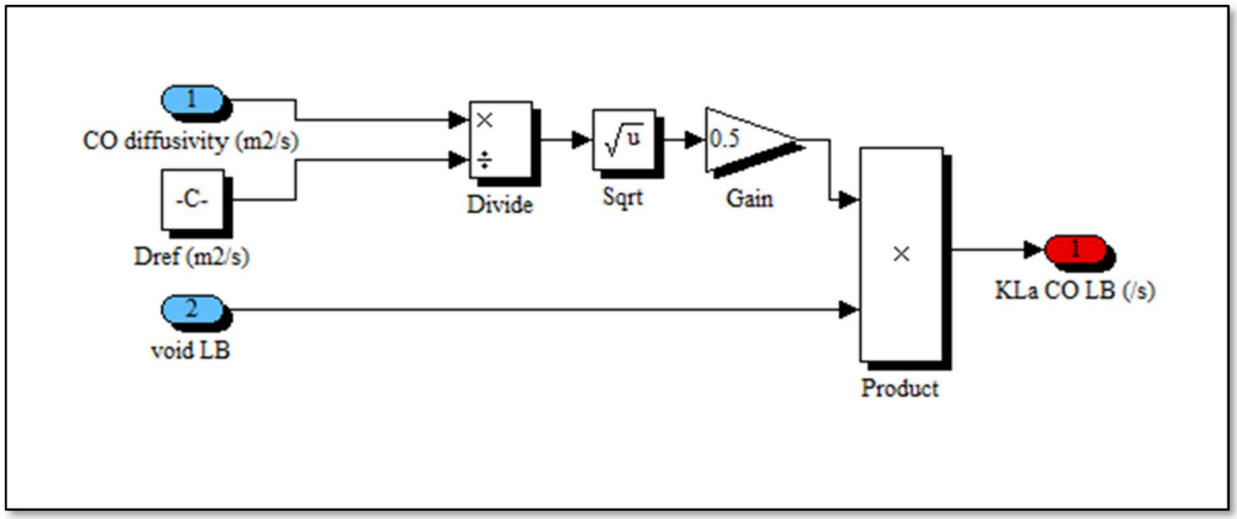

Figure 4.23: Large bubble CO mass transfer coefficient sub-model

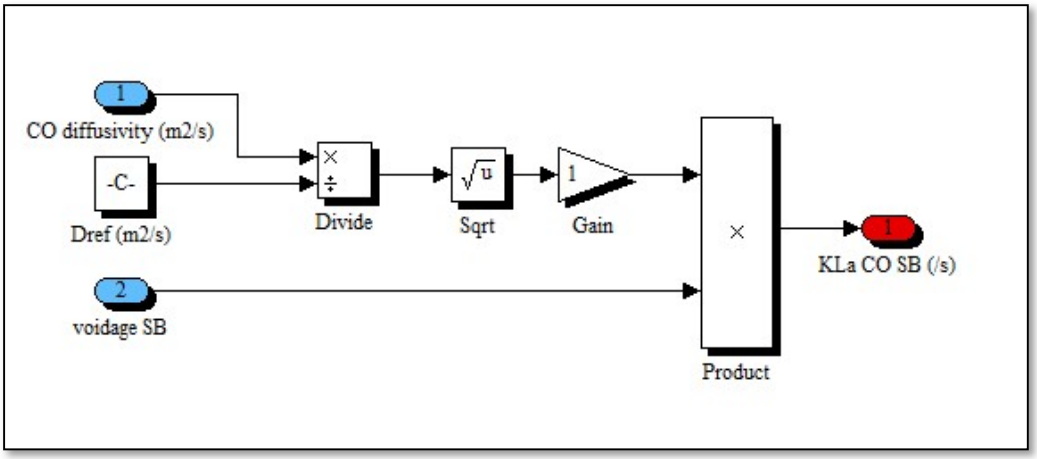

Figure 4.24: Small bubble CO mass transfer coefficient sub-model

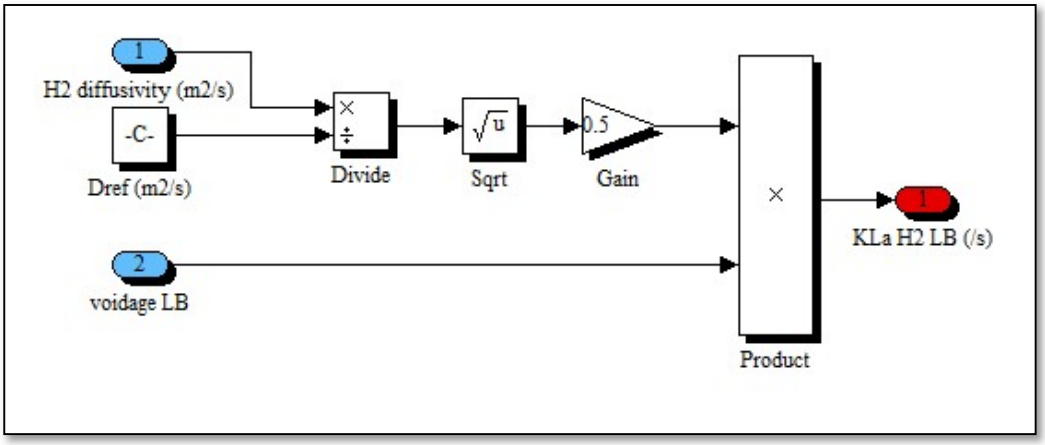

Figure 4.25: Large bubble H_2 mass transfer coefficient sub-model

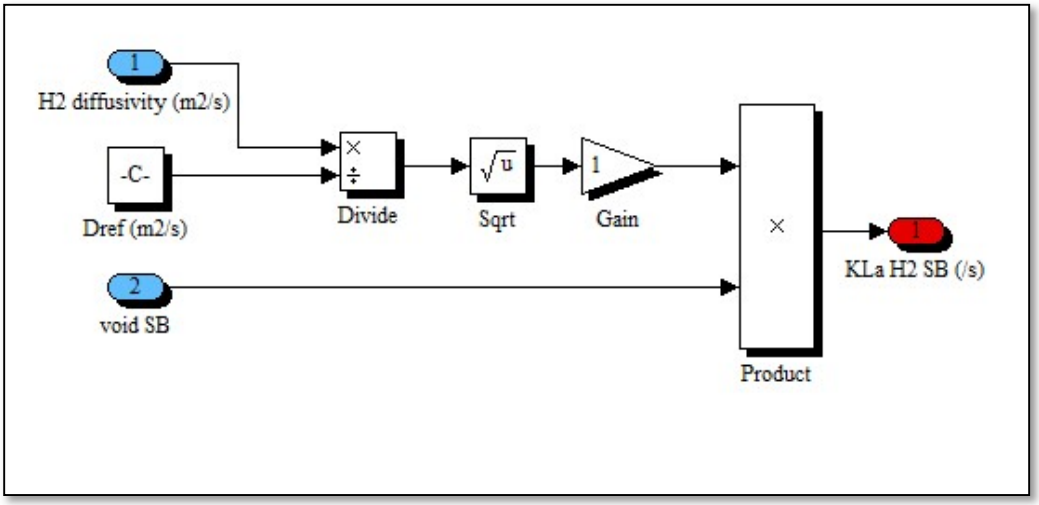

Figure 4.26: Small bubble H_2 mass transfer coefficient sub-model

4.8 Phase properties

The relevant gas/liquid physical and chemical property correlations were also translated into Simulink sub-models to serve as inputs into the various mass balance and hydrodynamics sub-models. The CO and H2 Henry's constants as given in Table 3.10 were modelled as shown in Figure 4.27 and Figure 4.28 respectively. The liquid density, viscosity and surface tension correlations sub-models are shown in Figure 4.29, Figure 4.30 and Figure 4.31 respectively.

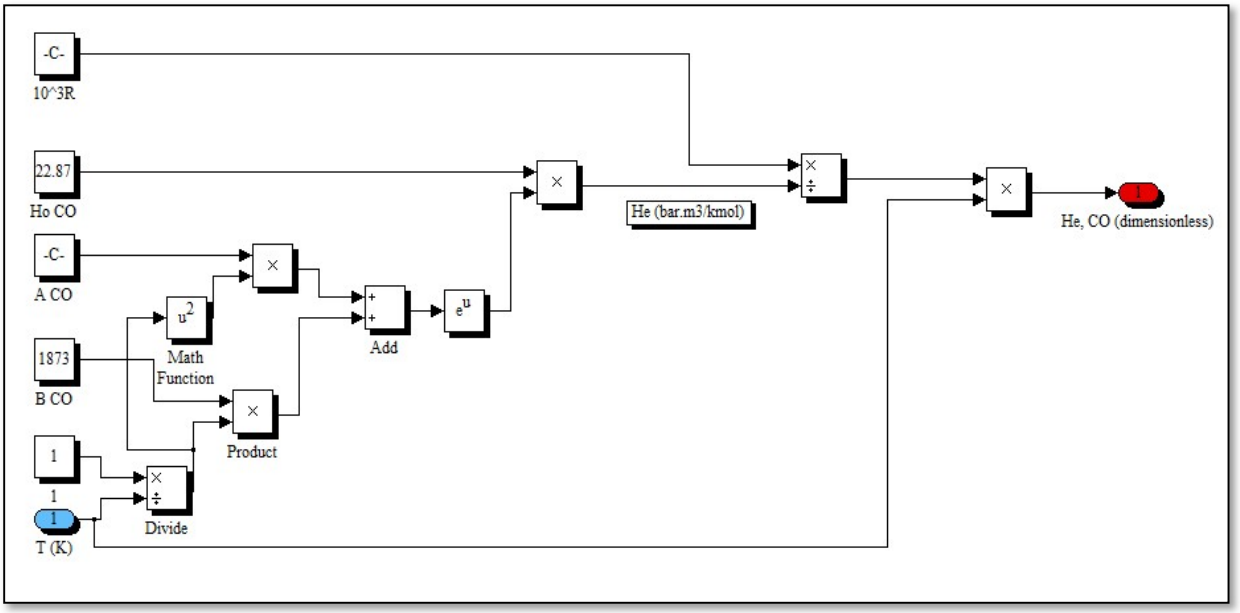

Figure 4.27: CO Henry's constant sub-model

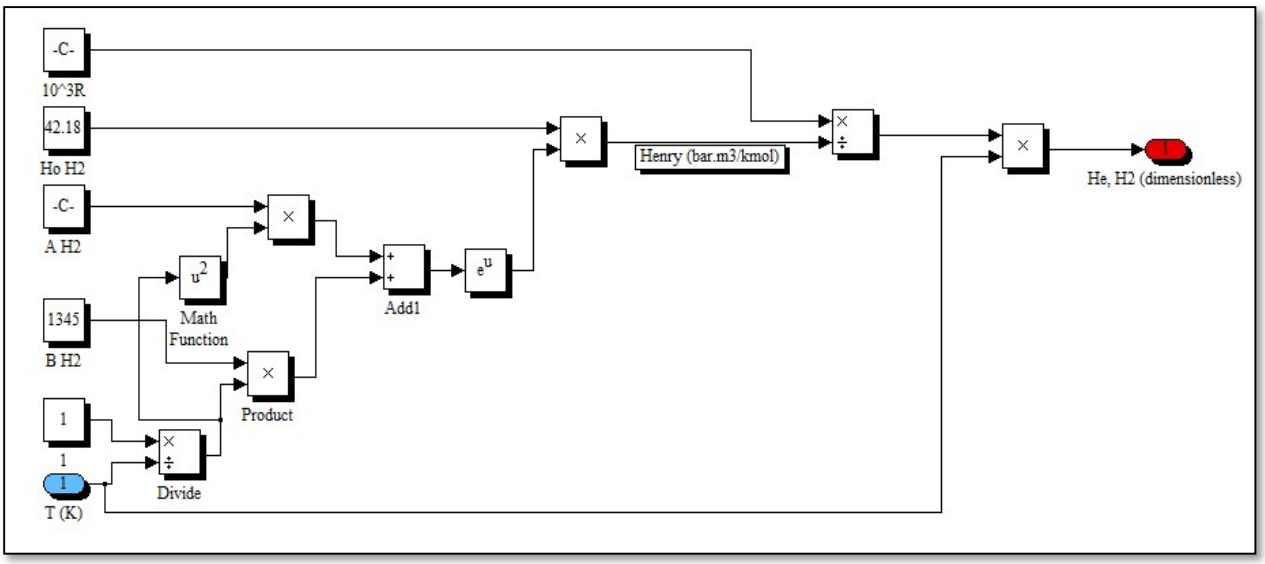

Figure 4.28: H_2 Henry's constant sub-model

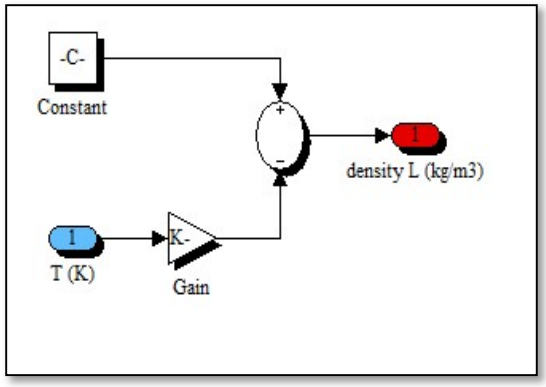

Figure 4.29: Liquid density sub-model

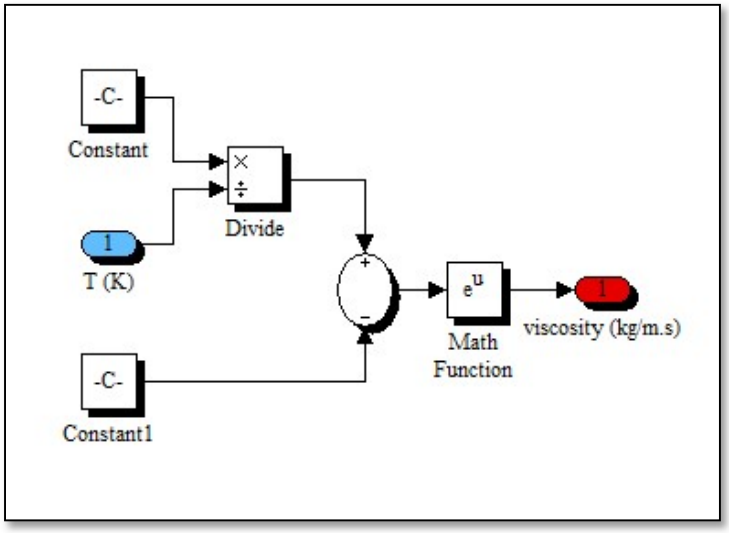

Figure 4.30: Liquid viscosity sub-model

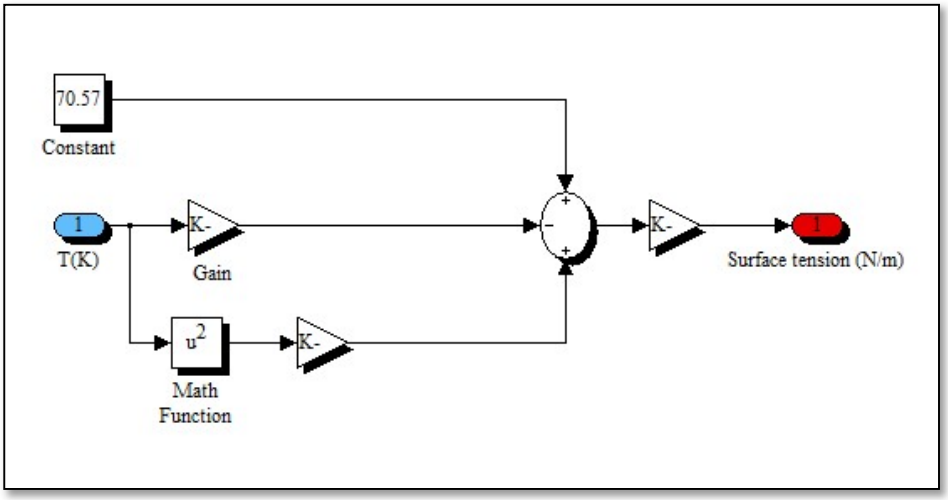

Figure 4.31: Liquid surface tension sub-model

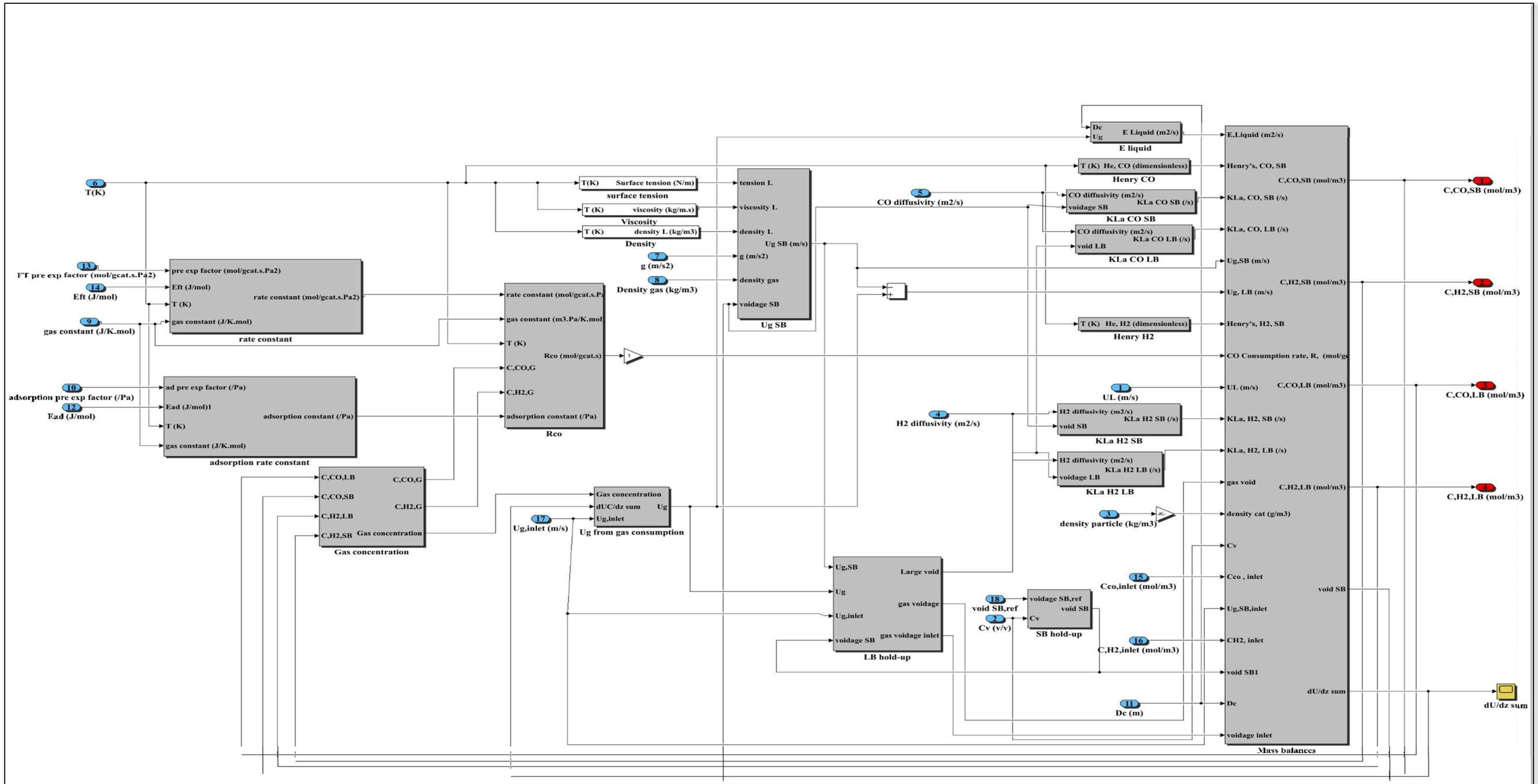

Figure 4.32: Overall FT Microchannel Reactor Model

4.9 Overall Model

The mass balances, kinetics, hydrodynamics and gas/liquid property Simulink sub-models described above were combined into an FT microchannel reactor model, as shown in Figure 4.32. A black-box type view of the overall system model is shown in Figure 4.33 where only the inputs and outputs from are shown. A complete C source code describing the entire model is provided in Appendix B.

4.10 Conclusion

In this chapter, the material balance ODEs developed in chapter 3 were translated into Simulink models using the Simulink modelling environment. The large bubble, small bubble and liquid phases were developed into discrete Simulink models coupled with the adoption of appropriate boundary conditions. The boundary conditions employed are of the Danckwerts type. Hydrodynamic properties including the superficial gas velocity, hold-up and dispersion coefficients were also translated into Simulink models for each respective compartment, i.e., small bubble, large bubble and liquid compartments. To complete the model, the kinetics, mass transfer and fluid properties were finally translated into Simulink sub-models. Through these translations, and the coupling of all the relevant sub-models, a comprehensive FT microchannel reactor model was developed with the capability to describe the concentration profile, kinetics and hydrodynamics within said reactor.

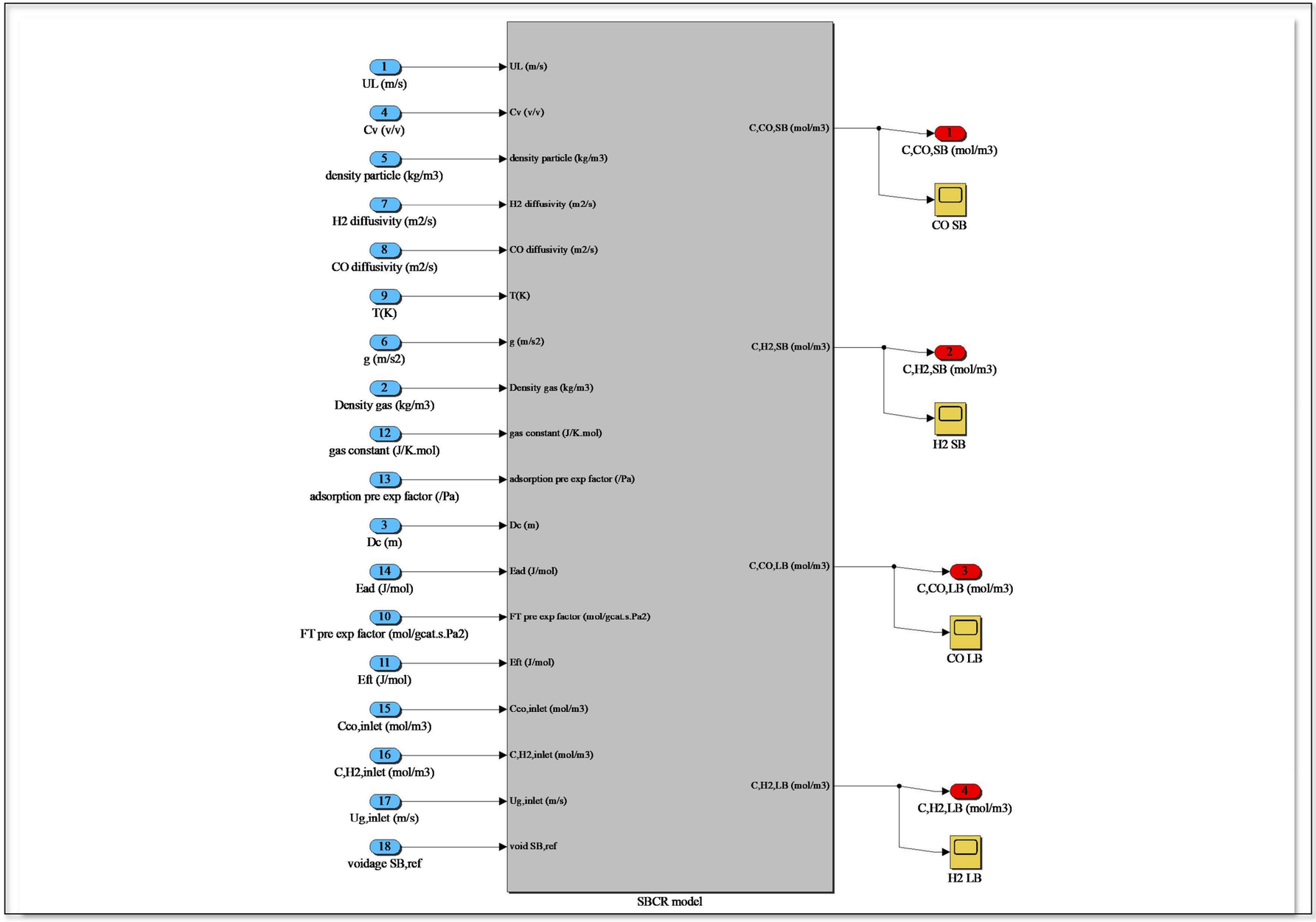

Figure 4.33: Overall FT Microchannel Reactor Model with inputs and outputs only

Chapter 5: Results & Discussion

In this section, results will be presented and discussed from the formulated microchannel FT reactor model based on the model set-up and structure given in the previous sections. This will help the reader gain a better understanding of the behaviours and physicochemical phenomena expected in microchannel FTS systems, which are a new form of application for FTS with distinct and clear advantages over conventional systems. Furthermore, in this chapter, the model will be validated against data from literature to demonstrate its accuracy in predicting micro-reactor behaviour. Finally, a techno-economic model will be presented, capable of assessing the economics around an FT micro-reactor-based flowsheet.

As stated in an earlier section, MATLAB through its Simulink environment was utilized as a numerical solver into which all the relations presented in the previous chapters were translated. These were then solved and selected results, mainly in the form of plots, are presented here.

It is important before the results are presented, to outline the details of the numerical solver employed so that the solver conditions and parameters can be understood. A few of the more important solver configuration parameters are given in Table 5.1.

Table 5.1: MATLAB Simulink solver configuration parameters used in the model solution

Solver Parameters	Description
Start time (z=0)	0
End time (z=L)	0.01
Solver type	Fixed step
Solver Method	Automatic
Fixed step size	0.00001

5.1 Model Results & Discussion

5.1.1 Model Results

The constructed model was simulated as per the typical microchannel FT reactor conditions in Table 3.6 and Table 3.8 together with the reactant feed concentrations given in Equations 3.100 and 3.101. Details of the conditions are given in Table 5.2. The model was solved and run between

over a length between 0 and 0.01 m, resulting in changes across the various reactor parameters over this length. To give a sense of the behaviour within the microchannel FT reactor, a summary of the values of some variables of concern is given at the final length of 0.01 m and compared to those at the inlet as shown in Table 5.3. It is evident from Table 5.3 that the reactant concentrations in all the phases present drop over the microchannel length and this is expected, following the assumption of axial dispersion in all phases and the consumption of the reactants through the catalyzed FT reaction. The large bubble class concentrations drop by approximately 69% while the small bubble and liquid phase concentrations are depleted completely. Also important to note is the apparent lack of reactants in the small bubble and liquid classes over the reactor length as seen in $C_{CO,SB}$, $C_{H2,SB}$, $C_{CO,L}$ and $C_{H2,L}$. This does not represent a total consumption of the reactants in these phases but it rather points to a balance between the gas/liquid mass transfer and reaction rates. The total syngas conversion was calculated using Equation 5.1.

$$X_{CO+H_2} = \frac{(C_{CO}+C_{H_2})_{inlet}-(C_{CO}+C_{H_2})_{outlet}}{(C_{CO}+C_{H_2})_{inlet}} \times 100 \qquad \text{Eq. 5.1}$$

Table 5.2: Model Inputs

Input	Unit	Value
Slurry velocity, U_L	m/s	0,02
Catalyst loading, C_v	-	0,3
Catalyst density	kg/m^3	647
H_2 diffusivity	m^2/s	45,5×10^{-9}
CO diffusivity	m^2/s	17.2×10^{-9}
T	K	513
g	m/s^2	9,81
Syngas density	kg/m^3	7
Ideal gas constant	J/K.mol	8,314
Adsorption pre-exponential factor	Pa^{-1}	1.243×10^{-12}
Column diameter	m	7
Adsorption activation energy	J/mol	-68474.1
Reaction pre-exponential factor	mol/g$_{cat}$.s.Pa^2	8.037×10^{-12}
Reaction activation energy	J/mol	37369.5

CO inlet concentration	mol/m^3	218.41
H_2 inlet concentration	mol/m^3	436.82
Inlet U_g	m/s	0,3
reference ε_{SB}	-	0,27

Table 5.3: Behaviour of specific variables across the length of the microchannel

Value				
Parameter	**Unit**	**Inlet (z=0)**	**Outlet (z=30)**	**% decrease**
$C_{CO,LB}$	mol/m^3	218.41	66.49	69.56
$C_{H2,LB}$	mol/m^3	436.82	132.9	69.57
$C_{CO,SB}$	mol/m^3	218.41	0	100
$C_{H2,SB}$	mol/m^3	436.82	0	100
$C_{CO,L}$	mol/m^3	42.3	0	100
$C_{H2,L}$	mol/m^3	32.3	0	100
U_g	m/s	0.3	0.001785	99
E_L	m^2/s	0.00001573	3.351×10^{-5}	77.7
E_{LB}	m^2/s	0.08136	3.787×10^{-5}	99
R_{CO}	$mol/g_{cat}.s$	1.69×10^{-5}	1.09×10^{-5}	35.5
ε_{SB}	-	0.004	0.004	0
ε_{LB}	-	0.149	0.007596	95
ε_L	-	0.8	0.9884	-19
Kla,CO_{LB}	s^{-1}	0.22	0.11	50
Kla,CO_{SB}	s^{-1}	0.1173	0.1173	0
$Kla,H_{2,LB}$	s^{-1}	0.362	0.1812	49.9
$Kla,H_{2,SB}$	s^{-1}	0.1908	0.1908	0
CO conversion	%	0	69.56	-
H_2 conversion	%	0	69.57	-
Syngas conversion	%	0	69.57	-

5.1.2 Model Discussion

5.1.2.1 Concentration gradients

In this section, the reactant concentration profiles in all phases will be considered to track the behaviour of the reactants through the length of the microreactor. Of the reactants, only the CO species concentration will be considered because the syngas is fed at the stoichiometrically required H_2/CO ratio of 2 and as the rate of reaction of the hydrogen molecules twice that of the CO molecules, the behaviour of both species is expected to be similar, i.e., the overall rate of conversion of CO should be equal to that of hydrogen as is evident from Table 5.3.

5.1.2.2 Concentration profile in large bubbles

Figure 5.1 shows how the large bubble class CO concentration decreases linearly over the length of the microchannel. To explain this, it would be necessary and efficient to consider the rate at which the CO species is depleted. The rate of depletion of CO, denoted $\frac{Ud_{CO,LB}}{dz}$ in the mass balance ode, is a function on the rate of mass transfer between the large bubble and the liquid phases which in turn depends on the gas-liquid mass transfer coefficient.

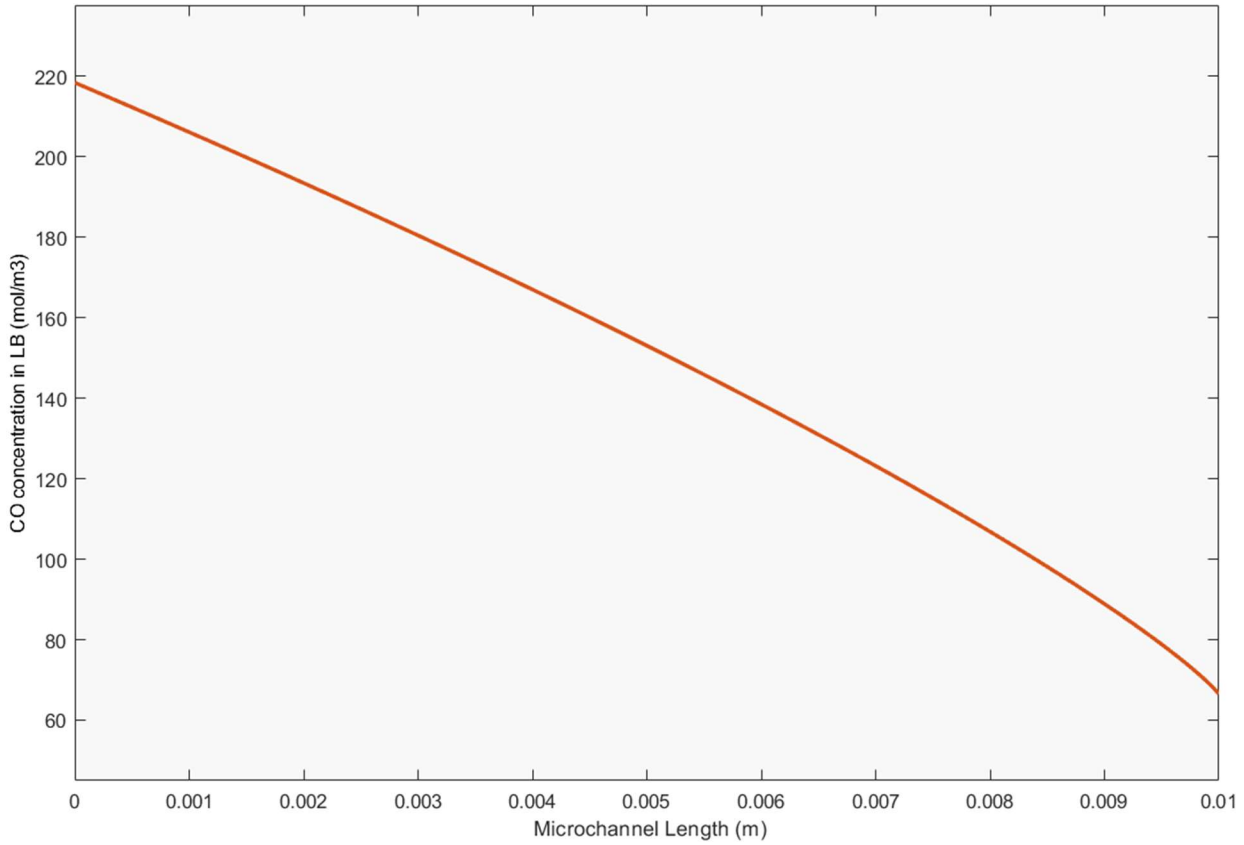

Figure 5.1: Large bubble phase CO concentration across microchannel length

The mass transfer coefficient between the liquid and large bubbles (Figure 5.2) itself depends on the large bubble hold-up as per Equation 3.87 (Maretto and Krishna, 1999). This large bubble hold-up (Figure 5.3) is a function of the superficial gas velocity (Equation 3.81) which decreases over the microchannel length according to Equation 3.77 (Figure 5.4) (Bukur, 1983 and Iliuta et al., 2007). The connections drawn in this explanation mean, in other words, that the mass transfer rate across the gas-liquid interphase is proportional to the superficial gas velocity so that as this is reduced, the mass transfer rate decreases proportionally. This has the effect of reducing the rate of depletion of CO from the large bubbles.

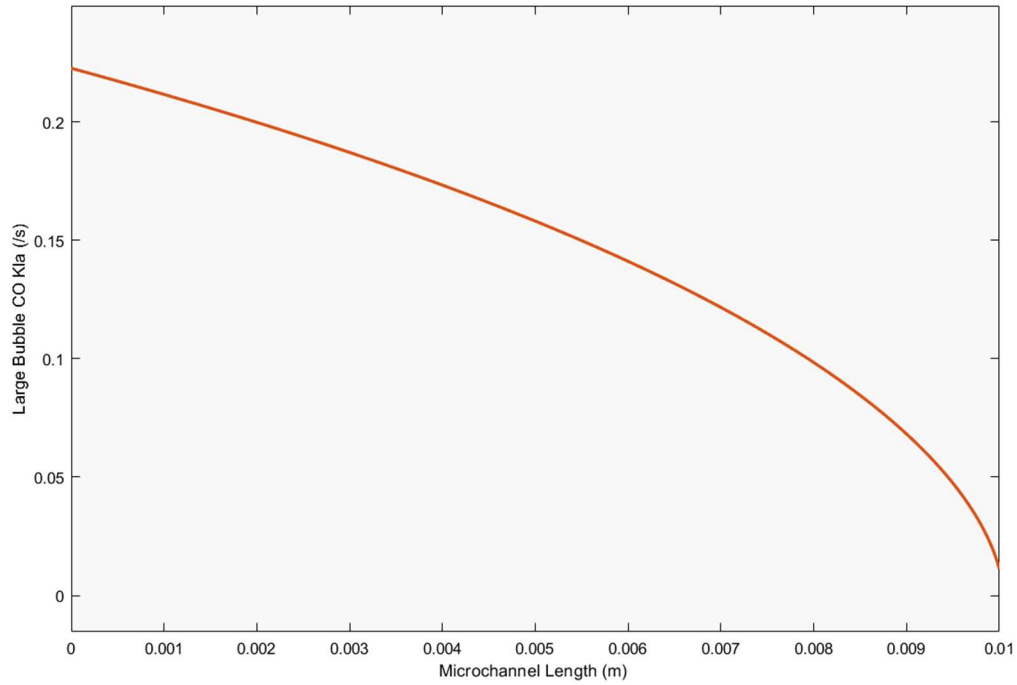

Figure 5.2: Large bubbles-liquid interface CO mass transfer coefficient over microchannel length

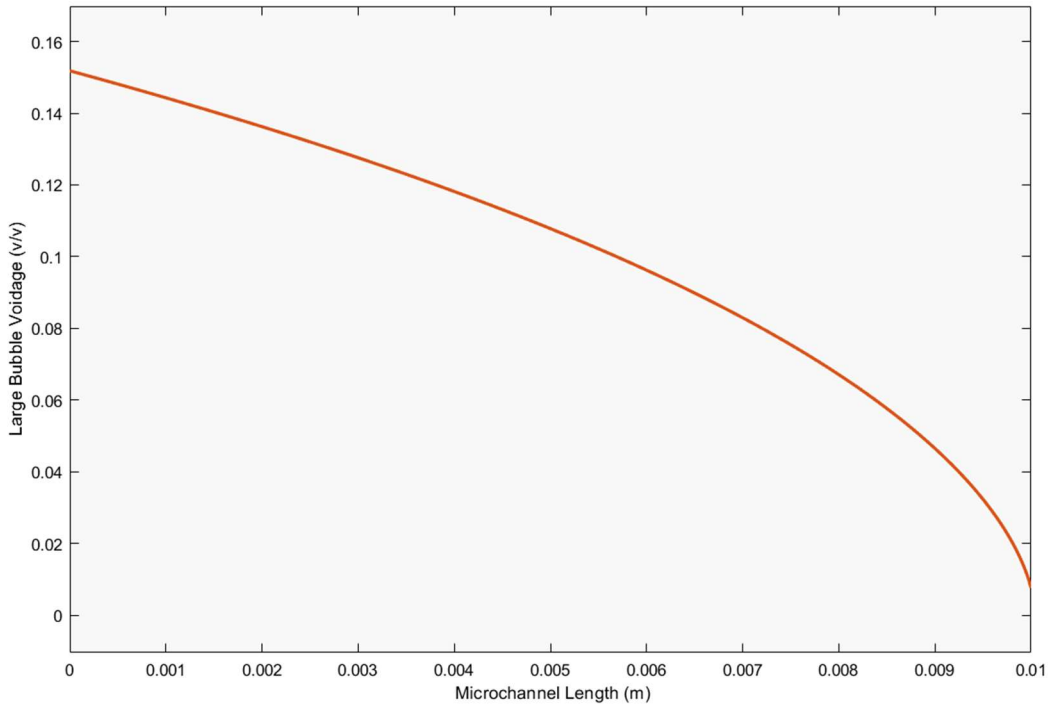

Figure 5.3: Large bubble phase hold-up over microchannel length

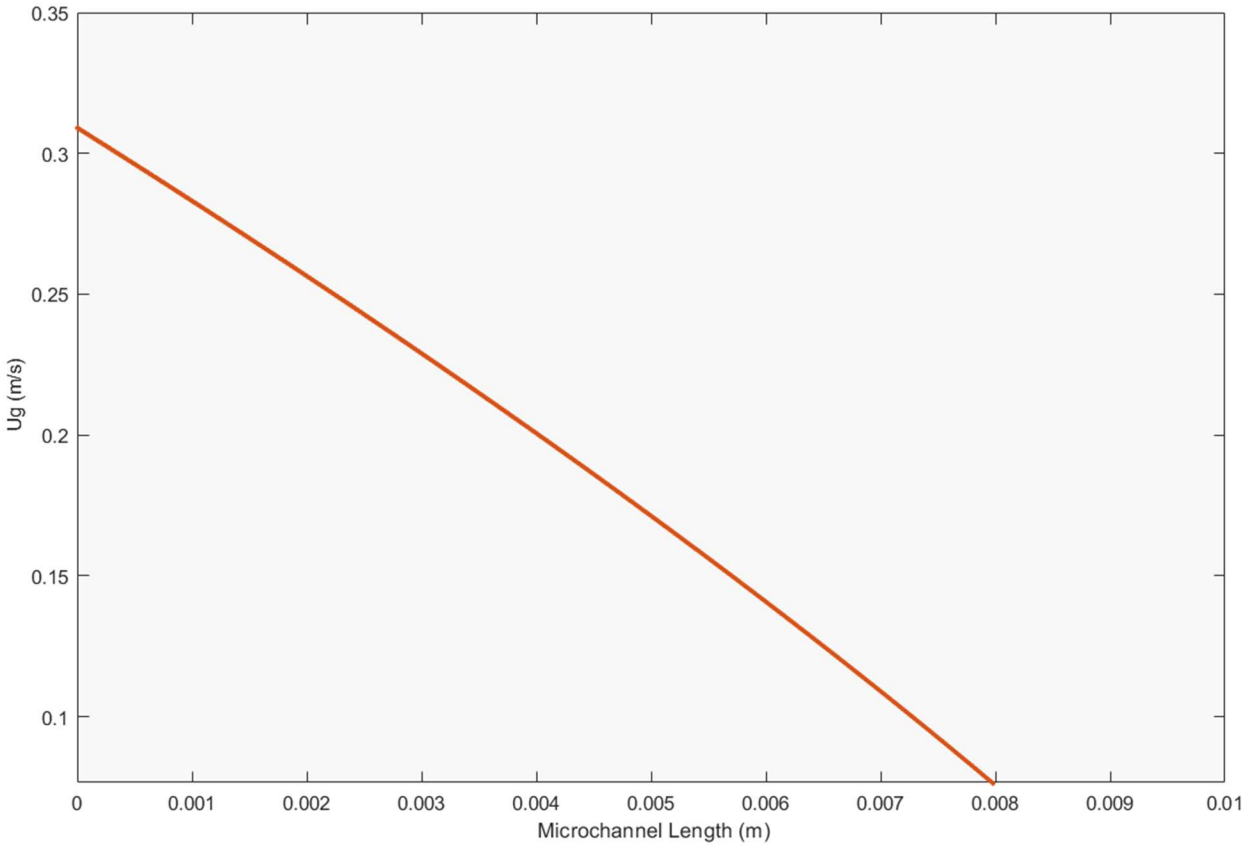

Figure 5.4: Superficial gas velocity over microchannel length

Additionally, the gas-liquid mass transfer rate is also affected by the CO concentration differential that exists between these phases. As seen in Figure 5.5, the concentration difference, $C_{CO,LB}{}^{*} - C_{CO,L}$, changes over the length of the microchannel, between 0 and 42 mol/m^3 ,and this has a direct impact on the CO depletion rate, $\frac{UdC_{CO,LB}}{dz}$. The large bubble CO concentration depends on the mass transfer coefficient and the concentration of the species in the liquid phase which is in turn dependent on the gas phase CO concentration and also on the reaction rate. This network of dependencies makes it rather clear that the concentrations of CO on both sides of the gas-liquid interphase are dependent on each other through the laws of mass transfer but in addition, the liquid phase CO concentration also depends on R_{CO} which is one of the primary sources, together with axial dispersion, of all the axial gradients, i.e., all parameters of interest change only as a result of chemical reaction and back-mixing.

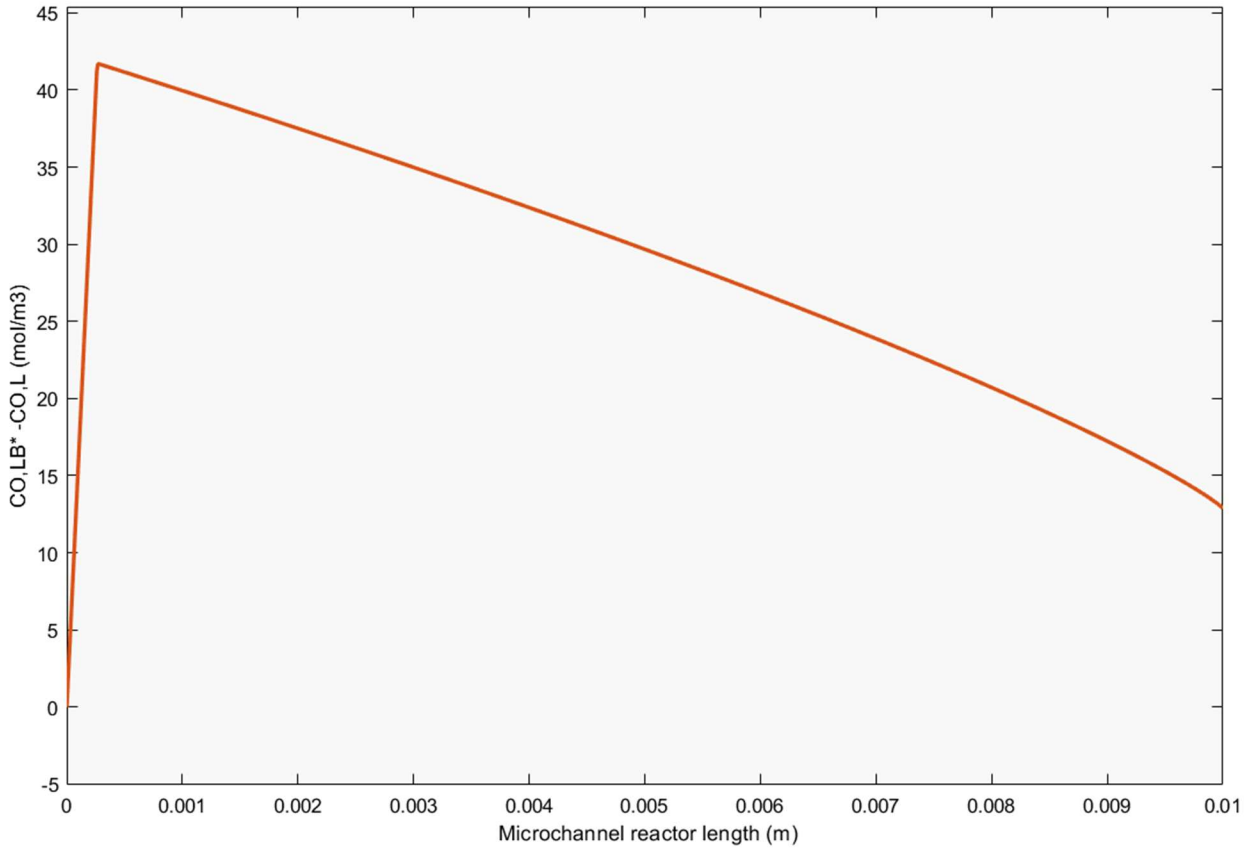

Figure 5.5: Interphase concentration difference between large bubble and liquid phases over microchannel length

In Figure 5.5, $C_{CO,LB}{}^{*} - C_{CO,L}$ initially increases sharply before dropping throughout the microchannel length. This sharp initial increase is because of the rapid disappearance of the initially present CO concentration (at $z = 0$) in the liquid phase as shown in Figure 5.6. The decrease in $C_{CO,LB}{}^{*} - C_{CO,L}$ following the initial rise indicates that the liquid phase CO concentration is constant over this particular length so that the decreasing large bubble CO concentration dominates and results in a downward $C_{CO,LB}{}^{*} - C_{CO,L}$ profile. This is evidence that the mass transfer rate across the large bubble and liquid interface is also a function of the reaction rate so that as the reaction rate decreases (Figure 5.7), the mass transfer rate decreases as well. This adds to the detrimental effect of the mass transfer coefficient on the CO depletion rate in the large bubble class over the length of the microchannel.

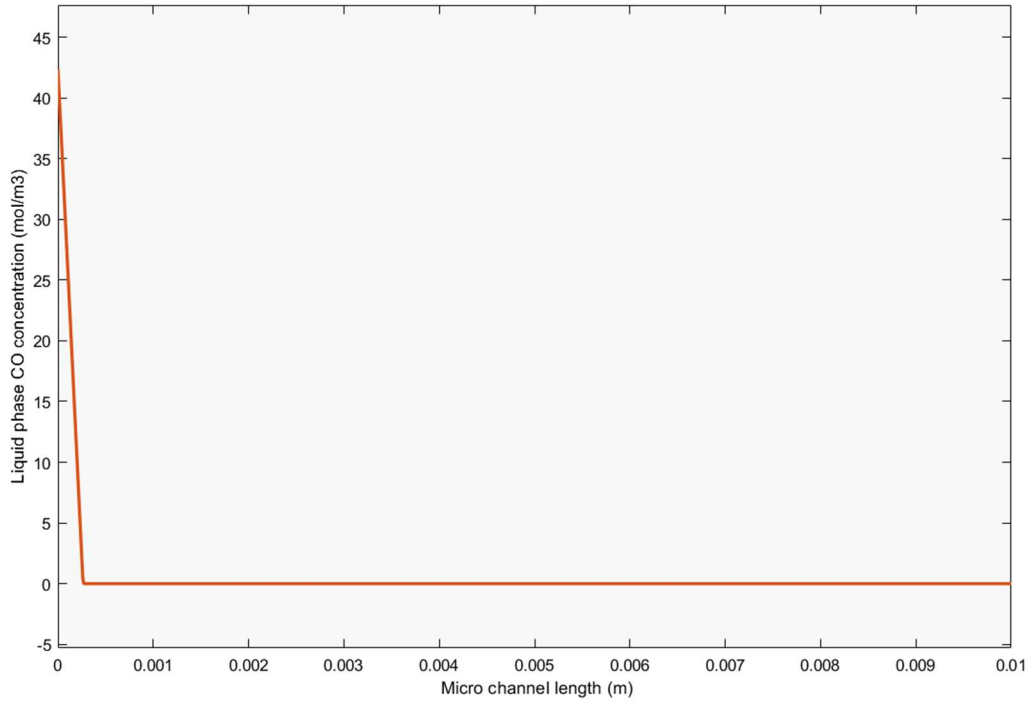

Figure 5.6: Axial change of CO concentration in the liquid phase over microchannel length

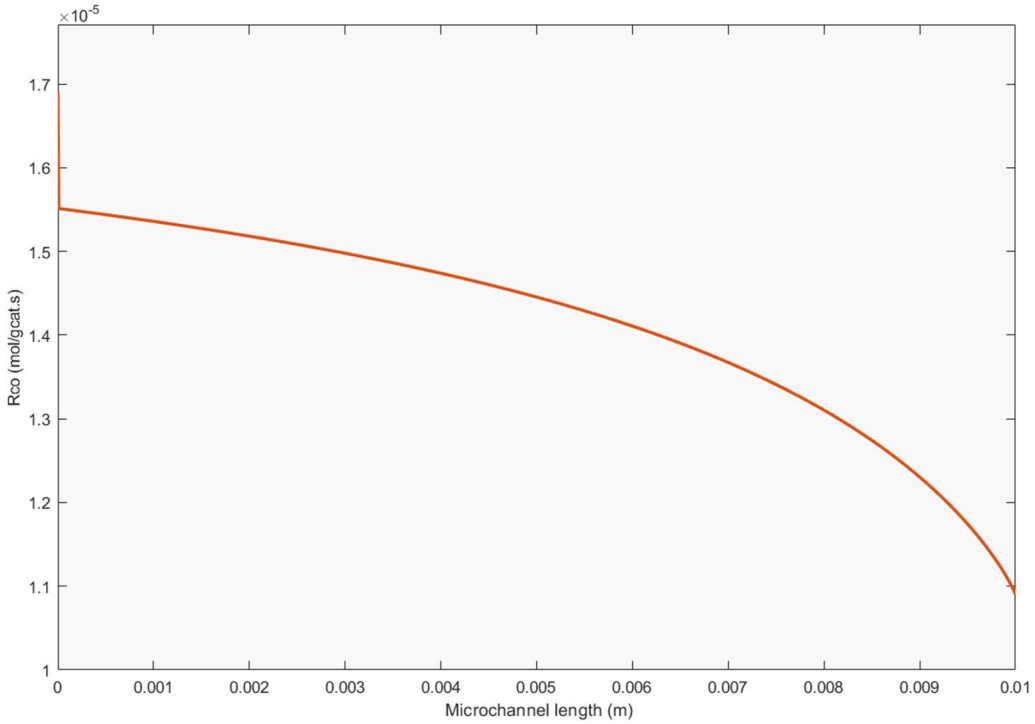

Figure 5.7: CO reaction rate over function of channel length

The large bubble CO concentration depletion rate, $\frac{UdC_{CO,LB}}{dz}$, is also affected by the back-mixing in the large bubble phase. As seen in Equation 3.53, dispersion in the large bubble class depends on both the large bubble class hold-up (Figure 5.3) and dispersion coefficient (Figure 5.8). Both these variables are dependent on the superficial gas velocity so that as it decreases, the E_{LB} and ε_{LB} will also decrease and together they will result in a lower large bubble class dispersion. A lower phase dispersion promotes a more plug flow-like regime and consequently elevated species depletion rates.

At this point it is evident that the drop in U_g across the microchannel length has two opposing effects on the large bubble class CO concentration depletion rate. It has, on the one hand a lowering effect on the mass transfer rate across the gas-liquid interphase resulting in a lower large CO concentration depletion rate and on the other hand, a decreasing effect on axial dispersion which works to increase the CO concentration depletion rate. The reduction in U_g also affects R_{CO} by lowering it and this reduces further the mass transfer rate across the gas-liquid interface and the large bubble CO concentration depletion rate.

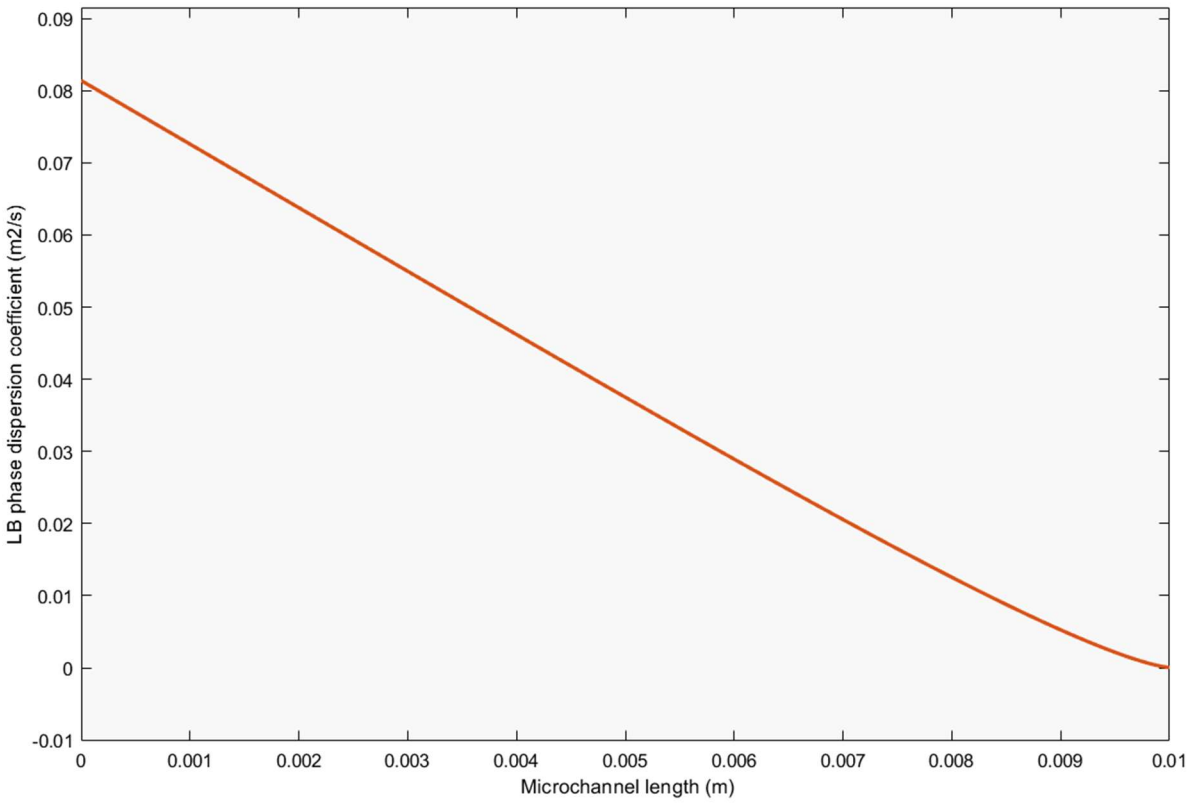

Figure 5.8: Large bubble phase dispersion coefficient over channel length

According to the simulation run on the model, $\frac{UdC_{CO,LB}}{dz}$ decreases over the length of the microchannel (Figure 5.9), where $\boldsymbol{\frac{UdC_{CO,LB}}{dz}}$ increases in the negative direction, which indicates that under the prevailing FT microchannel reactor conditions, a decreasing mass transfer rate effect takes precedence over that of a decreasing large bubble axial dispersion.

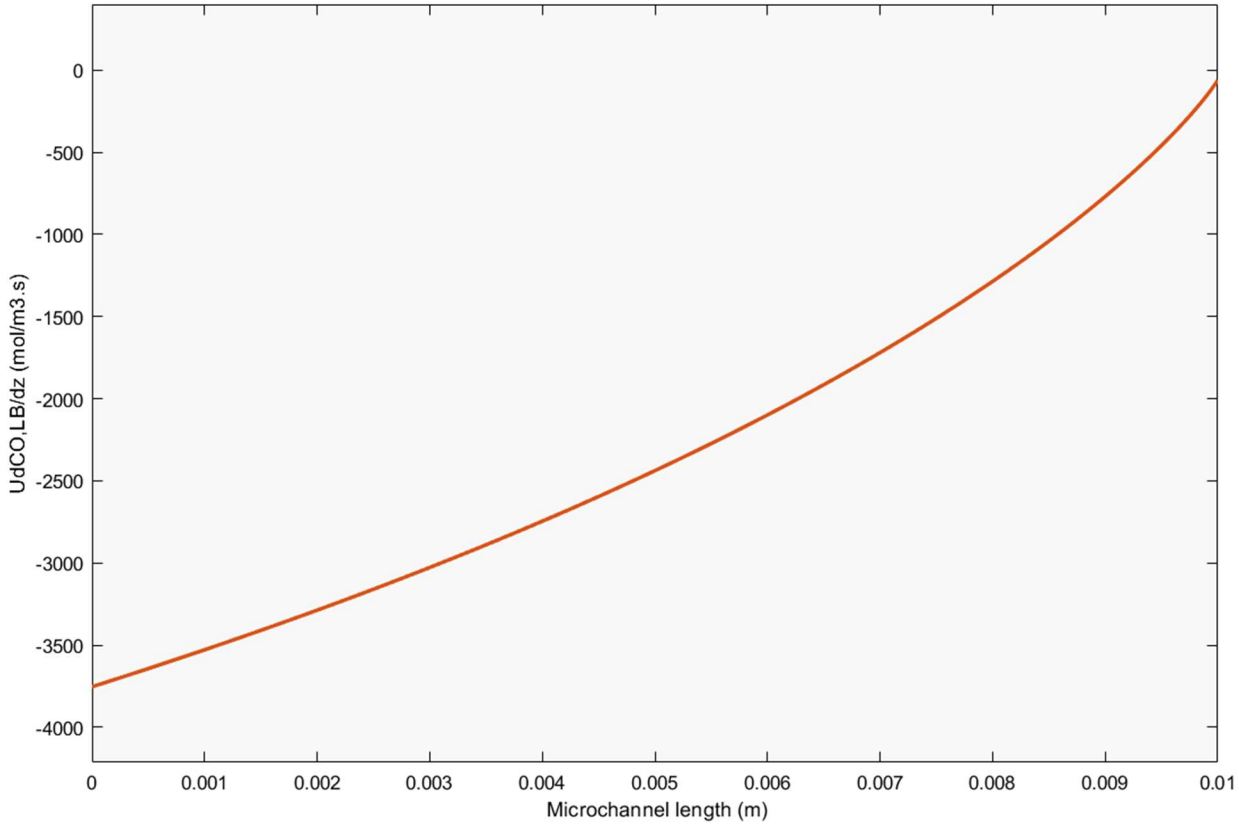

Figure 5.9: CO depletion rate in the large bubble phase over channel length

5.2.1.3 Concentration profile in small bubbles

Concerning the small bubble class CO concentration profile, it is worth noting that the change in the rate of depletion of small bubble CO concentration is independent of the small bubble-liquid phase mass transfer coefficient which remains uniform throughout the length of the microchannel. This uniformity is because of the constant nature of the small bubble hold-up, ε_{SB} over the microchannel length as assumed in the prior to the development of the model. This further means that the small bubble class axial dispersion, which depends on ε_{SB} and E_{SB}, will be a function of E_{SB} only which is in turn dependent on dependent on U_g. Given the decreasing nature of U_g over

the microchannel length, the small bubble class axial dispersion will decrease as well which should work towards increasing $\frac{Ud_{i,SB}}{dz}$ (Figure 5.10).

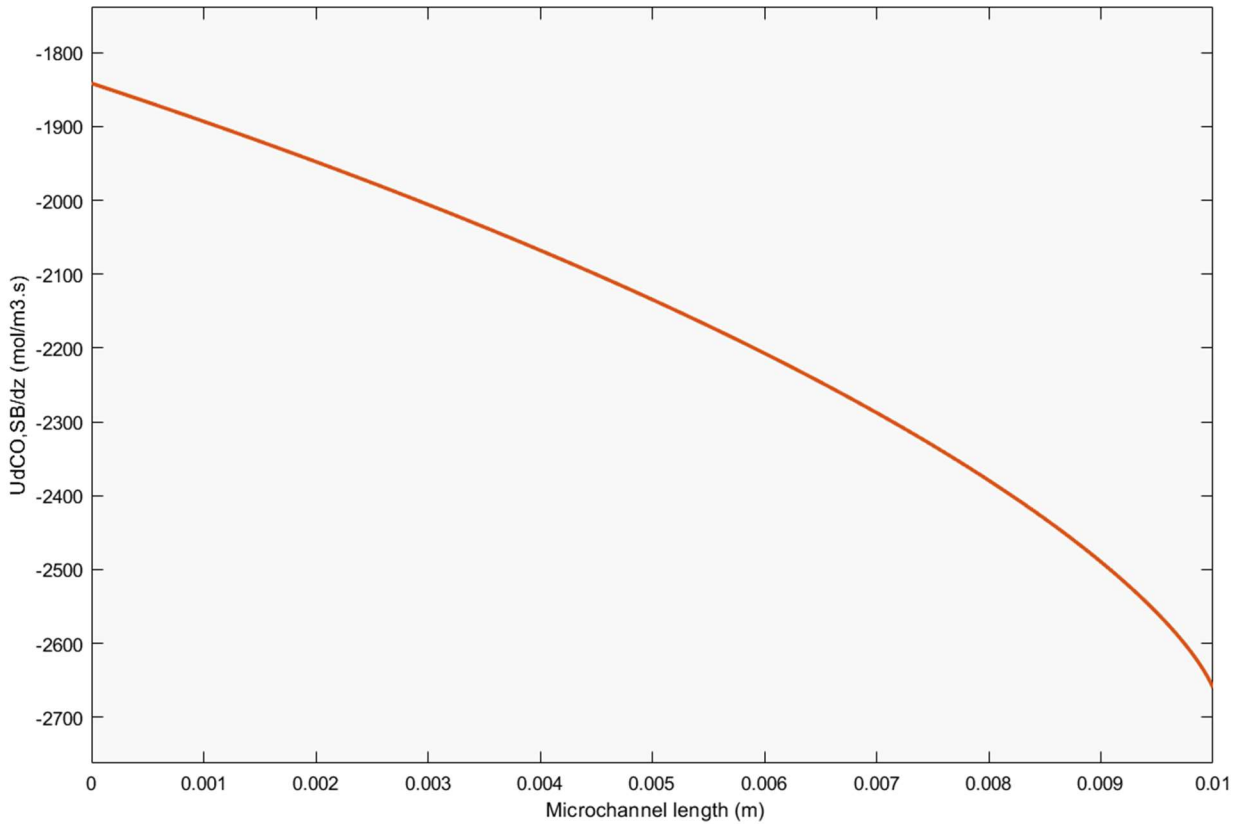

Figure 5.10: CO depletion rate in the small bubble phase over channel length

The small bubble class CO concentration depletion is rapid and this behaviour is partly caused by a quick decrease in the small bubble class CO concentration (Figure 5.11). This drop is caused by the relatively low axial dispersion in this phase as compared to the one in the liquid phase. Because of the lower axial dispersion coefficient, the small bubble phase will exhibit a more plug flow-like behaviour than is the case in the liquid phase and this will lead to greater a higher axial concentration differential. The main cause of this difference is the much lower initial small bubbles hold-up (0.004) versus that in the liquid phase (0.149) as given in Table 5.3.

Because of this sharp decrease, the concentration differential between the CO in the small bubble and liquid phases, $C_{CO,SB}{}^{*} - C_{CO,L}$, decreases momentarily, until the small bubble CO concentration is depleted, at which point $C_{CO,SB}{}^{*} - C_{CO,L}$ begins to increase until it reaches zero

(Figure 5.12). At this point, the effect of $C_{CO,SB}{}^{*} - C_{CO,L}$ becomes negligible and only the decreasing axial dispersion is responsible for the increasing depletion rate.

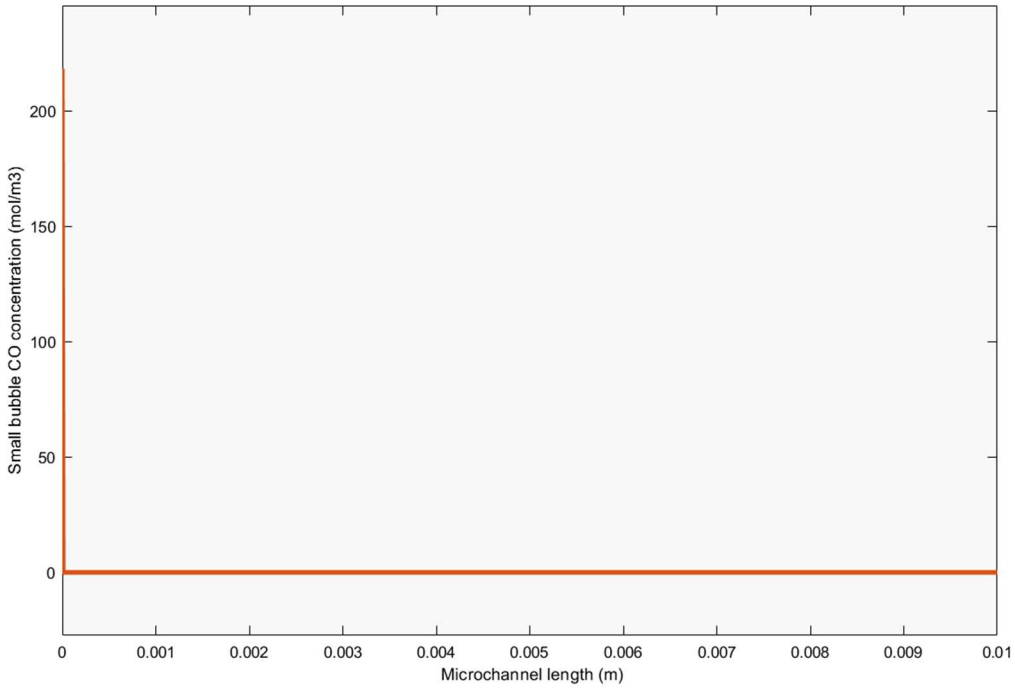

Figure 5.11: Small bubble phase CO concentration over channel length

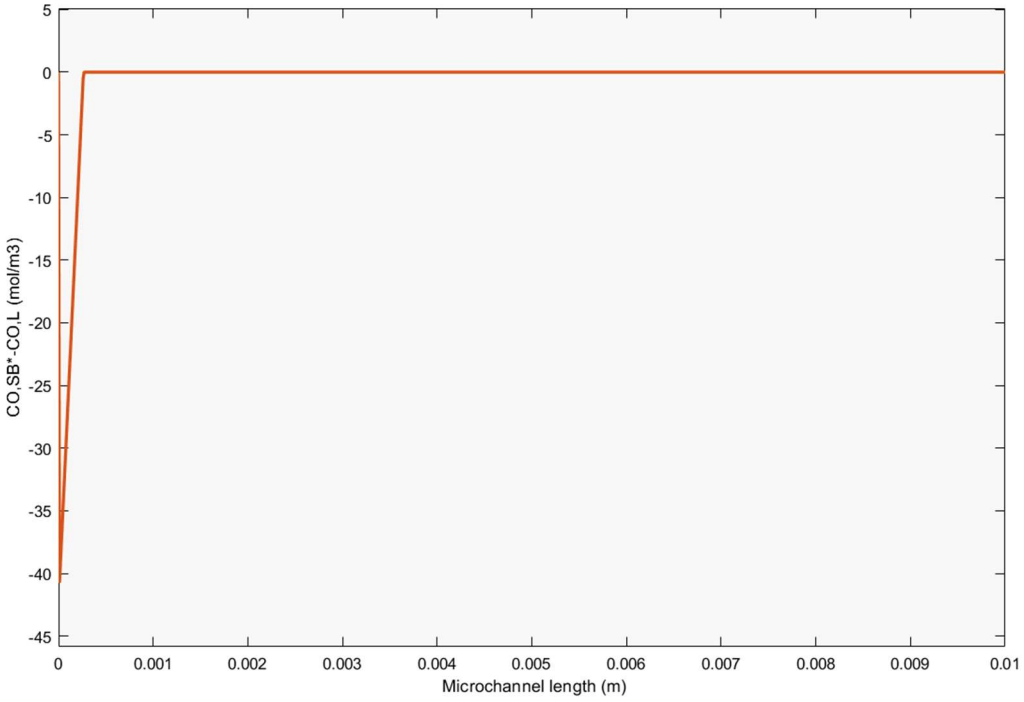

Figure 5.12: Interphase CO concentration difference between small bubble and liquid phases

5.2.1.4 Concentration profile in liquid phase

The depletion rate of the CO concentration in the liquid phase shows an increasing trend over the length of the microchannel (Figure 5.13). This trend is accompanied by an decrease in $C_{CO,LB}{}^{*} - C_{CO,L}$ as shown in Figure 5.5 while the concentration differential across the small bubbles-liquid interphase remains constant (Figure 5.12). This, together with a decreasing large bubble class mass transfer coefficient as a function of the decreasing superficial gas velocity, is evidence that the mass transfer rate across the large bubble-liquid phase interface decreases as a function of microchannel length.

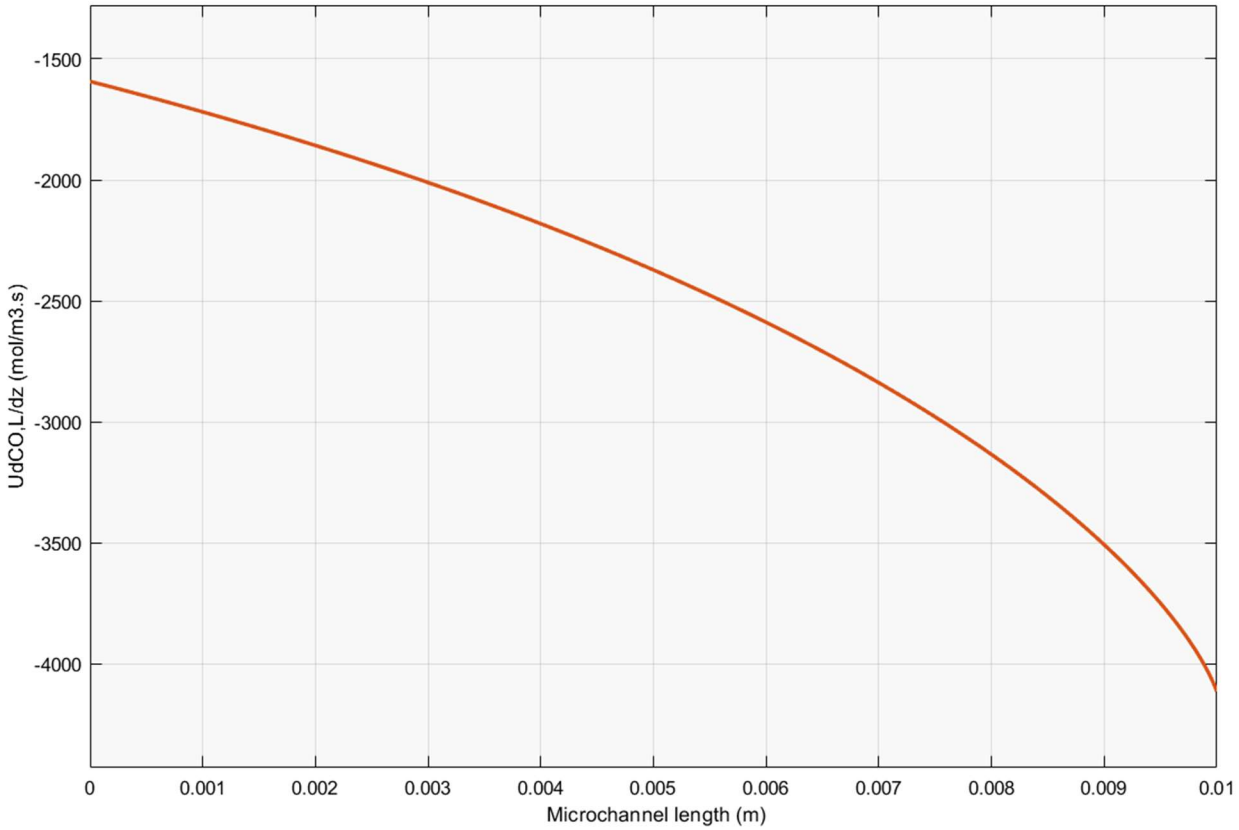

Figure 5.13: Rate of depletion of CO in the liquid phase over the height of the reactor

$\frac{UdC_{CO,L}}{dz}$ is further influenced by the liquid phase axial dispersion which has already been assumed to be equal between the small bubble and liquid phases. This means that dispersion will decrease as a function of the decreasing superficial gas velocity which should work towards increasing $\frac{Ud\ _{CO,L}}{dz}$. Also, as the rate of reaction decreases over the microchannel length, this should work

towards reducing $\frac{UdC_{CO,L}}{dz}$. Because $\frac{UdC_{CO,L}}{dz}$ increases along the microchannel length as evident in Figure 5.13, it can be concluded that the liquid phase axial dispersion coefficient has a greater effect on the liquid phase CO concentration depletion rate.

It is worthwhile to note that a liquid phase CO concentration of zero, as seen in Figure 5.6, does not mean the non-existence of CO species in the liquid phase but it rather indicates a sufficiently quick rate of reaction so that as the CO species is made available in the liquid phase, it is immediately consumed, i.e., the rate of mass transfer of CO to the liquid phase is equal to the rate of consumption of CO by reaction. The same argument applies in the small bubble class.

The decreasing superficial gas velocity profile over the length of the microchannel which is caused by the consumption of the reactants, is the primary contributor to the above-mentioned axial gradients. It influences the large bubble class hold-up which in turn affects the mass transfer and axial dispersion profiles in the large bubble class. It further affects the large bubble class axial dispersion as well as the liquid and small bubble class axial dispersion coefficients. This further points to the importance of the superficial gas velocity in the hydrodynamics and performance of the FT microchannel reactor.

5.1.3 Sensitivity analysis

To understand the effects of the hydrodynamics more clearly within a microchannel FT reactor, it is necessary to study the various independent parameters and how they affect the flow dynamics performance of the microreactor. To do this, specific sensitivity analyses were performed on the model to study the effects of individual parameters on the performance of the microchannel reactor. This will clarify the importance of these parameters in FT microchannel reactor modeling.

These individual parameters will be manipulated and their effect on microreactor performance assessed. To ensure the validity of this sensitivity analysis exercise, the effect of each parameter on the performance of the microreactor was carried out exclusively with the other relevant parameters remaining constant throughout. The values discussed in this section are those stemming from a complete simulation where these values are extracted after a simulation is run from z=0 to z=L.

5.2.2.1 Effect of superficial gas velocity

The superficial gas velocity is one of the most important determinants of FT microchannel reactor performance as it directly affects multiple reactor conditions which in turn influence the hydrodynamics. Firstly, U_g directly influences the flow regime prevalent in the microchannel which can either be bubbly, segmented, annular or churn-turbulent. These regimes have a real and direct effect on the performance of the microreactor through their effect on the hydrodynamics. A churn-turbulent flow regime, for example, will promote axial dispersion which influences the performance of the microreactor as discussed in the section 5.1.2. A higher axial dispersion will act to reduce syngas conversion so that as U_g is increased, the syngas conversion will be reduced. This is shown in Figure 5.14 where the effects of U_g on E_L and E_G are illustrated.

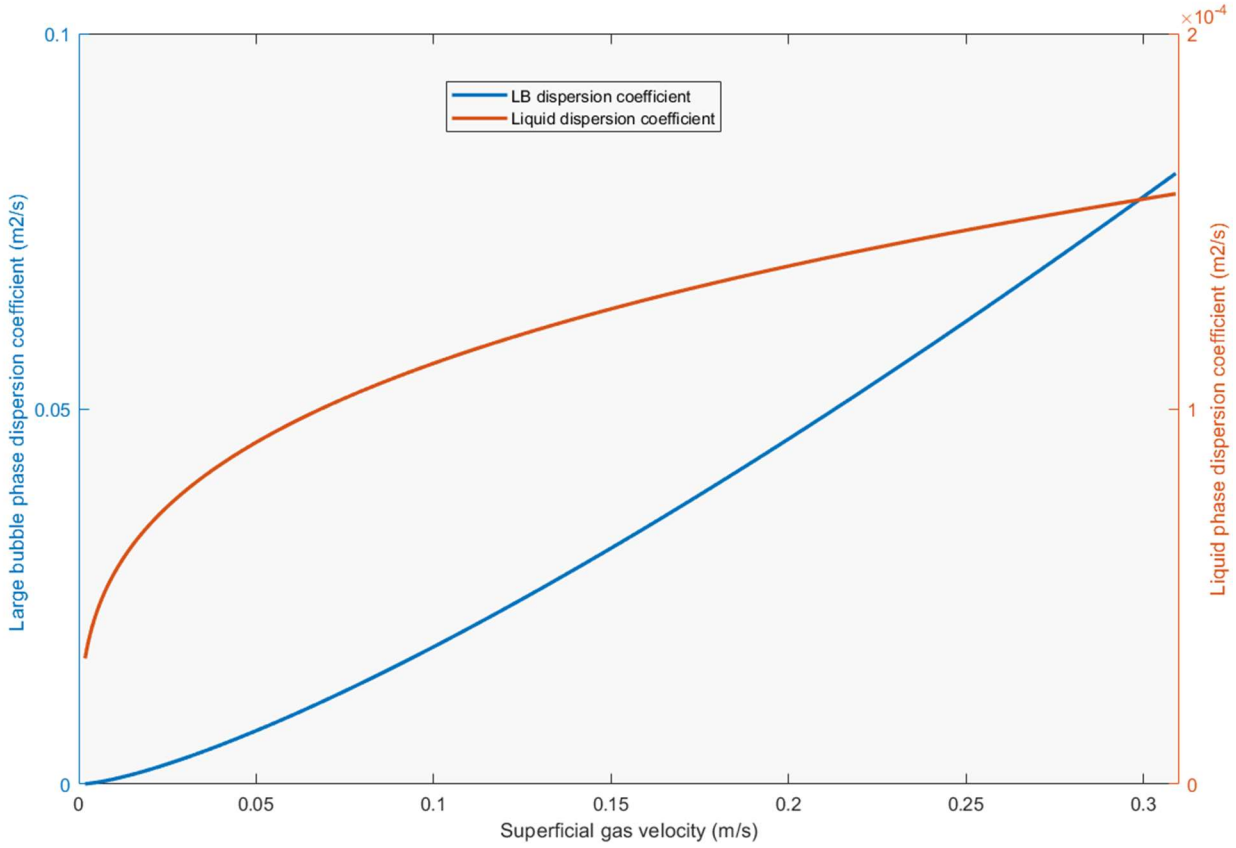

Figure 5.14: Effect of Ug on large bubble and liquid phase dispersion

Between a superficial gas velocity of 0.0018 and 0.309 m/s, the gas and liquid phase dispersion coefficients increases by 99.9% and 78.7% respectively. The superficial gas velocity increase is

directly responsible for the increase in the liquid phase dispersion coefficient as can be deduced from Equation 3.85. The gas phase dispersion coefficient depends on the total gas hold-up in addition to depending directly on the superficial gas velocity (Mangartz and Pilhofer, 1980). Furthermore, the total gas hold-up, through its relationship with the large bubble hold-up, is dependent on the superficial gas velocity so that as the superficial gas velocity decreases, the total gas hold-up drops as well as seen by the decrease from 0.158 to 0.015 (Figure 5.15). The superficial gas velocity, then, is solely responsible for the change in the gas phase dispersion coefficient across the length of the microchannel.

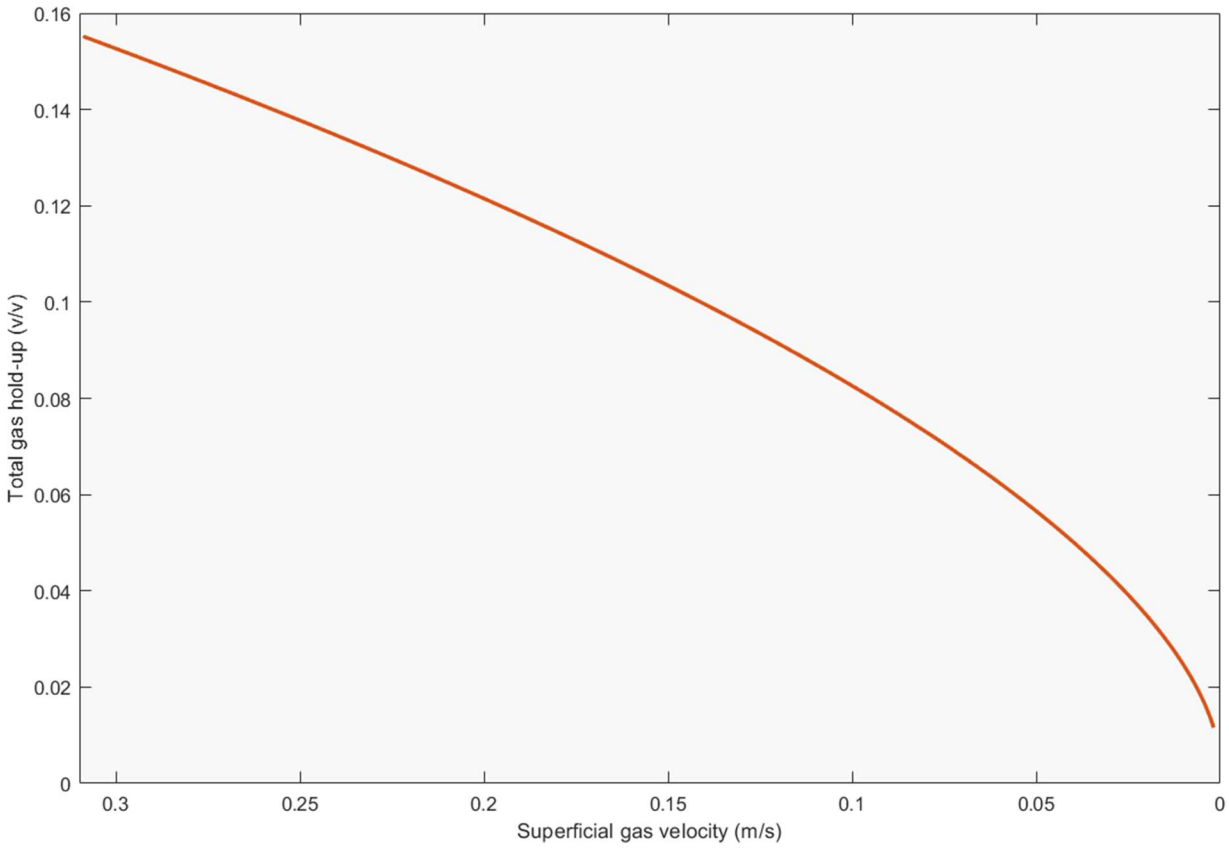

Figure 5.15: The effect of superficial gas velocity on total gas hold-up

Despite this, it's important to understand exactly how U_g influences E_G, i. e., directly or indirectly through its effect on the total gas hold-up. As per the gas phase dispersion correlation from Mangartz and Pilhofer (1980), the relative effects of total gas hold-up and U_g are represented by $\frac{U_g}{\varepsilon_g}$ so that in determining which of these two is more influential, it would be important to determine

which parameter is more affected across the length of the microreactor. It would be this parameter that can be considered more important to gas phase dispersion in the microreactor. This sensitivity analysis was conducted and the results are shown in Figure 5.16. $\frac{U_g}{\varepsilon_g}$ shows a decreasing trend in Figure 5.16 which means U_g is decreasing more rapidly than the total gas hold-up. This clearly indicates U_g's higher sensitivity to the change in microchannel length compared with that of the total gas hold-up meaning that U_g's effect on the gas phase dispersion is direct and not through its effect on the total gas hold-up.

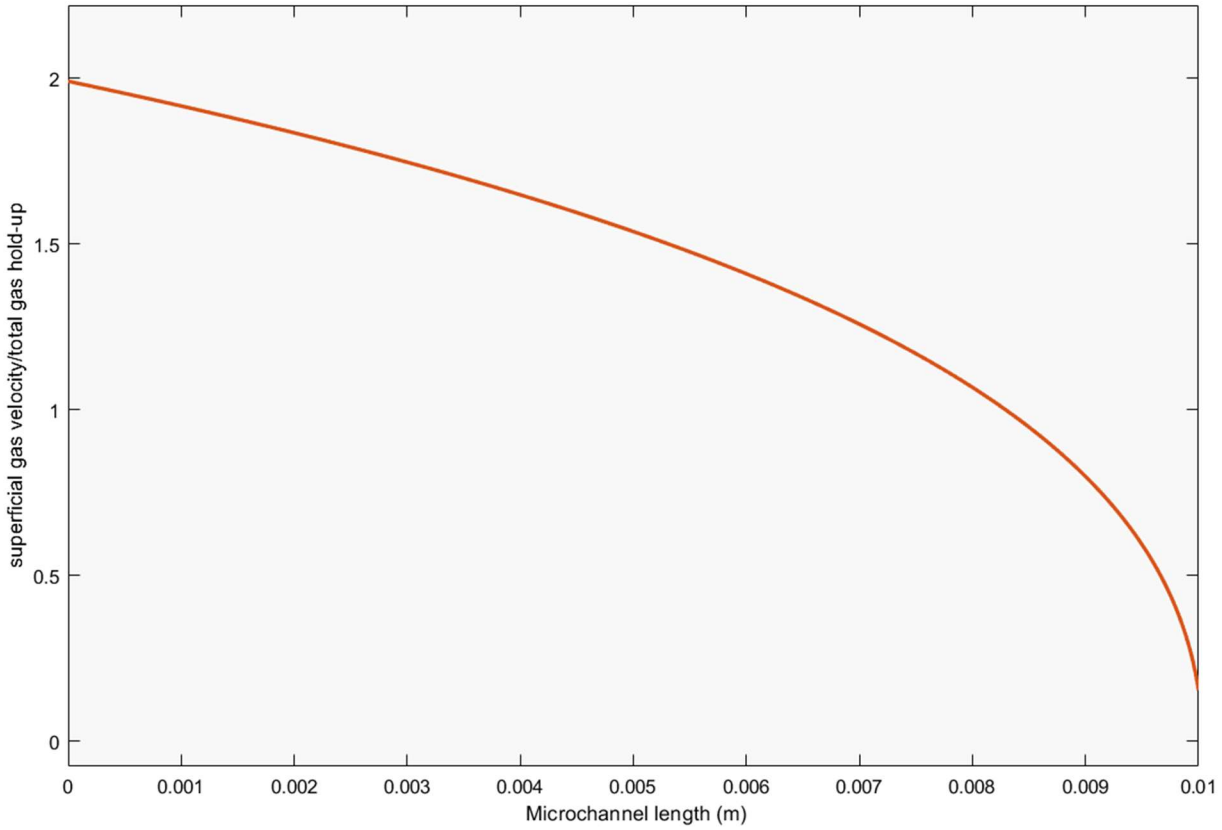

Figure 5.16: Relative sensitivities of superficial gas velocity and total gas hold-up to a change in reactor height

Additionally, the superficial gas velocity has a direct impact on the large bubble class hold-up which also affects the total syngas conversion. From the simulation, it was determined that increasing U_g will increase the large bubble hold-up as shown in Figure 5.17. The large bubble hold-up affects the reactor performance along two separate paths; firstly, a larger large bubble hold-up will increase the mass transfer coefficient across the large bubble-liquid phases thus

allowing more reactants to travel between the two phases and secondly, a larger large bubble hold-up will lead to a higher gas phase dispersion which directly affects performance.

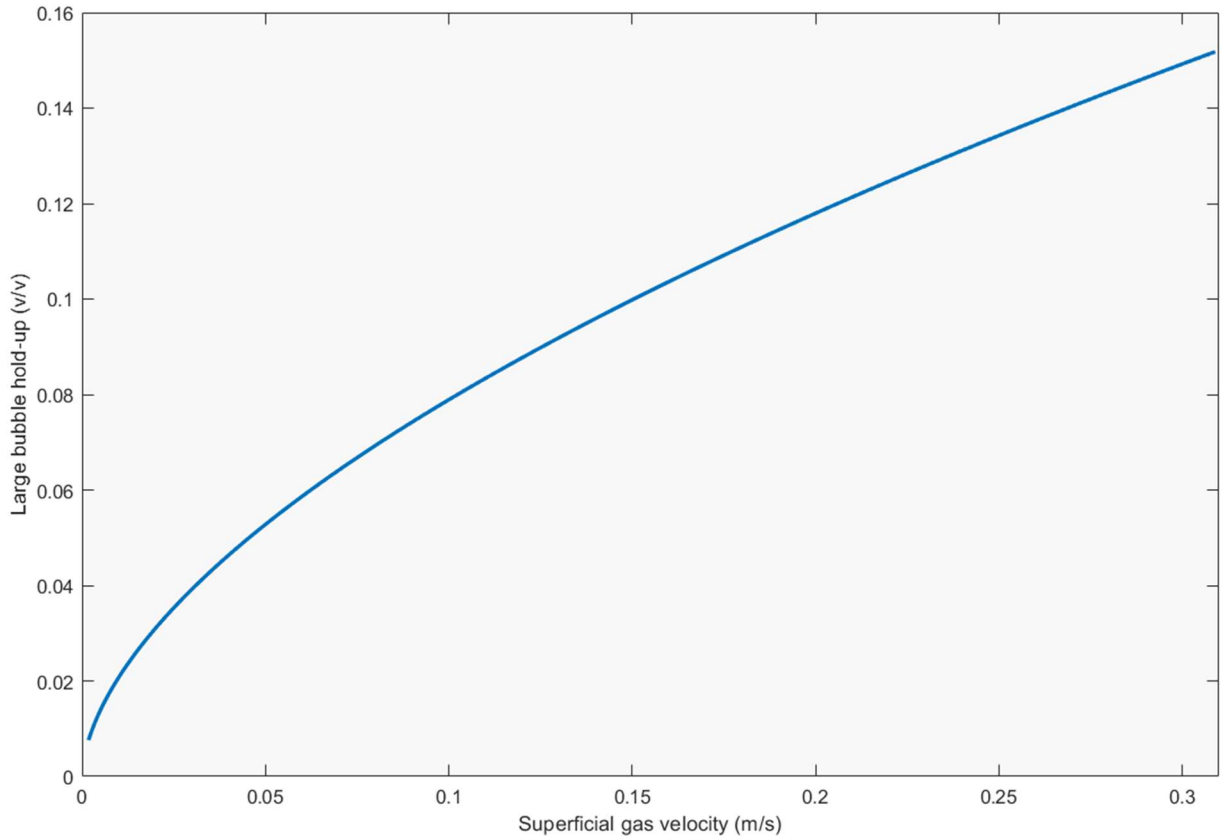

Figure 5.17: Effect of Ug on large bubble hold-up

Although E_G is directly affected by the total gas hold-up, the effect of the large bubble hold-up on E_G still holds as a result of the assumption that the small bubble hold-up is independent of microchannel length and remains constant throughout, meaning that an increase in the large bubble hold-up will lead to an increase in the total gas hold-up. This means that there are two opposite effects of ε_{LB} on FT microreactor performance so that increasing ε_{LB} will improve mass transfer rates and thus the reactor performance but this increase will also promote an increase the gas phase dispersion which will work to reduce the total syngas conversion. To determine the effect that is more dominant, a comparison was made between the effects of ε_{LB} on the mass transfer coefficient and the gas phase axial dispersion coefficient as shown in Figure 5.18.

From Figure 5.18, between a large bubble hold-up of 0.1492 and 0.0769, a gas phase axial dispersion coefficient change of -80% was realized while in the same range, a large bubble CO mass transfer coefficient change of -48% was recorded. This clearly shows that the main effect of gas hold-up on the microreactor performance is through its effect on the gas phase axial dispersion coefficient. It is apparent then, that increasing U_g will likewise increase the gas phase axial dispersion coefficient directly and indirectly as well, through affecting a higher large bubble hold-up. Both conditions will promote a lower total syngas conversion.

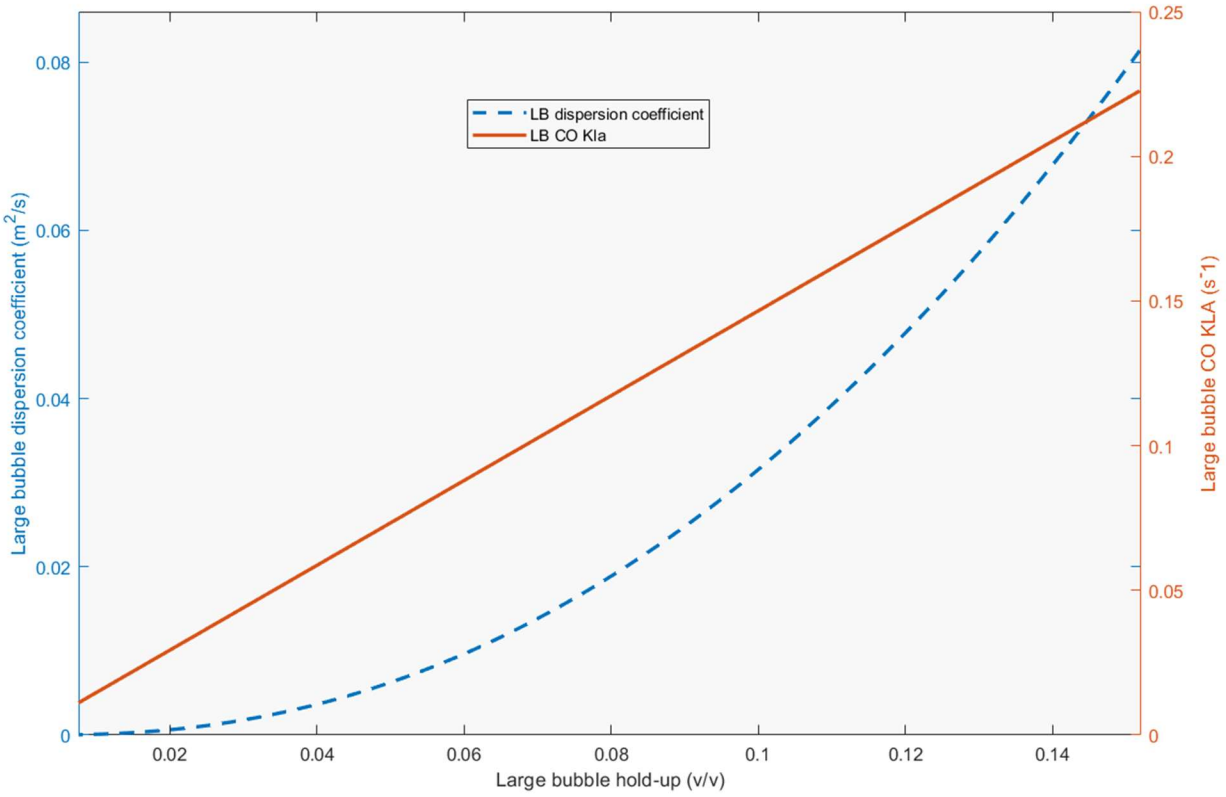

Figure 5.18: Comparative effects of large bubble hold-up on the large bubble dispersion coefficient and large bubble-liquid interface mass transfer coefficient

With the constant diameter of the microchannel, increasing the U_g will reduce the residence time of the reactants inside the microreactor reactor. The lower residence time will then work to reduce the total syngas conversion. The combined detrimental effects of increased axial dispersion and reduced residence time following an increase in U_g will have the overall effect of lowering the

total syngas conversion. This is reflected in Figure 5.19 where an increase in U_g reduces the total syngas conversion from 70% to 40%.

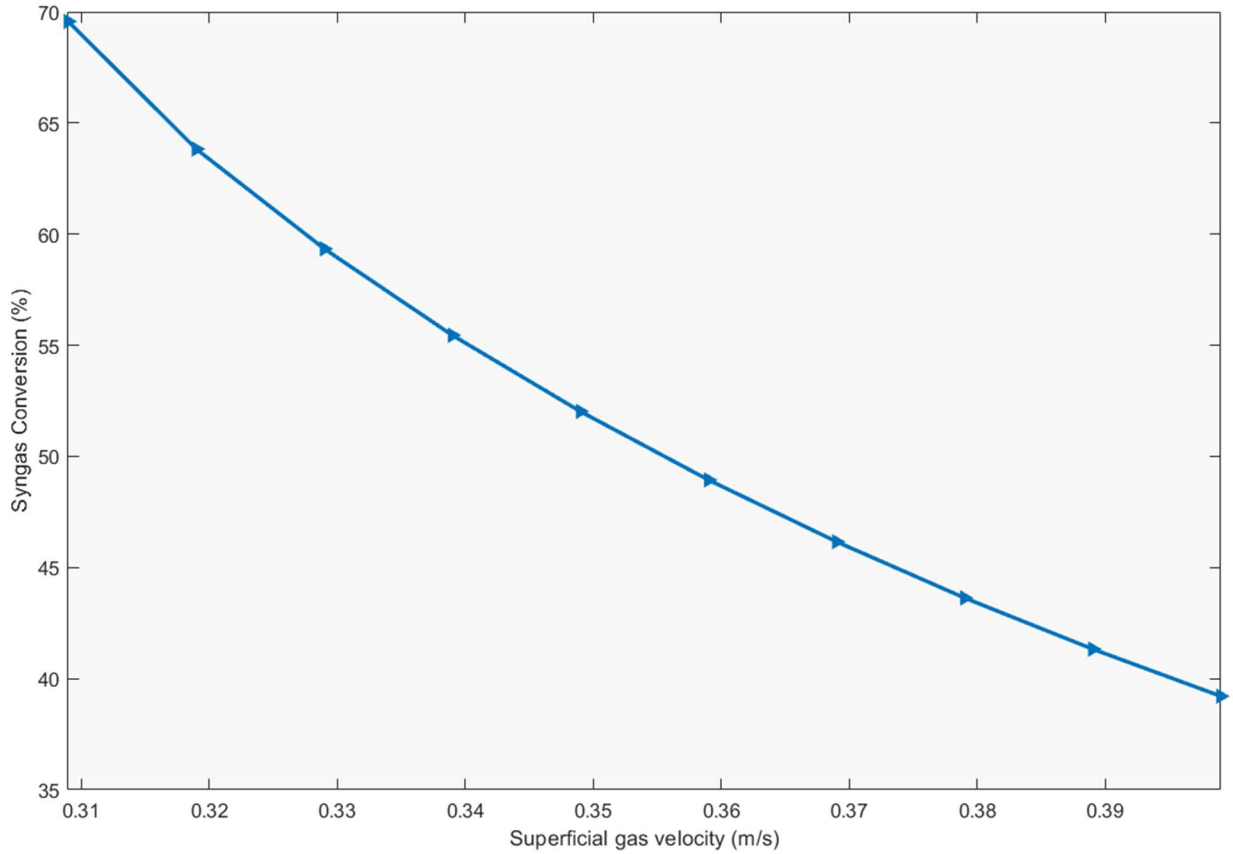

Figure 5.19: Effect of inlet superficial gas velocity on syngas conversion

5.2.2.2 Effect of reactor diameter

An increasing reactor diameter should directly increase the liquid and gas phase dispersion by as can be deduced from the respective dispersion correlations used in this model. This does not occur however, because of the two-fold impact that a changing diameter has on both dispersion coefficients. Firstly, increasing the diameter with the reactor throughput kept constant would, as can be expected, reduce U_g whose effect on the FT microchannel performance has already been discussed earlier in this report where it was determined that a decreasing U_g will reduce both the liquid and gas phase axial dispersion coefficients. This means that an increase in the reactor diameter will directly increase and indirectly decrease, through its effect on U_g, the dispersion coefficients in the two phases. As can be seen in Figure 5.20 where the diameter is increased from

2.6 x 10^{-3} to 3.4 x 10^{-3}, though, the overall impact is a decrease in the axial dispersion coefficients which means the dispersion coefficients are sensitive to a decreasing superficial gas velocity. Increasing the reactor diameter therefore, will reduce the axial dispersion in the gas and liquid phases by 98% and 8% respectively, such that the total syngas conversion is increased (Figure 5.21).

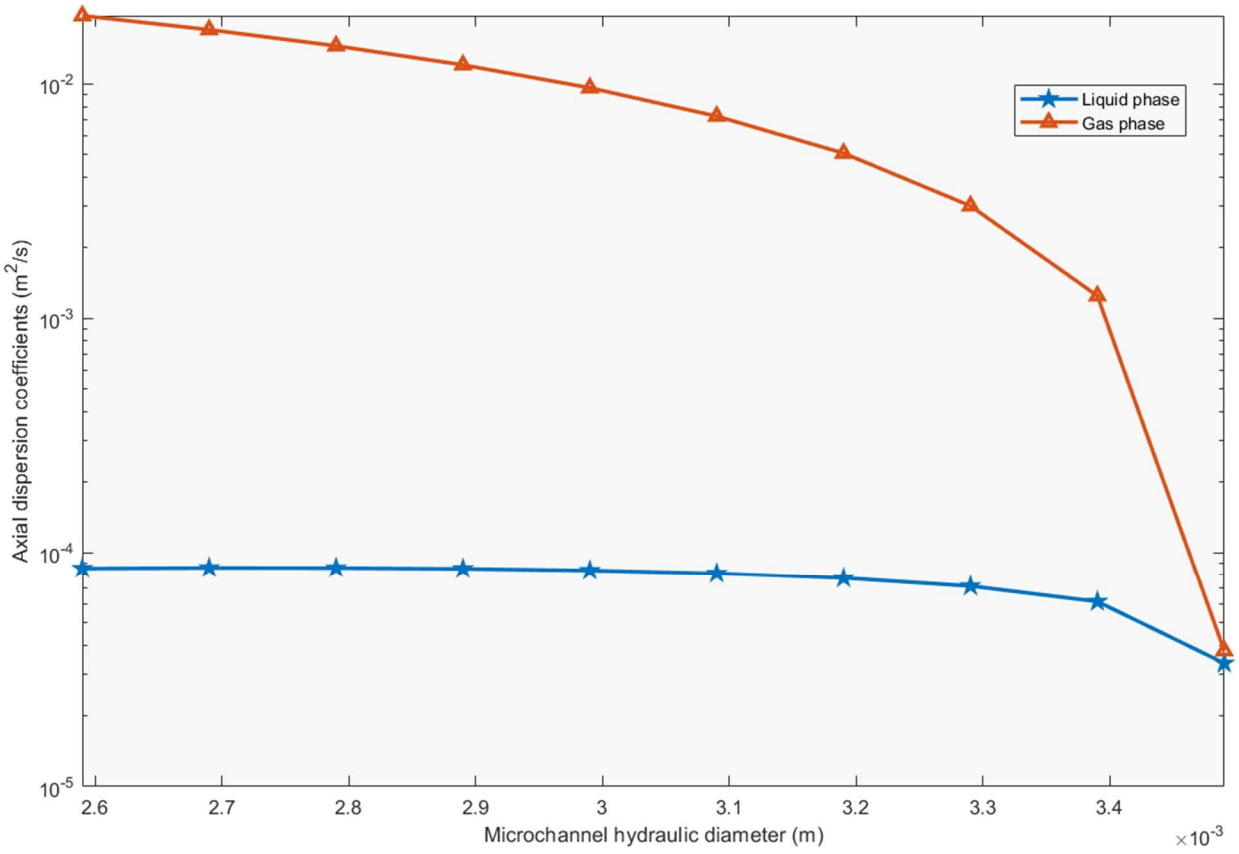

Figure 5.20: Effect of reactor diameter on the gas and liquid axial dispersion coefficients

Given that U_g decreases with an increase in the reactor diameter, the residence time of the reactants is expected to increase so that the reactants spend more time within the reactor which should work towards a higher syngas conversion. Overall, the effect of increasing the reactor diameter is an increased total syngas conversion (Figure 5.21) from 33% to 70% conversion as a result of the reduced dispersion and longer contact time.

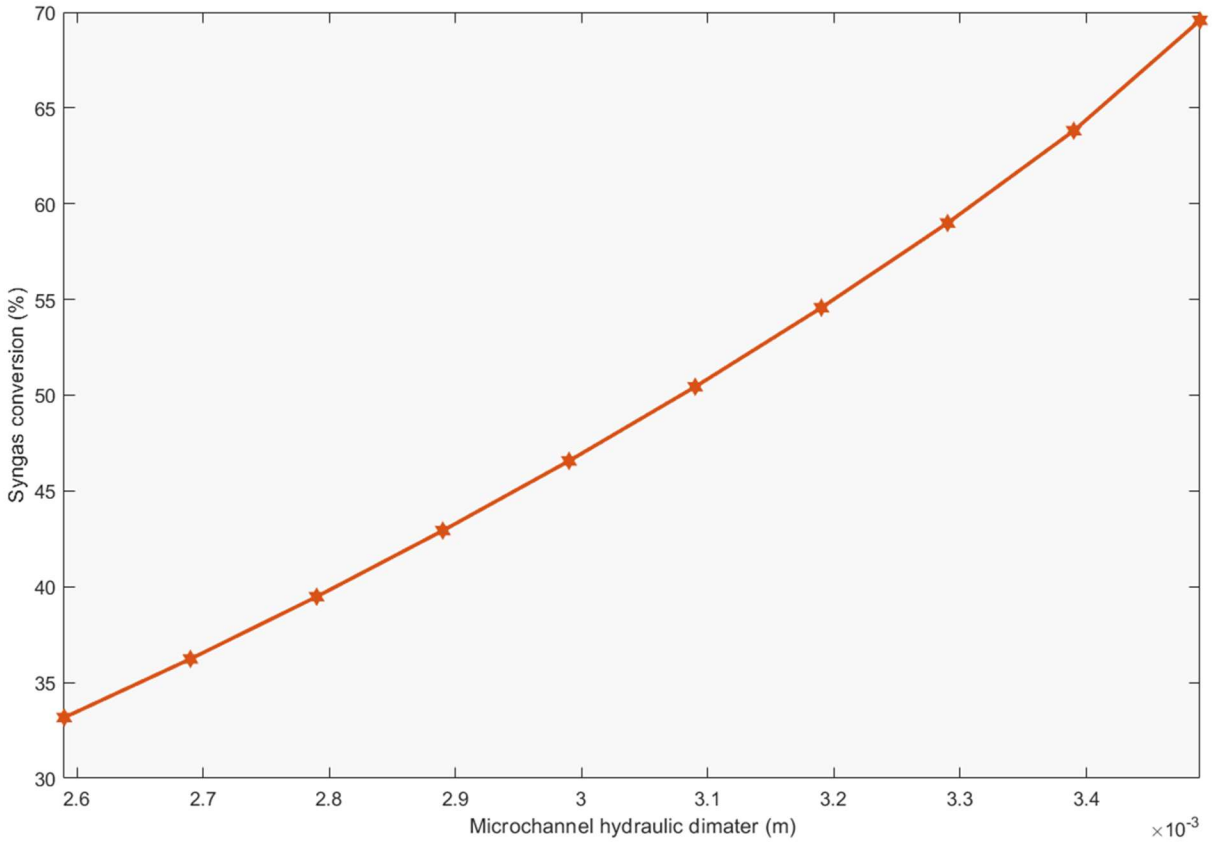

Figure 5.21: Effect of reactor diameter on syngas conversion

5.2.2.3 Effect of solids concentration

The solids concentration, in this case the catalyst concentration, has a direct effect on the small bubble hold-up (Equation 3.80) and the reactant consumption rate as per the consumption term in the material balance. An increase in the solids concentration between 0.38 and 0.3845 will reduce the small bubble hold-up by 75% as shown in Figure 5.22, which in turn will have the effect of reducing the small bubble mass transfer coefficient by 67% as shown in Figure 5.23. As can be expected, a greater solids concentration will act to increase the reactant consumption rate as is shown in Figure 5.24. This is shown by the fourfold increase in the reactant consumption rate.

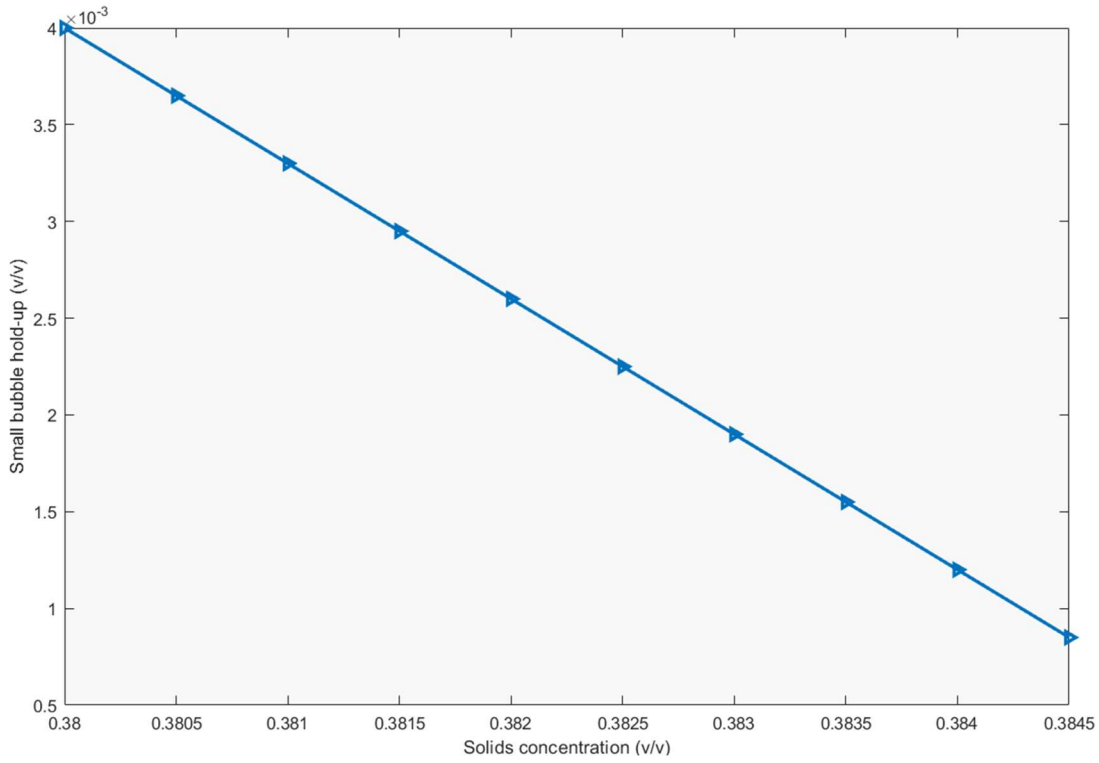

Figure 5.22: Small bubble hold-up as a function of solids concentration

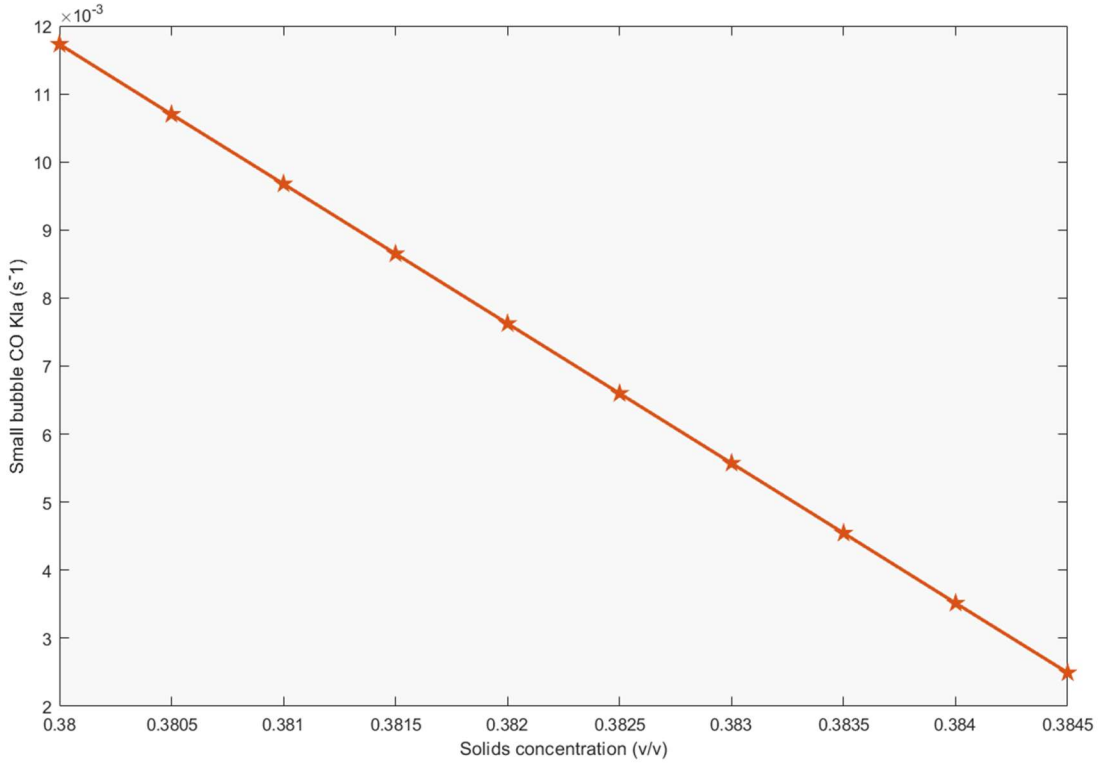

Figure 5.23: Effect of solids concentration on small bubbles mass transfer coefficient

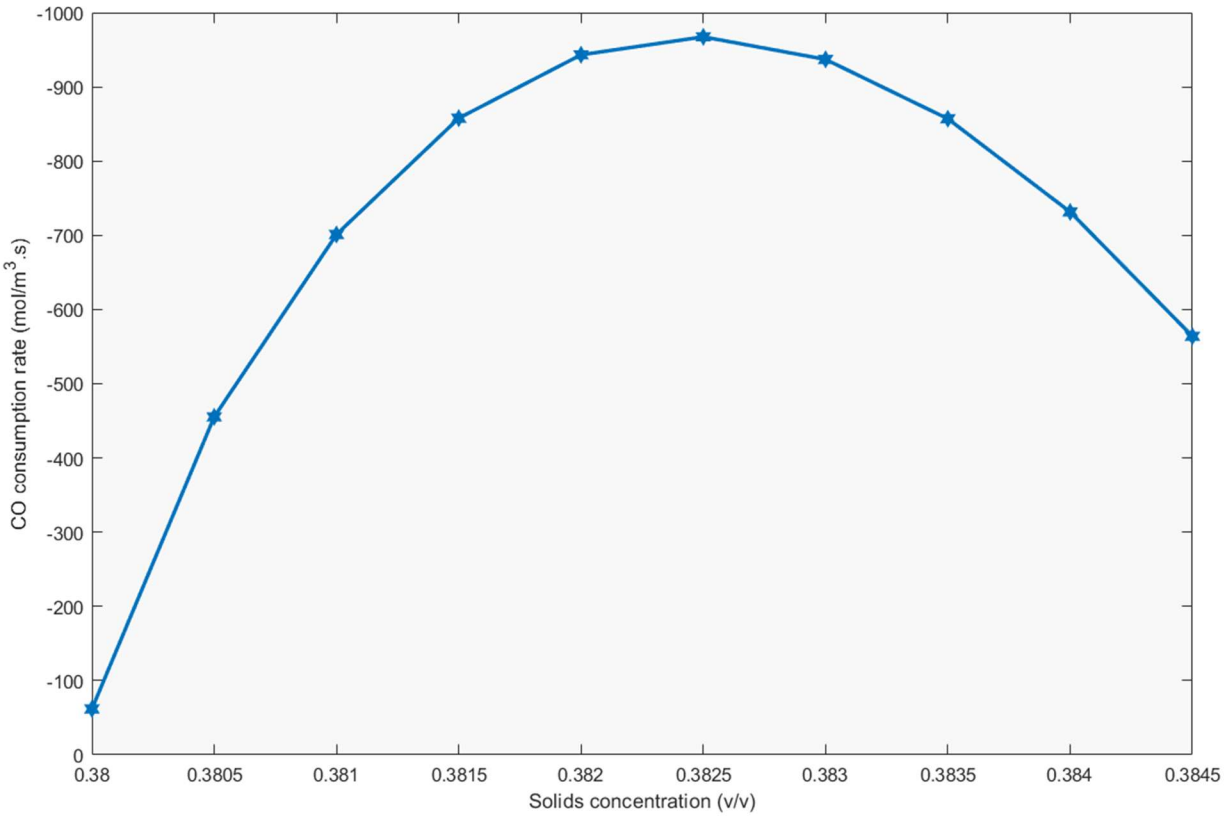

Figure 5.24: Effect of solid loading on reactant consumption rate

Generally, an increase in the catalyst loading should result in a higher conversion but as can be seen in Figure 5.25, the opposite is true in this case with the conversion dropping from 70% to 4%. This is certainly counter-intuitive but can be explained by the effect that the solids concentration has on the hydrodynamics, i.e., the flow structures at these much higher solids concentrations promote poor hydrodynamics such that the greater reaction surface area stemming from this increased solids concentration is not enough to counter this effect. The effect of solids concentration on the hydrodynamics is seen through the impact that an increasing solids concentration has on the large bubble hold-up. As the solids concentration is increased, the small bubble hold-up decreases and this in turn results in a decrease in the small bubble superficial gas velocity by 76%, as is evident in Figure 5.26. This ultimately has the effect of increasing the large bubble hold-up (98% increase) (Figure 5.27) as per Equation 3.82. Finally, the increased large bubble hold-up brings about a rise in the large bubble axial dispersion coefficient which is detrimental to syngas conversion.

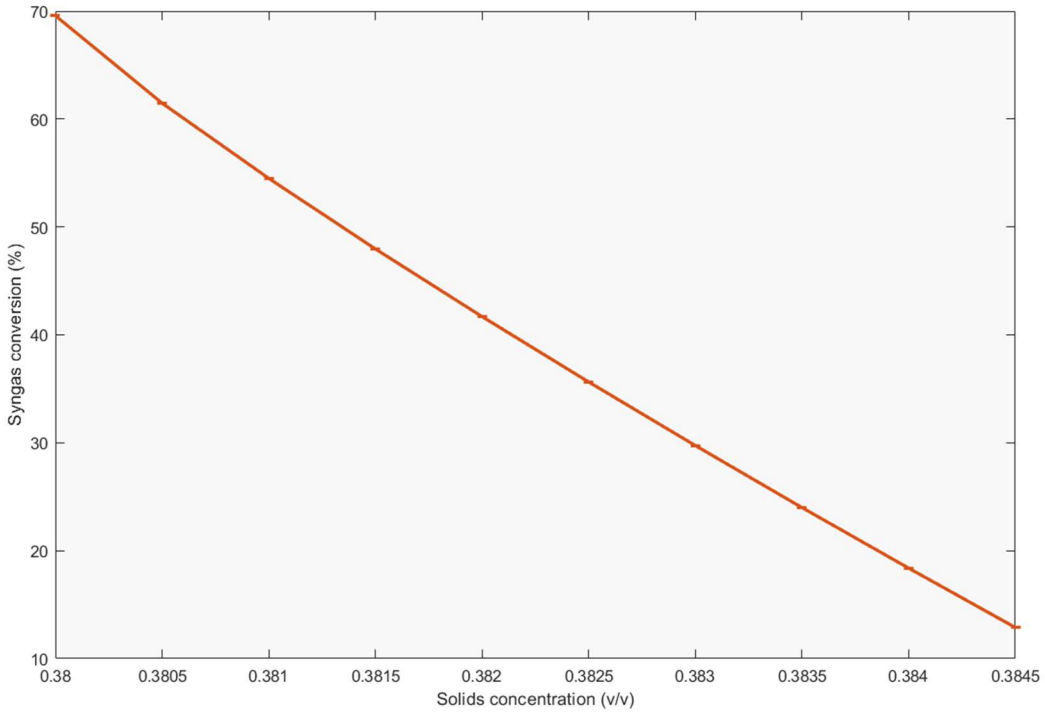

Figure 5.25: Effect of solids concentration on syngas conversion

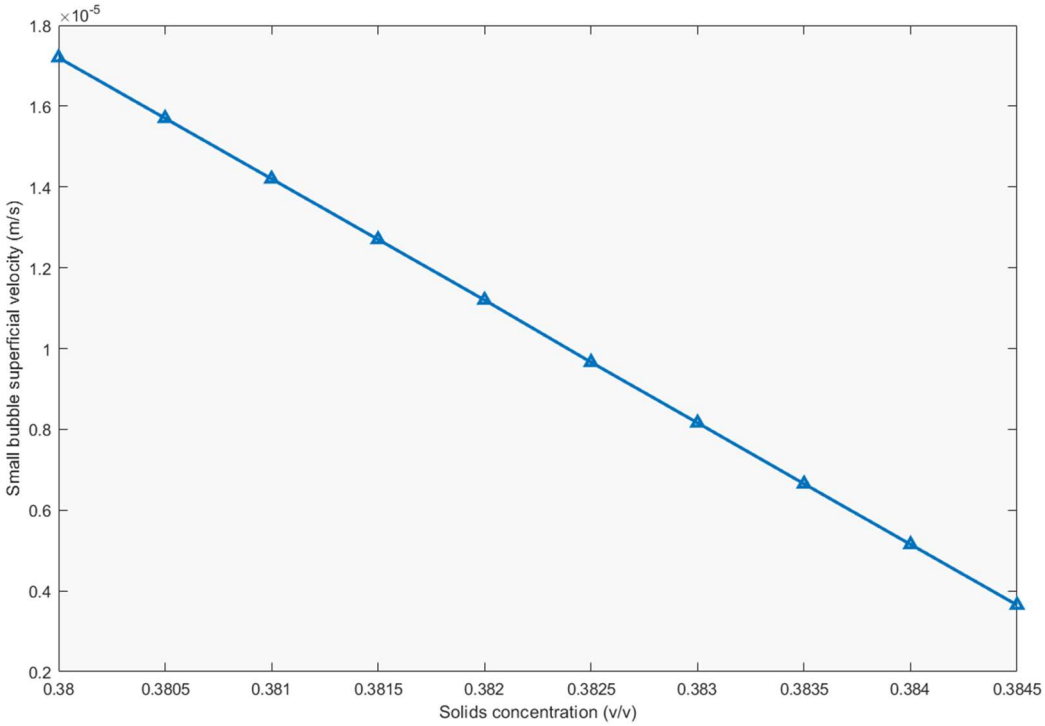

Figure 5.26: Small bubble superficial velocity as a function of solids concentration

Given a decreasing syngas conversion rate, a smaller superficial gas velocity reduction across the length of the microchannel will be realized such that as the solids concentration is increased, the final total superficial gas velocity at the outlet of the channel will increase from 0.001 m/s to 0.17 m/s as shown in Figure 5.28. This, along with the decrease in small bubble superficial gas velocity, will work towards increasing the large bubble hold-up which should further explain the reduction in syngas conversion as the solids concentration is increased (Figure 5.25). If the solids concentration is increased even further, the small bubble phase will be effectively decimated together with the small bubble superficial gas velocity and this should reduce the rate of large bubble hold-up increase (Equation 3.81) and consequently produce a slower increase in the large bubble axial dispersion coefficient. This will ultimately reduce the syngas conversion drop rate as can be seen at the higher solids concentrations in Figure 5.21.

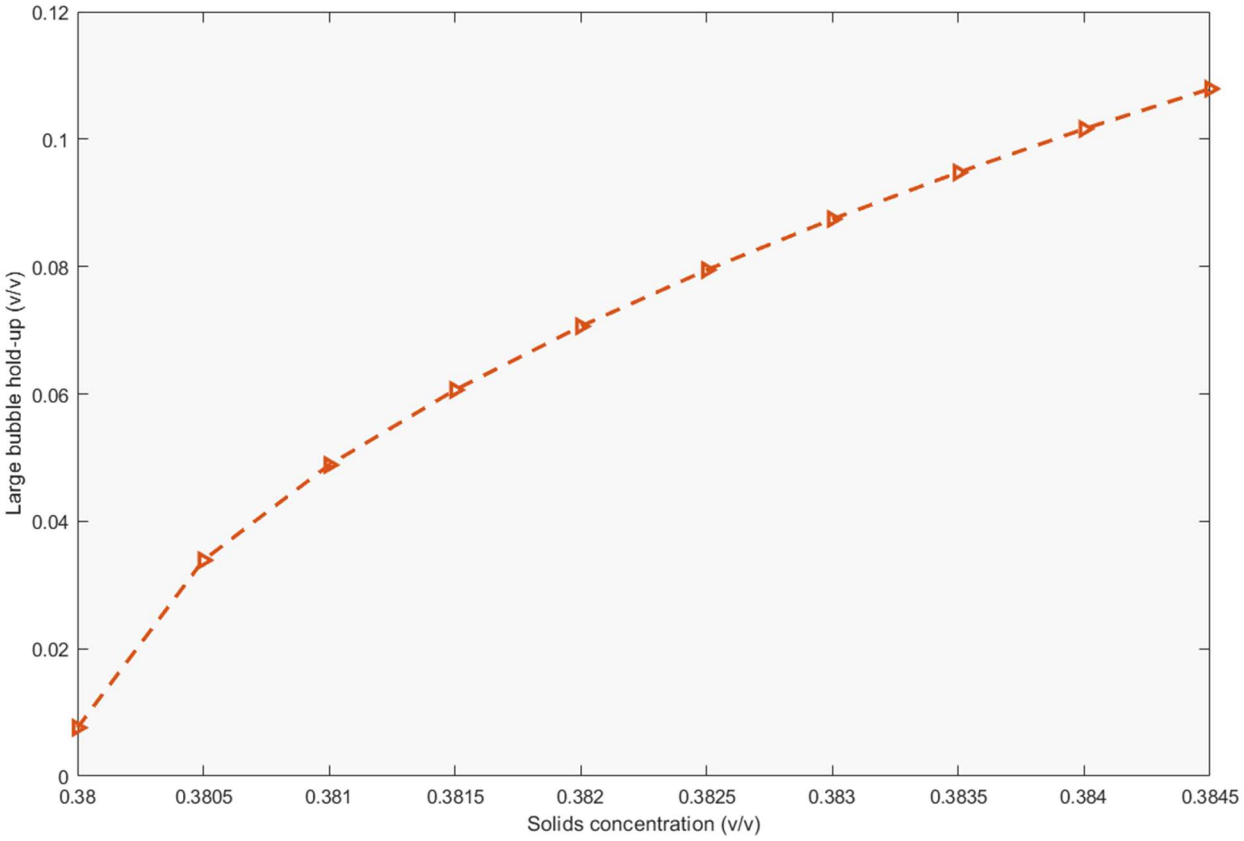

Figure 5.27: Large bubble hold-up behaviour with increasing solids concentration

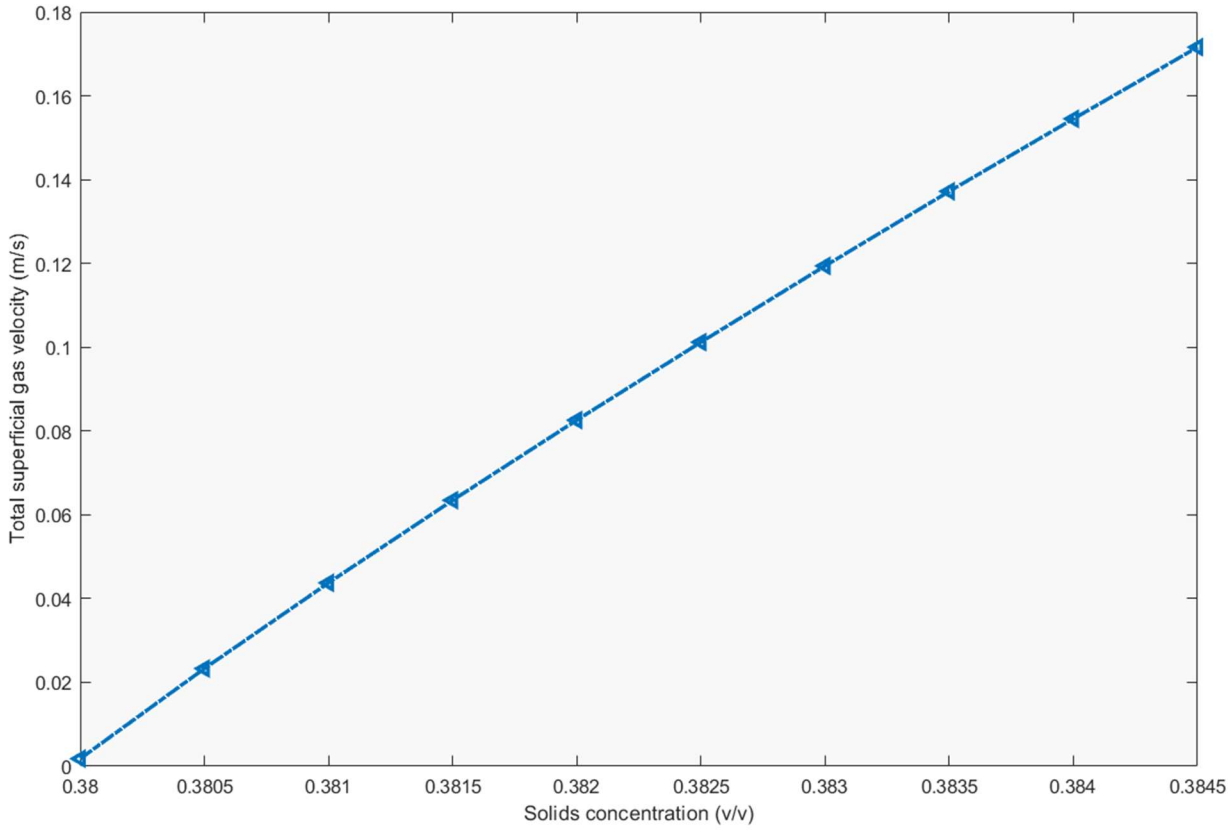

Figure 5.28: The total superficial gas velocity as a function of solids concentration

The falling sensitivity of syngas conversion to an increase in C_V will mean that more syngas should be available at the microchannel outlet so that there is a higher CO and H2 concentration at this point (Figure 5.29), a 200% and 133% increase respectively. These higher concentrations will allow a higher reaction rate. Given the rate at which the decrease in syngas conversion declines at the higher solid concentrations, the rate at which the reactant concentrations increase will also fall as seen in Figure 5.29, resulting in a decrease in the rate at which the reaction rate increases (Figure 5.30. This is perhaps more evident in Figure 5.24 where the rate of CO consumption is more dramatically affected at the higher C_V values to the point where this rate begins to not only stall but fall. This means that at such C_V values under the current operating conditions, any further increases begin to prove detrimental to the consumption rate and indeed the overall efficiency and performance of the microchannel reactor.

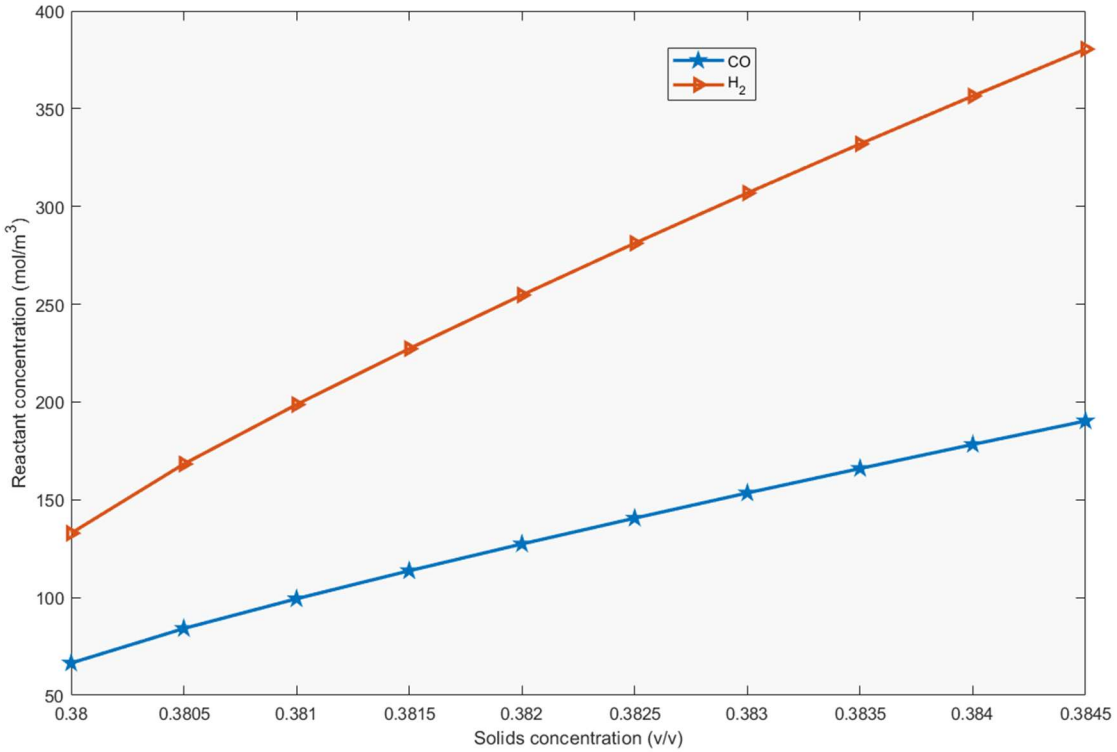

Figure 5.29: Gaseous reactant concentrations as a function of catalyst concentration

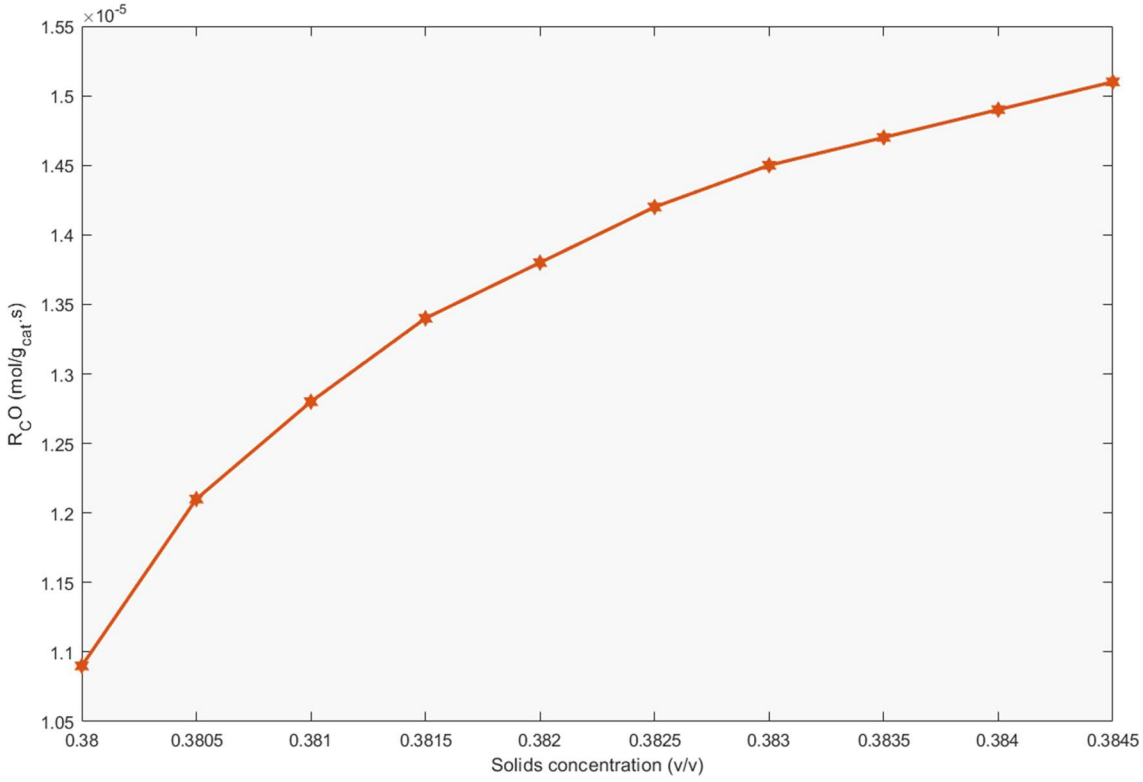

Figure 5.30: The rate of reaction as a function of solids concentration

5.2.2.4 Effect of temperature

Through its impact on the reaction rate and adsorption constants, the microreactor temperature will have a direct impact on the reaction kinetics. Increasing the microreactor temperature (470 K to 515 K) will increase the reaction rate constant and reduce the adsorption rate constant. The decrease in the adsorption rate constant is because of the exothermic nature of this adsorption process such that an increasing temperature will reduce the adsorption rate. The net effect was found to be that of an increase in the overall reaction rate indicating the dominance of surface reactions over the adsorption process.

The temperature inside the microreactor will also have an influence on the physical properties of the liquid phase including the density, surface tension and viscosity which will in turn influence the small bubble superficial gas velocity. With increasing temperature, the net effect is that of an increasing small bubble superficial gas velocity, with an increase of 36% (Figure 5.31). The small bubble phase superficial velocity has an influence on the large bubble hold-up which in turn influences the large bubble axial dispersion coefficient. The above-mentioned relationships between the temperature and large bubble hold-up (Figure 5.32) and temperature and large bubble axial dispersion coefficient (Figure 5.33) are shown below. It is clear then, that through its influence on the physical properties of the liquid phase, the temperature inside the FT microchannel reactor is important in characterizing the fluid dynamics therein.

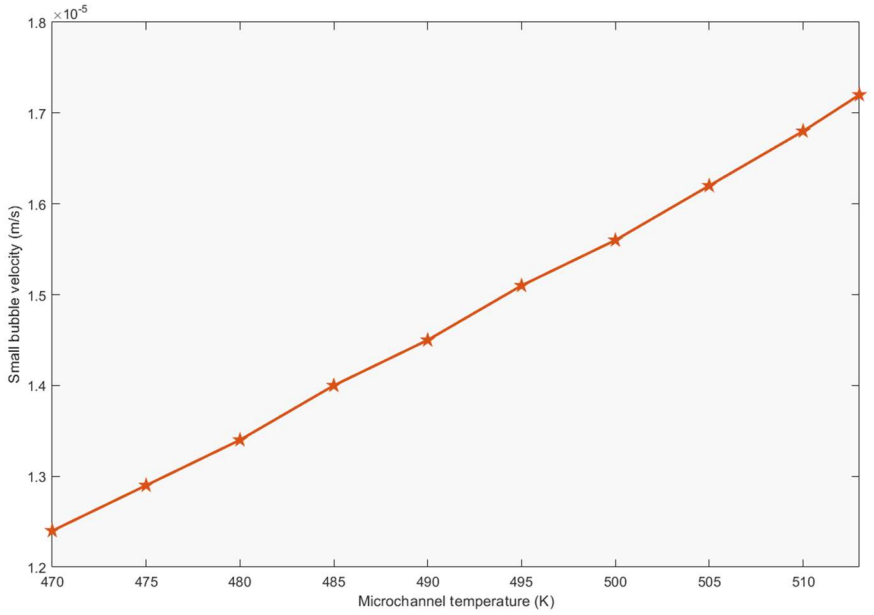

Figure 5.31: Effect of temperature on the small bubble phase superficial velocity

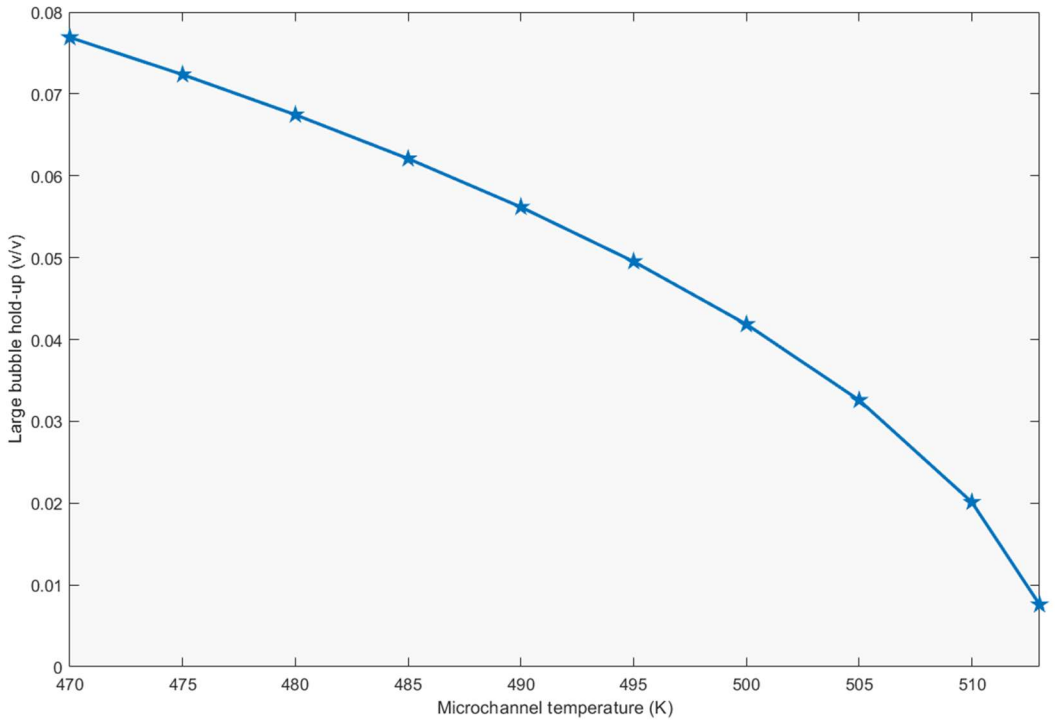

Figure 5.32: Effect of temperature on large bubble hold-up

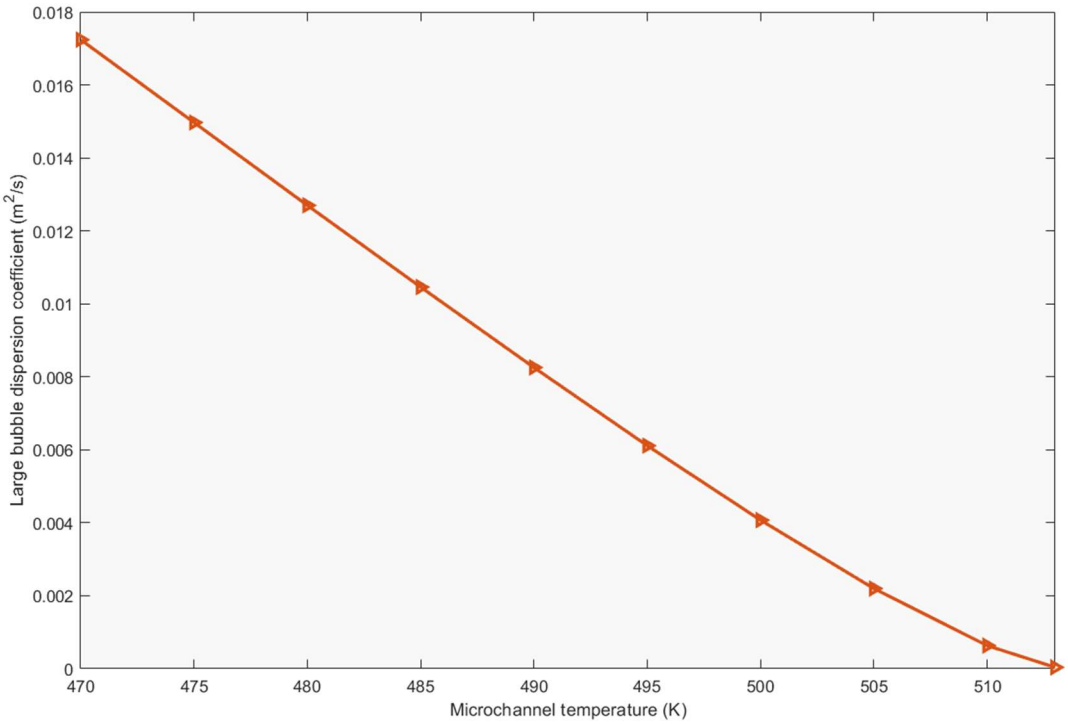

Figure 5.33: Effect of temperature on the gas phase dispersion coefficient

The overall effect of an increase in kinetics and a decrease in the gas phase dispersion coefficient as the microreactor temperature is increased is that of an increase in the syngas conversion as can be seen in Figure 5.34. Over a temperature increase between 470 K and 513 K, syngas conversion increases by 46.6%.

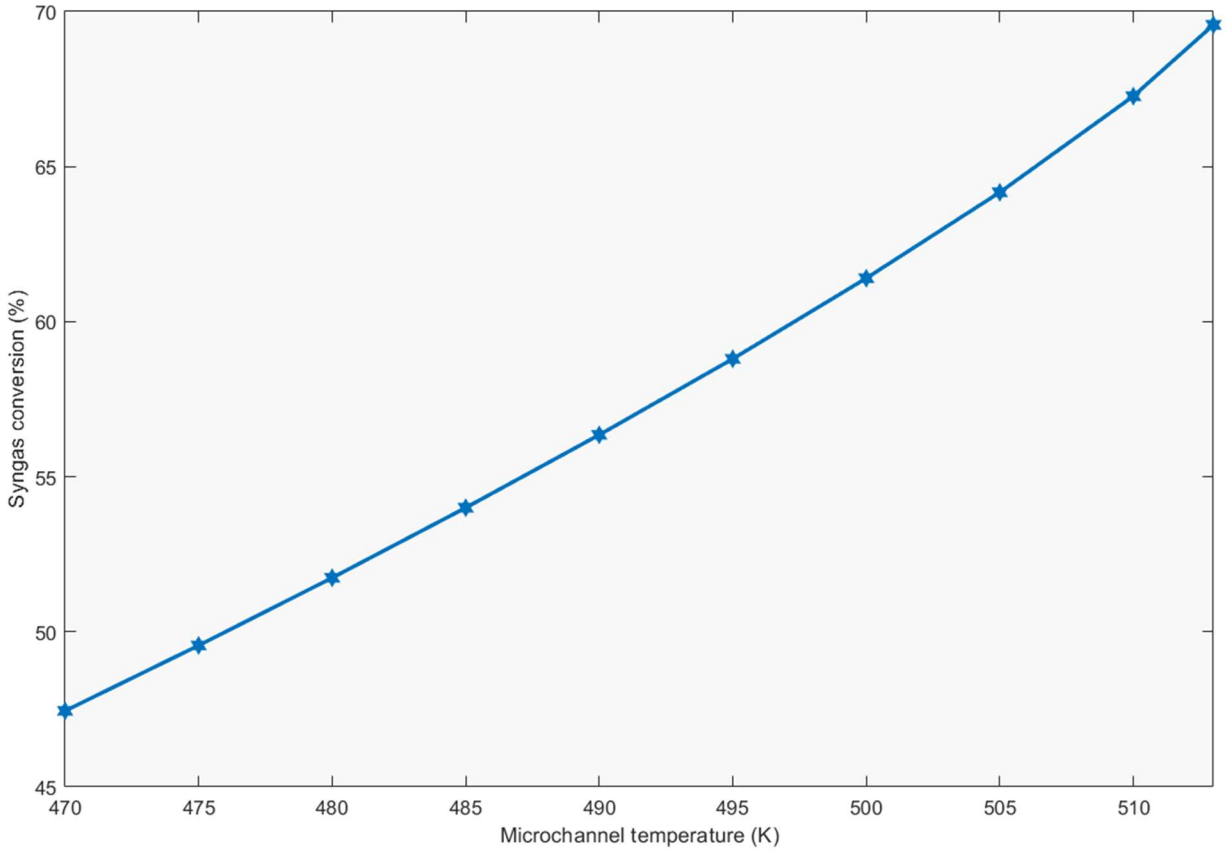

Figure 5.34: Effect of temperature on syngas conversion

5.1.4 Conclusion

In this chapter, the fate of the FT microchannel reactants and in particular CO, were analyzed across the length of the microchannel. Using a 2-bubble size bubbly flow approach, the rate of CO consumption in the gas phase was determined to be the most effective way of analyzing this particular system. It was determined that two key parameters primarily influence the performance of the microchannel reactor including the total superficial gas velocity and the axial dispersion, particularly in the gas phase. An increase in the superficial gas velocity was found to enhance axial dispersion in both liquid and gas phases and increase large bubble hold-up resulting in the net effect of a reduced syngas conversion. It was also determined that an increase in the microchannel

diameter resulted in an increase in syngas conversion through its obvious effect on residence time but also indirectly through its influence on the dispersion in the large bubble compartment primarily.

The solids concentration was found to enhance the syngas conversion up to a point, beyond which the effect of the decreasing small bubble hold-up outweighs the improved reactant consumption rate. This is an interesting observation given its counter-intuitive nature where continually increasing the solids loading would expectedly likewise continually improve the reaction kinetics but this has a limit and in the current scenario the limit is a loading of 0.3825. Increasing the temperature was found to improve the reaction kinetics and reduce the large bubble axial dispersion which had the net result of improving the kinetics.

5.2 Model Validation

It is important to analyze the accuracy of the developed model in predicting the performance of the micro reactor. Ideally, an experimental exercise would be undertaken wherein the conditions are as close as possible to those being simulated from the model. Given that the focus of this work was primarily on model development of this new reactor type, it was deemed beyond the scope of the current study to undertake experimental tests with laboratory microchannels. As a result, the results of the current model will be validated against, as much as possible, similar physical experimental results from various authors. This should give a good appraisal of the model's robustness and flexibility and its ability to be useful for various applications including simulations, designing and detailed micro-FT reactor studies.

5.2.1 Variable length FT Microchannel Reactor Study

5.2.1.1 Experimental Set-up

Deshmukh et al. (2010) carried out experiments in microchannels to prove the applicability of FTS in microreactors. The authors experimented on four variations of microchannels including 1 short and 2 long reactor types as well as pilot scale set-up with multiple channels. A H_2/CO ratio of 2, an inlet pressure of 350 psig, temperature of 210 °C and a catalyst contact time of 290 ms (milli seconds) were the conditions adopted throughout all the tests. The short channel had a characteristic gap of 1 mm and a width of 0.8 cm with a 3.8 cm long catalyst bed in the center of a 7 cm long process channel. A high cobalt loading catalyst from Oxford Catalysts, Ltd. (OCL)

was used in this short microchannel as well as in all the other microchannel configurations. The catalyst bed was placed between 2 beds of inert SiC particles at either end in an attempt to regulate the feed temperature of the syngas. It is not clear why the SiC was placed downstream of the catalyst bed.

The first long microchannel (Long A) had a characteristic gap of 1mm for two thirds of the length of the channel with the rest of the length at a gap of 0.5 mm. The channel had a width of 0.6 cm and catalyst bed height of 61.6 cm. A SiC bed was placed upstream of the catalyst bed to preheat the syngas feed to reaction conditions. The second long microchannel (Long B) is identical to the first, with the only exception being a uniform characteristic gap of 1mm throughout the entire length of the channel. All the aforementioned channels were cooled using a Marlotherm SH oil in 2 cooling channels flowing concurrently on either side of the channel.

The pilot scale reactor setup was made up of 276 microchannels with each channel having a characteristic gap of 1 mm and width of 0.3 mm. Each of the channels had a SiC bed of 1.9 cm in length upstream of the catalyst bed which took 17.1 cm of the entire channel length. 132 cooling water channels were attached to either side of the process channels in a crossflow configuration (Figure 5.35).

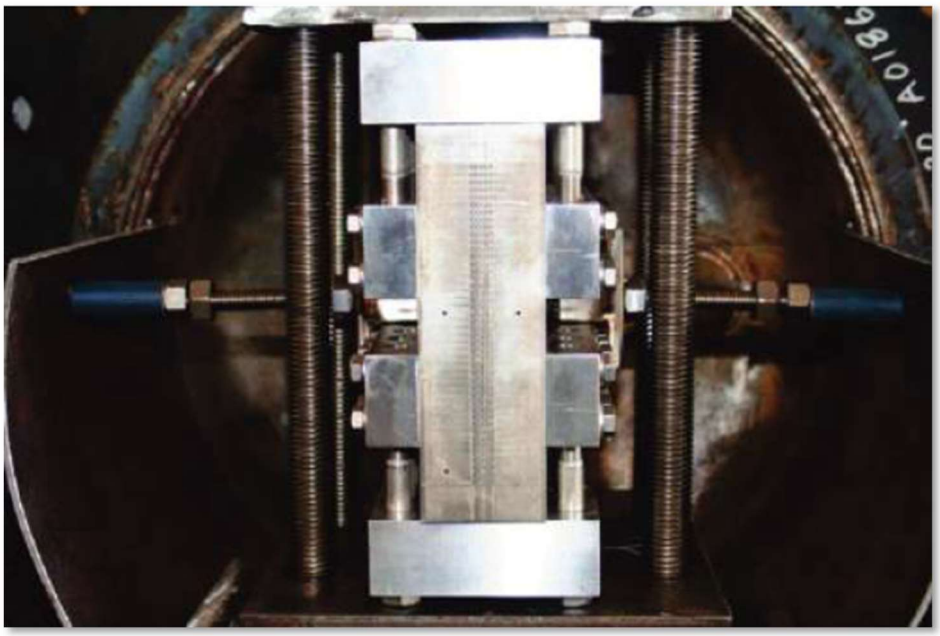

Figure 5.35: Pilot scale micro FT reactor system with 276 process channels and 132 coolant channels (Deshmukh et al. (2010)

5.2.1.2 Results

The performance results from the authors' tests showed a consistent CO conversion throughout the single channel and pilot multichannel set-ups at just over 70% (Figure 5.36). These results are comparable to the model results realized in the current study under the conditions given in Table 3.6 and Table 3.8. Under these conditions, a CO conversion of 69.56% was achieved as shown in Table 5.3 where the CO conversion profile over the channel height is illustrated. While the model microchannel had a slightly higher characteristic dimension at 3 mm, the channel length modelled was similar to the short experimental channel at a length of 1 cm. Comparison of the short channel and model performance results shows very good agreement with respect to CO conversion.

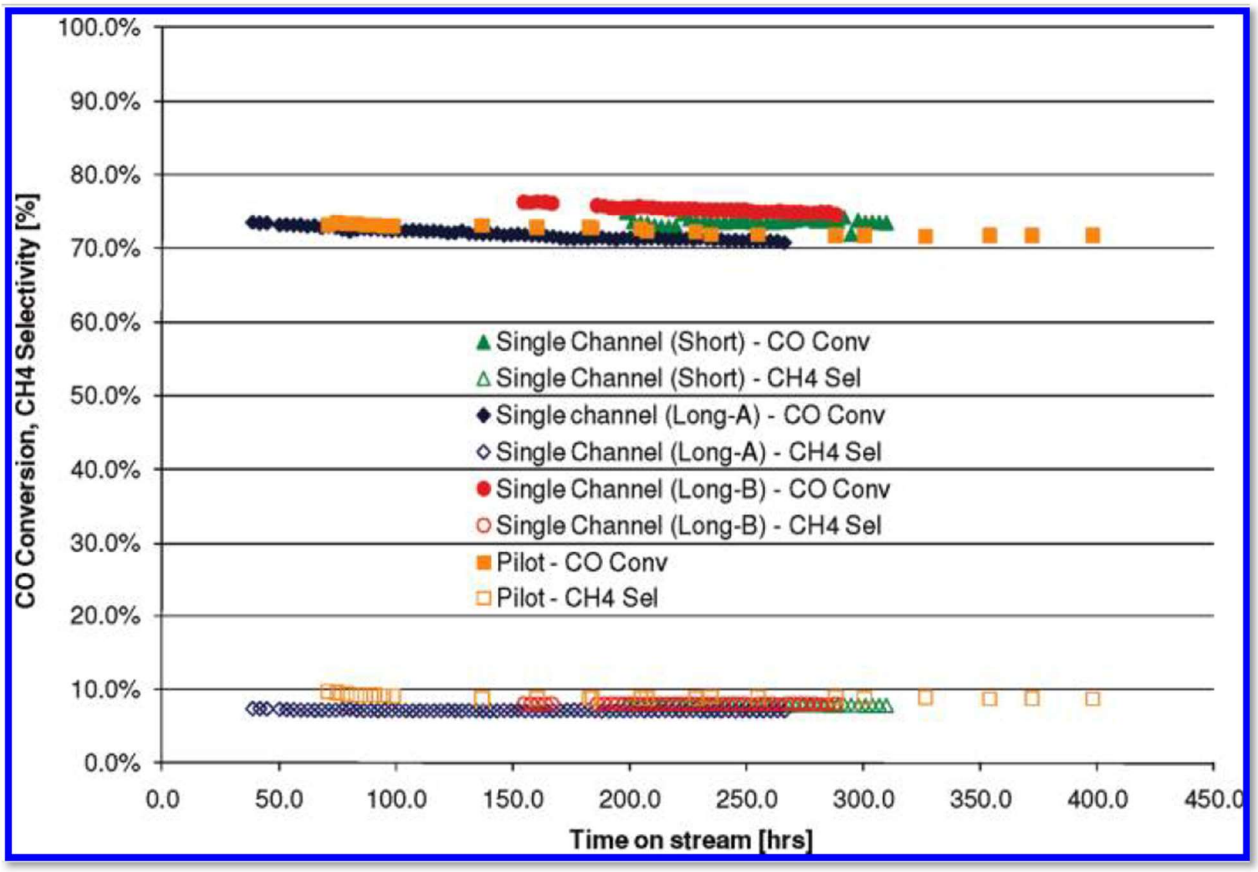

Figure 5.36: CO conversion and CH4 selectivity results over an extended test period (Deshmukh et al., 2010)

5.2.2 Powdered $Co/Re\text{-}Al_2O_3$ catalyzed Microchannel FTS study

5.2.2.1 Experimental set-up

Jarosch et al. (2005) studied FTS in a microchannel reactor using a powdered $Co/Re\text{-}Al_2O_3$ catalyst with Co to Re molar ratio of 21:1. The authors employed a microchannel with a characteristic gap of 0.51 mm, width of 1.27 cm and a total length of 8 cm. The catalyst bed was 2.5 – 3 cm long supported on either side by quartz wool to retain the particles in place. The reactor was operated under steady conditions of 225 - 250 °C, 21 -41 atm, and a contact time of 288 to 305 ms.

5.2.2.2 Results

The performance results from the authors' study are shown in Figure 5.37. It is evident that the CO conversion remained relatively constant at around 70% over the test period. This is comparable to the results obtained in the current study as shown in Table 5.3. As mentioned earlier, the current study conditions produce a CO conversion of 69.56% which is very similar to the experimental results achieved by Jarosch et al. (2005). While the experimental characteristic gap is smaller than that in the current model conditions, the current modelled channel achieves the same CO conversion with $1/8^{th}$ of the experimental channel length. This vast difference in performance can be attributed to the catalyst type and by extension the kinetics selected in the current modelling exercise where a Co/MgO catalyst supported on SiO_2 catalyst was employed which is more active.

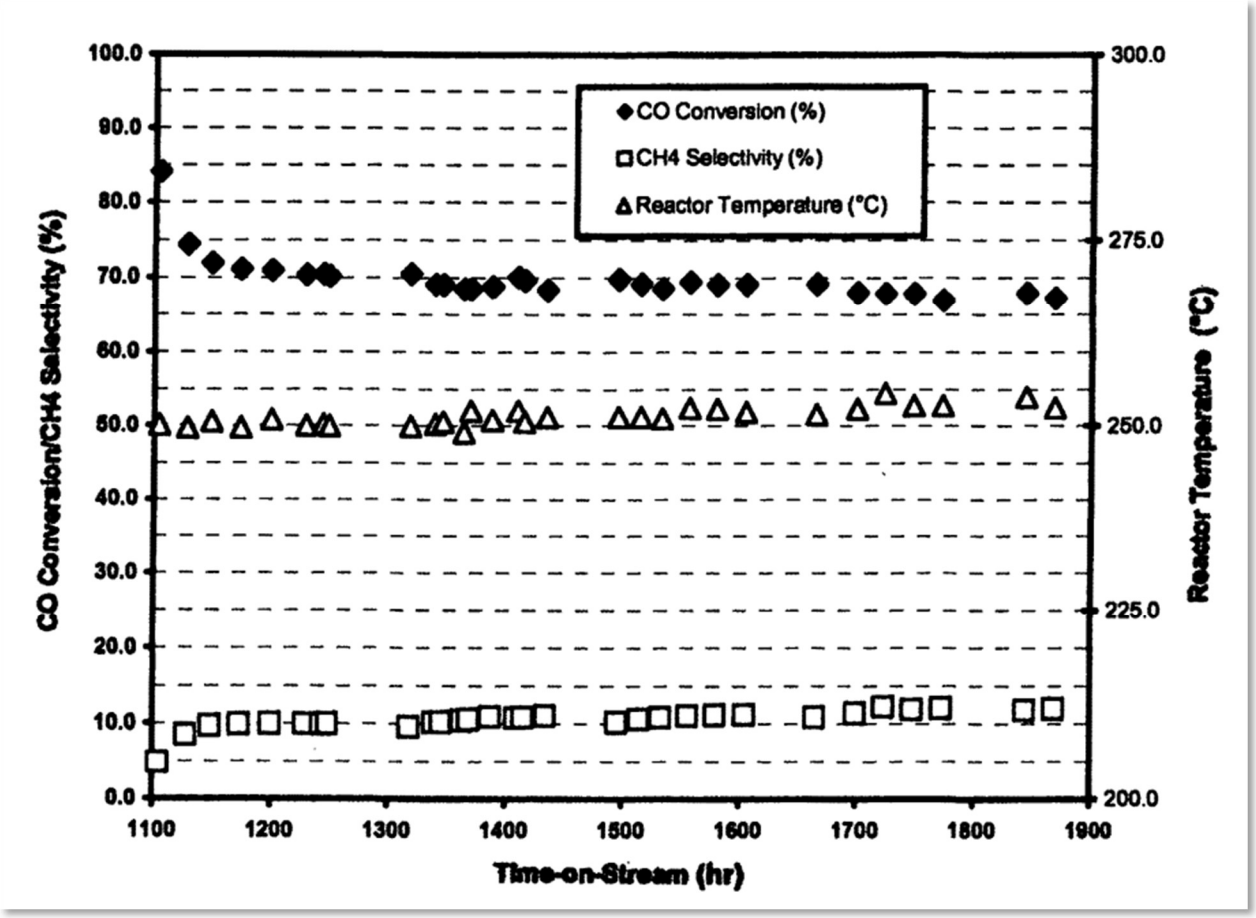

Figure 5.37: CO conversion, CH_4 selectivity and reactor temperature profiles form the FT microchannel test run (Jarosch et al, 2005)

5.2.3 Microchannel FTS under Cross-flow Oil-cooled Condition Study

5.2.3.1 Experimental conditions

Cao et al. (2009) studied intensified FTS in a microreactor channel. The authors tested a variety of operating conditions including a H_2/CO ratio between 1 -2.5, pressures between 10 -35 atm, temperature of 235°C and GHSV up to 60000 h^{-1}. The reactor was constructed with a 0.588 mm characteristic gap, 12.7 mm gap and a length of 37.3 mm with 0.2 g of catalyst in different sizes to test the effect of particle size on performance. The channel was flanked on both sides by oil filled cooling channels configured to flow cross-currently to the process channel. An illustration of the microreactor assembly is shown in Figure 5.38.

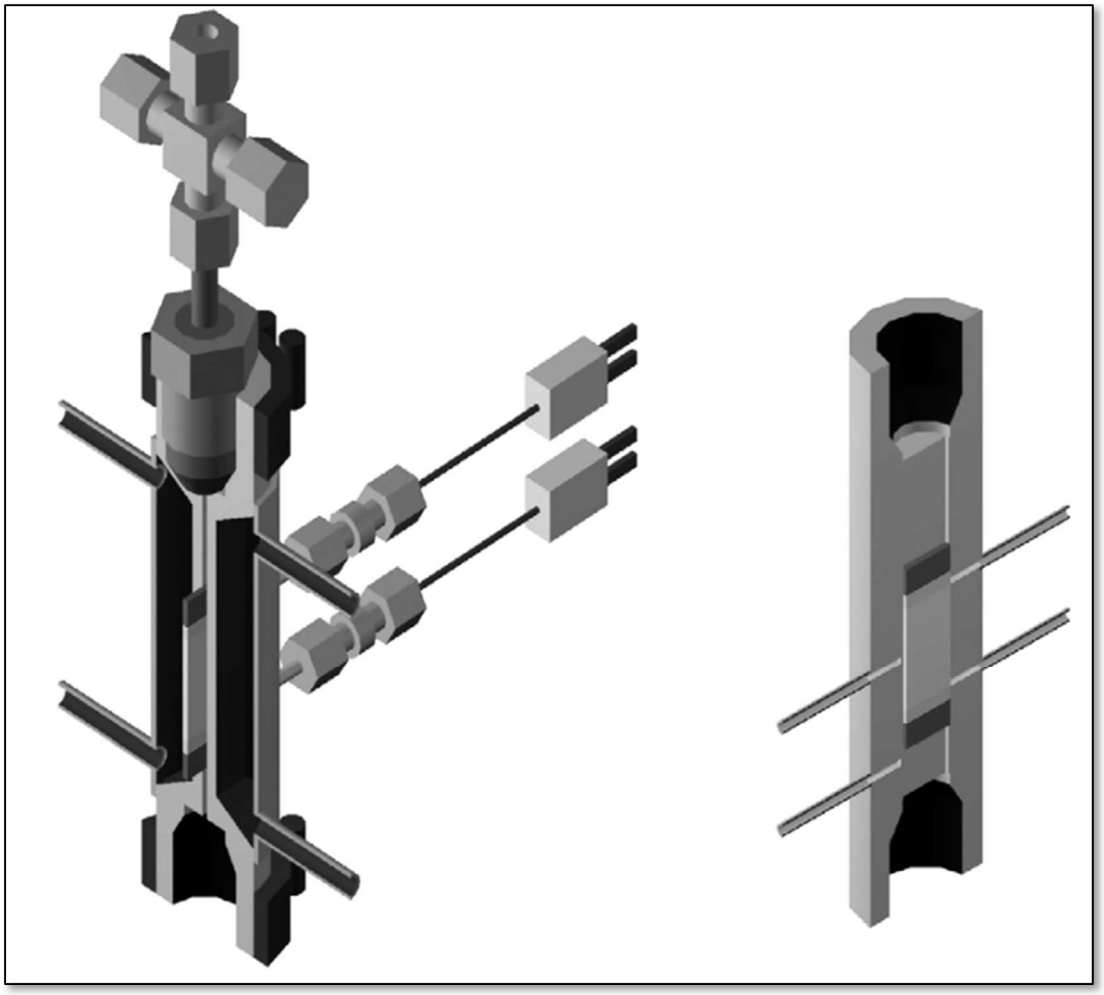

Figure 5.38: Illustration of the microreactor assembly used in the study by Cao et al. (2009)

5.2.3.2 Results

The authors used a 30 wt.% Co/4.5 wt.% Re/g-Al_2O_3 in two different sizes (45 and 150 µm) and it was the smaller 45 µm catalyst particles that achieved a higher CO conversion of 76.8% versus the 62.6% conversion realized with the larger 150 µm catalyst particles. These performance values were achieved at GHSVs of 20016 and 22886 h^{-1} for the 150 and 45 µm particle sizes respectively. While the flows used in these tests are relatively low compared to the ones used in the current modelling exercise, it is clear that the smaller catalyst particles produce the highest and closest CO conversion results to the ones obtained in the current study. At higher, more comparable space velocities of 60 000 h-1 (Figure 5.39), the authors realized lower CO conversions at around 63%, which is lower than what was realized in this current study at higher velocities. These

discrepancies, albeit slight, can be attributed to the difference in catalysts and kinetics realized between the authors' experimental process and the current study. The catalyst selected in the current study may be more active and thus produce better single pass conversion results. It is notable though that the discrepancies between the two studies are minimal which should provide a sufficient level of confidence in the accuracy of the current model.

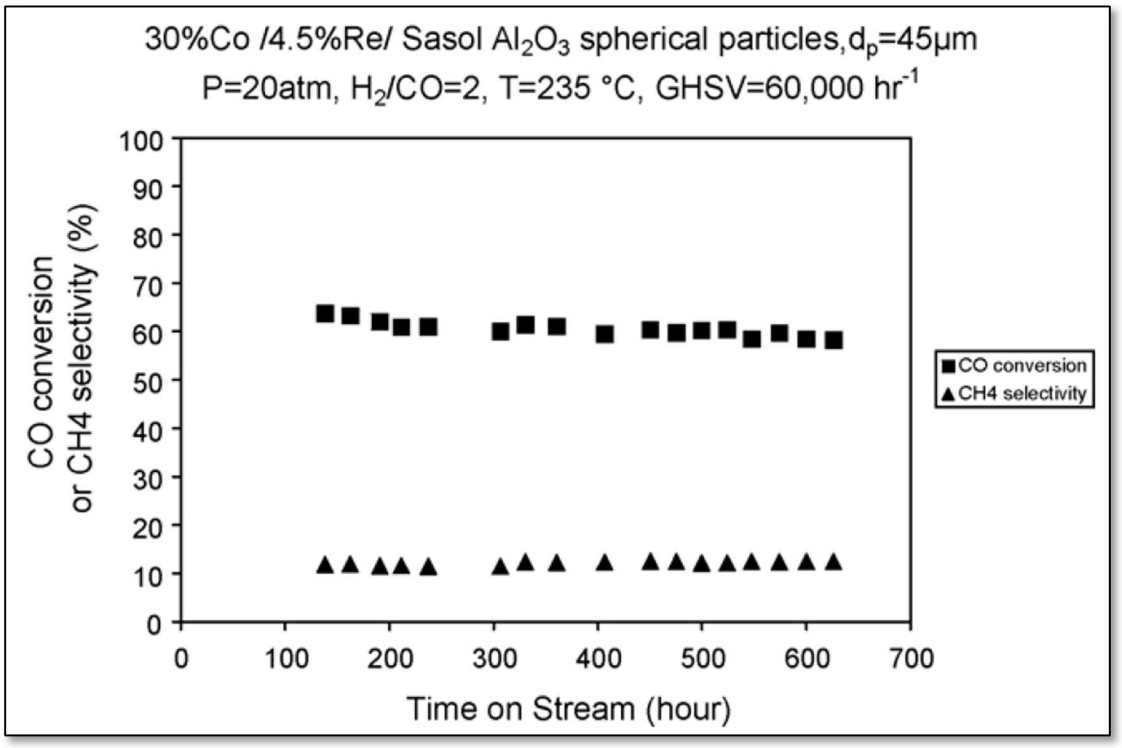

Figure 5.39: CO conversion and CH_4 selectivity results from study by Cao et al. (2009) throughout a 650 hour TOS.

5.2.4 Milli-structured fixed bed FT reactor study

5.2.4.1 Experimental Conditions

Knochen et al. (2010) studied FTS in a milli-structured fixed bed reactor under the conditions given in Table 5.4. The authors used a cylindrical channel which, while different to the rectangular shape being considered in the current study, should not be enough to disqualify the use of the authors' data for validation. Also different is the superficial gas velocity being considered by the authors which is an order of magnitude lower than the one selected for the current model.

Table 5.4: Experimental conditions from Knochen et al. (2010) versus the conditions being considered in the current study

	Value		
Condition	**Unit**	**Current study**	**Knochen et al.(2010)**
Temperature	°C	240	196 - 222
Pressure	bar	20	21 - 26
H_2/CO	-	2	2
Characteristic gap	mm	3.5	1.753
Width	mm	3.55	-
Length	mm	0.01	1500
Catalyst bed length	mm	-	1000
Superficial gas velocity	m/s	0.3	0.012 – 0.053
Catalyst type	-	Co/MgO catalyst supported on SiO_2	19 wt.% Co and 1% Re on γAl_2O_3
Cv	(v/v)	0.3	0.3

5.2.4.2 Results

The authors (Knochen et al., 2010) varied the temperature and measured the effect on CO conversion, pressure drop and liquid hold-up as can be seen in Figure 5.40. A maximum CO conversion of 75% was realized under the conditions described above. This value is close to the 69.56% CO conversion that was obtained in from the current simulation albeit under higher gas velocities as described in the preceding paragraph. All other operational parameters are comparable except for the much longer catalyst bed and reactor overall reactor length used in the cited authors' study. This does not, though, mean that there is more catalyst available for reaction because the larger catalyst mass is countered by the higher volumetric flowrate necessary to achieve the 0.3 catalyst loading. The main differentiator should instead be the type of catalyst used which will have a different density but more importantly will give effect to different reaction kinetics. Despite these differences the performance results between the current simulation and the study by Knochen et al. (2010) are comparable enough to justify a good level of confidence in the accuracy of the developed model.

By comparing the simulation results of the current model with experimental results from similar studies available in literature, sufficient accuracy of the model has been demonstrated. While there are discrepancies in the results between these considered studies and the model results from the current study, the differences were expected and within reason given the unavoidable variations of process conditions and assumptions inherent in the studies. Instead of attempting to develop a model capable of describing all conceivable variations of micro-FTS, which while possible would require significant resources, the aim here was to gather insights into the workings of the micro-FT reactor and how this new technology can unlock thus far untapped energy resources. Limited to this purpose, the validation exercise undertaken in this section should suffice in giving the reader the confidence that the model is fairly robust and accurate, so that the reader can confidently consider the ideas put forward in this work without concern over their validity or at least over the validity of the underlying model architecture.

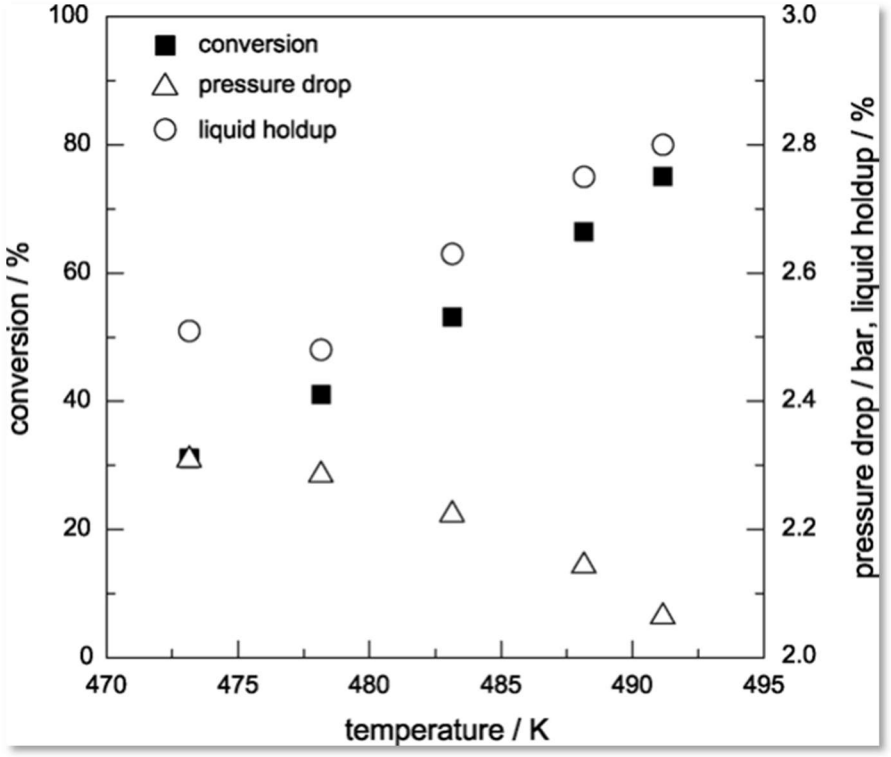

Figure 5.40: CO conversion, Pressure drop and liquid hold-up measured against reactor temperature as studied by Knochen et al. (2010)

5.2.5 Conclusion

In this chapter, the simulation results from the developed model were compared with those from literature experimental results under similar conditions in order to verify the model's accuracy. The results from the model were found to reasonably agree with those from various literature sources which should serve to validate the accuracy and dependability of the model in dealing with systems of a similar nature. As such, this model can be used for a variety of important activities including the design and/or simulation of an FT microchannel reactor system and to run optimization exercises with minimal costs. The model can also be used for studying and training purposes where the workings within the FT microchannel reactor, as detailed within the model, can be analyzed and used as a tool to train and upskill interested parties which may include engineers, researchers, technicians and indeed operators.

5.3 Economics Evaluation

Having analyzed the technical aspects of employing microchannel FT reactors for the production of synfuels, it is equally important to assess the economics of such an application. The FT Microreactor will have to operate in the wider context of a complete mini-XTL plant so that the economics cannot simply be limited to the reactor itself. To this end, the economics discussed in this chapter will focus on the whole plant including the syngas production, cleaning, conditioning and finally its conversion to syncrude in the FT microchannel reactor. This will be the scope of the economic evaluation exercise. Furthermore, the economic analysis will be limited to the plant capital and operational costs associated with producing a unit of product from the mini-XTL plant.

5.3.1 Literature Review

The economic models for mini-GTL plants incorporating microchannel FT reactor technology are not readily available in literature. LeViness et al. (2011) discusses the potential advantages of mini-GTL plants over conventional large-scale plants. The authors points out the economic advantages of microchannel FT reactors due to their significantly greater heat and mass transfer rates. The resulting efficiency gain enables the application of microchannel FT reactors in smaller scale installations. Combined with the use of high activity catalysts, microchannel FT reactors exhibit over 16 times the productivity of conventional fixed bed and slurry reactors (LeViness et al., 2011) as shown in Figure 5.41. The authors mention biomass to liquids (BTL) and off-shore GTL

processes as suitable applications for this technology, wherein syncrude, instead of unprocessed natural gas or biomass, can be transported to central refineries in a more cost-effective way.

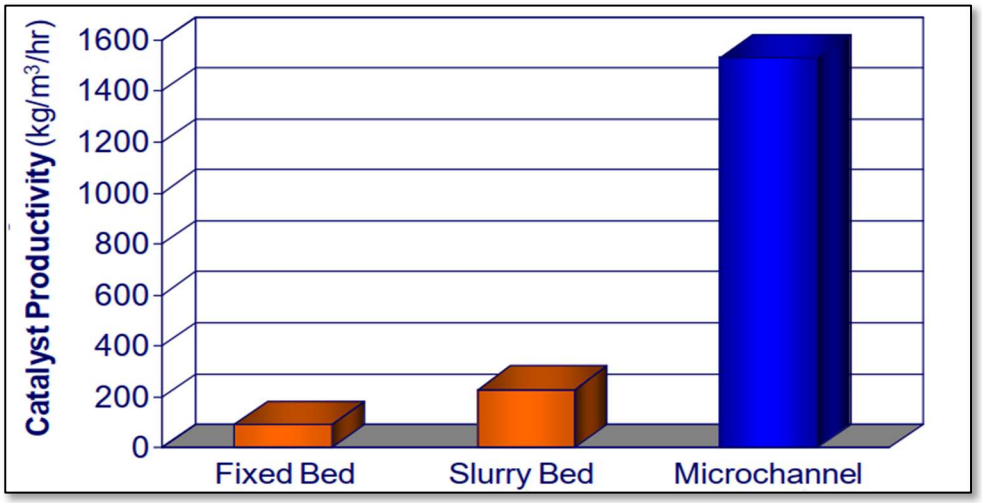

Figure 5.41: Comparison of catalyst productivity between the FT microchannel, fixed and slurry bed reactors (LeViness et al., 2011)

Jarosch et al. (2005) completed a study on the economics of a 30 000 bpd microchannel FT-based GTL process plant accounting for the capital costs using both ISBL and OSBL estimates. The authors developed a proprietary cost model which is different from those models used for conventional plants and shows a lower capital cost per barrel produced. Figure 5.42 shows the capital cost/bpd for the microchannel reactor compared with that of conventional reactors and it is clear from this model that the mini-GTL plant capital costs are consistently lower at the smaller plant capacities. The authors report that mini-GTL plants are more competitive at production rates below 30 000 bpd although it is clear from Figure 5.42 that the microchannel GTL plant remains competitive even at higher capacities up to 100 000 bpd. Whilst the authors calculated the capital cost of the microchannel GTL plant, the operating costs were not accounted for.

These results clearly show the advantages that microchannel FT technology can provide including the exploitation of stranded and associated natural gas, municipal solid waste (MSW) and construction and demolition waste (CDW) where it would be simply economically impractical to employ large scale XTL plants.

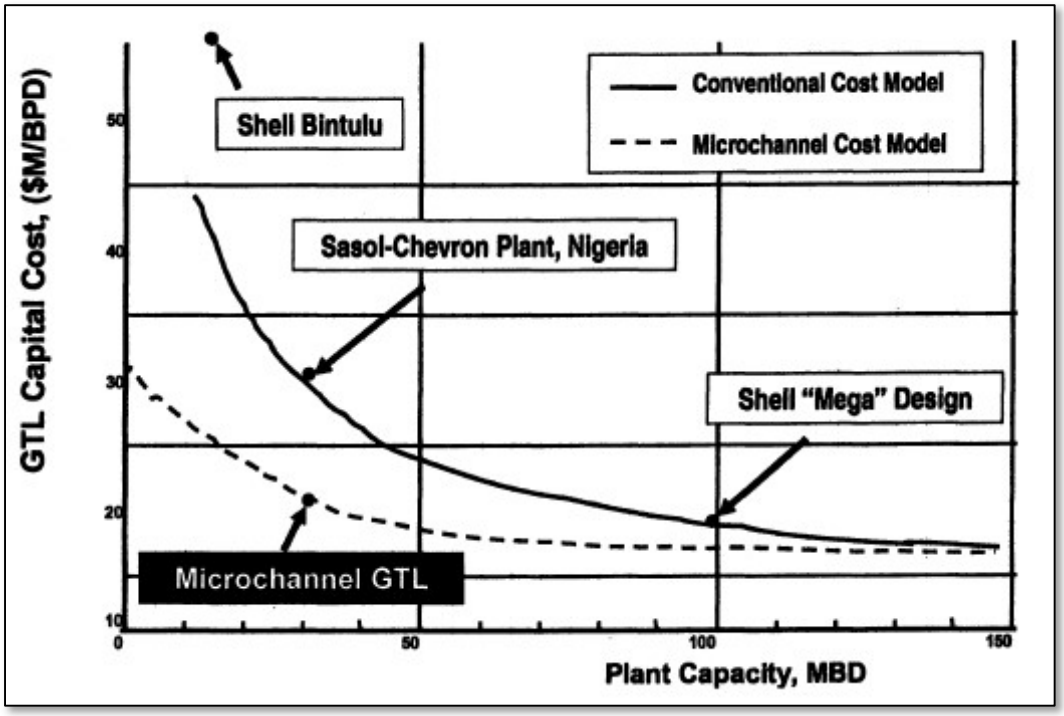

Figure 5.42: Capital cost comparison between microchannel GTL and conventional GTL plants (Jarosch et al., 2005)

5.3.2 Economic model

As was previously mentioned, the success and widespread adoption of the FT microreactor technology depends on its cost effectiveness when employed in a mini-XTL plant. As a matter of fact, the business case for the mini-XTL plant is its ability to process relatively low-volume carbon resources economically. It can be argued that this business case can only be supported if the problem of plant scale and efficiency can be adequately dealt with. To do this effectively, the construction costs per unit equivalent crude oil barrel (cost/bpd) has to be at least similar if not better than that of large-scale plants even when considering low-volume resources. This was illustrated by Jarosch et al. (2005) in the study discussed above where the cost/bpd was better than that of several large-scale GTL plants, even more so at the lower plant capacities. The economic analysis by Jarosch et al. (2005), while promising, does not offer any details regarding the break-down of these costs – what is known is that the focus was only on capital costs with the operational cost excluded. In this section, a high-level economic model with enough detail to allow the reader to get a sense of the relevant factors contributing to a cost estimate of a mini-GTL plant will be developed.

5.3.2.1 Plant set-up

Before the economic model can be developed, it is necessary to lay out the plant set-up and conditions on which the model will be based. The plant in question is a mini-GTL plant using associated or stranded natural gas as a resource (see Figure 5.43). The plant will operate under LTFT conditions and be geared towards the product of middle distillate and higher carbon chain products including diesel and wax. The battery limits of the plant will be from the feed to the production of syncrude from the FT reactor. It is expected that the syncrude will be transported to existing crude oil refineries where it will be processed to final liquid and other products. A plant syncrude production capacity of 1000 bpd is envisioned which is in the low-volume range. These conditions are summarised in Table 5.5.

Table 5.5: mini-GTL plant conditions

Parameter	Description
Plant type	LTFT
Target Products	Middle Distillates
FT Reactor	FT microchannel
Capacity	1000 bpd
Feedstock	Associated or stranded natural gas

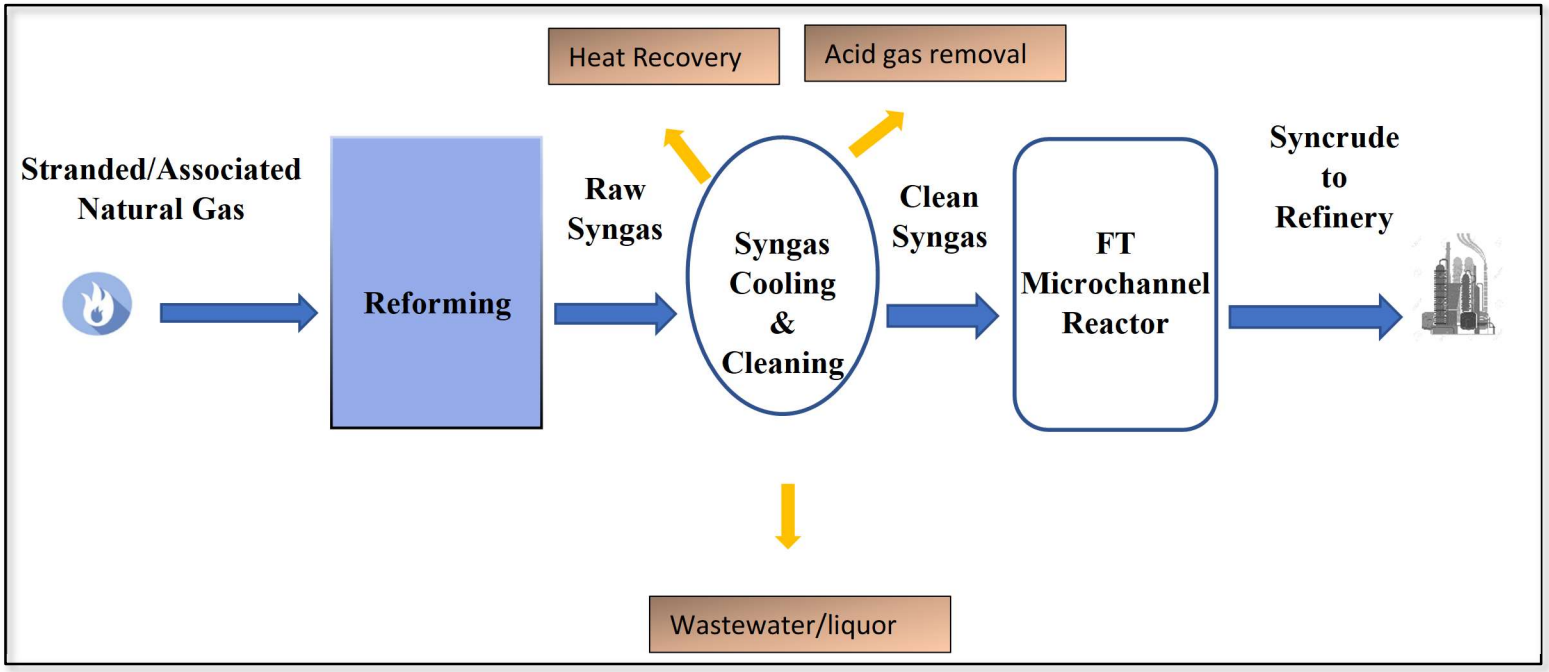

Figure 5.43: Illustration of a mini-GTL plant

5.3.2.2 Model assumptions

The following assumptions were made in developing the current economics model:

- The plant is located in South Africa
- Costs will be based on the South African Rand (ZAR)
- Economic climate will remain constant over the duration of the engineering, procurement and construction (EPC) process
- Sufficient feedstock will be available over the life of the plant
- Market demands will meet the supply of all products produced

5.3.2.3 Capital Cost Estimate

Given the lack of reliable public models for not only mini-GTL but for mini-XTL plants in general, the strategy used in this report is that of adapting existing large scale GTL economic models for use in a small-scale GTL plant. The work of Zennaro (2013) is instructive to this end given the level of detail provided in their modelling of capital and operational cost estimates of a 17 000 bpd SBCR-based GTL plant. Care will be taken to adjust the costs accordingly, taking into the account the relevant economies of scale. The economic analysis will include costs based on the costs of similar equipment in industry, cost data banks and estimates for similar plants in literature. The cost estimate will take the form of an engineering, procurement and construction (EPC) package as would typically be undertaken by constructors right up to the commissioning stage.

Based on the work of Zennaro (2013) and the typical cost/bbl ratio between large scale and microreactor-based GTL plants (Jarosch et al., 2005), a breakdown of the cost estimates was developed as shown in Table 5.6.

In Table 5.6, the capital costs are broken down according to the various activities that would have to take place to bring the plant online from initial planning and design to commissioning and start-up. Firstly, in engineering services, the main cost driver would be the hours spent by engineering personnel on the pre-determined work packages and deliverables. These will include among others the design, project management and procurement activities. Following the equipment specified in the engineering services phase would have to be supplied by the relevant suppliers. In this phase, the cost driver will be the equipment costs including spares. Once the relevant process plant equipment is supplied, the auxiliary equipment, infrastructure and materials would have to be

supplied including civil works materials, electrical and steel materials to name but a few. A complete list is given in Table 5.6. The costs of these bulk materials will be the main cost driver in this phase.

The cost of transporting the various goods and materials to site also has to be considered and this will include the cost itself, any necessary insurance taken out on the material being transported. Once all the process equipment and bulk materials have been supplied and checked, construction can commence. In this phase of the project, the main cost drivers will be the labour and all the necessary accommodations to be afforded to the respective personnel installing the supplied equipment and materials. These accommodations will include costs for the necessary heavy machinery to do the work, furnished offices and reasonable accommodation to name a few. During the commissioning phase, costs incurred would be towards the manhours of all required personnel to assist in the smooth erection of the plant and the commissioning. This is the last step considered for capex purposes before the plant begins operation and sustained production.

It will be noted from Table 5.6 that a large share of the capex would be spent on the cost of equipment (24%). This demostrates the crucial role that equipment costs play in GTL plant capital costs. Furthermore, the typical share of FT units in this cost is 24% (Zennaro, 2013), which is the highest. This is important in the context of this work precisely because the FT microchannel reactor put forward in this work is more efficient and should consequently be less expensive in cost/production terms, i.e., for a given plant throughput, a miniature microchannel reactor with its smaller size and scale-out capabilities will cost less. This means that a large portion of the equipment cost reduction between the 2022 cost data of the 17 000 bpd large scale GTL plant (Zennaro, 2013) and the more efficient 1000 bpd mini-GTL plant, from R9B to R355M, is due to the much cheaper FT microchannel unit. In total, there is a decrease in capital costs of over 95% as a result of not only the smaller scale of the mini-GTL but also because of the higher efficiency of the FT microchannel reactor-based plant. This increase in efficiency is demonstrated by the lower cost/bbl figure of R1.45M/bbl in the mini-GTL plant versus R2.18M/barrel in the large-scale plant. This is an increase of 33% in cost efficiency, a very promising figure in the context of the adoption of FT microreactor and indeed mini-XTL technology.

While care has been taken to ensure that the capital cost estimate data provided is relatively accurate, it is accepted that the real conditions in industry and the ever-changing economic climate

may lead to a significantly different estimate. It is apparent though, that there is a clear cost benefit to mini-XTL plants employing FT micro-reaction technology and that further analysis of the capital costs, given more access to information and data banks, may yield more insights.

Table 5.6: Capex Breakdown for a 1000 bpd mini-GTL plant

Package	TASK	Cost (Millions)				
		USD		ZAR		
		2013 (Zennaro, 2013)	2022 adjusted for inflation	2022	adjusted for efficiency	adjusted for size
1	**Engineering Services**	**133.00**	**151.87**	**2417.81**	**1611.88**	**94.82**
	Front-end engineering design					
	Detailed engineering					
	Management					
	Project control and administration					
	Quality assurance and HSE					
	Procurement					
2	**Equipment Supply**	**498.00**	**568.67**	**9053.17**	**6035.44**	**355.03**
	Air coolers					
	Blowers					
	Boilers					
	Capital spare parts					
	Catalysts					
	Chemicals					
	Columns					
	Compressors					
	Exchangers					
	Filters					
	Firefighting					
	Heaters					
	Laboratory equipment					
	Packages					
	Pumps					
	Reactor					

	Tanks					
3	**Bulk Materials Supply**	**369.00**	**421.36**	**6708.07**	**4472.05**	**263.06**
	Civil materials					
	DCS (distributed control system), ESD (emergency shut down),					
	FGS (fire gas system), BMS (burner management system), and MMS					
	(machine monitoring system)					
	Instrument equipment					
	Electrical equipment					
	Insulation materials					
	Paints					
	Piping, valves, and ladders					
	Steel structures					
	Telecommunications					
4	**Transportation**	**47.00**	**53.67**	**854.42**	**569.61**	**33.51**
	Transportation of materials offshore					
	Ocean freight					
	Transportation of materials onshore					
5	**Construction**	**830.00**	**947.78**	**15088.61**	**10059.07**	**591.71**
	Buildings (including necessary workshops, offices, canteens)					
	Civil and concrete					
	Heavy lift					
	Mechanical erections (equipment, piping, structure, and tanks)					
	Electrical/instrument/telecommunication erections					
	Painting and insulation					
	Work carried out at daily rates					
	Field running costs and temporary construction facilities					
	Assistance for commissioning					
6	**Erection Supervision**	**127.00**	**145.02**	**2308.74**	**1539.16**	**90.54**
	Expert EPC contractor personnel					
	International personnel					
	Local personnel					

	Vendors Personnel					
7	**Commisioning**	**35.00**	**39.97**	**636.27**	**424.18**	**24.95**
	Expert EPC contractor personnel **International personnel** **Vendor personnel** **Licensor personnel** **Training** **Licensor personnel** **Training** **Tools, chemicals, and consumables for precommissioning and commissioning**					
	Total	**2039.00**	**2328.33**	**37067.08**	**24711.39**	**1453.61**
	Cost/bbl	**0.12**	**0.14**	**2.18**	**1.45**	**1.45**

The operating costs and profitability estimates will not be covered in this work so that the economic analysis is limited to the capex estimate. This is reasonable, given that the economic viability of a GTL plant is influenced primarily by the capital cost estimate and this is expected to be the case in the mini-GTL plant as well (Jarosch et al, 2005). Indeed, it isn't expected that the operating costs which may include the equipment operating costs, administration and service costs will be any worse than that encountered in large scale GTL plants. Instead, these costs may be lower given the small and simple nature of the FT microchannel reactor and associated process units in the mini-GTL plant, enabling less resources to be deployed per barrel produced. It can be expected therefore that the main determinant in the profitability of a mini-GTL plant will be the capital costs, which have been shown to be lower than those in conventional large-scale GTL plants.

5.3.3 Conclusion

In this chapter, the economics of a mini-GTL plant based on the FT microchannel reactor technology were evaluated by considering the capital costs associated with constructing such a plant that would potentially use stranded/associated natural gas as the feedstock. It was determined that the FT unit is a main cost driver in the capital cost of a GTL plant and similarly in mini-GTL plants. The microchannel FT reactor in the proposed mini-GTL plant, being more efficient and thus cheaper, was determined to greatly influence the reduced cost of the mini-GTL versus that of the conventional large scale GTL plant. The capital cost estimate of the mini-GTL plant was found to be 95% lower than that from a conventional size GTL plant. More importantly, the cost/bbl estimate for the mini-GTL case was found to be 33% lower than in the conventional size case. This is a direct result of the improved efficiency brought about in large part by the FT microreactor unit. These results, although still requiring further assessments, demonstrate the potential economic benefits of using mini-GTL plants particularly for the processing of low-volume natural resource reserves where the plant capacity will be low. It is at this capacity level that the mini-GTL plant differentiates itself through its ability to run much more economically than the larger conventional GTL plants which rely heavily on economies of scale, i.e., they necessarily require larger plants to achieve lower cost/bbl figures so that they are less cost efficient at the lower capacities.

Chapter 6: Conclusions

The microchannel reactor, a relatively new application of process intensification has been envisioned for application in the FTS system because of its numerous potential advantages over conventional FT reactors. These include its ability to significantly enhance the heat and mass transfer efficiencies within the FT system and as a result open up new and previously neglected energy resources including biomass, stranded gas, associated gas and flared gas. These sources are normally wasted as the means to convert them to useful products have traditionally proven economically unviable but with FT microreactors offering more value through improved production per reactor volume, these sources can now be considered more seriously.

A mathematical model capable of accurately describing the operating environment within an FT microchannel reactor has been developed. The model was developed based on the principle of material conservation within the microchannel and all the relevant equations were numerically solved using Simulink in the MATLAB environment. In order to provide more insights into the physicochemical parameters governing this type of system, the fate of the reactants and in particular CO, were analyzed across the length of the microchannel. Using a 2-bubble size bubbly flow approach, the rate of CO consumption in the gas phase was determined to be the most effective way of analyzing this particular system.

It was determined that two key parameters primarily influence the performance of the microchannel reactor including the total superficial gas velocity and the axial dispersion, particularly in the gas phase. An increase in the superficial gas velocity was found to enhance axial dispersion in both liquid and gas phases and increase large bubble hold-up resulting in the net effect of a reduced syngas conversion. It was also determined that an increase in the microchannel diameter resulted in an increase in syngas conversion through its obvious effect on residence time but also indirectly through its influence on the dispersion in the large bubble compartment primarily. The solids concentration was found to enhance the syngas conversion up to a point, beyond which the effect of the decreasing small bubble hold-up outweighs the improved reactant consumption rate. This is an interesting observation given its counter-intuitive nature where continually increasing the solids loading would expectedly likewise continually improve the reaction kinetics but this has a limit and in the current scenario the limit is a loading of 0.3825. Increasing the temperature was found to improve the reaction kinetics and reduce the large bubble axial dispersion which had the net result of improving the kinetics.

The simulation results from the developed model were compared with those from literature experimental results under similar conditions in order to verify its accuracy. The results from the model were found to reasonably agree with those from various literature sources which should serve to validate the accuracy and dependability of the model in dealing with systems of a similar nature. As such, this model can be used for a variety of

important activities including the design and/or simulation of an FT microchannel reactor system and to run optimization exercises with minimal costs. The model can also be used for studying and training purposes where the workings within the FT microchannel reactor, as detailed within the model, can be analyzed and used as a tool to train and upskill interested parties which may include engineers, researchers, technicians and indeed operators.

The economics of a mini-GTL plant based on the FT microchannel reactor technology were evaluated by considering the capital costs associated with constructing such a plant that would potentially use stranded/associated natural gas as the feedstock. It was determined that the FT unit is a main cost driver in the capital cost of a GTL plant and similarly in mini-GTL plants. The microchannel FT reactor in the proposed mini-GTL plant, being more efficient and thus cheaper, was determined to greatly influence the reduced cost of the mini-GTL versus that of the conventional large scale GTL plant. The capital cost estimate of the mini-GTL plant was found to be 95% lower than that from a conventional size GTL plant. More importantly, the cost/bbl estimate for the mini-GTL case was found to be 33% lower than in the conventional size case. This is a direct result of the improved efficiency brought about in large part by the FT microreactor unit. These results, although still requiring further assessments, demonstrate the potential economic benefits of using mini-GTL plants particularly for the processing of low-volume natural resource reserves where the plant capacity will be low. It is at this capacity level that the mini-GTL plant differentiates itself through its ability to run much more economically than the larger conventional GTL plants which rely heavily on economies of scale, i.e., they necessarily require larger plants to achieve lower cost/bbl figures so that they are less cost efficient at the lower capacities.

Chapter 7: Recommendations

The mathematical model developed in this study can be used as a simulation tool for FT micro-reactor analysis and optimization and it can be employed as a design tool as well, to explore the various potential reactor configurations. There is sufficient potential from the model to warrant further study, including the further validation of the model through empirical methods. While validation through literature review provides insight into the model, a custom experimental set-up designed explicitly for testing and indeed improving the model would be useful in not only furthering our understanding of FTS in microchannels, but also in designing and simulating the FT microreactor environment. It is for this reason that a lab-scale and pilot scale model validation exercise is recommended. A pilot plant would also make it possible to study the heat transfer and pressure profile in the FT micro-reactor and to arrive at the relevant correlations, considering the actual shape and mechanical design of the reactor. This analysis would otherwise be more difficult, at least to a reasonable level of accuracy.

In industrial applications, microchannels can be 'scaled out' by stacking multiple channels together to effectively increase the operating volume and throughput. Feed flow maldistribution is a common issue where flow is distributed unevenly which can have negative selectivity and product distribution effects. It would be recommendable to perform a CFD analysis of the flow distribution and its relationship to the channels' pressure profile. Such a study would allow for the design of an adequate feed flow manifold configuration. This was out of the scope of this study but would be important in ensuring the FT micro-reactor model developed here is more complete.

A further study into the economics associated with an FT micro-reactor is recommended, with the use of more data and historical case studies. While this may prove difficult, given the novelty of this reactor, it remains important to source more detailed economic data to improve the economic model presented in this study. If FT micro-reactors are to be adopted in industry, the capital and operating expenses, and more importantly, the profitability achievable needs to be well-understood. A further, more detailed study on the economics is highly recommended.

FT micro-reactors show tremendous promise for unlocking previously untapped resources efficiently and a further understanding of the physico-chemical, structural, and economic parameters remains crucial. It is the author's intention that this work stimulates more inquisition into this subject and provides a platform for the ultimate industrial adoption of this novel technology.

References

1. Acrivos, A., Babcock, B. D., Pigford, R. J. (1959). Flow distributions in manifolds. *Chemical Engineering Science*, 10, 112-124.
2. Ajaev, V. S., Homsy, G. M. (2006). Modeling Shapes and Dynamics of Confined Bubbles. A*nnual Review of Fluid Mechanics*, 38, 277-307.
3. Ajmera, S. K., Delattre, C., Schmidt, M. A., Jensen, K. F. (2002). Microfabricated Differential Reactor for Heterogeneous Gas Phase Catalyst Testing. *Journal of Catalysis*, 209, 401–412.
4. Akita, K., Yoshida, F. (1973). Gas holdup and volumetric mass transfer coefficient in bubble columns. Effects of liquid properties. Industrial and Engineering Chemistry Process Design and Development, 12, 76–80.
5. Albright, L. F. (2009). *Albright's Chemical Engineering Handbook*. New York: CRC Press, Taylor and Francis group.
6. Almeida, L. C., Echave, F. J., Sanz, O., Centeno, M. A., Arzamendi, G., Gandia, L. M., Sousa-Aguiar, E. F., Odriozola, J. A., Montes, M. (2011). Fischer–Tropsch synthesis in microchannels. *Chemical Engineering Journal*, 167, 536–544.
7. Almeida, L. C., Sanz, O., D'olhaberriague, J., Yunes, S., Montes, M. (2013). Microchannel reactor for Fischer–Tropsch synthesis: Adaptation of a commercial unit for testing microchannel blocks. *Fuel*, 110, 171-177.
8. Aris, R. (1956). On the dispersion of a solute in a fluid flowing through a tube. *Proceedings of the Royal Society of London,* Series A, A23, 567–77.
9. Arzamendi, G., Diéguez, P. M., Montes, M., Odriozola, J. A., Sousa-Aguiard, E. F., Gandia, L. M. (2010). Computational fluid dynamics study of heat transfer in a microchannel reactor for low-temperature Fischer–Tropsch synthesis. *Chemical Engineering Journal*, 160, 915–922.
10. Bach, H. F, Pilhofer, T. (1978). Variations of gas hold-up in bubble columns with physical properties of liquids and operating parameters of column. *German Chemical Engineering*, 1, 270–275.
11. Baird, M. H. I., Rice, R. G. (1975). Axial dispersion in large unbaffled columns. The Chemical Engineering Journal, 9, 171-174.
12. Bakhtiary-Davijany, H., Hayer, F., Phan, X. K., Myrstad, R., Venvik, H. J., Pfeifer, P., Holmen, A. (2011). Characteristics of an Integrated Micro Packed Bed Reactor-Heat Exchanger for methanol synthesis from syngas. *Chemical Engineering journal*, 167, 496–503.

13. Basha, O. M., Sehabiague, L., Abdel-Wahab, A., Morsi, B. I. (2015). Fischer–Tropsch Synthesis in Slurry Bubble Column Reactors: Experimental Investigations and Modeling – A Review. *International Journal of Chemical Reactor Engineering*, 13(3), 201–288.
14. Begovich, J. M., Watson, J. (1978). *Hydrodynamic characteristics of three-phase fluidized beds*. Cambridge: Cambridge University Press.
15. Behkish, A. (1997). *Hydrodynamic and Mass Transfer Parameters in Large-Scale Slurry Bubble Column Reactors* (Doctoral thesis, University of Pittsburg, USA).
16. Behkish, A., Lemoine, R., Oukaci, R., Morsi, I. B. (2006). Novel correlations for gas holdup in large-scale slurry bubble column reactors operating under elevated pressures and temperatures. *Chemical Engineering Journal*, 115, 157–171.
17. Belloy, E., Sayah, A., Gijs, M. A. M. (2002). Micromachining of glass inertial sensors. *Journal of Microelectromechanical Systems*, 11(1), 85-90.
18. Boyer, C., Gazarian, J., Lecocq, V., Maury, S., Forret, A., Schweitzer, J., Souchon, V. (2016). Development of the Fischer-Tropsch Process: From the Reaction Concept to the Process Book. *Oil and Gas Science and Technology - Revue d'IFP Energies nouvelles, Institut Francais du Petrole*, 71(44).
19. Brady, R. C. III, and Pettit, R. (1981). Mechanism of the Fischer-Tropsch reaction. The chain propagation step. *Journal of the American Chemical Society*, 103(5), 1287–1289.
20. Brotz, W. Z. (1949). Zur Systematik der Fischer-Tropsch-Katalyse. *Zeitschrift für Elektrochemie*, 5, 301-306.
21. Bukur, D. B. (1983). Some Comments on Models for Fischer-Tropsch Reaction in Slurry Bubble Column Reactors. *Chemical Engineering Science*, 38(3),441-446.
22. Calderbank, P. H., Moo-Young, M. B. (1961). The continuous phase heat and mass transfer properties of dispersions. *Chemical Engineering Science*, 16, 39-54.
23. Cao, C., Hu, J., Li, S., Wilcox, W., Wang, Y. (2009). Intensified Fischer–Tropsch synthesis process with microchannel catalytic reactors. *Catalysis Today*, 140, 149–156.
24. Chang, J., Bai, L., Teng, B. T., Zhang, R. L., Yang, J., Xu, Y. Y., Xiang, H. W., Li, Y. W. (2007). Kinetic modeling of Fischer–Tropsch synthesis over Fe.Cu.K.SiO2 catalyst in slurry phase reactor. *Chemical Engineering Science*, 62, 4983 – 4991.
25. Chen, C. M., Leu, L. P. (2001). Hydrodynamics and mass transfer in threephase magnetic fluidized beds. *Powder Technology*, 117, 198–206.
26. Chiou, J. P. (1980). Advancement of Compact Heat Exchanger Theory Considering the Effects of Longitudinal Heat Conduction and Flow Nonuniformity. *American Society of Mechanical Engineers, Heat Transfer Division*, 10, 101-121.

27. Compact GTL. Commercial Demonstration Plant. Retrieved from https://www.compactgtl.com/technology/petrobas/
28. Craxford, S. R., and Rideal, E. K. (1939). The mechanism of the synthesis of hydrocarbons from water-gas. *Journal of the Chemical Society*, 1604-1614.
29. Davis, B. H. (2009). Fischer–Tropsch Synthesis: Reaction mechanisms for iron catalysts. *Catalysis Today*, 141, 25–33.
30. Davis, M. E., and Davis, R. J. (2003). Fundamentals of Chemical Reaction Engineering. New York: McGraw Hill.
31. De Deugd, R. M. (2004). *Fischer-Tropsch Synthesis Revisited; Efficiency and Selectivity Benefits from Imposing Temporal and/or Spatial Structure in the Reactor* (Doctoral thesis, Technische Universiteit Delft, Netherlands).
32. de Swart, J. W. A. (1996). *Scale-Up of a Fischer-Tropsch Slurry Reactor* (Doctoral thesis, University of Amsterdam, Netherlands).
33. Deckwer, W. D., Robert, W. F (Ed). (1991). *Bubble Column Reactors*. New York: John Wiley and Sons.
34. Deckwer, W. D., Burckhart, R., Zoll, G. (1974). Mixing and Mass Transfer in Tall Bubble Columns. Chemical Engineering Science, 29, 2177-2188.
35. Deckwer, W. D., Louisi, Y., Zaidi, A., Ralek, M. (1980). Hydrodynamic Properties of the Fischer-Tropsch Slurry Process. *Industrial and Engineering Chemistry Process Design and Development*, 19, 699-708.
36. Deckwer, W. D., Schumpe, A. (1993). Improved Tools for Bubble Column Reactor Design and Scale-up. *Chemical Engineering Science*, 48(5), 889-911.
37. Degaleesan, S., Dudukovic, M. P., Toseland, B. A., Bhatt, B. L. (1997). A Two-Compartment Convective-Diffusion Model for Slurry Bubble Column Reactors. Industrial and Engineering Chemistry Research, 36, 4670-4680.
38. Derevich, I. V., Ermolaev, V. S., Mordkovich, V. Z. (2012). Modeling of hydrodynamics in microchannel reactor for Fischer–Tropsch synthesis. *International Journal of Heat and Mass Transfer,* 55, 1695–1708.
39. Deshmukh, S. R., Tonkovich, A. L. Y., Jarosch, K. T., Schrader, L. (2010), Fitzgerald, S. P., Kilanowski, D. R., Lerou, J. J., Mazanec, T. J. (2010). Scale-Up of Microchannel Reactors for Fischer-Tropsch Synthesis. *Industrial & Engineering Chemistry Research*, 49, 10883–10888.
40. Djakovic, D. (2014). Gas to Liquids: Unlocking Value From Natural Gas. Texas A&M Gas and Fuels Research Initiative. Retrieved from http://gfrc.tamu.edu/wp-content/uploads/2015/04/Djakovic.pdf

41. Dongari, N., Sharma, A., Durst, F. (2009). Pressure-driven diffusive gas flows in micro-channels:from the Knudsen to the continuum regimes. Microfluid Nanofluid, 6, 679–692.
42. Dry, M. E. (2002). The Fischer–Tropsch process: 1950–2000. *Catalysis Today*, *71*, 227–241.
43. Dudukovic, M. P., Larachi, F., Mills, P., L. (1999). Multiphase reactors – revisited. *Chemical Engineering Science,* 54, 1975-1995.
44. Espinoza, R. L., Steynberg, A. P., Jager, B., Vosloo, A. C. (1999). Low temperature Fischer–Tropsch synthesis from a Sasol perspective. *Applied Catalysis A: General*, 186, 13–26.
45. Fan, L. S., Yang, G. Q., Lee, D. J., Tsuchiya, K., Luo, X. (1999). Some aspects of high-pressure phenomena of bubbles in liquid and liquid–solid suspensions. *Chemical Engineering Science*, 54, 4681–4709.
46. Fedorov, A. G., and Viskanta, R. (2000). Three-dimensional conjugate heat transfer in the microchannel heat sink for electronic packaging. *International Journal of Heat and Mass Transfer*, 43, 199-415.
47. Field, R. W., Davidson J. F. (1980). Axial dispersion in bubble columns. Transactions of the Institution of Chemical Engineers, 58, 228–236.
48. Fischer, F., and Tropsch, H. (1926). The Synthesis of Petroleum at Atmospheric Pressures from Gasification Products of Coal. *Brennstoff-Chemie*, 7, 97-104.
49. Fletcher, D. F., Haynes, B. S., Aubin, J., Xuereb, C. (2009). Modelling of Microfluidic Devices. In V. Hessel, A. Renken, J. C. Schouten & J. Yoshida (Eds.), *Micro Process Engineering* (Vol 1., pp. 117-139). Weinheim: WILEY-VCH Verlag GmbH & Co. KGaA. J.
50. Gandhi, B., Prakash, A., Bergougnou, M. A. (1999). Hydrodynamic behaviour of slurry bubble column at high solids concentrations. *Powder Technology*, 103, 80–94.
51. Ghobeity, A., Spelt, J. K., Papini, M. (2008). Abrasive jet micro-machining of planar areas and transitional slopes. *Journal of Micromechanics and Microengineering*, 18(5), 055014.
52. Groen, J. S., Oldeman, R. G. C., Mudde, R. F., Van den Akker, H. E. A. (1996). Coherent Structures and Axial Dispersion in Bubble Column Reactors. *Chemical Engineering Science*, 51(10), 2511-2520.
53. Groen, J.S. (2004). Scales and Structures in Bubbly Flows: Experimental analysis of the flow in bubble columns and in bubbling fluidized beds (Doctoral thesis, Delft University of Technology, Netherlands)
54. Gumuslu, G., Avci, A. K. (2011). Parametric Analysis of Fischer-Tropsch Synthesis in a Catalytic Microchannel Reactor. *AIChE Journal*, 58(1), 227-235.
55. Gunter, T., Zechner, B., Wiesegger, L. E., Kirschneck, D. (2009). Principles and Guidelines of Selection of Microstructured Devices for Mixing and Reaction. In V. Hessel, A. Renken, J. C. Schouten & J. Yoshida (Eds.), *Micro Process Engineering* (Vol 3., pp. 43-67). Weinheim: WILEY-VCH Verlag GmbH & Co. KGaA. J.

56. Gunther, A., Jensen, K. F. (2006). Multiphase microfluidics: from flow characteristics to chemical and materials synthesis. *Royal Society of Chemistry: Lab chip*, 6, 1487–1503.
57. Gunther, A., Kreutzer, M. T. (2009). Multiphase Flow. In V. Hessel, A. Renken, J. C. Schouten & J. Yoshida (Eds.), *Micro Process Engineering* (Vol 1., pp. 1-32). Weinheim: WILEY-VCH Verlag GmbH & Co. KGaA. J.
58. Guo, Y. X., Rathor, M. N., Ti. H. C. (1997). Hydrodynamics and mass transfer studies in a novel external-loop airlift reactor. Chemical Engineering Journal, 67, 205–14.
59. Guo, Z. Y., and Li, Z. X. (2003). Size effect on single-phase channel flow and heat transfer at microscale. *International Journal of Heat and Mass Transfer*, 24, 284-298.
60. Hassan, J. M., Mohamed, T. A., Mohammed, W. S., Alawee, W. H. (2015). Experimental and Numerical Study on the Improvement of Uniformity Flow for Three-lateral Dividing Manifold. *International Journal of Engineering and Technology*, 12(1), pp. 29-37.
61. Hazel, A., and Heil, M. (2002). Steady finite-Reynolds-number flows in three-dimensional collapsible tubes. *Journal of Fluid Mechanics*, 486, 79-103.
62. Hazel, A., and Heil, M. (2002). The steady propagation of a semi-infinite bubble into a tube of elliptical or rectangular cross-section. *Journal of Fluid Mechanics*, 470, 91-114.
63. Herington, E. F. G. (1946). The Fischer-Tropsch synthesis considered as a polymerization reaction. *Chemistry and Industry*, 65, 346-347.
64. Hessel, V., Hardt, S., Lowe, H. (2004). *Chemical Micro Process Engineering – Fundamentals, Modelling and Reactions*. Weinheim: Wiley-VCH Verlag GmbH & Co.KGaA.
65. Hessel, V., Lob, P. (2009). Homogenous reactions. In V. Hessel, A. Renken, J. C. Schouten & J. Yoshida (Eds.), *Micro Process Engineering* (Vol 1., pp. 367-390). Weinheim: WILEY-VCH Verlag GmbH & Co. KGaA. J.
66. Hetsroni, G., Mosyak, A., Pogrebnyak, E., Yarin, L. P. (2005). Fluid flow in micro-channels. *International Journal of Heat and Mass Transfer*, 48, 1982–1998.
67. Hetsroni, G., Mosyak, A., Pogrebnyak, E., Yarin, L. P. (2005). Heat transfer in micro-channels: Comparison of experiments with theory and numerical results. *International Journal of Heat and Mass Transfer*, 48(25–26), 5580-5601.
68. Hikita, A., Kikukawa, H. (1974). Liquid-Phase Mixing in Bubble Columns: Effect of Liquid Properties. The Chemical Engineering Journal, 8, 191-197.
69. Hinze, J. O. (1959). *Turbulence*. New York: McGraw Hill.
70. Hoek, A. (2005). The Shell GTL process: towards a world scale project in qatar. Chemie Ingenieur Technik, 77(8), 1172-1172.

71. Holmen, A., Venvik, H. J., Myrstad, R., Zhu, J., Chen, D. (2013). Monolithic, microchannel and carbon nanofibers/carbon felt reactors for syngas conversion by Fischer-Tropsch synthesis. *Catalysis Today*, 216, 150-157.
72. Hughmark, G. A. (1967). Holdup and mass transfer in bubble columns. *Industrial and Engineering Chemistry Process Design and Development*, 6, 218–220.
73. Iliuta, I., Larachi, F., Anfray, J., Dromard, N., Schweic D. (2007). Multicomponent Multicompartment Model for Fischer–Tropsch SCBR. *AIChE Journal*, 53(8), 2062–2083.
74. Inga, J. R. (1997). *Scale-up and scale-down of slurry reactors: A new methodology* (Doctoral thesis, University of Pittsburgh, USA).
75. Inga, J. R., and Morsi, B. I. (1996). A Novel Approach for the Assessment of the Rate-Limiting Step in Fischer-Tropsch Slurry Process. *Energy and Fuels*, 10, 566-572.
76. Jarosch, K. T., Tonkovich, A. L. Y., Perry, S. T., Kuhlmann, D., Wang, Y. (2005). Microchannel Reactors for Intensifying Gas-to-Liquid Technology. *Microreactor Technology and Process Intensification*, 16, 258-272.
77. Jiang, P. X., Fan, M. H., Si, G. S., Ren, Z. P. (2001). Thermal-hydraulic performance of small scale micro-channel and porous-media heat-exchangers. *International Journal of Heat and Mass Transfer,* 44, 039–1051.
78. Jiang, P., Lin, T. J., Luo, X., Fan L. S. (1995). Flow visualization of high pressure (21 MPa) bubble column: bubble characteristics. *Chemical Engineering Research and Design*, 73, 269–74.
79. Jordan, U., Schumpe, A. (2001).The gas density effect on mass transfer in bubble columns with organic liquids. *Chemical Engineering Science*, 56, 6267–6272.
80. Jung, I., Kshetrimayum, K. S., Park, S., Na, J., Lee, Y., An, J., Park, S., Lee, S., Han, C. (2016). Computational Fluid Dynamics Based Optimal Design of Guiding Channel Geometry in U-Type Coolant Layer Manifold of Large-Scale Microchannel Fischer−Tropsch Reactor. *Industrial & Engineering Chemistry Research*, 55, 505−515.
81. Jung, Y., and Kwak, H. Y. (2008). Fluid flow and heat transfer in microchannels with rectangular cross section. *International Journal of Heat and Mass Transfer*, 44, 1041–1049.
82. Kaisare, N. S., Stefanidis, G. D., Vlachos, D. G. (2009). Transport Phenomena in Microscale Flows. In V. Hessel, A. Renken, J. C. Schouten & J. Yoshida (Eds.), *Micro Process Engineering* (Vol 1., pp. 283-300). Weinheim: WILEY-VCH Verlag GmbH & Co. KGaA. J.
83. Kara, S., Kelkar, G. B., Shah, Y. T., Car, N. L. (1982). Hydrodynamics and Axial Mixing in a Three-phase Bubble Column. *Industrial and Engineering Chemistry Process Design and Development*, 21, 584-594.

84. Kashid, M. N., Agar, D. W., Renken, A., Kiwi-Minsker, L. (2009). Heterogenous Multiphase Reactions. In V. Hessel, A. Renken, J. C. Schouten & J. Yoshida (Eds.), *Micro Process Engineering* (Vol 1., pp. 395-435). Weinheim: WILEY-VCH Verlag GmbH & Co. KGaA. J.
85. Kim, D., Yu, C., Yoon, S. H., Choi, J. S. (2011). Effects of manifold geometries on flow distribution to parallel microchannels. Journal of Mechanical Science and Technology 25(12), 3069-3074.
86. Kim, S. D., Kim, H. S., Han, J. H. (1992). Axial Dispersion Characteristics in Three-phase Fluidised Beds. Chemical Engineering Science, 47(13/14), 3419-3426.
87. Kito, M., Tabei, K., Murata, K. (1978). Gas and liquid holdups in mobile beds under the counter-current flow of air and liquid.). *Industrial and Engineering Chemistry Process Design and Development*, 17, 568–71.
88. Knochen, J., Güttel, R., Knobloch, C., Turek, T. (2010). Fischer–Tropsch synthesis in milli-structured fixed-bed reactors: Experimental study and scale-up considerations. *Chemical Engineering and Processing: Process Intensification*, 49, 958–964.
89. Kockmann, N. (2008). *Transport Phenomena in Micro Process Engineering*. Berlin: Springer.
90. Kolb, G. (2013). Review: Microstructured reactors for distributed and renewable production of fuels and electrical energy. *Chemical Engineering and Processing: Process Intensification,* 65, 1–44.
91. Kolmogorov, A. (1941). The Local Structure of Turbulence in Incompressible Viscous Fluid for Very Large Reynolds Numbers. Doklady Akademiia Nauk SSSR, 30, 301-305.
92. Krishna, R., and Sie, S. T. (2000). Design and scale-up of the Fischer–Tropsch bubble column slurry reactor. *Fuel Processing Technology*, 64, 73–105.
93. Kshetrimayum, K. S., Jung, I., Na, J., Park, S., Lee, Y., Park, S., Lee, C., Han, C. (2016). CFD Simulation of Microchannel Reactor Block for Fischer−Tropsch Synthesis: Effect of Coolant Type and Wall Boiling Condition on Reactor Temperature. *Industrial & Engineering Chemistry Research*, 55, 543−554.
94. Lemoine, R., Behkish, A., Sehabiague, L., Heintz, Y. J., Oukaci, R., Morsi, B. I. (2008). An Algorithm for Predicting the Hydrodynamic and Mass Transfer Parameters in Bubble Column and Slurry Bubble Column Reactors. *Fuel Processing Technology*, 89(4), 322-343.
95. Lerou, J. J., Tonkovich, A. L., Silva, L., Perry, S., McDaniel, S. (2010). Microchannel reactor architecture enables greener processes. *Chemical Engineering Science*, 65, 380--385.
96. Letzel, H. M., Schouten, J. C., Krishna, R., van den Bleek, C. M. (1999). Gas holdup and mass transfer in bubble column reactors operated at elevated pressure. *Chemical Engineering Science*, *54*(13-14), 2237-2246.
97. Levenspiel, O. (1999). *Chemical Reaction Engineering* (3rd edition). New York: Wiley.

98. LeViness, S., Deshmukh, S. R., Richard, L. A., Robota. H. J. (2014). Velocys Fischer–Tropsch Synthesis Technology—New Advances on State-of-the-Art. *Topics in Catalysis*, 57, 518-525.

99. LeViness, S., Tonkovich, A. L., Jarosch, K., Fitzgerald, S., Yang, B., McDaniel, J. (2011). Improved Fischer-Tropsch Economics Enabled by Microchannel Technology. *Velocys White Paper*.

100. Maestri, M., Beretta, A., Groppi, G., Tronconi, E., Forzatti, P. (2005). Comparison among structured and packed-bed reactors for the catalytic partial oxidation of CH_4 at short contact times. *Catalysis Today*, 105, 709–717.

101. Maitlis, P. M., and de Klerk, A (Eds.). (2013). *Greener Fischer-Tropsch Processes for Fuels and Feedstocks.* Weinheim: 2013 Wiley-VCH Verlag and Co. KGaA.

102. Mamabolo, B. A. (2018). *Modelling of a Slurry Bubble Column Reactor for Fischer-Tropsch Synthesis* (Master's thesis, Wits University).

103. Mamabolo. B. A, Nkazi, D. (2019). Modeling of a Slurry Bubble Column Reactor Using a Two-Phase Two-Bubble Class Approach-A Hydrodynamics Study. *Energy & Fuels*, 33, 612−628.

104. Mangartz K. H., Pilhofer, T. H. (1980). Untersuchungen zur Gasphasendispersion in Blasensaulenreaktoren. Verfahrenstechnik (Mainz).

105. Mansoor, M. M., Wong, K. C., Siddique, M. (2012). Numerical investigation of fluid flow and heat transfer under high heat flux using rectangular micro-channels. *International Communications in Heat and Mass Transfer*, 39, 291–297.

106. Maretto, C., and Krishna, R. (1999). Modelling of a bubble column slurry reactor for Fischer-Tropsch synthesis. *Catalysis Today*, 52, 279-289.

107. Mohammed, S., Datt, M. (2013). Sasol: an industrial perspective. Retrieved from http://cheminnerweb.ukzn.ac.za/Libraries/APCH221_Notes/Sasol_Slides.sflb.ashx

108. Murphy-McGreevey, C. (2019). Increased Shale Oil Production and Political Conflict Contribute to Increase in Global Gas Flaring. Retrieved from https://www.worldbank.org/en/news/press-release/2019/06/12/increased-shale-oil-production-and-political-conflict-contribute-to-increase-in-global-gas-flaring

109. Na, J., Kshetrimayum, K. S., Lee, U., Han, C. (2017). Multi-Objective Optimization of Microchannel Reactor for Fischer-Tropsch Synthesis Using Computational Fluid Dynamics and Genetic Algorithm. *Chemical Engineering Journal*, 313, 1521-1534.

110. Nettelhoff, H., Ledakowics, S., Kokuun, R., Deckwer, W. D. (1985). Kinetics of the Fischer-Tropsch Synthesis in the Slurry Phase on a Pottasium Promoted Iron catalyst. *Industrial and Engineering Chemistry Process Design and Development* 24(4), 1043-1049.

111. Ohki, Y., Inoue, H. (1969). Longitudinal mixing of the liquid phase in bubble columns. Chemical Engineering Science, 25, 1-16.

112. Ojeda, M., Nabar, R., Nilekar, A. U., Ishikawa, A., Mavrikakis, M., Iglesia, E. (2010). CO activation pathways and the mechanism of Fischer–Tropsch synthesis. *Journal of catalysis*, 272(5), 287–297.

113. Oryx GTL. Retrieved from https://www.qp.com.qa/en/QPActivities/Pages/SubsidiariesAndJointVenturesDetails.aspx?aid=37

114. Ouyang, X., Besser, R. S. (2003). Development of a microreactor-based parallel catalyst analysis system for synthesis gas conversion. *Catalysis Today*, 84, 33–41.

115. Oyevaar, M., De La Rie, T., Van der Sluijs, C., Westerterp, K. (1989). Interfacial areas and gas hold-ups in bubble columns and packed bubble columns at elevated pressures. *Chemical Engineering and Processing: Process Intensification*, 26, 1–14.

116. Pan, M., Tang, Y., Pan, L., Lu, L. (2008). Optimal design of complex manifold geometries for uniform flow distribution between microchannels. *Chemical Engineering Journal*, 137, 339–346.

117. Park, S., Jung, I., Lee, U., Na, J., Kshetrimayum, S. K., Lee, Y., Lee, C., Han, C. (2015). Design and modeling of large-scale cross-current multichannel Fischer–Tropsch reactor using channel decomposition and cell-coupling method. *Chemical Engineering Science*, 134, 448–456.

118. Pearl GTL Overview. Retrieved from http://www.shell.com/about-us/major-projects/pearl-gtl/pearl-gtl-an-overview.html

119. Peng, X. F., and Peterson, G. P. (1996) Convective heat transfer and flow friction for water flow in microchannel structures. *International Journal of Heat and Mass Transfer*, 39(19), 2599–2608.

120. PetroSA: Operations and Refinery. Retrieved from http://www.petrosa.co.za/innovation_in_action/Pages/Operations-and-Refinery.aspx

121. Pigford, R. L., Ashraf, M., Miron, Y. D. (1983). Flow Distribution in Piping Manifolds. *Industrial and Engineering Chemistry Fundamentals*, 22, 463-471.

122. Pilhofer, T. H., Bach, H. F., Mangartz, K. H. (1978). Determination of Fluid Dynamic Parameters in Bubble Column Design. Fifth International Symposium on Chemical Reaction Englneering, Houston, 31, 372–383.

123. Pohar, A., Plazl, I. (2009). Process Intensification through Microreactor Application. *Chemical and Biochemical Engineering*, Q. 23, 4, 537–544.

124. Pratt, J. W. (2012). A Fischer-Tropsch Synthesis Reactor Model Framework for Liquid Biofuels Production. SANDIA Report: SAND2012-7848.

125. Rados, N., Al-Dahhan, M. H., Dudukovic, M. P. (2005). Dynamic Modeling of Slurry Bubble Column Reactors. *Industrial and Engineering Chemistry Research*, *44*, 6086-6094.

126. Reilly, I. G., Scott, D. S., De Bruijn, T., Jain, A., Piskorz, J. (1986). A correlation for gas holdup in turbulent coalescing bubble columns. *Canadian Journal of Chemical Engineering*, 64, 705–717.

127. Rocky Mountain GTL.RMGTL Carseland, Alberta Canada GTL Plant. Retrieved from http://rockymountaingtl.com/projects/

128. Sarup, B., and Wojciechowski, B. W. (1989). Studies of the fischer-tropsch synthesis on a cobalt catalyst II. Kinetics of carbon monoxide conversion to methane and to higher hydrocarbons. *The Canadian Journal of Chemical Engineering*, 67(1), 62-74.

129. Sasol Nigeria Operations. Retrieved from http://www.sasol.com/nigeria

130. Schweich, D., Fongarland, P., Anfray, J. (2007). Kinetic study and modeling of Fischer-Tropsch reaction over a Co/Al2O3 catalyst in a slurry reactor. *Chemical Engineering Science*, 62, 5353-5356.

131. Schweitzer, J. M., Viguie, J. C. (2009). Reactor Modeling of a Slurry Bubble Column for Fischer-Tropsch Synthesis. *Oil and Gas Science and Technology*, 64(1), 63-77.

132. Sehabiague, L. (2012). *Modeling, Scale-up and Optimization of Slurry Bubble Column Reactors for Fischer-Tropsch Synthesis* (Doctoral thesis, University of Pittsburgh, USA).

133. Serizawa, A., Feng, Z., Kawara, Z. (2002). Two-phase flow in microchannels. *Experimental Thermal and Fluid Science*, 26(6–7), 703-714.

134. Shah, R. K., and London, A. L. (1978). *Laminar Flow Forced Convection in Ducts: A Source Book for Compact Heat Exchanger Analytical Data*. Academic Press.

135. Shin, M., Park, N., Park, M., Jun, K., Ha, K. (2013). Computational fluid dynamics model of a modular multichannel reactor for Fischer–Tropsch synthesis: Maximum utilization of catalytic bed by microchannel heat exchangers. *Chemical Engineering Journal*, 234, 23–32.

136. Sinnot, R. K. (2005). *Chemical Engineering Design* (Vol 6, 4th edition). New York: Elsevier.

137. Solovitz, S. A., and Mainka, J. (2011). Manifold Design for Micro-Channel Cooling with Uniform Flow Distribution. *Journal of Fluids Engineering*, 133(5), 051103.

138. Song, H., Tice, J. D., Ismagilov, R. F. (2003). A Microfluidic System for Controlling Reaction. *Angewandte Chemie International Edition*, 42, 767.

139. Soriano, J. P., (2005). *Mass Transfer Characteristics in an Agitated Slurry Reactor Operating Under Fischer-Tropsch Conditions* (M.S. Thesis, University of Pittsburgh, USA).

140. Speight, J. G. (2008). *Synthetic Fuels Handbook: Properties, Process and Performance*. New York: The McGraw-Hill Companies.

141. Steynberg, A. P., and Dry, M. E (Eds.). (2004). *Fischer-Tropsch Technology*. Elsevier Science and Technology Books.

142. Tau, L., Dabbagh, H., Bao, S., Davis, B. H. (1990). Fischer-Tropsch synthesis. Evidence for two chain growth mechanisms. *Catalysis Letters*, 7, 127-140.

143. Taylor, G. (1953). Dispersion of Soluble Matter in Solvent Flowing Slowly Through a Tube. *Proceedings of the Royal Society of London,* Series A, A219, 186-203.

144. Therning, P., Rasmuson, A. (2001). Liquid dispersion, gas holdup and frictional pressure drop in a packed bubble column at elevated pressures. *Chemical Engineering Journal*, 81, 331–335.

145. Tomor, A., and Kristof, G. (2016). Validation of a Discrete Model for Flow Distribution in Dividing-Flow Manifolds: Numerical and Experimental Studies. Periodica Polytechnica Mechanical Engineering, 60(1), 41-49.

146. Towell, G. D., Ackermann, G. H. (1972). Axial mixing of liquid and gas in large bubble reactors. In: Proceedings of the Fifth European-Second International Symposium on Chemical Reaction Engineering. Vol. B3-1. Elsevier, Amsterdam, the Netherlands.

147. Trachsel, F., von Rohr, P. F. (2009). Heat Transfer in Homogenous Systems. In V. Hessel, A. Renken, J. C. Schouten & J. Yoshida (Eds.), *Micro Process Engineering* (Vol 1., pp. 253-279). Weinheim: WILEY-VCH Verlag GmbH & Co. KGaA. J.

148. Tso, C. P., and Mahulikar. (1998). The use of the Brinkman number for single phase forced convective heat transfer in microchannels. *International Journal of Heat and Mass Transfer*, 4(12), 1759-1769.

149. Tuckerman, D. B., Pease, R. F. W. (1981). High Performance Heat Sinking for VLSI. Electron Device Letters, 2,126-129.

150. Valdes, J. R., Miana, M. J., Pelegay, J. L., Nunez, J. L., Putz, T. (2007). Numerical investigation of the influence of roughness on the laminar incompressible fluid flow through annular microchannels. *International Journal of Heat and Mass Transfer*, 50, 1865–1878.

151. van der Laan, G. P. (1999). *Kinetics, Selectivity and Scale Up of the Fischer-Tropsch Synthesis* (Doctoral thesis, University of Groningen, Netherlands).

152. van Steen, E., and Schulz, H. (1999). Polymerisation kinetics of the Fischer-Tropsch CO hydrogenation using iron and cobalt based catalysts. *Applied Catalysis A: General*, 186, 309-320.

153. Velocys Projects. Bayou Fuels. Retrieved from https://www.velocys.com/projects/bayou-fuels/

154. Velocys-Altalto. Transforming waste into sustainable advanced biofuels. Retrieved from https://www.velocys.com/projects/altalto/

155. Vermeer, D. J., Krishna, R. (1981). Hydrodynamics and Mass Transfer in Bubble Columns Operating in the Churn-Turbulent Regime. *Industrial and Engineering Chemistry Process Design and Development*, 20, 475-482.

156. Wachi, S., Nojima, Y. (1990). Gas-phase dispersion in bubble columns. Chemical Engineering Science, 45, 901-905.

157. Wang, J. (2011). Theory of flow distribution in manifolds. *Chemical Engineering Journal,* 168, 1331–1345.

158. Wilkinson, P. M., Dlerendonck L. V. (1990). Pressure and gas density effects on bubble break-up and gas hold-up in bubble columns. *Chemical Engineering Science*, 45, 2309–2315.

159. Withers, H. P., Jr., Eliezer, K. F., Mitchell, J. W. (1990). Slurry-Phase Fischer-Tropsch Synthesis and Kinetic Studies over Supported Cobalt Carbonyl Derived Catalysts. *Industrial and Engineering Chemistry Research*, 29(9), 1807-1814.

160. Wojciekowski, B. W. (1988). The Kinetics of the Fischer-Tropsch Synthesis. *Catalysis Reviews, Science and Engineering*, 30(4).

161. Wong, H., Radke, C. J., Morris, S. (1995). The motion of long bubbles in polygonal capillaries. Part 2. Drag, fluid pressure and fluid flow. *Journal of Fluid Mechanics*, 292, 95-110.

162. Wong, H., Radke, C. J., Morris, S. (1995). The motion of long bubbles in polygonal capillaries. Part 1. Thin films. *Journal of Fluid Mechanics*, 292, 71-94.

163. World Bank. (2019). Top 30 flaring countries - table (2013-2018). Retrieved from http://pubdocs.worldbank.org/en/603281560185748682/pdf/Gas-flaring-volumes-Top-30-countries-2014-2018.pdf

164. Wu, H. Y., and Cheng, P. (2003). An experimental study of convective heat transfer in silicon microchannels with different surface conditions. *International Journal of Heat and Mass Transfer*, 46, 2547-2556.

165. Wu, Q., Wang, X., Wang, T., Han, M., Sha Z., Wang, J. (2013). Effect of Liquid Viscosity on Hydrodynamics and Bubble Behaviour of an External-loop Airlift Reactor. *Canadian Journal of Chemical Engineering*, 91, 1957-1963.

166. Yates, I. C., and Satterfield, C. N. (1991). Intrinsic Kinetics of the Fischer-Tropsch Synthesis on a Cobalt Catalyst. *Energy and Fuels*, 5, 168-173.

167. Zennaro, R. (2013). Fischer–Tropsch Process Economics. In Maitlis, P. M. & de Klerk, A. (Eds.), *Greener Fischer-Tropsch Processes for Fuels and Feedstocks* (1st Edition). Wiley-VCH Verlag GmbH & Co. KGaA.

168. Zhou, J., Ding, M., Meng, Z., Zhang, Y., Sun, Z. (2018). Reducing the Flow Distribution in Central-Type Compact Parallel Flow Heat Exchangers Having Optimized Tube Structure. *Frontiers in Energy Research*, 6(35).

169. Zou, R., Jiang, X., Li, B., Zu, Y., Zhang, L. (1988). Studies on gas holdup in a bubble column operated at elevated temperature. *Industrial and Engineering Chemistry Research*, 27, 1910–1916.

170. Xu, B., Ooi, K. T., Mavriplis, C., Zaghloul, M. E. (2002). Evaluation of viscous dissipation in liquid flow in microchannels. *Journal of Micromechanics and Microengineering*, 13, 53–57.

Appendices

Appendix A: Simulink Boundary Condition Models

Large bubble phase

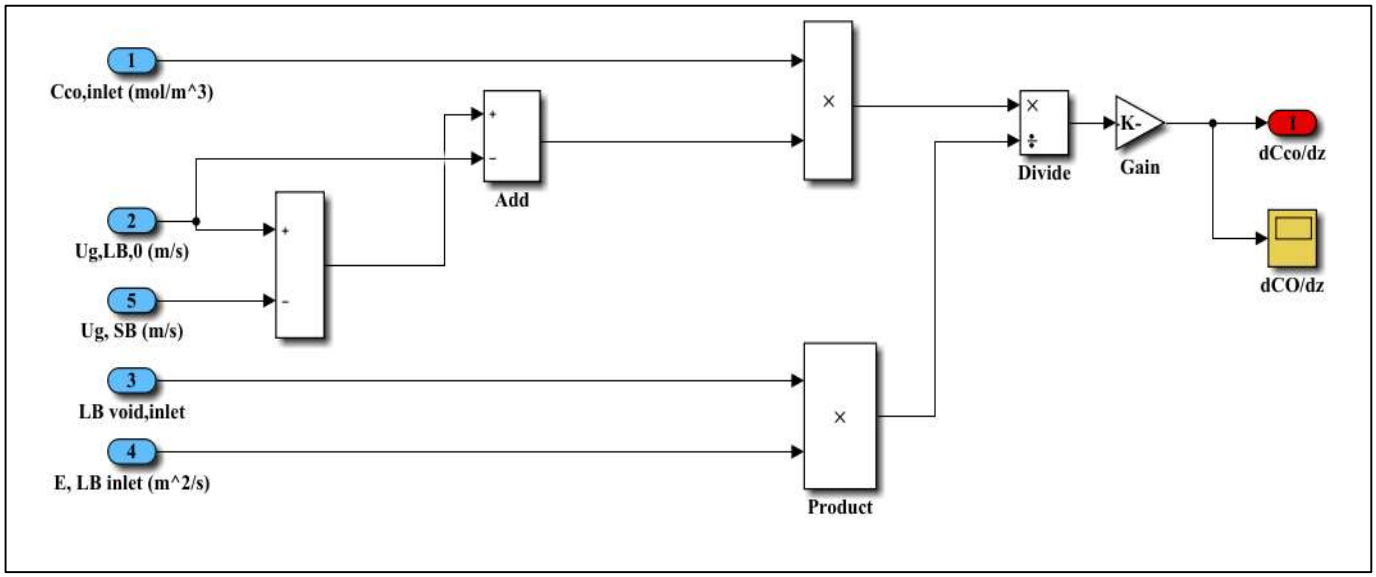

Figure A.1: LB CO inlet boundary condition model

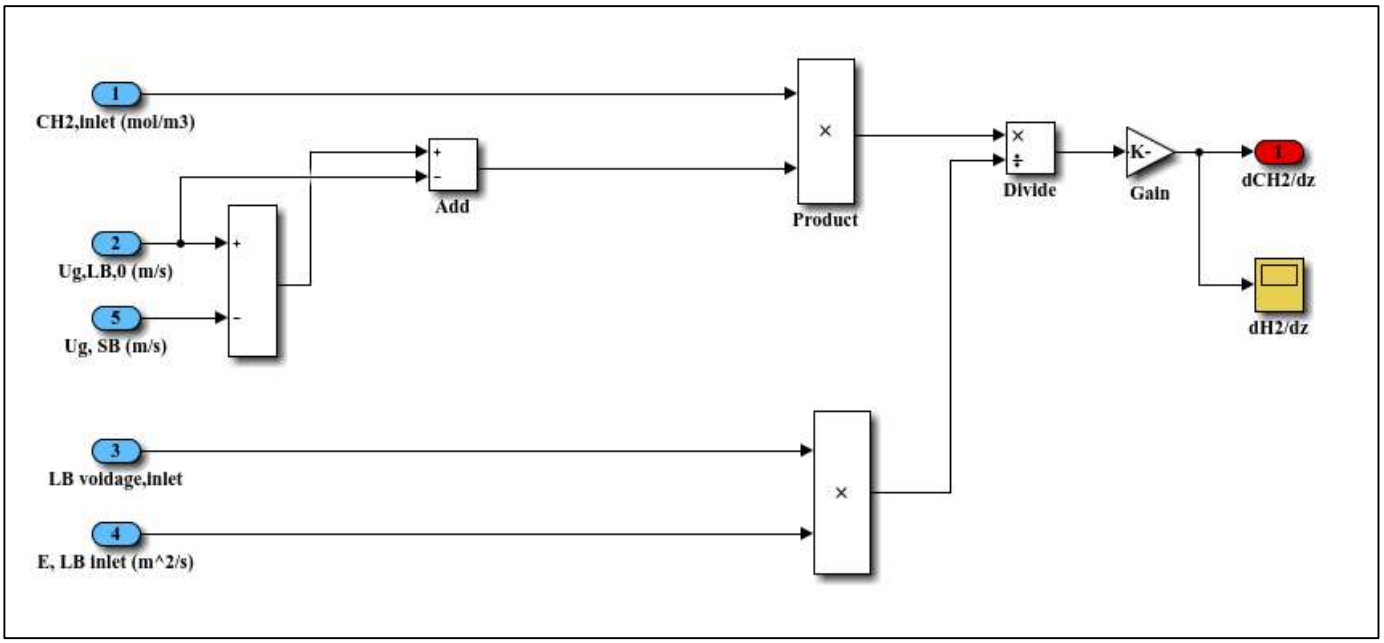

Figure A.2: LB H_2 inlet boundary condition model

The inlet large bubble class dispersion coefficients used in both the CO and H_2 boundary condition models was calculated from the inlet values of the superficial gas velocity and the large bubble hold-up in the large bubble dispersion coefficient correlation suggested by Mangartz and Pilhofer (1980) in Table 3.1. The Simulink model can be seen in Figure.

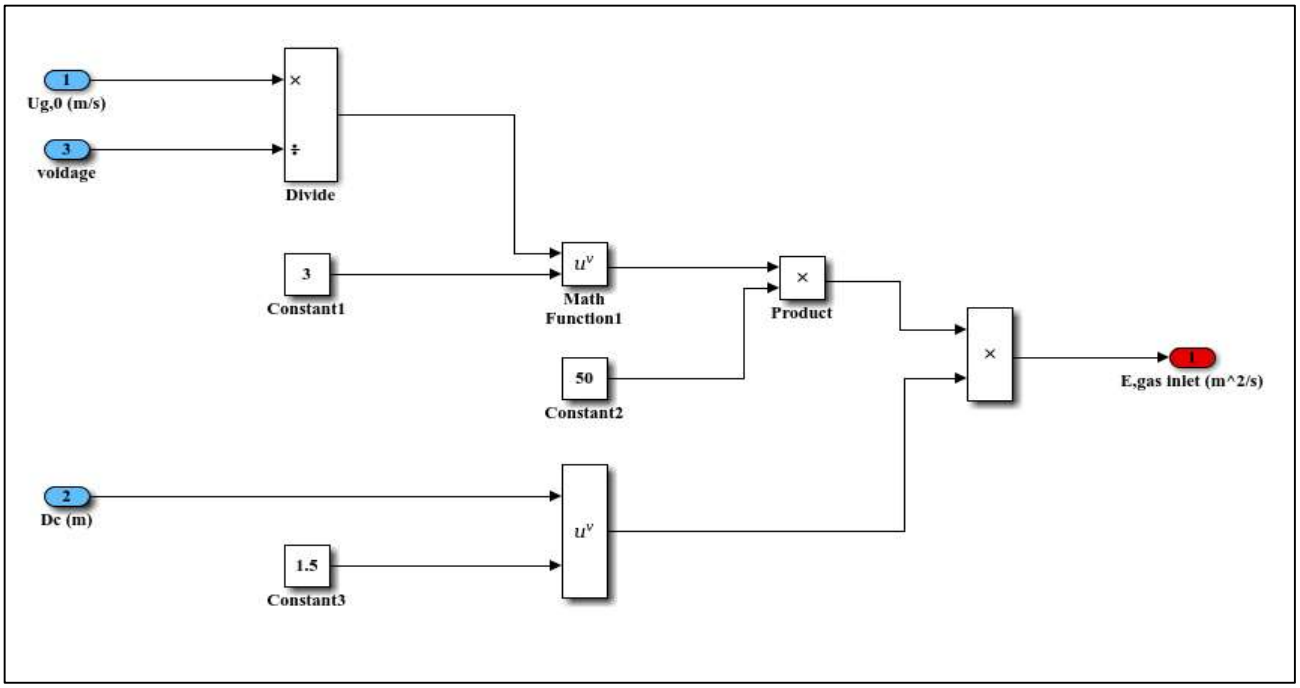

Figure A.3: Inlet large bubble axial dispersion coefficient model

Small bubble phase

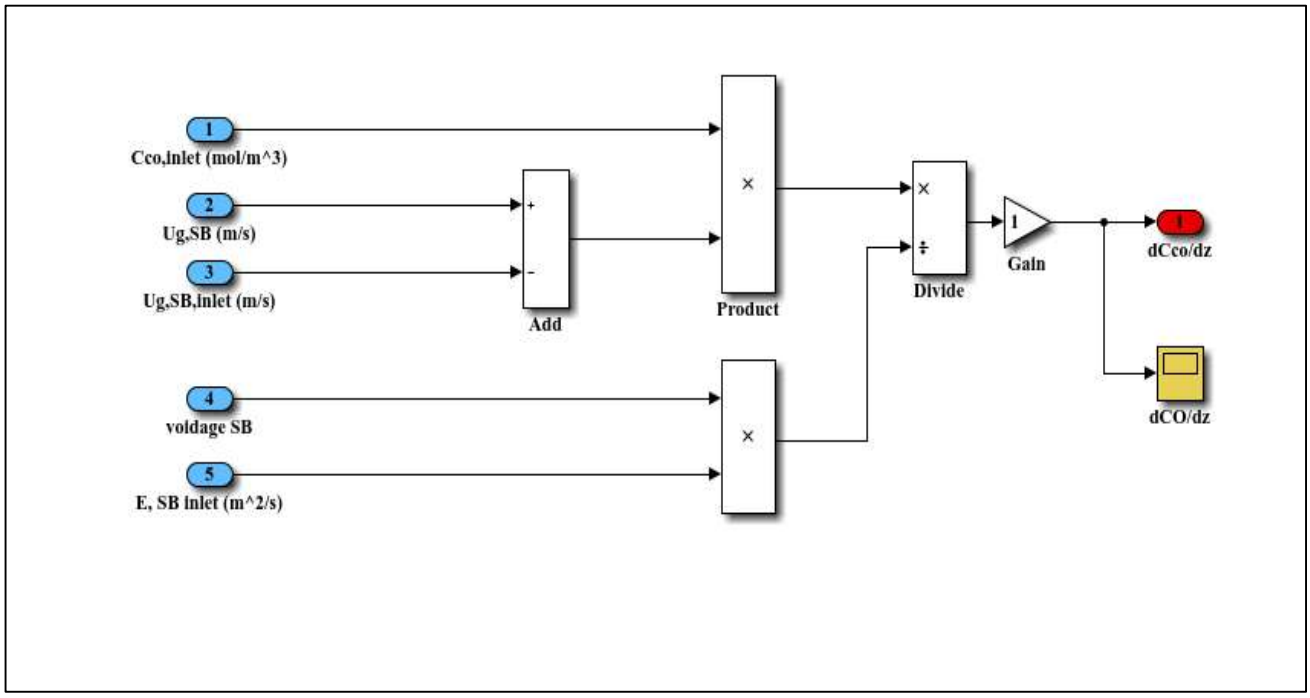

Figure A.4: Small bubble CO inlet boundary condition model

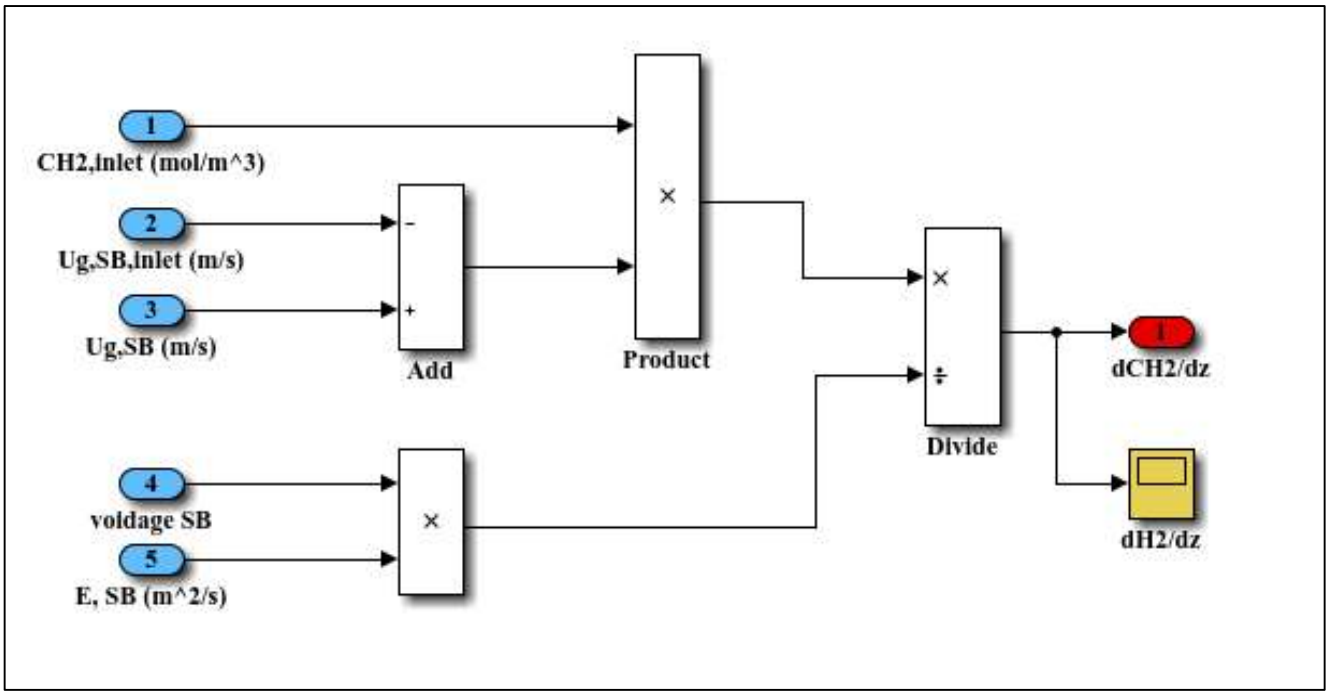

Figure A.5: Small bubble H_2 inlet boundary condition model

The small bubble class inlet axial dispersion coefficient for CO and H_2 was calculated from the inlet superficial gas velocity using the correlation by Baird and Rice (1975) in Equation 3.85 and the Simulink model is shown in Figure .

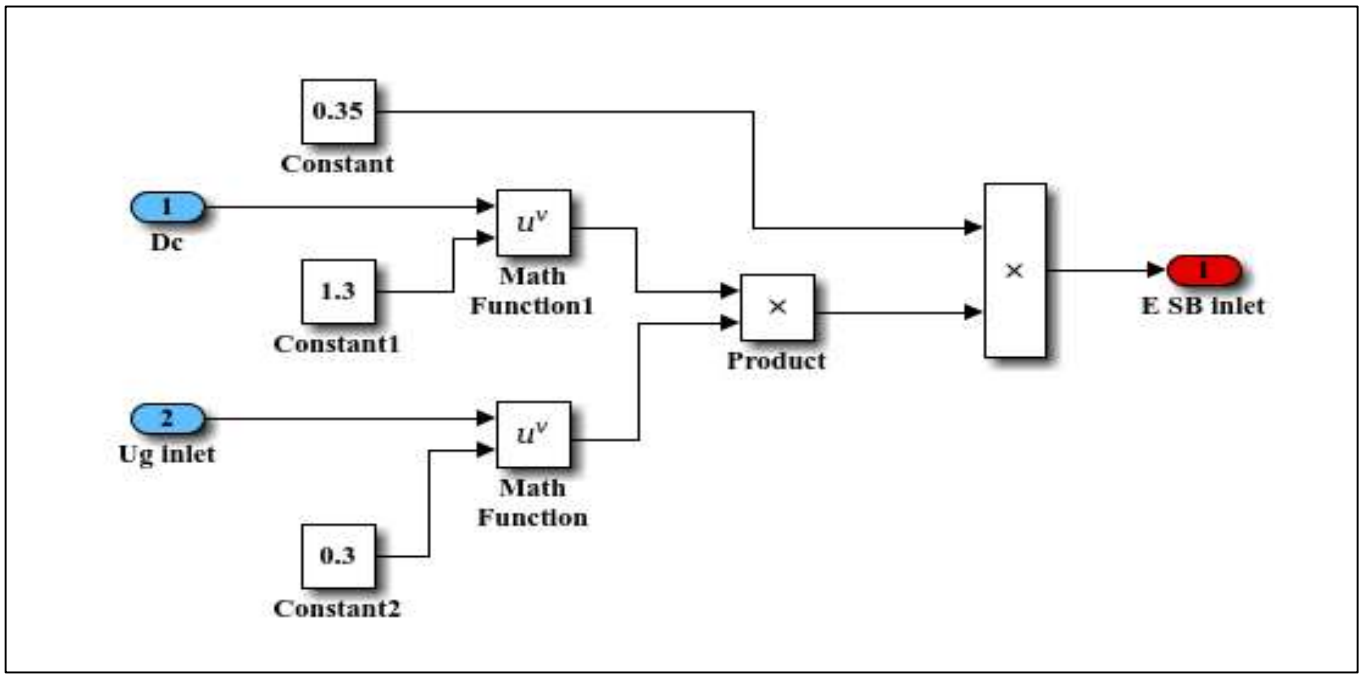

Figure A.6: Small bubble inlet axial dispersion coefficient model

Liquid phase

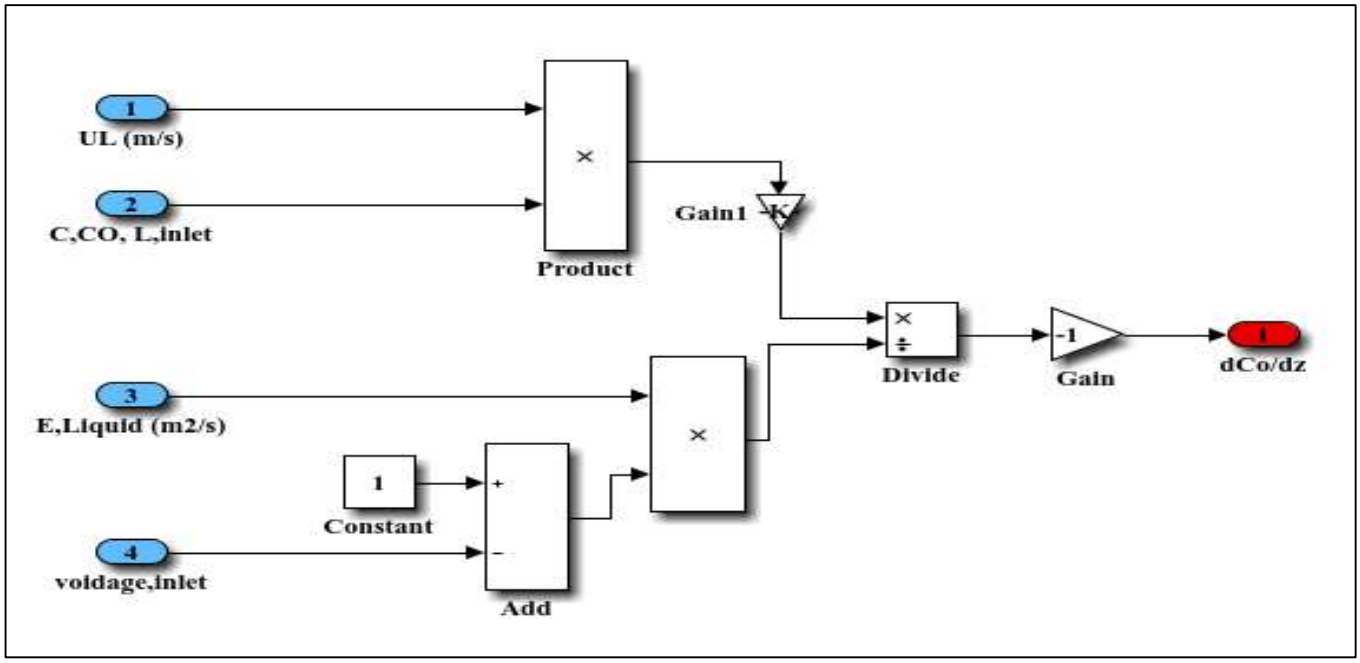

Figure A.7: Liquid phase CO inlet boundary condition model

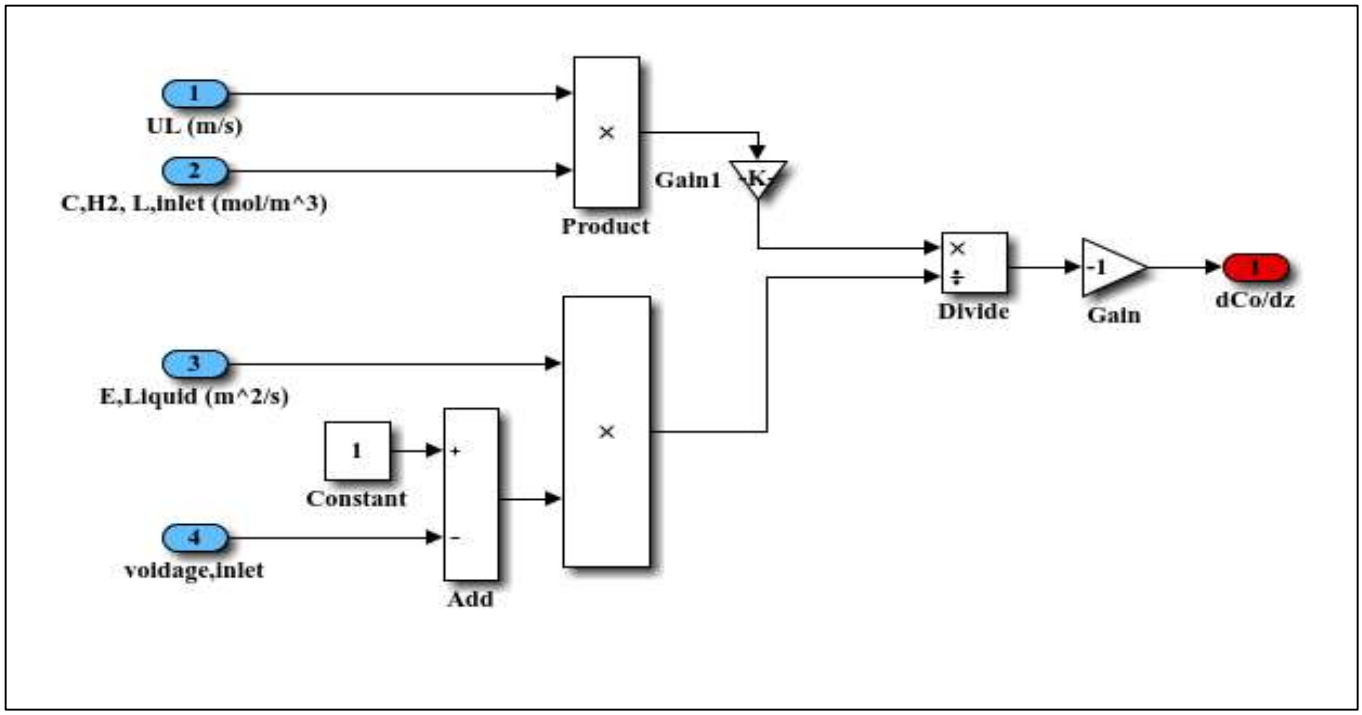

Figure A.8: Liquid phase H_2 inlet boundary condition model

The inlet liquid phase axial dispersion coefficient was calculated from the small bubble dispersion coefficient.

Appendix B: C source code of the complete mathematical model

```
/*
  * Microchannel.c
*
  * Academic License - for use in teaching, academic research, and meeting
  * course requirements at degree granting institutions only.  Not for
  * government, commercial, or other organizational use.
*
  * Code generation for model "Microchannel".
*
  * Model version              : 8.9
  * Simulink Coder version : 9.4 (R2020b) 29-Jul-2020
  * C source code generated on : Thu May 26 20:02:46 2022
*
  * Target selection: grt.tlc
  * Note: GRT includes extra infrastructure and instrumentation for prototyping
  * Embedded hardware selection: 32-bit Generic
  * Emulation hardware selection:
  *    Differs from embedded hardware (MATLAB Host)
  * Code generation objectives: Unspecified
  * Validation result: Not run
*/

#include  "Microchannel.h"
#include "Microchannel_private.h"

/* Block signals (default storage) */
B_Microchannel_T Microchannel_B;

/* Continuous states */
X_Microchannel_T  Microchannel_X;

/* Block states (default storage) */
DW_Microchannel_T Microchannel_DW;

/* External inputs (root inport signals with default storage) */
ExtU_Microchannel_T Microchannel_U;

/* External outputs (root outports fed by signals with default storage) */
ExtY_Microchannel_T Microchannel_Y;

/* Real-time model */
static RT_MODEL_Microchannel_T Microchannel_M_;
RT_MODEL_Microchannel_T *const Microchannel_M = &Microchannel_M_;

/*
  * This function updates continuous states using the ODE3 fixed-step
  * solver algorithm
*/
static void rt_ertODEUpdateContinuousStates(RTWSolverInfo *si )
```

```
{
/* Solver Matrices */
static const real_T rt_ODE3_A[3] = {1.0/2.0,
3.0/4.0, 1.0
};

static const real_T rt_ODE3_B[3][3] = {
{ 1.0/2.0, 0.0, 0.0 },

{ 0.0, 3.0/4.0, 0.0 },

{ 2.0/9.0, 1.0/3.0, 4.0/9.0 }
};

time_T t = rtsiGetT(si);
time_T tnew = rtsiGetSolverStopTime(si);
time_T h = rtsiGetStepSize(si);
real_T *x = rtsiGetContStates(si);
ODE3_IntgData *id = (ODE3_IntgData *)rtsiGetSolverData(si);real_T
*y = id->y;
real_T  *f0  =  id->f[0];
real_T  *f1  =  id->f[1];
real_T  *f2  =  id->f[2];
real_T hB[3];
int_T i;
int_T          nXc          =          13;
rtsiSetSimTimeStep(si,MINOR_TIME_STEP);

/* Save the state values at time t in y, we'll use x as ynew. */
(void) memcpy(y, x,
(uint_T)nXc*sizeof(real_T));

/* Assumes that rtsiSetT and ModelOutputs are up-to-date */
/* f0 = f(t,y) */ rtsiSetdX(si,
f0); Microchannel_derivatives();

/* f(:,2) = feval(odefile, t + hA(1), y + f*hB(:,1), args(:)(*)); */
hB[0] = h * rt_ODE3_B[0][0];
for (i = 0; i < nXc; i++) { x[i]
= y[i] + (f0[i]*hB[0]);
}

rtsiSetT(si, t + h*rt_ODE3_A[0]);
rtsiSetdX(si, f1);
Microchannel_step();
Microchannel_derivatives();

/* f(:,3) = feval(odefile, t + hA(2), y + f*hB(:,2), args(:)(*)); */
```

```
for (i = 0; i <= 1; i++) { hB[i]
= h * rt_ODE3_B[1][i];
}

for (i = 0; i < nXc; i++) {
x[i] = y[i] + (f0[i]*hB[0] + f1[i]*hB[1]);
}

rtsiSetT(si, t + h*rt_ODE3_A[1]);
rtsiSetdX(si, f2);
Microchannel_step();
Microchannel_derivatives();

/* tnew = t + hA(3);
ynew = y + f*hB(:,3); */for (i
= 0; i <= 2; i++) {
hB[i] = h * rt_ODE3_B[2][i];
}

for (i = 0; i < nXc; i++) {
x[i] = y[i] + (f0[i]*hB[0] + f1[i]*hB[1] + f2[i]*hB[2]);
}

rtsiSetT(si, tnew);
rtsiSetSimTimeStep(si,MAJOR_TIME_STEP);
}

/*
  * Output and update for action system:
  *    '<S2>/If Action Subsystem1'
  *    '<S2>/If Action Subsystem'
  *    '<S3>/If Action Subsystem1'
  *    '<S3>/If Action Subsystem'
*/
void Microchannel_IfActionSubsystem1(real_T rtu_In1,
B_IfActionSubsystem1_Microcha_T *localB)
{
/* Inport: '<S41>/In1' */
localB->In1 = rtu_In1;
}

real_T rt_powd_snf(real_T u0, real_T u1)
{
real_T tmp;
real_T tmp_0;
real_T y;
if (rtIsNaN(u0) || rtIsNaN(u1)) {y =
(rtNaN);
} else {
```

```
tmp = fabs(u0); tmp_0 =
fabs(u1); if
(rtIsInf(u1)) {
if (tmp == 1.0) {y =
1.0;
} else if (tmp > 1.0) {if (u1 >
0.0) {
y = (rtInf);
} else {
y = 0.0;
}
} else if (u1 > 0.0) {y =
0.0;
} else {
y = (rtInf);
}
} else if (tmp_0 == 0.0) {y =
1.0;
} else if (tmp_0 == 1.0) {if
(u1 > 0.0) {
y = u0;
} else {
y = 1.0 / u0;
}
} else if (u1 == 2.0) {y =
u0 * u0;
} else if ((u1 == 0.5) && (u0 >= 0.0)) {y =
sqrt(u0);
} else if ((u0 < 0.0) && (u1 > floor(u1))) {y =
(rtNaN);
} else {
y = pow(u0, u1);
}
}

return y;
}

/* Model step function */
void Microchannel_step(void)
{
/* local block i/o variables */
real_T rtb_Divide_m;
real_T rtb_Add; real_T
Divide_h_tmp;real_T
rtb_Add5; real_T
rtb_Divide_p;
real_T rtb_MathFunction_on;real_T
rtb_Product2_k;
```

```
real_T rtb_Product5_p;
real_T rtb_Product_bj;
real_T  rtb_Sqrt; int8_T
rtAction;
if (rtmIsMajorTimeStep(Microchannel_M)) {
/* set solver stop time */
if (!(Microchannel_M->Timing.clockTick0+1)) {
rtsiSetSolverStopTime(&Microchannel_M->solverInfo,
((Microchannel_M->Timing.clockTickH0 + 1) *Microchannel_M-
>Timing.stepSize0 * 4294967296.0));
} else {
rtsiSetSolverStopTime(&Microchannel_M->solverInfo,
((Microchannel_M->Timing.clockTick0 + 1) * Microchannel_M->Timing.stepSize0 +
Microchannel_M->Timing.clockTickH0 *Microchannel_M->Timing.stepSize0 *
4294967296.0));
}
}                                        /* end MajorTimeStep */

/* Update absolute time of base rate at minor time step */if
(rtmIsMinorTimeStep(Microchannel_M)) {
Microchannel_M->Timing.t[0] = rtsiGetT(&Microchannel_M->solverInfo);
}

if (rtmIsMajorTimeStep(Microchannel_M)) {
/* Constant: '<Root>/Cco,inlet' */ Microchannel_B.Ccoinlet =
Microchannel_P.Ccoinlet_Value;
}

/* Integrator: '<S24>/Integrator 2' */
/* Limited  Integrator  */
if (Microchannel_DW.Integrator2_IWORK != 0) {
Microchannel_X.Integrator2_CSTATE = Microchannel_B.Ccoinlet;
}

if (Microchannel_X.Integrator2_CSTATE >= Microchannel_P.Integrator2_UpperSat)
{
Microchannel_X.Integrator2_CSTATE = Microchannel_P.Integrator2_UpperSat;
} else {
if (Microchannel_X.Integrator2_CSTATE <= Microchannel_P.Integrator2_LowerSat)
{
Microchannel_X.Integrator2_CSTATE = Microchannel_P.Integrator2_LowerSat;
}
}

/* Integrator: '<S24>/Integrator 2' */ Microchannel_B.Integrator2
= Microchannel_X.Integrator2_CSTATE;

/* Outport: '<Root>/C,CO,SB (mol//m3)' */ Microchannel_Y.CCOSBmolm3
= Microchannel_B.Integrator2;
```

```
if (rtmIsMajorTimeStep(Microchannel_M)) {
/* Constant: '<Root>/C,H2 inlet' */ Microchannel_B.CH2inlet =
Microchannel_P.CH2inlet_Value;
}

/* Integrator: '<S27>/Integrator 2' */
/* Limited  Integrator  */
if (Microchannel_DW.Integrator2_IWORK_l != 0) {
Microchannel_X.Integrator2_CSTATE_h = Microchannel_B.CH2inlet;
}

if (Microchannel_X.Integrator2_CSTATE_h >=
Microchannel_P.Integrator2_UpperSat_o) {
Microchannel_X.Integrator2_CSTATE_h = Microchannel_P.Integrator2_UpperSat_o;
} else {
if (Microchannel_X.Integrator2_CSTATE_h <=
Microchannel_P.Integrator2_LowerSat_n) {
Microchannel_X.Integrator2_CSTATE_h =
Microchannel_P.Integrator2_LowerSat_n;
}
}

/* Integrator: '<S27>/Integrator 2' */ Microchannel_B.Integrator2_b
= Microchannel_X.Integrator2_CSTATE_h;

/* Outport: '<Root>/C,H2,SB (mol//m3)' */ Microchannel_Y.CH2SBmolm3
= Microchannel_B.Integrator2_b;

/* Integrator: '<S25>/Integrator1' */
/* Limited  Integrator  */
if (Microchannel_DW.Integrator1_IWORK != 0) {
Microchannel_X.Integrator1_CSTATE = Microchannel_B.Ccoinlet;
}

if (Microchannel_X.Integrator1_CSTATE >= Microchannel_P.Integrator1_UpperSat)
{
Microchannel_X.Integrator1_CSTATE = Microchannel_P.Integrator1_UpperSat;
} else {
if (Microchannel_X.Integrator1_CSTATE <= Microchannel_P.Integrator1_LowerSat)
{
Microchannel_X.Integrator1_CSTATE = Microchannel_P.Integrator1_LowerSat;
}
}

/* Integrator: '<S25>/Integrator1' */ Microchannel_B.Integrator1
= Microchannel_X.Integrator1_CSTATE;

/* Outport: '<Root>/C,CO,LB (mol//m3)' */ Microchannel_Y.CCOLBmolm3
= Microchannel_B.Integrator1;
```

```
/* Integrator: '<S28>/Integrator 2' */
/* Limited  Integrator  */
if (Microchannel_DW.Integrator2_IWORK_p != 0) {
Microchannel_X.Integrator2_CSTATE_hb = Microchannel_B.CH2inlet;
}

if (Microchannel_X.Integrator2_CSTATE_hb >=
Microchannel_P.Integrator2_UpperSat_b) {
Microchannel_X.Integrator2_CSTATE_hb = Microchannel_P.Integrator2_UpperSat_b;
} else {
if (Microchannel_X.Integrator2_CSTATE_hb <=
Microchannel_P.Integrator2_LowerSat_k) {
Microchannel_X.Integrator2_CSTATE_hb =
Microchannel_P.Integrator2_LowerSat_k;
}
}

/* Integrator: '<S28>/Integrator 2' */
Microchannel_B.Integrator2_k = Microchannel_X.Integrator2_CSTATE_hb;

/* Outport: '<Root>/C,H2,LB (mol//m3)' */
Microchannel_Y.CH2LBmolm3 = Microchannel_B.Integrator2_k;if
(rtmIsMajorTimeStep(Microchannel_M)) {
}

/* Gain: '<Root>/Gain' incorporates:
    *  Product: '<Root>/Divide'
    *  Sum: '<Root>/Add1'
*/
Microchannel_B.Gain = (Microchannel_B.Ccoinlet - Microchannel_B.Integrator1) /
Microchannel_B.Ccoinlet * Microchannel_P.Gain_Gain;
if (rtmIsMajorTimeStep(Microchannel_M)) {
}

/* Gain: '<Root>/Gain2' incorporates:
    *  Product: '<Root>/Divide2'
    *  Sum: '<Root>/Add3'
*/
Microchannel_B.Gain2 = (Microchannel_B.CH2inlet - Microchannel_B.Integrator2_k)
/ Microchannel_B.CH2inlet * Microchannel_P.Gain2_Gain;if
(rtmIsMajorTimeStep(Microchannel_M)) {
/* Scope: '<Root>/H2 LB' */
if (rtmIsMajorTimeStep(Microchannel_M)) {
StructLogVar *svar = (StructLogVar *)Microchannel_DW.H2LB_PWORK.LoggedData;LogVar *var
= svar->signals.values;

/* time */
{
```

```
double locTime = (((Microchannel_M->Timing.clockTick1+
Microchannel_M->Timing.clockTickH1* 4294967296.0)) *1.0E-5);
;
rt_UpdateLogVar((LogVar *)svar->time, &locTime, 0);
}

/* signals */
{
real_T up0[1];
up0[0] = Microchannel_B.Integrator2_k; rt_UpdateLogVar((LogVar
*)var, up0, 0);
}
}

/* Scope: '<Root>/H2 SB' */
if (rtmIsMajorTimeStep(Microchannel_M)) {
StructLogVar *svar = (StructLogVar *)Microchannel_DW.H2SB_PWORK.LoggedData;LogVar *var
= svar->signals.values;

/* time */
{
double locTime = (((Microchannel_M->Timing.clockTick1+
Microchannel_M->Timing.clockTickH1* 4294967296.0)) *1.0E-5);
;
rt_UpdateLogVar((LogVar *)svar->time, &locTime, 0);
}

/* signals */
{
real_T up0[1];
up0[0] = Microchannel_B.Integrator2_b; rt_UpdateLogVar((LogVar
*)var, up0, 0);
}
}

/* Sum: '<Root>/Add4' */
Microchannel_B.Add4 = Microchannel_B.Ccoinlet + Microchannel_B.CH2inlet;
}

/* Gain: '<Root>/Gain1' incorporates:
    *  Product: '<Root>/Divide1'
    *  Sum: '<Root>/Add2'
*/
Microchannel_B.Gain1 = (((Microchannel_B.Ccoinlet + Microchannel_B.CH2inlet) -
Microchannel_B.Integrator1) - Microchannel_B.Integrator2_k) / Microchannel_B.Add4
* Microchannel_P.Gain1_Gain;
if (rtmIsMajorTimeStep(Microchannel_M)) {
```

```
/* ToWorkspace: '<Root>/To Workspace' */
{
double locTime = (((Microchannel_M->Timing.clockTick1+
Microchannel_M->Timing.clockTickH1* 4294967296.0)) *1.0E-5);
;
if (rtmIsMajorTimeStep(Microchannel_M)) {
rt_UpdateStructLogVar((StructLogVar *)
Microchannel_DW.ToWorkspace_PWORK.LoggedData,&locTime, &Microchannel_B.Gain1);
}
}

/* Product: '<S2>/Divide' incorporates:
      *  Constant: '<Root>/Dc (m)1'
      *  Constant: '<S2>/Q (m3//s)'
      *  Gain: '<S2>/Gain'
      *  Math: '<S2>/Math Function'
*/
rtb_Divide_m = Microchannel_P.Qm3s_Value / (Microchannel_P.Dcm1_Value *
Microchannel_P.Dcm1_Value * Microchannel_P.Gain_Gain_g);

     /* If: '<S2>/If' incorporates:
*        Constant: '<Root>/Dc (m)1'
      *  Constant: '<S2>/Ug'
*/
if (rtmIsMajorTimeStep(Microchannel_M)) {
rtAction = (int8_T)!(Microchannel_P.Dcm1_Value != 0.00349);
Microchannel_DW.If_ActiveSubsystem = rtAction;
} else {
rtAction = Microchannel_DW.If_ActiveSubsystem;
}

switch (rtAction) {case
0:
/* Outputs for IfAction SubSystem: '<S2>/If Action Subsystem1' incorporates:
        *  ActionPort: '<S41>/Action Port'
*/ Microchannel_IfActionSubsystem1(rtb_Divide_m,
&Microchannel_B.IfActionSubsystem1);

/* End of Outputs for SubSystem: '<S2>/If Action Subsystem1' */break;

case 1:
/* Outputs for IfAction SubSystem: '<S2>/If Action Subsystem' incorporates:
*  ActionPort: '<S40>/Action Port'
*/ Microchannel_IfActionSubsystem1(Microchannel_P.Ug_Value,
```

```
&Microchannel_B.IfActionSubsystem);

/* End of Outputs for SubSystem: '<S2>/If Action Subsystem' */break;
}

/* End of If: '<S2>/If' */

/* Sum: '<S2>/Add' */
rtb_Add = Microchannel_B.IfActionSubsystem.In1 +Microchannel_B.IfActionSubsystem1.In1;

     /* If: '<S3>/If' incorporates:
*        Constant: '<Root>/Dc (m)1'
      *  Constant: '<Root>/Ug,inlet'
*/
if (rtmIsMajorTimeStep(Microchannel_M)) {
rtAction = (int8_T)!(Microchannel_P.Dcm1_Value != 0.00349);
Microchannel_DW.If_ActiveSubsystem_o = rtAction;
} else {
rtAction = Microchannel_DW.If_ActiveSubsystem_o;
}

switch (rtAction) {case
0:
/* Outputs for IfAction SubSystem: '<S3>/If Action Subsystem1' incorporates:
        *  ActionPort: '<S43>/Action Port'
*/ Microchannel_IfActionSubsystem1(rtb_Add,
&Microchannel_B.IfActionSubsystem1_c);

/* End of Outputs for SubSystem: '<S3>/If Action Subsystem1' */break;

case 1:
/* Outputs for IfAction SubSystem: '<S3>/If Action Subsystem' incorporates:
        *  ActionPort: '<S42>/Action Port'
*/ Microchannel_IfActionSubsystem1(Microchannel_P.Uginlet_Value,
&Microchannel_B.IfActionSubsystem_c);

/* End of Outputs for SubSystem: '<S3>/If Action Subsystem' */break;
}

/* End of If: '<S3>/If' */

/* Sum: '<Root>/Add' */
Microchannel_B.Add = Microchannel_B.IfActionSubsystem_c.In1 +
```

```
Microchannel_B.IfActionSubsystem1_c.In1;

/* Product: '<S8>/Divide' incorporates:
      *  Constant: '<Root>/T(K)1'
      *  Constant: '<S8>/1'
*/
rtb_MathFunction_on = Microchannel_P.u_Value / Microchannel_P.TK1_Value;

/* Product: '<S8>/Product3' incorporates:
      *  Constant: '<Root>/T(K)1'
*  Constant: '<S8>/10^3R'
      *  Constant: '<S8>/A CO'
      *  Constant: '<S8>/B CO'
      *  Constant: '<S8>/Ho CO'
      *  Math: '<S8>/Math Function'
      *  Math: '<S8>/Math Function1'
      *  Product: '<S8>/Divide1'
      *  Product: '<S8>/Product'
      *  Product: '<S8>/Product1'
      *  Product: '<S8>/Product2'
      *  Sum: '<S8>/Add'
*
      * About '<S8>/Math Function1':
      *  Operator: exp
*/
Microchannel_B.Product3 = Microchannel_P.u03R_Value / (exp (rtb_MathFunction_on
* rtb_MathFunction_on * Microchannel_P.ACO_Value +
Microchannel_P.BCO_Value * rtb_MathFunction_on) *
Microchannel_P.HoCO_Value) * Microchannel_P.TK1_Value;

/* Product: '<S15>/Product1' */
Microchannel_B.Product1 = Microchannel_B.Product3 * Microchannel_B.Ccoinlet;
}

/* Integrator: '<S26>/Integrator 2' */
/* Limited  Integrator  */
if (Microchannel_DW.Integrator2_IWORK_g != 0) {
Microchannel_X.Integrator2_CSTATE_d = Microchannel_B.Product1;
}

if (Microchannel_X.Integrator2_CSTATE_d >=
Microchannel_P.Integrator2_UpperSat_e) {
Microchannel_X.Integrator2_CSTATE_d = Microchannel_P.Integrator2_UpperSat_e;
} else {
if (Microchannel_X.Integrator2_CSTATE_d <=
Microchannel_P.Integrator2_LowerSat_i) {
Microchannel_X.Integrator2_CSTATE_d =
Microchannel_P.Integrator2_LowerSat_i;
}
```

```
}

/* Integrator:  '<S26>/Integrator  2'  */ Microchannel_B.Integrator2_a
= Microchannel_X.Integrator2_CSTATE_d;if
(rtmIsMajorTimeStep(Microchannel_M)) {
}

/* Integrator: '<S19>/Integrator' */
/* Limited  Integrator  */
if (Microchannel_DW.Integrator_IWORK != 0) {
Microchannel_X.Integrator_CSTATE = Microchannel_B.Add;
}

if (Microchannel_X.Integrator_CSTATE >= Microchannel_P.Integrator_UpperSat) {
Microchannel_X.Integrator_CSTATE = Microchannel_P.Integrator_UpperSat;
} else {
if (Microchannel_X.Integrator_CSTATE <= Microchannel_P.Integrator_LowerSat)
{
Microchannel_X.Integrator_CSTATE = Microchannel_P.Integrator_LowerSat;
}
}

/* Integrator:  '<S19>/Integrator'  */ Microchannel_B.Integrator
= Microchannel_X.Integrator_CSTATE;if
(rtmIsMajorTimeStep(Microchannel_M)) {
/* Product: '<S17>/Product1' incorporates:
      *  Constant: '<Root>/Cv (v//v)1'
      *  Constant: '<Root>/void SB,ref'
      *  Constant: '<S17>/Constant'
      *  Constant: '<S17>/Constant1'
      *  Product: '<S17>/Divide'
      *  Product: '<S17>/Product'
*  Sum: '<S17>/Add'
*/
Microchannel_B.Product1_c = (Microchannel_P.Constant_Value -
Microchannel_P.Constant1_Value / Microchannel_P.voidSBref_Value *
Microchannel_P.Cvvv1_Value) * Microchannel_P.voidSBref_Value;

/* Math: '<S14>/Math Function3' incorporates:
      *  Constant: '<S14>/Constant5'
      *  Constant: '<S14>/D column'
*/
if ((Microchannel_P.Dcolumn_Value < 0.0) && (Microchannel_P.Constant5_Value >
floor(Microchannel_P.Constant5_Value))) {
Divide_h_tmp = -rt_powd_snf(-Microchannel_P.Dcolumn_Value,
Microchannel_P.Constant5_Value);
} else {
Divide_h_tmp = rt_powd_snf(Microchannel_P.Dcolumn_Value,
Microchannel_P.Constant5_Value);
```

```
}

/* End of Math: '<S14>/Math Function3' */

/* Product: '<S14>/Divide1' incorporates:
      *  Constant: '<S14>/Constant4'
*/
Microchannel_B.Divide1 = Microchannel_P.Constant4_Value / Divide_h_tmp;

/* Gain: '<S23>/Gain2' incorporates:
      *  Constant: '<Root>/T(K)1'
      *  Constant: '<S23>/Constant'
      *  Gain: '<S23>/Gain'
      *  Gain: '<S23>/Gain1'
      *  Math: '<S23>/Math Function'
*   Sum: '<S23>/Add1'
*/
rtb_MathFunction_on = ((Microchannel_P.Constant_Value_e -
Microchannel_P.Gain_Gain_j * Microchannel_P.TK1_Value) +
Microchannel_P.TK1_Value * Microchannel_P.TK1_Value *
Microchannel_P.Gain1_Gain_k) * Microchannel_P.Gain2_Gain_o;

/* Product: '<S18>/Divide' incorporates:
      *  Constant: '<Root>/T(K)1'
      *  Constant: '<S20>/Constant'
      *  Constant: '<S20>/Constant1'
      *  Math: '<S20>/Math Function'
      *  Product: '<S20>/Divide'
*   Sum: '<S20>/Add1'
*
      * About '<S20>/Math Function':
      *  Operator: exp
*/
rtb_Divide_p = rtb_MathFunction_on / exp(Microchannel_P.Constant_Value_m /
Microchannel_P.TK1_Value - Microchannel_P.Constant1_Value_d);

/* Math: '<S18>/Math Function' incorporates:
      *  Constant: '<S18>/Constant5'
*/
if ((rtb_MathFunction_on < 0.0) && (Microchannel_P.Constant5_Value_j > floor
(Microchannel_P.Constant5_Value_j))) {
rtb_Add5 = -rt_powd_snf(-rtb_MathFunction_on,
Microchannel_P.Constant5_Value_j);
} else {
rtb_Add5 = rt_powd_snf(rtb_MathFunction_on,
Microchannel_P.Constant5_Value_j);
}

/* End of Math: '<S18>/Math Function' */
```

```
/* Sum: '<S4>/Add1' incorporates:
      *  Constant: '<Root>/T(K)1'
      *  Constant: '<S4>/Constant'
      *  Gain: '<S4>/Gain'
*/
rtb_Sqrt = Microchannel_P.Constant_Value_k - Microchannel_P.Gain_Gain_b *
Microchannel_P.TK1_Value;

/* Math: '<S18>/Math Function2' incorporates:
      *  Constant: '<S18>/Constant2'
*/
if ((rtb_MathFunction_on < 0.0) && (Microchannel_P.Constant2_Value_e > floor
(Microchannel_P.Constant2_Value_e))) {
rtb_MathFunction_on = -rt_powd_snf(-rtb_MathFunction_on,
Microchannel_P.Constant2_Value_e);
} else {
rtb_MathFunction_on = rt_powd_snf(rtb_MathFunction_on,
Microchannel_P.Constant2_Value_e);
}

/* End of Math: '<S18>/Math Function2' */

/* Product: '<S18>/Divide1' incorporates:
      *  Constant: '<Root>/g (m//s2)1'
      *  Product: '<S18>/Product1'
      *  Product: '<S18>/Product2'
*/
rtb_Add5 = rtb_Add5 * rtb_Sqrt / (rtb_MathFunction_on *Microchannel_P.gms21_Value);

/* Math: '<S18>/Math Function3' incorporates:
      *  Constant: '<S18>/Constant3'
*/
if ((rtb_Add5 < 0.0) && (Microchannel_P.Constant3_Value > floor
(Microchannel_P.Constant3_Value))) {
rtb_Add5 = -rt_powd_snf(-rtb_Add5, Microchannel_P.Constant3_Value);
} else {
rtb_Add5 = rt_powd_snf(rtb_Add5, Microchannel_P.Constant3_Value);
}

/* End of Math: '<S18>/Math Function3' */

/* Product: '<S18>/Divide2' incorporates:
      *  Constant: '<Root>/density G'
*/
rtb_Sqrt /= Microchannel_P.densityG_Value;

/* Math: '<S18>/Math Function4' incorporates:
```

```
      *  Constant: '<S18>/Constant4'
*/
if ((rtb_Sqrt < 0.0) && (Microchannel_P.Constant4_Value_n > floor
(Microchannel_P.Constant4_Value_n))) {
rtb_Sqrt = -rt_powd_snf(-rtb_Sqrt, Microchannel_P.Constant4_Value_n);
} else {
rtb_Sqrt = rt_powd_snf(rtb_Sqrt, Microchannel_P.Constant4_Value_n);
}

/* End of Math: '<S18>/Math Function4' */

/* Product: '<S18>/Product' incorporates:
      *  Constant: '<S18>/Constant'
*/
Microchannel_B.Product = Microchannel_P.Constant_Value_p * rtb_Divide_p *
rtb_Add5 * rtb_Sqrt * Microchannel_B.Product1_c;
}

/* Sum: '<S14>/Add' */
rtb_Divide_p = Microchannel_B.Integrator - Microchannel_B.Product;

/* Math: '<S14>/Math Function1' incorporates:
    *  Constant: '<S14>/Constant3'
*/
if ((rtb_Divide_p < 0.0) && (Microchannel_P.Constant3_Value_c > floor
(Microchannel_P.Constant3_Value_c))) {
rtb_Product_bj = -rt_powd_snf(-rtb_Divide_p,
Microchannel_P.Constant3_Value_c);
} else {
rtb_Product_bj = rt_powd_snf(rtb_Divide_p, Microchannel_P.Constant3_Value_c);
}

/* End of Math: '<S14>/Math Function1' */

/* Math: '<S14>/Math Function4' incorporates:
    *  Constant: '<S14>/Constant6'
*/
if ((rtb_Divide_p < 0.0) && (Microchannel_P.Constant6_Value > floor
(Microchannel_P.Constant6_Value))) {
rtb_Divide_p = -rt_powd_snf(-rtb_Divide_p, Microchannel_P.Constant6_Value);
} else {
rtb_Divide_p = rt_powd_snf(rtb_Divide_p, Microchannel_P.Constant6_Value);
}

/* End of Math: '<S14>/Math Function4' */

/* Product: '<S14>/Product' incorporates:
    *  Constant: '<S14>/Constant1'
    *  Constant: '<S14>/Constant2'
```

```
    *  Product: '<S14>/Divide'
*/
Microchannel_B.Product_m = Microchannel_P.Constant1_Value_e *
Microchannel_B.Divide1 * (Microchannel_P.Constant2_Value / rtb_Product_bj) *
rtb_Divide_p;

/* Sum: '<S14>/Add3' incorporates:
    *  Constant: '<S14>/Constant7'
    *  Product: '<S14>/Product2'
*  Sum: '<S14>/Add2'
*/
Microchannel_B.Add3 = (Microchannel_P.Constant7_Value -
Microchannel_B.Product_m) * Microchannel_B.Product1_c +
Microchannel_B.Product_m;

/* Product: '<S6>/Divide' incorporates:
    *  Product: '<S1>/Divide'
*/
rtb_MathFunction_on = Microchannel_B.Integrator / Microchannel_B.Add3;

/* Math: '<S6>/Math Function1' incorporates:
    *  Constant: '<S6>/Constant'
    *  Product: '<S6>/Divide'
*/
if ((rtb_MathFunction_on < 0.0) && (Microchannel_P.Constant_Value_k0 > floor
(Microchannel_P.Constant_Value_k0))) {
rtb_Product_bj = -rt_powd_snf(-rtb_MathFunction_on,Microchannel_P.Constant_Value_k0);
} else {
rtb_Product_bj = rt_powd_snf(rtb_MathFunction_on,Microchannel_P.Constant_Value_k0);
}

/* End of Math: '<S6>/Math Function1' */ if
(rtmIsMajorTimeStep(Microchannel_M)) {
/* Math: '<S6>/Math Function' incorporates:
      *  Constant: '<Root>/Dc (m)1'
      *  Constant: '<S6>/Constant2'
*/
if ((Microchannel_P.Dcm1_Value < 0.0) && (Microchannel_P.Constant2_Value_b >
floor(Microchannel_P.Constant2_Value_b))) {
/* Math: '<S6>/Math Function' */
Microchannel_B.MathFunction = -rt_powd_snf(-Microchannel_P.Dcm1_Value,
Microchannel_P.Constant2_Value_b);
} else {
/* Math: '<S6>/Math Function' */
Microchannel_B.MathFunction = rt_powd_snf(Microchannel_P.Dcm1_Value,
Microchannel_P.Constant2_Value_b);
}
```

```
/* End of Math: '<S6>/Math Function' */
}

/* Product: '<S6>/Product1' incorporates:
    *  Constant: '<S6>/Constant1'
    *  Product: '<S6>/Product'
*/
Microchannel_B.Product1_o = rtb_Product_bj * Microchannel_P.Constant1_Value_i *
Microchannel_B.MathFunction;
if (rtmIsMajorTimeStep(Microchannel_M)) {
/* Scope: '<S1>/C,CO,L1' */
if (rtmIsMajorTimeStep(Microchannel_M)) {StructLogVar
*svar = (StructLogVar *)
Microchannel_DW.CCOL1_PWORK.LoggedData;LogVar *var
= svar->signals.values;

/* time */
{
double locTime = (((Microchannel_M->Timing.clockTick1+
Microchannel_M->Timing.clockTickH1* 4294967296.0)) *1.0E-5);
;
rt_UpdateLogVar((LogVar *)svar->time, &locTime, 0);
}

/* signals */
{
real_T up0[1];
up0[0] = Microchannel_B.Product1_o;
rt_UpdateLogVar((LogVar *)var, up0, 0);
}
}

/* Product: '<S9>/Divide' incorporates:
      *  Constant: '<Root>/T(K)1'
      *  Constant: '<S9>/1'
*/
rtb_Sqrt = Microchannel_P.u_Value_o / Microchannel_P.TK1_Value;

/* Product: '<S9>/Product3' incorporates:
      *  Constant: '<Root>/T(K)1'
*  Constant: '<S9>/10^3R'
      *  Constant: '<S9>/A H2'
      *  Constant: '<S9>/B H2'
      *  Constant: '<S9>/Ho H2'
      *  Math: '<S9>/Math Function'
      *  Math: '<S9>/Math Function1'
      *  Product: '<S9>/Divide1'
```

```
      *  Product: '<S9>/Product'
      *  Product: '<S9>/Product1'
      *  Product: '<S9>/Product2'
*  Sum: '<S9>/Add1'
*
      * About '<S9>/Math Function1':
      *  Operator: exp
*/
Microchannel_B.Product3_p = Microchannel_P.u03R_Value_i / (exp(rtb_Sqrt *
rtb_Sqrt * Microchannel_P.AH2_Value + Microchannel_P.BH2_Value * rtb_Sqrt)
       * Microchannel_P.HoH2_Value) * Microchannel_P.TK1_Value;

/* Product: '<S15>/Product'  */ Microchannel_B.Product_p =
Microchannel_B.Product3_p *
Microchannel_B.CH2inlet;
}

/* Integrator: '<S29>/Integrator 2' */
/* Limited  Integrator  */
if (Microchannel_DW.Integrator2_IWORK_m != 0) {
Microchannel_X.Integrator2_CSTATE_a = Microchannel_B.Product_p;
}

if (Microchannel_X.Integrator2_CSTATE_a >=
Microchannel_P.Integrator2_UpperSat_ej) {
Microchannel_X.Integrator2_CSTATE_a = Microchannel_P.Integrator2_UpperSat_ej;
} else {
if (Microchannel_X.Integrator2_CSTATE_a <=
Microchannel_P.Integrator2_LowerSat_i2) {
Microchannel_X.Integrator2_CSTATE_a =
Microchannel_P.Integrator2_LowerSat_i2;
}
}

/* Integrator:  '<S29>/Integrator  2'  */ Microchannel_B.Integrator2_d
= Microchannel_X.Integrator2_CSTATE_a;if
(rtmIsMajorTimeStep(Microchannel_M)) {
/* Product: '<S22>/Product1' incorporates:
      *  Constant: '<Root>/A,FT'
      *  Constant: '<Root>/EFT'
      *  Constant: '<Root>/T(K)1'
      *  Constant: '<Root>/gas const'
      *  Gain: '<S22>/Gain'
      *  Math: '<S22>/Math Function'
      *  Product: '<S22>/Divide'
      *  Product: '<S22>/Product'
*
      * About '<S22>/Math Function':
      *  Operator: exp
```

```
*/
Microchannel_B.Product1_b = exp(Microchannel_P.Gain_Gain_gq *Microchannel_P.EFT_Value /
(Microchannel_P.TK1_Value * Microchannel_P.gasconst_Value)) * Microchannel_P.AFT_Value;

/* Product: '<S16>/Product3' incorporates:
      *  Constant: '<Root>/T(K)1'
      *  Constant: '<Root>/gas const'
      *  Product: '<S21>/Product'
*/
rtb_Product2_k = Microchannel_P.gasconst_Value * Microchannel_P.TK1_Value;

/* Product: '<S16>/Product3' */
Microchannel_B.Product3_ph = rtb_Product2_k;

/* Math: '<S16>/Math Function' */ Microchannel_B.MathFunction_m =
Microchannel_B.Product3_ph *
Microchannel_B.Product3_ph;

/* Product: '<S21>/Product1' incorporates:
      *  Constant: '<Root>/Aad'
      *  Constant: '<Root>/Ead'
      *  Gain: '<S21>/Gain'
      *  Math: '<S21>/Math Function'
      *  Product: '<S21>/Divide'
*
      * About '<S21>/Math Function':
      *  Operator: exp
*/
Microchannel_B.Product1_d = exp(Microchannel_P.Gain_Gain_n * Microchannel_P.Ead_Value /
rtb_Product2_k) * Microchannel_P.Aad_Value;
}

/* Sum: '<S7>/Add1' */
rtb_Product_bj = Microchannel_B.Integrator1 + Microchannel_B.Integrator2;

/* Sum: '<S7>/Add2' */
rtb_Divide_p = Microchannel_B.Integrator2_k + Microchannel_B.Integrator2_b;

/* Sum: '<S16>/Add1' incorporates:
    *  Constant: '<S16>/Constant'
    *  Product: '<S16>/Product2'
*/
rtb_Product2_k = Microchannel_B.Product1_d * Microchannel_B.Product3_ph *rtb_Product_bj
+ Microchannel_P.Constant_Value_g;

/* Gain: '<S1>/Gain' incorporates:
    *  Math: '<S16>/Math Function1'
    *  Product: '<S16>/Divide'
```

```
    *  Product: '<S16>/Product'
*/
Microchannel_B.Gain_b = Microchannel_B.Product1_b * rtb_Product_bj *
rtb_Divide_p * Microchannel_B.MathFunction_m / (rtb_Product2_k *
rtb_Product2_k) * Microchannel_P.Gain_Gain_l;
if (rtmIsMajorTimeStep(Microchannel_M)) {
}

/* Product: '<S1>/Divide' */
Microchannel_B.Divide = rtb_MathFunction_on;if
(rtmIsMajorTimeStep(Microchannel_M)) {
/* Sqrt: '<S10>/Sqrt' incorporates:
      *  Constant: '<Root>/CO diff'
      *  Constant: '<S10>/Dref (m2//s)'
      *  Product: '<S10>/Divide'
*/
rtb_Sqrt = sqrt(Microchannel_P.COdiff_Value / Microchannel_P.Drefm2s_Value);

/* Gain: '<S10>/Gain' */
Microchannel_B.Gain_o = Microchannel_P.Gain_Gain_bx * rtb_Sqrt;
}

/* Product: '<S10>/Product' */
Microchannel_B.Product_d = Microchannel_B.Gain_o * Microchannel_B.Product_m;if
(rtmIsMajorTimeStep(Microchannel_M)) {
/* Sqrt: '<S11>/Sqrt' incorporates:
      *  Constant: '<Root>/CO diff'
      *  Constant: '<S11>/Dref (m2//s)'
      *  Product: '<S11>/Divide'
*/
rtb_Sqrt = sqrt(Microchannel_P.COdiff_Value / Microchannel_P.Drefm2s_Value_h);

/* Product: '<S11>/Product' incorporates:
      *  Gain: '<S11>/Gain'
*/
Microchannel_B.Product_n = Microchannel_P.Gain_Gain_e * rtb_Sqrt *
Microchannel_B.Product1_c;

/* ToWorkspace: '<S1>/To Workspace' */
if (rtmIsMajorTimeStep(Microchannel_M)) {
rt_UpdateStructLogVar((StructLogVar *)
Microchannel_DW.ToWorkspace_PWORK_g.LoggedData,(NULL), &Microchannel_B.Gain_b);
}

/* ToWorkspace: '<S1>/To Workspace2' */
{
double locTime = (((Microchannel_M->Timing.clockTick1+
Microchannel_M->Timing.clockTickH1* 4294967296.0)) *
```

```
1.0E-5);
;
if (rtmIsMajorTimeStep(Microchannel_M)) {
rt_UpdateStructLogVar((StructLogVar *)
Microchannel_DW.ToWorkspace2_PWORK.LoggedData,&locTime,
&Microchannel_B.Integrator);
}
}

/* ToWorkspace: '<S1>/To Workspace3' */
{
double locTime = (((Microchannel_M->Timing.clockTick1+
Microchannel_M->Timing.clockTickH1* 4294967296.0)) *1.0E-5);
;
if (rtmIsMajorTimeStep(Microchannel_M)) {
rt_UpdateStructLogVar((StructLogVar *)
Microchannel_DW.ToWorkspace3_PWORK.LoggedData,&locTime,
&Microchannel_B.Product1_o);
}
}

/* Math: '<S5>/Math Function' incorporates:
      *  Constant: '<Root>/Dc (m)1'
      *  Constant: '<S5>/Constant'
*/
if ((Microchannel_P.Dcm1_Value < 0.0) && (Microchannel_P.Constant_Value_i >
floor(Microchannel_P.Constant_Value_i))) {
/* Math: '<S5>/Math Function' */
Microchannel_B.MathFunction_g = -rt_powd_snf(-Microchannel_P.Dcm1_Value,
Microchannel_P.Constant_Value_i);
} else {
/* Math: '<S5>/Math Function' */
Microchannel_B.MathFunction_g = rt_powd_snf(Microchannel_P.Dcm1_Value,
Microchannel_P.Constant_Value_i);
}

/* End of Math: '<S5>/Math Function' */
}

/* Math: '<S5>/Math Function2' incorporates:
    *  Constant: '<S5>/Constant1'
*/
if ((Microchannel_B.Integrator < 0.0) && (Microchannel_P.Constant1_Value_h >
floor(Microchannel_P.Constant1_Value_h))) {
Divide_h_tmp = -rt_powd_snf(-Microchannel_B.Integrator,
Microchannel_P.Constant1_Value_h);
} else {
Divide_h_tmp = rt_powd_snf(Microchannel_B.Integrator,
```

```
Microchannel_P.Constant1_Value_h);
}

/* End of Math: '<S5>/Math Function2' */

/* Product: '<S5>/Product' incorporates:
    *  Constant: '<S5>/K'
*/
Microchannel_B.Product_dy = Microchannel_P.K_Value *
Microchannel_B.MathFunction_g * Divide_h_tmp;
if (rtmIsMajorTimeStep(Microchannel_M)) {
/* ToWorkspace: '<S1>/To Workspace4' */
{
double locTime = (((Microchannel_M->Timing.clockTick1+
Microchannel_M->Timing.clockTickH1* 4294967296.0)) *1.0E-5);
;
if (rtmIsMajorTimeStep(Microchannel_M)) {
rt_UpdateStructLogVar((StructLogVar *)
Microchannel_DW.ToWorkspace4_PWORK.LoggedData,&locTime,
&Microchannel_B.Product_dy);
}
}

/* ToWorkspace: '<S1>/To Workspace5' */
{
double locTime = (((Microchannel_M->Timing.clockTick1+
Microchannel_M->Timing.clockTickH1* 4294967296.0)) *1.0E-5);
;
if (rtmIsMajorTimeStep(Microchannel_M)) {
rt_UpdateStructLogVar((StructLogVar *)
Microchannel_DW.ToWorkspace5_PWORK.LoggedData,&locTime,
&Microchannel_B.Product_m);
}
}

/* ToWorkspace: '<S1>/To Workspace6' */
{
double locTime = (((Microchannel_M->Timing.clockTick1+
Microchannel_M->Timing.clockTickH1* 4294967296.0)) *1.0E-5);
;
if (rtmIsMajorTimeStep(Microchannel_M)) {
rt_UpdateStructLogVar((StructLogVar *)
Microchannel_DW.ToWorkspace6_PWORK.LoggedData,&locTime,
&Microchannel_B.Product_d);
}
}
```

```
/* ToWorkspace: '<S1>/To Workspace7' */
{
double locTime = (((Microchannel_M->Timing.clockTick1+
Microchannel_M->Timing.clockTickH1* 4294967296.0)) *1.0E-5);
;
if (rtmIsMajorTimeStep(Microchannel_M)) {
rt_UpdateStructLogVar((StructLogVar *)
Microchannel_DW.ToWorkspace7_PWORK.LoggedData,&locTime, &Microchannel_B.Add3);
}
}

/* Sum: '<S14>/Add1' */
rtb_Sqrt = Microchannel_B.Add - Microchannel_B.Product;

/* Math: '<S14>/Math Function2' incorporates:
      *  Constant: '<S14>/Constant9'
*/
if ((rtb_Sqrt < 0.0) && (Microchannel_P.Constant9_Value > floor
(Microchannel_P.Constant9_Value))) {
rtb_Add5 = -rt_powd_snf(-rtb_Sqrt, Microchannel_P.Constant9_Value);
} else {
rtb_Add5 = rt_powd_snf(rtb_Sqrt, Microchannel_P.Constant9_Value);
}

/* End of Math: '<S14>/Math Function2' */

/* Math: '<S14>/Math Function6' incorporates:
      *  Constant: '<S14>/Constant12'
*/
if ((rtb_Sqrt < 0.0) && (Microchannel_P.Constant12_Value > floor
(Microchannel_P.Constant12_Value))) {
rtb_Sqrt = -rt_powd_snf(-rtb_Sqrt, Microchannel_P.Constant12_Value);
} else {
rtb_Sqrt = rt_powd_snf(rtb_Sqrt, Microchannel_P.Constant12_Value);
}

/* End of Math: '<S14>/Math Function6' */

/* Math: '<S14>/Math Function5' incorporates:
      *  Constant: '<S14>/Constant11'
      *  Constant: '<S14>/D column'
*/
if ((Microchannel_P.Dcolumn_Value < 0.0) && (Microchannel_P.Constant11_Value
> floor(Microchannel_P.Constant11_Value))) { Divide_h_tmp = -
rt_powd_snf(-Microchannel_P.Dcolumn_Value,
Microchannel_P.Constant11_Value);
```

```
} else {
Divide_h_tmp = rt_powd_snf(Microchannel_P.Dcolumn_Value,
Microchannel_P.Constant11_Value);
}

/* End of Math: '<S14>/Math Function5' */

/* Product: '<S14>/Product1' incorporates:
      *  Constant: '<S14>/Constant1'
      *  Constant: '<S14>/Constant4'
      *  Constant: '<S14>/Constant8'
      *  Product: '<S14>/Divide2'
      *  Product: '<S14>/Divide3'
*/
rtb_Sqrt *= Microchannel_P.Constant4_Value / Divide_h_tmp *
Microchannel_P.Constant1_Value_e * (Microchannel_P.Constant8_Value /rtb_Add5);

/* Sum: '<S14>/Add5' incorporates:
      *  Constant: '<S14>/Constant10'
      *  Product: '<S14>/Product3'
*  Sum: '<S14>/Add4'
*/
rtb_Add5 = (Microchannel_P.Constant10_Value - rtb_Sqrt) *
Microchannel_B.Product1_c + rtb_Sqrt;

/* Product: '<S32>/Divide' */
rtb_MathFunction_on = Microchannel_B.Add / rtb_Add5;

/* Math: '<S32>/Math Function1' incorporates:
      *  Constant: '<S32>/Constant4'
*/
if ((rtb_MathFunction_on < 0.0) && (Microchannel_P.Constant4_Value_m > floor
(Microchannel_P.Constant4_Value_m))) {
rtb_MathFunction_on = -rt_powd_snf(-rtb_MathFunction_on,
Microchannel_P.Constant4_Value_m);
} else {
rtb_MathFunction_on = rt_powd_snf(rtb_MathFunction_on,
Microchannel_P.Constant4_Value_m);
}

/* End of Math: '<S32>/Math Function1' */

/* Math: '<S32>/Math Function' incorporates:
      *  Constant: '<Root>/Dc (m)1'
      *  Constant: '<S32>/Constant3'
*/
if ((Microchannel_P.Dcm1_Value < 0.0) && (Microchannel_P.Constant3_Value_k >
floor(Microchannel_P.Constant3_Value_k))) {
```

```
Divide_h_tmp = -rt_powd_snf(-Microchannel_P.Dcm1_Value,
Microchannel_P.Constant3_Value_k);
} else {
Divide_h_tmp = rt_powd_snf(Microchannel_P.Dcm1_Value,Microchannel_P.Constant3_Value_k);
}

/* End of Math: '<S32>/Math Function' */

/* Gain: '<S33>/Gain' incorporates:
      *  Constant: '<S32>/Constant2'
      *  Product: '<S32>/Product4'
      *  Product: '<S32>/Product5'
      *  Product: '<S33>/Divide'
      *  Product: '<S33>/Product'
      *  Product: '<S33>/Product2'
*  Sum: '<S33>/Add'
*  Sum: '<S33>/Add2'
*/
Microchannel_B.Gain_bh = ((Microchannel_B.Add - Microchannel_B.Product) -
Microchannel_B.Add) * Microchannel_B.Ccoinlet / (rtb_MathFunction_on *
Microchannel_P.Constant2_Value_n * Divide_h_tmp * rtb_Sqrt) *
Microchannel_P.Gain_Gain_k;
}

/* Integrator: '<S25>/Integrator' */
if (Microchannel_DW.Integrator_IWORK_k != 0) {
Microchannel_X.Integrator_CSTATE_n = Microchannel_B.Gain_bh;
}

/* Integrator: '<S25>/Integrator' */
Microchannel_B.Integrator_c = Microchannel_X.Integrator_CSTATE_n;

/* Sum: '<S1>/Add' */
rtb_Product2_k = Microchannel_B.Integrator - Microchannel_B.Product;

/* Product: '<S25>/Product2' */
Microchannel_B.Product2 = Microchannel_B.Integrator_c * rtb_Product2_k;if
(rtmIsMajorTimeStep(Microchannel_M)) {
/* Math: '<S30>/Math Function1' incorporates:
      *  Constant: '<Root>/Dc (m)1'
      *  Constant: '<S30>/Constant1'
*/
if ((Microchannel_P.Dcm1_Value < 0.0) && (Microchannel_P.Constant1_Value_dq >
floor(Microchannel_P.Constant1_Value_dq))) {
Divide_h_tmp = -rt_powd_snf(-Microchannel_P.Dcm1_Value,
Microchannel_P.Constant1_Value_dq);
} else {
Divide_h_tmp = rt_powd_snf(Microchannel_P.Dcm1_Value,
```

```
Microchannel_P.Constant1_Value_dq);
}

/* End of Math: '<S30>/Math Function1' */

/* Math: '<S30>/Math Function' incorporates:
      *  Constant: '<S30>/Constant2'
*/
if ((Microchannel_B.Add < 0.0) && (Microchannel_P.Constant2_Value_p > floor
(Microchannel_P.Constant2_Value_p))) {
rtb_MathFunction_on = -rt_powd_snf(-Microchannel_B.Add,
Microchannel_P.Constant2_Value_p);
} else {
rtb_MathFunction_on = rt_powd_snf(Microchannel_B.Add,Microchannel_P.Constant2_Value_p);
}

/* End of Math: '<S30>/Math Function' */

/* Product: '<S30>/Product5' incorporates:
      *  Constant: '<S30>/Constant3'
      *  Product: '<S30>/Product4'
*/
rtb_Product5_p = Divide_h_tmp * rtb_MathFunction_on *Microchannel_P.Constant3_Value_e;

/* Gain: '<S31>/Gain' incorporates:
      *  Product: '<S31>/Divide'
      *  Product: '<S31>/Product'
      *  Product: '<S31>/Product4'
*  Sum: '<S31>/Add'
*/
Microchannel_B.Gain_h = (Microchannel_B.Product - Microchannel_B.Add) *
Microchannel_B.Ccoinlet / (Microchannel_B.Product1_c * rtb_Product5_p) *
Microchannel_P.Gain_Gain_f;
}

/* Integrator: '<S24>/Integrator 1' */
if (Microchannel_DW.Integrator1_IWORK_o != 0) {
Microchannel_X.Integrator1_CSTATE_j = Microchannel_B.Gain_h;
}

/* Integrator: '<S24>/Integrator 1' */ Microchannel_B.Integrator1_b
= Microchannel_X.Integrator1_CSTATE_j;

/* Product: '<S24>/Product1' */
Microchannel_B.Product1_k = Microchannel_B.Integrator1_b *
Microchannel_B.Product;
if (rtmIsMajorTimeStep(Microchannel_M)) {
```

```
/* Product: '<S37>/Divide' */
rtb_MathFunction_on = Microchannel_B.Add / rtb_Add5;

/* Math: '<S37>/Math Function1' incorporates:
      *  Constant: '<S37>/Constant1'
*/
if ((rtb_MathFunction_on < 0.0) && (Microchannel_P.Constant1_Value_k > floor
(Microchannel_P.Constant1_Value_k))) {
rtb_MathFunction_on = -rt_powd_snf(-rtb_MathFunction_on,
Microchannel_P.Constant1_Value_k);
} else {
rtb_MathFunction_on = rt_powd_snf(rtb_MathFunction_on,
Microchannel_P.Constant1_Value_k);
}

/* End of Math: '<S37>/Math Function1' */

/* Math: '<S37>/Math Function' incorporates:
      *  Constant: '<Root>/Dc (m)1'
      *  Constant: '<S37>/Constant3'
*/
if ((Microchannel_P.Dcm1_Value < 0.0) && (Microchannel_P.Constant3_Value_a >
floor(Microchannel_P.Constant3_Value_a))) {
Divide_h_tmp = -rt_powd_snf(-Microchannel_P.Dcm1_Value,
Microchannel_P.Constant3_Value_a);
} else {
Divide_h_tmp = rt_powd_snf(Microchannel_P.Dcm1_Value,Microchannel_P.Constant3_Value_a);
}

/* End of Math: '<S37>/Math Function' */

/* Gain: '<S38>/Gain' incorporates:
      *  Constant: '<S37>/Constant2'
      *  Product: '<S37>/Product'
      *  Product: '<S37>/Product5'
      *  Product: '<S38>/Divide'
      *  Product: '<S38>/Product'
      *  Product: '<S38>/Product4'
*  Sum: '<S38>/Add'
*  Sum: '<S38>/Add2'
*/
Microchannel_B.Gain_p = ((Microchannel_B.Add - Microchannel_B.Product) -
Microchannel_B.Add) * Microchannel_B.CH2inlet / (rtb_MathFunction_on *
Microchannel_P.Constant2_Value_c * Divide_h_tmp * rtb_Sqrt) *
Microchannel_P.Gain_Gain_f1;
}

/* Integrator: '<S28>/Integrator 1' */
```

```
if (Microchannel_DW.Integrator1_IWORK_f != 0) {
Microchannel_X.Integrator1_CSTATE_f = Microchannel_B.Gain_p;
}

/* Integrator: '<S28>/Integrator 1' */ Microchannel_B.Integrator1_l
= Microchannel_X.Integrator1_CSTATE_f;

/* Product: '<S28>/Product2' */
rtb_Product2_k *= Microchannel_B.Integrator1_l;if
(rtmIsMajorTimeStep(Microchannel_M)) {
/* Math: '<S35>/Math Function1' incorporates:
      *  Constant: '<Root>/Dc (m)1'
      *  Constant: '<S35>/Constant1'
*/
if ((Microchannel_P.Dcm1_Value < 0.0) && (Microchannel_P.Constant1_Value_f >
floor(Microchannel_P.Constant1_Value_f))) {
Divide_h_tmp = -rt_powd_snf(-Microchannel_P.Dcm1_Value,
Microchannel_P.Constant1_Value_f);
} else {
Divide_h_tmp = rt_powd_snf(Microchannel_P.Dcm1_Value,Microchannel_P.Constant1_Value_f);
}

/* End of Math: '<S35>/Math Function1' */

/* Math: '<S35>/Math Function' incorporates:
      *  Constant: '<S35>/Constant2'
*/
if ((Microchannel_B.Add < 0.0) && (Microchannel_P.Constant2_Value_a > floor
(Microchannel_P.Constant2_Value_a))) {
rtb_MathFunction_on = -rt_powd_snf(-Microchannel_B.Add,
Microchannel_P.Constant2_Value_a);
} else {
rtb_MathFunction_on = rt_powd_snf(Microchannel_B.Add,Microchannel_P.Constant2_Value_a);
}

/* End of Math: '<S35>/Math Function' */

/* Product: '<S36>/Divide' incorporates:
      *  Constant: '<S35>/Constant'
      *  Product: '<S35>/Product'
      *  Product: '<S35>/Product5'
      *  Product: '<S36>/Product'
      *  Product: '<S36>/Product4'
*  Sum: '<S36>/Add'
*/
Microchannel_B.Divide_a = (Microchannel_B.Product - Microchannel_B.Add) *
Microchannel_B.CH2inlet / (Divide_h_tmp * rtb_MathFunction_on *
```

```
Microchannel_P.Constant_Value_mf * Microchannel_B.Product1_c);
}

/* Integrator: '<S27>/Integrator 1' */
if (Microchannel_DW.Integrator1_IWORK_k != 0) {
Microchannel_X.Integrator1_CSTATE_d = Microchannel_B.Divide_a;
}

/* Integrator: '<S27>/Integrator 1' */ Microchannel_B.Integrator1_g
= Microchannel_X.Integrator1_CSTATE_d;

/* Product: '<S27>/Product1' */
rtb_MathFunction_on = Microchannel_B.Integrator1_g * Microchannel_B.Product;

/* Sum: '<S15>/Add' */
Microchannel_B.Add_e = ((Microchannel_B.Product2 + Microchannel_B.Product1_k)
+ rtb_Product2_k) + rtb_MathFunction_on;if
(rtmIsMajorTimeStep(Microchannel_M)) {
/* Scope: '<S5>/Scope' */
if (rtmIsMajorTimeStep(Microchannel_M)) {StructLogVar
*svar = (StructLogVar *)
Microchannel_DW.Scope_PWORK.LoggedData;LogVar *var
= svar->signals.values;

/* time */
{
double locTime = (((Microchannel_M->Timing.clockTick1+
Microchannel_M->Timing.clockTickH1* 4294967296.0)) *1.0E-5);
;
rt_UpdateLogVar((LogVar *)svar->time, &locTime, 0);
}

/* signals */
{
real_T up0[1];
up0[0] = Microchannel_B.Product_dy;
rt_UpdateLogVar((LogVar *)var, up0, 0);
}
}

/* Gain: '<S1>/Gain1' incorporates:
      *  Constant: '<Root>/density p (kg//m3)'
*/
Microchannel_B.Gain1_g = Microchannel_P.Gain1_Gain_j *
Microchannel_P.densitypkgm3_Value;
}

/* Sum: '<S7>/Add3' */
```

```
Microchannel_B.Add3_h = rtb_Product_bj + rtb_Divide_p;if
(rtmIsMajorTimeStep(Microchannel_M)) {
/* Scope: '<S11>/Scope' */
if (rtmIsMajorTimeStep(Microchannel_M)) {StructLogVar
*svar = (StructLogVar *)
Microchannel_DW.Scope_PWORK_n.LoggedData;LogVar
*var = svar->signals.values;

/* time */
{
double locTime = (((Microchannel_M->Timing.clockTick1+
Microchannel_M->Timing.clockTickH1* 4294967296.0)) *1.0E-5);
;
rt_UpdateLogVar((LogVar *)svar->time, &locTime, 0);
}

/* signals */
{
real_T up0[1];
up0[0] = Microchannel_B.Product_n;
rt_UpdateLogVar((LogVar *)var, up0, 0);
}
}

/* Gain: '<S12>/Gain' incorporates:
      *  Constant: '<Root>/H2 diff'
      *  Constant: '<S12>/Dref (m2//s)'
      *  Product: '<S12>/Divide'
      *  Sqrt: '<S12>/Sqrt'
*/
Microchannel_B.Gain_m = sqrt(Microchannel_P.H2diff_Value /
Microchannel_P.Drefm2s_Value_f) * Microchannel_P.Gain_Gain_k2;
}

/* Product: '<S12>/Product' */
Microchannel_B.Product_dt = Microchannel_B.Gain_m * Microchannel_B.Product_m;if
(rtmIsMajorTimeStep(Microchannel_M)) {
/* Scope: '<S12>/Scope' */
if (rtmIsMajorTimeStep(Microchannel_M)) {StructLogVar
*svar = (StructLogVar *)
Microchannel_DW.Scope_PWORK_c.LoggedData;LogVar
*var = svar->signals.values;

/* time */
{
double locTime = (((Microchannel_M->Timing.clockTick1+
Microchannel_M->Timing.clockTickH1* 4294967296.0)) *1.0E-5);
```

```
;
rt_UpdateLogVar((LogVar *)svar->time, &locTime, 0);
}

/* signals */
{
real_T up0[1];
up0[0] = Microchannel_B.Product_dt;
rt_UpdateLogVar((LogVar *)var, up0, 0);
}
}

/* Product: '<S13>/Product' incorporates:
      *  Constant: '<Root>/H2 diff'
      *  Constant: '<S13>/Dref (m2//s)'
      *  Gain: '<S13>/Gain'
      *  Product: '<S13>/Divide'
      *  Sqrt: '<S13>/Sqrt'
*/
Microchannel_B.Product_i = sqrt(Microchannel_P.H2diff_Value /
Microchannel_P.Drefm2s_Value_d) * Microchannel_P.Gain_Gain_p *
Microchannel_B.Product1_c;

/* Scope: '<S13>/Scope' */
if (rtmIsMajorTimeStep(Microchannel_M)) {StructLogVar
*svar = (StructLogVar *)
Microchannel_DW.Scope_PWORK_k.LoggedData;LogVar
*var = svar->signals.values;

/* time */
{
double locTime = (((Microchannel_M->Timing.clockTick1+
Microchannel_M->Timing.clockTickH1* 4294967296.0)) *1.0E-5);
;
rt_UpdateLogVar((LogVar *)svar->time, &locTime, 0);
}

/* signals */
{
real_T up0[1];
up0[0] = Microchannel_B.Product_i;
rt_UpdateLogVar((LogVar *)var, up0, 0);
}
}

/* Scope: '<S14>/Scope' */
if (rtmIsMajorTimeStep(Microchannel_M)) {StructLogVar
*svar = (StructLogVar *)
```

```
Microchannel_DW.Scope_PWORK_cl.LoggedData;LogVar
*var = svar->signals.values;

/* time */
{
double locTime = (((Microchannel_M->Timing.clockTick1+
Microchannel_M->Timing.clockTickH1* 4294967296.0)) *1.0E-5);
;
rt_UpdateLogVar((LogVar *)svar->time, &locTime, 0);
}

/* signals */
{
real_T up0[1];
up0[0] = Microchannel_B.Product_m;
rt_UpdateLogVar((LogVar *)var, up0, 0);
}
}
}

/* Sum: '<S24>/Add3' incorporates:
    *  Constant: '<S24>/Constant1'
*/
Microchannel_B.Add3_p = Microchannel_P.Constant1_Value_dqi -
Microchannel_B.Add3;
if (rtmIsMajorTimeStep(Microchannel_M)) {
}

/* Product: '<S28>/Product1' incorporates:
    *  Product: '<S28>/Product'
*  Sum: '<S28>/Add'
*/
Microchannel_B.Product1_bk = (Microchannel_B.Product3_p *
Microchannel_B.Integrator2_k - Microchannel_B.Integrator2_d) *
Microchannel_B.Product_dt;
if (rtmIsMajorTimeStep(Microchannel_M)) {
}

/* Product:  '<S24>/Product3'  */ Microchannel_B.Product3_b
= Microchannel_B.Integrator2 *
Microchannel_B.Product3;

/* Sum: '<S24>/Add' */
Microchannel_B.Add_d = Microchannel_B.Product3_b -
Microchannel_B.Integrator2_a;

/* Product: '<S24>/Product' */
Microchannel_B.Product_ic = Microchannel_B.Add_d * Microchannel_B.Product_n;
```

```
if (rtmIsMajorTimeStep(Microchannel_M)) {
}

/* Gain: '<S24>/Gain' */
Microchannel_B.Gain_i = Microchannel_P.Gain_Gain_o * Microchannel_B.Product_ic;if
(rtmIsMajorTimeStep(Microchannel_M)) {
}

/* Product: '<S24>/Product2' incorporates:
    *  Product: '<S27>/Product2'
*/
rtb_Divide_p = Microchannel_B.Product1_c * Microchannel_B.Product_dy;

/* Product: '<S24>/Divide' incorporates:
    *  Gain: '<S24>/Gain1'
    *  Product: '<S24>/Product2'
*  Sum: '<S24>/Add1'
*/
Microchannel_B.Divide_i = (Microchannel_B.Gain_i - Microchannel_B.Product1_k) /
(rtb_Divide_p * Microchannel_P.Gain1_Gain_n);
if (rtmIsMajorTimeStep(Microchannel_M)) {
/* Scope: '<S24>/C, CO,SB(mol//m3)8' */ if
(rtmIsMajorTimeStep(Microchannel_M)) {
StructLogVar *svar = (StructLogVar *) Microchannel_DW.CCOSBmolm38_PWORK.LoggedData;
LogVar *var = svar->signals.values;

/* time */
{
double locTime = (((Microchannel_M->Timing.clockTick1+
Microchannel_M->Timing.clockTickH1* 4294967296.0)) *1.0E-5);
;
rt_UpdateLogVar((LogVar *)svar->time, &locTime, 0);
}

/* signals */
{
real_T up0[1];
up0[0] = Microchannel_B.Add3_p;
rt_UpdateLogVar((LogVar *)var, up0, 0);
}
}
}

/* Sum: '<S25>/Add' incorporates:
    *  Product: '<S25>/Product'
*/
Microchannel_B.Add_g = Microchannel_B.Product3 * Microchannel_B.Integrator1 -
```

```
Microchannel_B.Integrator2_a;
if (rtmIsMajorTimeStep(Microchannel_M)) {
}

/* Product: '<S25>/Product1' */
Microchannel_B.Product1_p = Microchannel_B.Add_g * Microchannel_B.Product_d;if
(rtmIsMajorTimeStep(Microchannel_M)) {
}

/* Product: '<S25>/Product3' incorporates:
    *  Product: '<S28>/Product3'
*/
rtb_Sqrt = Microchannel_B.Product_m * Microchannel_B.Product1_o;

/* Product: '<S25>/Divide' incorporates:
    *  Product: '<S25>/Product3'
*  Sum: '<S25>/Add1'
*/
Microchannel_B.Divide_c = (Microchannel_B.Product2 + Microchannel_B.Product1_p)
/ rtb_Sqrt;
if (rtmIsMajorTimeStep(Microchannel_M)) {
}

/* Product: '<S26>/Product1' incorporates:
    *  Constant: '<Root>/Cv (v//v)1'
*/
Microchannel_B.Product1_a = Microchannel_B.Add3_p * Microchannel_B.Gain_b *
Microchannel_B.Gain1_g * Microchannel_P.Cvvv1_Value;
if (rtmIsMajorTimeStep(Microchannel_M)) {
/* Gain: '<S34>/Gain' incorporates:
      *  Constant: '<Root>/UL (m//s)1'
      *  Constant: '<S34>/Constant'
      *  Gain: '<S34>/Gain1'
      *  Product: '<S34>/Divide'
      *  Product: '<S34>/Product'
      *  Product: '<S34>/Product3'
*  Sum: '<S34>/Add'
*/
Microchannel_B.Gain_d = Microchannel_P.ULms1_Value * Microchannel_B.Product1
       * Microchannel_P.Gain1_Gain_g / ((Microchannel_P.Constant_Value_k3 -
       rtb_Add5) * rtb_Product5_p) * Microchannel_P.Gain_Gain_lb;
}

/* Integrator: '<S26>/Integrator 1' */
if (Microchannel_DW.Integrator1_IWORK_i != 0) {
Microchannel_X.Integrator1_CSTATE_c = Microchannel_B.Gain_d;
}

/* Integrator: '<S26>/Integrator 1' */
```

```
Microchannel_B.Integrator1_a = Microchannel_X.Integrator1_CSTATE_c;

/* Product: '<S26>/Product' incorporates:
    *  Constant: '<Root>/UL (m//s)1'
*/
Microchannel_B.Product_mr = Microchannel_B.Integrator1_a *Microchannel_P.ULms1_Value;
if (rtmIsMajorTimeStep(Microchannel_M)) {
}

/* Product: '<S26>/Product2' incorporates:
    *  Product: '<S29>/Product2'
*/
Divide_h_tmp = Microchannel_B.Add3_p * Microchannel_B.Product_dy;

/* Product: '<S26>/Divide' incorporates:
    *  Gain: '<S26>/Gain'
    *  Product: '<S26>/Product2'
*  Sum: '<S26>/Add'
*/
Microchannel_B.Divide_h = (((Microchannel_B.Product_ic -
Microchannel_B.Product_mr) - Microchannel_B.Product1_a) +
Microchannel_B.Product1_p) / (Divide_h_tmp * Microchannel_P.Gain_Gain_of);
if (rtmIsMajorTimeStep(Microchannel_M)) {
}

/* Product: '<S27>/Product' incorporates:
    *  Product: '<S27>/Product3'
*  Sum: '<S27>/Add'
*/
rtb_Product_bj = (Microchannel_B.Integrator2_b * Microchannel_B.Product3_p -
Microchannel_B.Integrator2_d) * Microchannel_B.Product_i;

/* Product: '<S27>/Divide' incorporates:
    *  Gain: '<S27>/Gain'
    *  Gain: '<S27>/Gain1'
*  Sum: '<S27>/Add1'
*/
Microchannel_B.Divide_b = (Microchannel_P.Gain_Gain_i * rtb_Product_bj -
rtb_MathFunction_on) / (rtb_Divide_p * Microchannel_P.Gain1_Gain_a);
if (rtmIsMajorTimeStep(Microchannel_M)) {
}

/* Product: '<S28>/Divide' incorporates:
*  Sum: '<S28>/Add1'
*/
Microchannel_B.Divide_c2 = (rtb_Product2_k + Microchannel_B.Product1_bk) /
rtb_Sqrt;
if (rtmIsMajorTimeStep(Microchannel_M)) {
```

```
/* Scope: '<S29>/C, H2, L (mol//m3)' */ if
(rtmIsMajorTimeStep(Microchannel_M)) {
StructLogVar *svar = (StructLogVar *)
Microchannel_DW.CH2Lmolm3_PWORK.LoggedData;
LogVar *var = svar->signals.values;

/* time */
{
double locTime = (((Microchannel_M->Timing.clockTick1+
Microchannel_M->Timing.clockTickH1* 4294967296.0)) *1.0E-5);
;
rt_UpdateLogVar((LogVar *)svar->time, &locTime, 0);
}

/* signals */
{
real_T up0[1];
up0[0] = Microchannel_B.Integrator2_d; rt_UpdateLogVar((LogVar
*)var, up0, 0);
}
}

/* Gain: '<S39>/Gain' incorporates:
      *  Constant: '<Root>/UL (m//s)1'
      *  Constant: '<S39>/Constant'
      *  Gain: '<S39>/Gain1'
      *  Product: '<S39>/Divide'
      *  Product: '<S39>/Product'
      *  Product: '<S39>/Product3'
*  Sum: '<S39>/Add'
*/
Microchannel_B.Gain_g = Microchannel_P.ULms1_Value * Microchannel_B.Product_p *
Microchannel_P.Gain1_Gain_c / ((Microchannel_P.Constant_Value_iw - rtb_Add5) *
rtb_Product5_p) *Microchannel_P.Gain_Gain_nv;
}

/* Integrator: '<S29>/Integrator 1' */
if (Microchannel_DW.Integrator1_IWORK_a != 0) {
Microchannel_X.Integrator1_CSTATE_n = Microchannel_B.Gain_g;
}

/* Integrator: '<S29>/Integrator 1' */ Microchannel_B.Integrator1_j
= Microchannel_X.Integrator1_CSTATE_n;

/* Product: '<S29>/Divide' incorporates:
    *  Constant: '<Root>/Cv (v//v)1'
    *  Constant: '<Root>/UL (m//s)1'
```

```
    *  Gain: '<S15>/Gain'
    *  Gain: '<S29>/Gain'
    *  Product: '<S29>/Product'
    *  Product: '<S29>/Product1'
*  Sum: '<S29>/Add'
*/
Microchannel_B.Divide_j = (((rtb_Product_bj - Microchannel_B.Integrator1_j *
Microchannel_P.ULms1_Value) - Microchannel_P.Gain_Gain_e2 * Microchannel_B.Gain_b
* Microchannel_B.Add3_p * Microchannel_B.Gain1_g * Microchannel_P.Cvvv1_Value) +
Microchannel_B.Product1_bk) / (Divide_h_tmp *Microchannel_P.Gain_Gain_o1);
if (rtmIsMajorTimeStep(Microchannel_M)) {
/* Scope: '<S19>/Scope' */
if (rtmIsMajorTimeStep(Microchannel_M)) {StructLogVar
*svar = (StructLogVar *)
Microchannel_DW.Scope_PWORK_p.LoggedData;LogVar
*var = svar->signals.values;

/* time */
{
double locTime = (((Microchannel_M->Timing.clockTick1+
Microchannel_M->Timing.clockTickH1* 4294967296.0)) *1.0E-5);
;
rt_UpdateLogVar((LogVar *)svar->time, &locTime, 0);
}

/* signals */
{
real_T up0[1];
up0[0] = Microchannel_B.Integrator;
rt_UpdateLogVar((LogVar *)var, up0, 0);
}
}
}

/* Product: '<S19>/Divide' */
Microchannel_B.Divide_o = 1.0 / Microchannel_B.Add3_h * Microchannel_B.Add_e;if
(rtmIsMajorTimeStep(Microchannel_M)) {
}

/* Clock: '<S1>/Clock' incorporates:
    *  Clock: '<Root>/Clock'
*/
rtb_Add5 = Microchannel_M->Timing.t[0];

/* Clock: '<S1>/Clock' */ Microchannel_B.Clock
= rtb_Add5;
if (rtmIsMajorTimeStep(Microchannel_M)) {
```

```
/* ToWorkspace: '<S1>/To Workspace1' */
{
double locTime = (((Microchannel_M->Timing.clockTick1+
Microchannel_M->Timing.clockTickH1* 4294967296.0)) *1.0E-5);
;
if (rtmIsMajorTimeStep(Microchannel_M)) {
rt_UpdateStructLogVar((StructLogVar *)
Microchannel_DW.ToWorkspace1_PWORK.LoggedData,&locTime, &Microchannel_B.Clock);
}
}
}

/* Clock: '<Root>/Clock' */
Microchannel_B.Clock_o = rtb_Add5;
if (rtmIsMajorTimeStep(Microchannel_M)) {
}

if (rtmIsMajorTimeStep(Microchannel_M)) {
/* Matfile logging */
rt_UpdateTXYLogVars(Microchannel_M->rtwLogInfo, (Microchannel_M->Timing.t));
}                                      /* end MajorTimeStep */

if (rtmIsMajorTimeStep(Microchannel_M)) {
/* Update for Integrator: '<S24>/Integrator 2' */
Microchannel_DW.Integrator2_IWORK = 0;

/* Update for Integrator: '<S27>/Integrator 2' */Microchannel_DW.Integrator2_IWORK_l =
0;

/* Update for Integrator: '<S25>/Integrator1' */
Microchannel_DW.Integrator1_IWORK = 0;

/* Update for Integrator: '<S28>/Integrator 2' */Microchannel_DW.Integrator2_IWORK_p =
0;

/* Update for Integrator: '<S26>/Integrator 2' */Microchannel_DW.Integrator2_IWORK_g =
0;

/* Update for Integrator: '<S19>/Integrator' */
Microchannel_DW.Integrator_IWORK = 0;

/* Update for Integrator: '<S29>/Integrator 2' */Microchannel_DW.Integrator2_IWORK_m =
0;

/* Update for Integrator: '<S25>/Integrator' */
Microchannel_DW.Integrator_IWORK_k = 0;
```

```
/* Update for Integrator: '<S24>/Integrator 1' */Microchannel_DW.Integrator1_IWORK_o =
0;

/* Update for Integrator: '<S28>/Integrator 1' */Microchannel_DW.Integrator1_IWORK_f =
0;

/* Update for Integrator: '<S27>/Integrator 1' */Microchannel_DW.Integrator1_IWORK_k =
0;

/* Update for Integrator: '<S26>/Integrator 1' */Microchannel_DW.Integrator1_IWORK_i =
0;

/* Update for Integrator: '<S29>/Integrator 1' */Microchannel_DW.Integrator1_IWORK_a =
0;
}                                      /* end MajorTimeStep */

if (rtmIsMajorTimeStep(Microchannel_M)) {
/* signal main to stop simulation */
{                                      /* Sample time: [0.0s, 0.0s] */
if ((rtmGetTFinal(Microchannel_M)!=-1) &&
!((rtmGetTFinal(Microchannel_M)-(((Microchannel_M->Timing.clockTick1+
Microchannel_M->Timing.clockTickH1* 4294967296.0)) * 1.0E-5)) >
(((Microchannel_M->Timing.clockTick1+
Microchannel_M->Timing.clockTickH1* 4294967296.0)) * 1.0E-5) *(DBL_EPSILON))) {
rtmSetErrorStatus(Microchannel_M, "Simulation finished");
}
}

rt_ertODEUpdateContinuousStates(&Microchannel_M->solverInfo);

/* Update absolute time for base rate */
/* The "clockTick0" counts the number of times the code of this task has
      * been executed. The absolute time is the multiplication of "clockTick0"
      * and "Timing.stepSize0". Size of "clockTick0" ensures timer will not
      * overflow during the application lifespan selected.
      * Timer of this task consists of two 32 bit unsigned integers.
      * The two integers represent the low bits Timing.clockTick0 and the high bits
      * Timing.clockTickH0. When the low bit overflows to 0, the high bits increment.
*/
if (!(++Microchannel_M->Timing.clockTick0)) {
++Microchannel_M->Timing.clockTickH0;
}

Microchannel_M->Timing.t[0] = rtsiGetSolverStopTime
(&Microchannel_M->solverInfo);

{
/* Update absolute timer for sample time: [1.0E-5s, 0.0s] */
```

```
/* The "clockTick1" counts the number of times the code of this task has
        * been executed. The resolution of this integer timer is 1.0E-5, which is the ↙
 step size
        * of the task. Size of "clockTick1" ensures timer will not overflow during the
        * application lifespan selected.
        * Timer of this task consists of two 32 bit unsigned integers.
        * The two integers represent the low bits Timing.clockTick1 and the high bits
        * Timing.clockTickH1. When the low bit overflows to 0, the high bits ↙
 increment.
*/
Microchannel_M->Timing.clockTick1++;
if (!Microchannel_M->Timing.clockTick1) {
Microchannel_M->Timing.clockTickH1++;
}
}
}                                      /* end MajorTimeStep */
}

/* Derivatives for root system: '<Root>' */
void Microchannel_derivatives(void)
{
XDot_Microchannel_T *_rtXdot;
boolean_T lsat;
boolean_T usat;
_rtXdot = ((XDot_Microchannel_T *) Microchannel_M->derivs);

/* Derivatives for Integrator: '<S24>/Integrator 2' */lsat
= (Microchannel_X.Integrator2_CSTATE <=
Microchannel_P.Integrator2_LowerSat); usat =
(Microchannel_X.Integrator2_CSTATE >=
Microchannel_P.Integrator2_UpperSat);
if ((!lsat) && (!usat)) || (lsat && (Microchannel_B.Integrator1_b > 0.0)) ||
(usat && (Microchannel_B.Integrator1_b < 0.0))) {
_rtXdot->Integrator2_CSTATE = Microchannel_B.Integrator1_b;
} else {
/* in saturation */
_rtXdot->Integrator2_CSTATE = 0.0;
}

/* End of Derivatives for Integrator: '<S24>/Integrator 2' */

/* Derivatives for Integrator: '<S27>/Integrator 2' */lsat
= (Microchannel_X.Integrator2_CSTATE_h <=
Microchannel_P.Integrator2_LowerSat_n); usat =
(Microchannel_X.Integrator2_CSTATE_h >=
Microchannel_P.Integrator2_UpperSat_o);
if ((!lsat) && (!usat)) || (lsat && (Microchannel_B.Integrator1_g > 0.0)) ||
(usat && (Microchannel_B.Integrator1_g < 0.0))) {
_rtXdot->Integrator2_CSTATE_h = Microchannel_B.Integrator1_g;
```

```
} else {
/* in saturation */
_rtXdot->Integrator2_CSTATE_h = 0.0;
}

/* End of Derivatives for Integrator: '<S27>/Integrator 2' */

/* Derivatives for Integrator: '<S25>/Integrator1' */lsat =
(Microchannel_X.Integrator1_CSTATE <=
Microchannel_P.Integrator1_LowerSat); usat =
(Microchannel_X.Integrator1_CSTATE >=
Microchannel_P.Integrator1_UpperSat);
if (((!lsat) && (!usat)) || (lsat && (Microchannel_B.Integrator_c > 0.0)) ||(usat
&& (Microchannel_B.Integrator_c < 0.0))) {
_rtXdot->Integrator1_CSTATE = Microchannel_B.Integrator_c;
} else {
/* in saturation */
_rtXdot->Integrator1_CSTATE = 0.0;
}

/* End of Derivatives for Integrator: '<S25>/Integrator1' */

/* Derivatives for Integrator: '<S28>/Integrator 2' */lsat
= (Microchannel_X.Integrator2_CSTATE_hb <=
     Microchannel_P.Integrator2_LowerSat_k); usat =
           (Microchannel_X.Integrator2_CSTATE_hb >=
            Microchannel_P.Integrator2_UpperSat_b);
if (((!lsat) && (!usat)) || (lsat && (Microchannel_B.Integrator1_l > 0.0)) ||
(usat && (Microchannel_B.Integrator1_l < 0.0))) {
_rtXdot->Integrator2_CSTATE_hb = Microchannel_B.Integrator1_l;
} else {
/* in saturation */
_rtXdot->Integrator2_CSTATE_hb = 0.0;
}

/* End of Derivatives for Integrator: '<S28>/Integrator 2' */

/* Derivatives for Integrator: '<S26>/Integrator 2' */lsat
= (Microchannel_X.Integrator2_CSTATE_d <=
Microchannel_P.Integrator2_LowerSat_i); usat =
(Microchannel_X.Integrator2_CSTATE_d >=
Microchannel_P.Integrator2_UpperSat_e);
if (((!lsat) && (!usat)) || (lsat && (Microchannel_B.Integrator1_a > 0.0)) ||
(usat && (Microchannel_B.Integrator1_a < 0.0))) {
_rtXdot->Integrator2_CSTATE_d = Microchannel_B.Integrator1_a;
} else {
/* in saturation */
_rtXdot->Integrator2_CSTATE_d = 0.0;
}
```

```
/* End of Derivatives for Integrator: '<S26>/Integrator 2' */

/* Derivatives for Integrator: '<S19>/Integrator' */
lsat = (Microchannel_X.Integrator_CSTATE <= Microchannel_P.Integrator_LowerSat); usat
=   (Microchannel_X.Integrator_CSTATE   >=   Microchannel_P.Integrator_UpperSat);   if
((((!lsat) && (!usat)) || (lsat && (Microchannel_B.Divide_o > 0.0)) || (usat
&& (Microchannel_B.Divide_o < 0.0))) {
_rtXdot->Integrator_CSTATE = Microchannel_B.Divide_o;
} else {
/* in saturation */
_rtXdot->Integrator_CSTATE = 0.0;
}

/* End of Derivatives for Integrator: '<S19>/Integrator' */

/* Derivatives for Integrator: '<S29>/Integrator 2' */lsat
= (Microchannel_X.Integrator2_CSTATE_a <=
Microchannel_P.Integrator2_LowerSat_i2); usat =
(Microchannel_X.Integrator2_CSTATE_a >=
Microchannel_P.Integrator2_UpperSat_ej);
if ((((!lsat) && (!usat)) || (lsat && (Microchannel_B.Integrator1_j > 0.0)) ||
(usat && (Microchannel_B.Integrator1_j < 0.0))) {
_rtXdot->Integrator2_CSTATE_a = Microchannel_B.Integrator1_j;
} else {
/* in saturation */
_rtXdot->Integrator2_CSTATE_a = 0.0;
}

/* End of Derivatives for Integrator: '<S29>/Integrator 2' */

/* Derivatives for Integrator: '<S25>/Integrator' */
_rtXdot->Integrator_CSTATE_n = Microchannel_B.Divide_c;

/* Derivatives for Integrator: '<S24>/Integrator 1' */
_rtXdot->Integrator1_CSTATE_j = Microchannel_B.Divide_i;

/* Derivatives for Integrator: '<S28>/Integrator 1' */
_rtXdot->Integrator1_CSTATE_f = Microchannel_B.Divide_c2;

/* Derivatives for Integrator: '<S27>/Integrator 1' */
_rtXdot->Integrator1_CSTATE_d = Microchannel_B.Divide_b;

/* Derivatives for Integrator: '<S26>/Integrator 1' */
_rtXdot->Integrator1_CSTATE_c = Microchannel_B.Divide_h;

/* Derivatives for Integrator: '<S29>/Integrator 1' */
_rtXdot->Integrator1_CSTATE_n = Microchannel_B.Divide_j;
}
```

```
/* Model initialize function */
void Microchannel_initialize(void)
{
/* Registration code */

/* initialize non-finites */
rt_InitInfAndNaN(sizeof(real_T));

/* non-finite (run-time) assignments */
Microchannel_P.Integrator2_UpperSat = rtInf;
Microchannel_P.Integrator2_UpperSat_o = rtInf;
Microchannel_P.Integrator1_UpperSat = rtInf;
Microchannel_P.Integrator2_UpperSat_b = rtInf;
Microchannel_P.Integrator2_UpperSat_e = rtInf;
Microchannel_P.Integrator_UpperSat = rtInf;
Microchannel_P.Integrator2_UpperSat_ej = rtInf;

/* initialize real-time model */
(void) memset((void *)Microchannel_M, 0,
sizeof(RT_MODEL_Microchannel_T));

{
/* Setup solver object */
rtsiSetSimTimeStepPtr(&Microchannel_M->solverInfo,
&Microchannel_M->Timing.simTimeStep); rtsiSetTPtr(&Microchannel_M-
>solverInfo, &rtmGetTPtr(Microchannel_M));
rtsiSetStepSizePtr(&Microchannel_M->solverInfo,
&Microchannel_M->Timing.stepSize0); rtsiSetdXPtr(&Microchannel_M-
>solverInfo, &Microchannel_M->derivs);
rtsiSetContStatesPtr(&Microchannel_M->solverInfo, (real_T **)
&Microchannel_M->contStates);
rtsiSetNumContStatesPtr(&Microchannel_M->solverInfo,
&Microchannel_M->Sizes.numContStates);
rtsiSetNumPeriodicContStatesPtr(&Microchannel_M->solverInfo,
&Microchannel_M->Sizes.numPeriodicContStates);
rtsiSetPeriodicContStateIndicesPtr(&Microchannel_M->solverInfo,
&Microchannel_M->periodicContStateIndices);
rtsiSetPeriodicContStateRangesPtr(&Microchannel_M->solverInfo,
&Microchannel_M->periodicContStateRanges);
rtsiSetErrorStatusPtr(&Microchannel_M->solverInfo, (&rtmGetErrorStatus
(Microchannel_M)));
rtsiSetRTModelPtr(&Microchannel_M->solverInfo, Microchannel_M);
}

rtsiSetSimTimeStep(&Microchannel_M->solverInfo, MAJOR_TIME_STEP);
Microchannel_M->intgData.y = Microchannel_M->odeY; Microchannel_M-
>intgData.f[0] = Microchannel_M->odeF[0]; Microchannel_M-
>intgData.f[1] = Microchannel_M->odeF[1];
```

```
Microchannel_M->intgData.f[2] = Microchannel_M->odeF[2];
Microchannel_M->contStates = ((X_Microchannel_T *) &Microchannel_X);
rtsiSetSolverData(&Microchannel_M->solverInfo, (void *)
&Microchannel_M->intgData); rtsiSetSolverName(&Microchannel_M-
>solverInfo, "ode3"); rtmSetTPtr(Microchannel_M, &Microchannel_M-
>Timing.tArray[0]);rtmSetTFinal(Microchannel_M, 0.01);
Microchannel_M->Timing.stepSize0 = 1.0E-5;
rtmSetFirstInitCond(Microchannel_M, 1);

/* Setup for data logging */
{
static RTWLogInfo rt_DataLoggingInfo;
rt_DataLoggingInfo.loggingInterval = NULL;
Microchannel_M->rtwLogInfo = &rt_DataLoggingInfo;
}

/* Setup for data logging */
{
rtliSetLogXSignalInfo(Microchannel_M->rtwLogInfo, (NULL));
rtliSetLogXSignalPtrs(Microchannel_M->rtwLogInfo, (NULL));
rtliSetLogT(Microchannel_M->rtwLogInfo, "tout");
rtliSetLogX(Microchannel_M->rtwLogInfo, "");
rtliSetLogXFinal(Microchannel_M->rtwLogInfo, "");
rtliSetLogVarNameModifier(Microchannel_M->rtwLogInfo, "rt_");
rtliSetLogFormat(Microchannel_M->rtwLogInfo, 0);
rtliSetLogMaxRows(Microchannel_M->rtwLogInfo, 1000);
rtliSetLogDecimation(Microchannel_M->rtwLogInfo, 1);

/*
      * Set pointers to the data and signal info for each output
*/
{
static void * rt_LoggedOutputSignalPtrs[] = {
&Microchannel_Y.CCOSBmolm3, &Microchannel_Y.CH2SBmolm3,
&Microchannel_Y.CCOLBmolm3, &Microchannel_Y.CH2LBmolm3
};

rtliSetLogYSignalPtrs(Microchannel_M->rtwLogInfo, ((LogSignalPtrsType)
rt_LoggedOutputSignalPtrs));
}

{
static int_T rt_LoggedOutputWidths[] = {1,
1,
1,
```

```
1
};

static int_T rt_LoggedOutputNumDimensions[] = {1,
1,
1,
1
};

static int_T rt_LoggedOutputDimensions[] = {1,
1,
1,
1
};

static boolean_T rt_LoggedOutputIsVarDims[] = {0,
0,
0
};

static void* rt_LoggedCurrentSignalDimensions[] = {(NULL),
(NULL),
(NULL),(NULL)
};

static int_T rt_LoggedCurrentSignalDimensionsSize[] = {4,
4,
4
};

static   BuiltInDTypeId   rt_LoggedOutputDataTypeIds[]   =   {
SS_DOUBLE,
SS_DOUBLE,
SS_DOUBLE,SS_DOUBLE
};

static int_T rt_LoggedOutputComplexSignals[] = {0,
0,
```

```
0
};

static RTWPreprocessingFcnPtr rt_LoggingPreprocessingFcnPtrs[] = {(NULL),
(NULL),
(NULL),(NULL)
};

static const char_T *rt_LoggedOutputLabels[] = {"",
"",
"",
"" };

static const char_T *rt_LoggedOutputBlockNames[] = {
"Microchannel/C,CO,SB (mol//m3)", "Microchannel/C,H2,SB
(mol//m3)", "Microchannel/C,CO,LB (mol//m3)",
"Microchannel/C,H2,LB (mol//m3)" };

static RTWLogDataTypeConvert rt_RTWLogDataTypeConvert[] = {
         { 0, SS_DOUBLE, SS_DOUBLE, 0, 0, 0, 1.0, 0, 0.0 },

         { 0, SS_DOUBLE, SS_DOUBLE, 0, 0, 0, 1.0, 0, 0.0 },

         { 0, SS_DOUBLE, SS_DOUBLE, 0, 0, 0, 1.0, 0, 0.0 },

         { 0, SS_DOUBLE, SS_DOUBLE, 0, 0, 0, 1.0, 0, 0.0 }
};

static RTWLogSignalInfo rt_LoggedOutputSignalInfo[] = {
{
4,
rt_LoggedOutputWidths,
rt_LoggedOutputNumDimensions,
rt_LoggedOutputDimensions,
rt_LoggedOutputIsVarDims,
rt_LoggedCurrentSignalDimensions,
rt_LoggedCurrentSignalDimensionsSize,
rt_LoggedOutputDataTypeIds,
rt_LoggedOutputComplexSignals, (NULL),
rt_LoggingPreprocessingFcnPtrs,

{ rt_LoggedOutputLabels },(NULL),
(NULL),
```

```
(NULL),

{ rt_LoggedOutputBlockNames },

{ (NULL) },(NULL),
rt_RTWLogDataTypeConvert
}
};

        rtliSetLogYSignalInfo(Microchannel_M->rtwLogInfo,
                              rt_LoggedOutputSignalInfo);

/* set currSigDims field */
rt_LoggedCurrentSignalDimensions[0]     =     &rt_LoggedOutputWidths[0];
rt_LoggedCurrentSignalDimensions[1]     =     &rt_LoggedOutputWidths[1];
rt_LoggedCurrentSignalDimensions[2]     =     &rt_LoggedOutputWidths[2];
rt_LoggedCurrentSignalDimensions[3]  =  &rt_LoggedOutputWidths[3];
}

rtliSetLogY(Microchannel_M->rtwLogInfo,  "yout");
}

/* block I/O */
(void) memset(((void *) &Microchannel_B), 0,
sizeof(B_Microchannel_T));

/* states (continuous) */
{
(void) memset((void *)&Microchannel_X, 0,
sizeof(X_Microchannel_T));
}

/* states (dwork) */
(void) memset((void *)&Microchannel_DW, 0,
sizeof(DW_Microchannel_T));

/* external inputs */
(void)memset(&Microchannel_U, 0, sizeof(ExtU_Microchannel_T));

/* external outputs */
(void) memset((void *)&Microchannel_Y, 0,
sizeof(ExtY_Microchannel_T));

/* Matfile logging */
rt_StartDataLoggingWithStartTime(Microchannel_M->rtwLogInfo, 0.0, rtmGetTFinal
(Microchannel_M), Microchannel_M->Timing.stepSize0, (&rtmGetErrorStatus
(Microchannel_M)));
```

```
/* SetupRuntimeResources for Scope: '<Root>/H2 LB' */
{
RTWLogSignalInfo rt_ScopeSignalInfo;
static int_T rt_ScopeSignalWidths[] = { 1 };

static int_T rt_ScopeSignalNumDimensions[] = { 1 }; static

int_T rt_ScopeSignalDimensions[] = { 1 }; static void

*rt_ScopeCurrSigDims[] = { (NULL) }; static int_T

rt_ScopeCurrSigDimsSize[] = { 4 }; static const char_T

*rt_ScopeSignalLabels[] = { "" };static char_T

rt_ScopeSignalTitles[] = "";
static int_T rt_ScopeSignalTitleLengths[] = { 0 }; static

boolean_T rt_ScopeSignalIsVarDims[] = { 0 };static int_T

rt_ScopeSignalPlotStyles[] = { 0 }; BuiltInDTypeId

dTypes[1] = { SS_DOUBLE };

static char_T rt_ScopeBlockName[] = "Microchannel/H2 LB";static
int_T rt_ScopeFrameData[] = { 0 };

static RTWPreprocessingFcnPtr rt_ScopeSignalLoggingPreprocessingFcnPtrs[] =
{ (NULL)
};

rt_ScopeSignalInfo.numSignals = 1; rt_ScopeSignalInfo.numCols =
rt_ScopeSignalWidths; rt_ScopeSignalInfo.numDims =
rt_ScopeSignalNumDimensions; rt_ScopeSignalInfo.dims =
rt_ScopeSignalDimensions; rt_ScopeSignalInfo.isVarDims =
rt_ScopeSignalIsVarDims; rt_ScopeSignalInfo.currSigDims =
rt_ScopeCurrSigDims; rt_ScopeSignalInfo.currSigDimsSize =
rt_ScopeCurrSigDimsSize;rt_ScopeSignalInfo.dataTypes = dTypes;
rt_ScopeSignalInfo.complexSignals = (NULL);
rt_ScopeSignalInfo.frameData = rt_ScopeFrameData;
rt_ScopeSignalInfo.preprocessingPtrs =
rt_ScopeSignalLoggingPreprocessingFcnPtrs;
rt_ScopeSignalInfo.labels.cptr = rt_ScopeSignalLabels;
rt_ScopeSignalInfo.titles = rt_ScopeSignalTitles;
rt_ScopeSignalInfo.titleLengths = rt_ScopeSignalTitleLengths;
rt_ScopeSignalInfo.plotStyles = rt_ScopeSignalPlotStyles;
rt_ScopeSignalInfo.blockNames.cptr = (NULL);
```

```
rt_ScopeSignalInfo.stateNames.cptr = (NULL);
rt_ScopeSignalInfo.crossMdlRef = (NULL);
rt_ScopeSignalInfo.dataTypeConvert = (NULL);
Microchannel_DW.H2LB_PWORK.LoggedData = rt_CreateStructLogVar(
Microchannel_M->rtwLogInfo,0.0,
rtmGetTFinal(Microchannel_M),
Microchannel_M->Timing.stepSize0,
(&rtmGetErrorStatus(Microchannel_M)),"H2LB",
1,
5000000,
1,
1.0E-5,
&rt_ScopeSignalInfo,
rt_ScopeBlockName);
if (Microchannel_DW.H2LB_PWORK.LoggedData == (NULL))return;
}

/* SetupRuntimeResources for Scope: '<Root>/H2 SB' */
{
RTWLogSignalInfo rt_ScopeSignalInfo;
static int_T rt_ScopeSignalWidths[] = { 1 };

static int_T rt_ScopeSignalNumDimensions[] = { 1 }; static

int_T rt_ScopeSignalDimensions[] = { 1 }; static void

*rt_ScopeCurrSigDims[] = { (NULL) }; static int_T

rt_ScopeCurrSigDimsSize[] = { 4 }; static const char_T

*rt_ScopeSignalLabels[] = { "" };

static char_T rt_ScopeSignalTitles[] = "";
static int_T rt_ScopeSignalTitleLengths[] = { 0 }; static

boolean_T rt_ScopeSignalIsVarDims[] = { 0 };static int_T

rt_ScopeSignalPlotStyles[] = { 0 }; BuiltInDTypeId

dTypes[1] = { SS_DOUBLE };

static char_T rt_ScopeBlockName[] = "Microchannel/H2 SB";static
int_T rt_ScopeFrameData[] = { 0 };

static RTWPreprocessingFcnPtr rt_ScopeSignalLoggingPreprocessingFcnPtrs[] =
{
```

```
(NULL)
};

rt_ScopeSignalInfo.numSignals  =  1; rt_ScopeSignalInfo.numCols =
rt_ScopeSignalWidths; rt_ScopeSignalInfo.numDims =
rt_ScopeSignalNumDimensions; rt_ScopeSignalInfo.dims =
rt_ScopeSignalDimensions; rt_ScopeSignalInfo.isVarDims =
rt_ScopeSignalIsVarDims; rt_ScopeSignalInfo.currSigDims =
rt_ScopeCurrSigDims; rt_ScopeSignalInfo.currSigDimsSize  =
rt_ScopeCurrSigDimsSize;rt_ScopeSignalInfo.dataTypes = dTypes;
rt_ScopeSignalInfo.complexSignals = (NULL);
rt_ScopeSignalInfo.frameData = rt_ScopeFrameData;
rt_ScopeSignalInfo.preprocessingPtrs =
rt_ScopeSignalLoggingPreprocessingFcnPtrs;
rt_ScopeSignalInfo.labels.cptr = rt_ScopeSignalLabels;
rt_ScopeSignalInfo.titles = rt_ScopeSignalTitles;
rt_ScopeSignalInfo.titleLengths = rt_ScopeSignalTitleLengths;
rt_ScopeSignalInfo.plotStyles = rt_ScopeSignalPlotStyles;
rt_ScopeSignalInfo.blockNames.cptr = (NULL);
rt_ScopeSignalInfo.stateNames.cptr = (NULL);
rt_ScopeSignalInfo.crossMdlRef = (NULL);
rt_ScopeSignalInfo.dataTypeConvert = (NULL);
Microchannel_DW.H2SB_PWORK.LoggedData  =  rt_CreateStructLogVar(
Microchannel_M->rtwLogInfo,0.0,
rtmGetTFinal(Microchannel_M),
Microchannel_M->Timing.stepSize0,
(&rtmGetErrorStatus(Microchannel_M)),"COSB",
1,
5000000,
1,
1.0E-5,
&rt_ScopeSignalInfo,
rt_ScopeBlockName);
if  (Microchannel_DW.H2SB_PWORK.LoggedData  ==  (NULL))return;
}

/* SetupRuntimeResources for ToWorkspace: '<Root>/To Workspace' */
{
static int_T rt_ToWksWidths[] = { 1 };

static int_T rt_ToWksNumDimensions[] = { 1 };static

int_T rt_ToWksDimensions[] = { 1 }; static

boolean_T rt_ToWksIsVarDims[] = { 0 };
```

```
static void *rt_ToWksCurrSigDims[] = { (NULL) };static

int_T rt_ToWksCurrSigDimsSize[] = { 4 };

static BuiltInDTypeId rt_ToWksDataTypeIds[] = { SS_DOUBLE };static

int_T rt_ToWksComplexSignals[] = { 0 };

static int_T rt_ToWksFrameData[] = { 0 };

static RTWPreprocessingFcnPtr rt_ToWksLoggingPreprocessingFcnPtrs[] = {(NULL)
};

static const char_T *rt_ToWksLabels[] = { "" };

static RTWLogSignalInfo rt_ToWksSignalInfo = {
1,
rt_ToWksWidths, rt_ToWksNumDimensions,
rt_ToWksDimensions, rt_ToWksIsVarDims,
rt_ToWksCurrSigDims,
rt_ToWksCurrSigDimsSize,
rt_ToWksDataTypeIds,
rt_ToWksComplexSignals, rt_ToWksFrameData,
rt_ToWksLoggingPreprocessingFcnPtrs,

{ rt_ToWksLabels },(NULL),
(NULL),
(NULL),

{ (NULL) },

{ (NULL) },(NULL),
(NULL)
};

static const char_T rt_ToWksBlockName[] = "Microchannel/To Workspace";
Microchannel_DW.ToWorkspace_PWORK.LoggedData = rt_CreateStructLogVar(
Microchannel_M->rtwLogInfo,0.0,
rtmGetTFinal(Microchannel_M),
Microchannel_M->Timing.stepSize0,
(&rtmGetErrorStatus(Microchannel_M)),
```

```
"syncon",1,
0,
1,
1.0E-5,
&rt_ToWksSignalInfo,
rt_ToWksBlockName);
if (Microchannel_DW.ToWorkspace_PWORK.LoggedData == (NULL))return;
}

/* SetupRuntimeResources for Scope: '<S1>/C,CO,L1' */
{
RTWLogSignalInfo rt_ScopeSignalInfo;
static int_T rt_ScopeSignalWidths[] = { 1 };

static int_T rt_ScopeSignalNumDimensions[] = { 1 }; static

int_T rt_ScopeSignalDimensions[] = { 1 }; static void

*rt_ScopeCurrSigDims[] = { (NULL) }; static int_T

rt_ScopeCurrSigDimsSize[] = { 4 }; static const char_T

*rt_ScopeSignalLabels[] = { "" };static char_T

rt_ScopeSignalTitles[] = "";
static int_T rt_ScopeSignalTitleLengths[] = { 0 }; static

boolean_T rt_ScopeSignalIsVarDims[] = { 0 };static int_T

rt_ScopeSignalPlotStyles[] = { 0 }; BuiltInDTypeId

dTypes[1] = { SS_DOUBLE };

static char_T rt_ScopeBlockName[] = "Microchannel/SBCR model/C,CO,L1";static
int_T rt_ScopeFrameData[] = { 0 };

static RTWPreprocessingFcnPtr rt_ScopeSignalLoggingPreprocessingFcnPtrs[] =
{ (NULL)
};

rt_ScopeSignalInfo.numSignals = 1; rt_ScopeSignalInfo.numCols =
rt_ScopeSignalWidths; rt_ScopeSignalInfo.numDims =
rt_ScopeSignalNumDimensions;rt_ScopeSignalInfo.dims =
rt_ScopeSignalDimensions; rt_ScopeSignalInfo.isVarDims =
rt_ScopeSignalIsVarDims; rt_ScopeSignalInfo.currSigDims =
rt_ScopeCurrSigDims;
```

```
rt_ScopeSignalInfo.currSigDimsSize = rt_ScopeCurrSigDimsSize;
rt_ScopeSignalInfo.dataTypes = dTypes;
rt_ScopeSignalInfo.complexSignals = (NULL);
rt_ScopeSignalInfo.frameData = rt_ScopeFrameData;
rt_ScopeSignalInfo.preprocessingPtrs =
rt_ScopeSignalLoggingPreprocessingFcnPtrs; rt_ScopeSignalInfo.labels.cptr
= rt_ScopeSignalLabels; rt_ScopeSignalInfo.titles =
rt_ScopeSignalTitles; rt_ScopeSignalInfo.titleLengths =
rt_ScopeSignalTitleLengths; rt_ScopeSignalInfo.plotStyles =
rt_ScopeSignalPlotStyles; rt_ScopeSignalInfo.blockNames.cptr = (NULL);
rt_ScopeSignalInfo.stateNames.cptr = (NULL);
rt_ScopeSignalInfo.crossMdlRef = (NULL);
rt_ScopeSignalInfo.dataTypeConvert = (NULL);
Microchannel_DW.CCOL1_PWORK.LoggedData = rt_CreateStructLogVar(
Microchannel_M->rtwLogInfo,0.0,
rtmGetTFinal(Microchannel_M),
Microchannel_M->Timing.stepSize0,
(&rtmGetErrorStatus(Microchannel_M)),"ELB",
1,
5000,
1,
1.0E-5,
&rt_ScopeSignalInfo,
rt_ScopeBlockName);
if (Microchannel_DW.CCOL1_PWORK.LoggedData == (NULL))return;
}

/* SetupRuntimeResources for ToWorkspace: '<S1>/To Workspace' */
{
static int_T rt_ToWksWidths[] = { 1 };

static int_T rt_ToWksNumDimensions[] = { 1 }; static

int_T rt_ToWksDimensions[] = { 1 }; static boolean_T

rt_ToWksIsVarDims[] = { 0 }; static void

*rt_ToWksCurrSigDims[] = { (NULL) };static int_T

rt_ToWksCurrSigDimsSize[] = { 4 };

static BuiltInDTypeId rt_ToWksDataTypeIds[] = { SS_DOUBLE };static

int_T rt_ToWksComplexSignals[] = { 0 };
```

```
static int_T rt_ToWksFrameData[] = { 0 };

static RTWPreprocessingFcnPtr rt_ToWksLoggingPreprocessingFcnPtrs[] = {(NULL)
};

static const char_T *rt_ToWksLabels[] = { "" };

static RTWLogSignalInfo rt_ToWksSignalInfo = {
1,
rt_ToWksWidths, rt_ToWksNumDimensions,
rt_ToWksDimensions, rt_ToWksIsVarDims,
rt_ToWksCurrSigDims,
rt_ToWksCurrSigDimsSize,
rt_ToWksDataTypeIds,
rt_ToWksComplexSignals, rt_ToWksFrameData,
rt_ToWksLoggingPreprocessingFcnPtrs,

{ rt_ToWksLabels },(NULL),
(NULL),
(NULL),

{ (NULL) },

{ (NULL) },(NULL),
(NULL)
};

static const char_T rt_ToWksBlockName[] =
"Microchannel/SBCR model/To Workspace";
Microchannel_DW.ToWorkspace_PWORK_g.LoggedData = rt_CreateStructLogVar(
Microchannel_M->rtwLogInfo,
0.0,
rtmGetTFinal(Microchannel_M),
Microchannel_M->Timing.stepSize0,
(&rtmGetErrorStatus(Microchannel_M)),"Rco",
0,
0,
1,
1.0E-5,
&rt_ToWksSignalInfo,
rt_ToWksBlockName);
if (Microchannel_DW.ToWorkspace_PWORK_g.LoggedData == (NULL))
```

```
return;
}

/* SetupRuntimeResources for ToWorkspace: '<S1>/To Workspace2' */
{
static int_T rt_ToWksWidths[] = { 1 };

static int_T rt_ToWksNumDimensions[] = { 1 }; static

int_T rt_ToWksDimensions[] = { 1 }; static boolean_T

rt_ToWksIsVarDims[] = { 0 }; static void

*rt_ToWksCurrSigDims[] = { (NULL) };static int_T

rt_ToWksCurrSigDimsSize[] = { 4 };

static BuiltInDTypeId rt_ToWksDataTypeIds[] = { SS_DOUBLE };static

int_T rt_ToWksComplexSignals[] = { 0 };

static int_T rt_ToWksFrameData[] = { 0 };

static RTWPreprocessingFcnPtr rt_ToWksLoggingPreprocessingFcnPtrs[] = {(NULL)
};

static const char_T *rt_ToWksLabels[] = { "" };

static RTWLogSignalInfo rt_ToWksSignalInfo = {
1,
rt_ToWksWidths, rt_ToWksNumDimensions,
rt_ToWksDimensions, rt_ToWksIsVarDims,
rt_ToWksCurrSigDims,
rt_ToWksCurrSigDimsSize,
rt_ToWksDataTypeIds,
rt_ToWksComplexSignals, rt_ToWksFrameData,
rt_ToWksLoggingPreprocessingFcnPtrs,

{ rt_ToWksLabels },(NULL),
(NULL),
(NULL),

{ (NULL) },
```

```
{ (NULL) },(NULL),
(NULL)
};

static const char_T rt_ToWksBlockName[] =
"Microchannel/SBCR model/To Workspace2";
Microchannel_DW.ToWorkspace2_PWORK.LoggedData = rt_CreateStructLogVar(
Microchannel_M->rtwLogInfo,
0.0,
rtmGetTFinal(Microchannel_M),
Microchannel_M->Timing.stepSize0,
(&rtmGetErrorStatus(Microchannel_M)),
"Gasflow",
1,
0,
1,
1.0E-5,
&rt_ToWksSignalInfo,
rt_ToWksBlockName);
if (Microchannel_DW.ToWorkspace2_PWORK.LoggedData == (NULL))return;
}

/* SetupRuntimeResources for ToWorkspace: '<S1>/To Workspace3' */
{
static int_T rt_ToWksWidths[] = { 1 };

static int_T rt_ToWksNumDimensions[] = { 1 }; static

int_T rt_ToWksDimensions[] = { 1 }; static boolean_T

rt_ToWksIsVarDims[] = { 0 }; static void

*rt_ToWksCurrSigDims[] = { (NULL) };static int_T

rt_ToWksCurrSigDimsSize[] = { 4 };

static BuiltInDTypeId rt_ToWksDataTypeIds[] = { SS_DOUBLE };static

int_T rt_ToWksComplexSignals[] = { 0 };

static int_T rt_ToWksFrameData[] = { 0 };

static RTWPreprocessingFcnPtr rt_ToWksLoggingPreprocessingFcnPtrs[] = {(NULL)
};

static const char_T *rt_ToWksLabels[] = { "" };
```

```
static RTWLogSignalInfo rt_ToWksSignalInfo = {1,
rt_ToWksWidths, rt_ToWksNumDimensions,
rt_ToWksDimensions, rt_ToWksIsVarDims,
rt_ToWksCurrSigDims,
rt_ToWksCurrSigDimsSize,
rt_ToWksDataTypeIds,
rt_ToWksComplexSignals, rt_ToWksFrameData,
rt_ToWksLoggingPreprocessingFcnPtrs,

{ rt_ToWksLabels },(NULL),
(NULL),
(NULL),

{ (NULL) },

{ (NULL) },(NULL),
(NULL)
};

static const char_T rt_ToWksBlockName[] =
"Microchannel/SBCR model/To Workspace3";
Microchannel_DW.ToWorkspace3_PWORK.LoggedData = rt_CreateStructLogVar(
Microchannel_M->rtwLogInfo,
0.0,
rtmGetTFinal(Microchannel_M),
Microchannel_M->Timing.stepSize0,
(&rtmGetErrorStatus(Microchannel_M)),"EG",
1,
0,
1,
1.0E-5,
&rt_ToWksSignalInfo,
rt_ToWksBlockName);
if (Microchannel_DW.ToWorkspace3_PWORK.LoggedData == (NULL))return;
}

/* SetupRuntimeResources for ToWorkspace: '<S1>/To Workspace4' */
{
static int_T rt_ToWksWidths[] = { 1 };
```

```
static int_T rt_ToWksNumDimensions[] = { 1 }; static

int_T rt_ToWksDimensions[] = { 1 }; static boolean_T

rt_ToWksIsVarDims[] = { 0 }; static void

*rt_ToWksCurrSigDims[] = { (NULL) };static int_T

rt_ToWksCurrSigDimsSize[] = { 4 };

static BuiltInDTypeId rt_ToWksDataTypeIds[] = { SS_DOUBLE };static

int_T rt_ToWksComplexSignals[] = { 0 };

static int_T rt_ToWksFrameData[] = { 0 };

static RTWPreprocessingFcnPtr rt_ToWksLoggingPreprocessingFcnPtrs[] = {(NULL)
};

static const char_T *rt_ToWksLabels[] = { "" };

static RTWLogSignalInfo rt_ToWksSignalInfo = {
1,
rt_ToWksWidths, rt_ToWksNumDimensions,
rt_ToWksDimensions, rt_ToWksIsVarDims,
rt_ToWksCurrSigDims,
rt_ToWksCurrSigDimsSize,
rt_ToWksDataTypeIds,
rt_ToWksComplexSignals, rt_ToWksFrameData,
rt_ToWksLoggingPreprocessingFcnPtrs,

{ rt_ToWksLabels },(NULL),
(NULL),
(NULL),

{ (NULL) },

{ (NULL) },(NULL),
(NULL)
};

static const char_T rt_ToWksBlockName[] =
"Microchannel/SBCR model/To Workspace4";
```

```
Microchannel_DW.ToWorkspace4_PWORK.LoggedData = rt_CreateStructLogVar(
Microchannel_M->rtwLogInfo,
0.0,
rtmGetTFinal(Microchannel_M),
Microchannel_M->Timing.stepSize0,
(&rtmGetErrorStatus(Microchannel_M)),"Eliq",
1,
0,
1,
1.0E-5,
&rt_ToWksSignalInfo,
rt_ToWksBlockName);
if (Microchannel_DW.ToWorkspace4_PWORK.LoggedData == (NULL))return;
}

/* SetupRuntimeResources for ToWorkspace: '<S1>/To Workspace5' */
{
static int_T rt_ToWksWidths[] = { 1 };

static int_T rt_ToWksNumDimensions[] = { 1 }; static

int_T rt_ToWksDimensions[] = { 1 }; static boolean_T

rt_ToWksIsVarDims[] = { 0 }; static void

*rt_ToWksCurrSigDims[] = { (NULL) };static int_T

rt_ToWksCurrSigDimsSize[] = { 4 };

static BuiltInDTypeId rt_ToWksDataTypeIds[] = { SS_DOUBLE };static

int_T rt_ToWksComplexSignals[] = { 0 };

static int_T rt_ToWksFrameData[] = { 0 };

static RTWPreprocessingFcnPtr rt_ToWksLoggingPreprocessingFcnPtrs[] = {(NULL)
};

static const char_T *rt_ToWksLabels[] = { "" };

static RTWLogSignalInfo rt_ToWksSignalInfo = {
1,
rt_ToWksWidths,
rt_ToWksNumDimensions,
rt_ToWksDimensions,
rt_ToWksIsVarDims,
```

```
rt_ToWksCurrSigDims, rt_ToWksCurrSigDimsSize,
rt_ToWksDataTypeIds, rt_ToWksComplexSignals,
rt_ToWksFrameData,
rt_ToWksLoggingPreprocessingFcnPtrs,

{ rt_ToWksLabels },(NULL),
(NULL),
(NULL),

{ (NULL) },

{ (NULL) },(NULL),
(NULL)
};

static const char_T rt_ToWksBlockName[] =
"Microchannel/SBCR model/To Workspace5";
Microchannel_DW.ToWorkspace5_PWORK.LoggedData = rt_CreateStructLogVar(
Microchannel_M->rtwLogInfo,
0.0,
rtmGetTFinal(Microchannel_M),
Microchannel_M->Timing.stepSize0,
(&rtmGetErrorStatus(Microchannel_M)),"vLB",
1,
0,
1,
1.0E-5,
&rt_ToWksSignalInfo,
rt_ToWksBlockName);
if (Microchannel_DW.ToWorkspace5_PWORK.LoggedData == (NULL))return;
}

/* SetupRuntimeResources for ToWorkspace: '<S1>/To Workspace6' */
{
static int_T rt_ToWksWidths[] = { 1 };

static int_T rt_ToWksNumDimensions[] = { 1 }; static

int_T rt_ToWksDimensions[] = { 1 }; static boolean_T

rt_ToWksIsVarDims[] = { 0 }; static void

*rt_ToWksCurrSigDims[] = { (NULL) };
```

```
static int_T rt_ToWksCurrSigDimsSize[] = { 4 };

static BuiltInDTypeId rt_ToWksDataTypeIds[] = { SS_DOUBLE };static

int_T rt_ToWksComplexSignals[] = { 0 };

static int_T rt_ToWksFrameData[] = { 0 };

static RTWPreprocessingFcnPtr rt_ToWksLoggingPreprocessingFcnPtrs[] = {(NULL)
};

static const char_T *rt_ToWksLabels[] = { "" };

static RTWLogSignalInfo rt_ToWksSignalInfo = {
1,
rt_ToWksWidths, rt_ToWksNumDimensions,
rt_ToWksDimensions, rt_ToWksIsVarDims,
rt_ToWksCurrSigDims,
rt_ToWksCurrSigDimsSize,
rt_ToWksDataTypeIds,
rt_ToWksComplexSignals, rt_ToWksFrameData,
rt_ToWksLoggingPreprocessingFcnPtrs,

{ rt_ToWksLabels },(NULL),
(NULL),
(NULL),

{ (NULL) },

{ (NULL) },(NULL),
(NULL)
};

static const char_T rt_ToWksBlockName[] =
"Microchannel/SBCR model/To Workspace6";
Microchannel_DW.ToWorkspace6_PWORK.LoggedData = rt_CreateStructLogVar(
Microchannel_M->rtwLogInfo,
0.0,
rtmGetTFinal(Microchannel_M),
Microchannel_M->Timing.stepSize0,
(&rtmGetErrorStatus(Microchannel_M)),
"COLBKLA",
```

```
1,
0,
1,
1.0E-5,
&rt_ToWksSignalInfo,
rt_ToWksBlockName);
if (Microchannel_DW.ToWorkspace6_PWORK.LoggedData == (NULL))return;
}

/* SetupRuntimeResources for ToWorkspace: '<S1>/To Workspace7' */
{
static int_T rt_ToWksWidths[] = { 1 };

static int_T rt_ToWksNumDimensions[] = { 1 }; static

int_T rt_ToWksDimensions[] = { 1 }; static boolean_T

rt_ToWksIsVarDims[] = { 0 }; static void

*rt_ToWksCurrSigDims[] = { (NULL) };static int_T

rt_ToWksCurrSigDimsSize[] = { 4 };

static BuiltInDTypeId rt_ToWksDataTypeIds[] = { SS_DOUBLE };static

int_T rt_ToWksComplexSignals[] = { 0 };

static int_T rt_ToWksFrameData[] = { 0 };

static RTWPreprocessingFcnPtr rt_ToWksLoggingPreprocessingFcnPtrs[] = {(NULL)
};

static const char_T *rt_ToWksLabels[] = { "" };

static RTWLogSignalInfo rt_ToWksSignalInfo = {
1,
rt_ToWksWidths, rt_ToWksNumDimensions,
rt_ToWksDimensions, rt_ToWksIsVarDims,
rt_ToWksCurrSigDims,
rt_ToWksCurrSigDimsSize,
rt_ToWksDataTypeIds,
rt_ToWksComplexSignals, rt_ToWksFrameData,
rt_ToWksLoggingPreprocessingFcnPtrs,
```

```
{ rt_ToWksLabels },(NULL),
(NULL),
(NULL),

{ (NULL) },

{ (NULL) },(NULL),
(NULL)
};

static const char_T rt_ToWksBlockName[] =
"Microchannel/SBCR model/To Workspace7";
Microchannel_DW.ToWorkspace7_PWORK.LoggedData = rt_CreateStructLogVar(
Microchannel_M->rtwLogInfo,
0.0,
rtmGetTFinal(Microchannel_M),
Microchannel_M->Timing.stepSize0,
(&rtmGetErrorStatus(Microchannel_M)),
"totalvoid",
1,
0,
1,
1.0E-5,
&rt_ToWksSignalInfo,
rt_ToWksBlockName);
if (Microchannel_DW.ToWorkspace7_PWORK.LoggedData == (NULL))return;
}

/* SetupRuntimeResources for Scope: '<S5>/Scope' */
{
RTWLogSignalInfo rt_ScopeSignalInfo;
static int_T rt_ScopeSignalWidths[] = { 1 };

static int_T rt_ScopeSignalNumDimensions[] = { 1 }; static

int_T rt_ScopeSignalDimensions[] = { 1 }; static void

*rt_ScopeCurrSigDims[] = { (NULL) }; static int_T

rt_ScopeCurrSigDimsSize[] = { 4 }; static const char_T

*rt_ScopeSignalLabels[] = { "" };static char_T

rt_ScopeSignalTitles[] = "";
static int_T rt_ScopeSignalTitleLengths[] = { 0 };
```

```
static boolean_T rt_ScopeSignalIsVarDims[] = { 0 };static

int_T rt_ScopeSignalPlotStyles[] = { 0 }; BuiltInDTypeId

dTypes[1] = { SS_DOUBLE };

static char_T rt_ScopeBlockName[] = "Microchannel/SBCR model/E liquid/Scope";static
int_T rt_ScopeFrameData[] = { 0 };

static RTWPreprocessingFcnPtr rt_ScopeSignalLoggingPreprocessingFcnPtrs[] =
{ (NULL)
};

rt_ScopeSignalInfo.numSignals  =  1; rt_ScopeSignalInfo.numCols =
rt_ScopeSignalWidths; rt_ScopeSignalInfo.numDims =
rt_ScopeSignalNumDimensions; rt_ScopeSignalInfo.dims =
rt_ScopeSignalDimensions; rt_ScopeSignalInfo.isVarDims =
rt_ScopeSignalIsVarDims; rt_ScopeSignalInfo.currSigDims =
rt_ScopeCurrSigDims; rt_ScopeSignalInfo.currSigDimsSize =
rt_ScopeCurrSigDimsSize;rt_ScopeSignalInfo.dataTypes = dTypes;
rt_ScopeSignalInfo.complexSignals = (NULL);
rt_ScopeSignalInfo.frameData = rt_ScopeFrameData;
rt_ScopeSignalInfo.preprocessingPtrs =
rt_ScopeSignalLoggingPreprocessingFcnPtrs; rt_ScopeSignalInfo.labels.cptr
= rt_ScopeSignalLabels; rt_ScopeSignalInfo.titles =
rt_ScopeSignalTitles; rt_ScopeSignalInfo.titleLengths =
rt_ScopeSignalTitleLengths; rt_ScopeSignalInfo.plotStyles =
rt_ScopeSignalPlotStyles; rt_ScopeSignalInfo.blockNames.cptr = (NULL);
rt_ScopeSignalInfo.stateNames.cptr = (NULL);
rt_ScopeSignalInfo.crossMdlRef = (NULL);
rt_ScopeSignalInfo.dataTypeConvert = (NULL);
Microchannel_DW.Scope_PWORK.LoggedData  =  rt_CreateStructLogVar(
Microchannel_M->rtwLogInfo,0.0,
rtmGetTFinal(Microchannel_M),
Microchannel_M->Timing.stepSize0,
(&rtmGetErrorStatus(Microchannel_M)),"EL",
1,
5000,
1,
1.0E-5,
&rt_ScopeSignalInfo,
rt_ScopeBlockName);
if  (Microchannel_DW.Scope_PWORK.LoggedData  ==  (NULL))return;
```

```
}

/* SetupRuntimeResources for Scope: '<S11>/Scope' */
{
RTWLogSignalInfo rt_ScopeSignalInfo;
static int_T rt_ScopeSignalWidths[] = { 1 };

static int_T rt_ScopeSignalNumDimensions[] = { 1 }; static

int_T rt_ScopeSignalDimensions[] = { 1 }; static void

*rt_ScopeCurrSigDims[] = { (NULL) }; static int_T

rt_ScopeCurrSigDimsSize[] = { 4 }; static const char_T

*rt_ScopeSignalLabels[] = { "" };static char_T

rt_ScopeSignalTitles[] = "";
static int_T rt_ScopeSignalTitleLengths[] = { 0 }; static

boolean_T rt_ScopeSignalIsVarDims[] = { 0 };static int_T

rt_ScopeSignalPlotStyles[] = { 1 }; BuiltInDTypeId

dTypes[1] = { SS_DOUBLE };

static char_T rt_ScopeBlockName[] =
"Microchannel/SBCR model/KLa CO SB/Scope";
static int_T rt_ScopeFrameData[] = { 0 };

static RTWPreprocessingFcnPtr rt_ScopeSignalLoggingPreprocessingFcnPtrs[] =
{ (NULL)
};

rt_ScopeSignalInfo.numSignals = 1; rt_ScopeSignalInfo.numCols =
rt_ScopeSignalWidths; rt_ScopeSignalInfo.numDims =
rt_ScopeSignalNumDimensions; rt_ScopeSignalInfo.dims =
rt_ScopeSignalDimensions; rt_ScopeSignalInfo.isVarDims =
rt_ScopeSignalIsVarDims; rt_ScopeSignalInfo.currSigDims =
rt_ScopeCurrSigDims; rt_ScopeSignalInfo.currSigDimsSize =
rt_ScopeCurrSigDimsSize;rt_ScopeSignalInfo.dataTypes = dTypes;
rt_ScopeSignalInfo.complexSignals = (NULL);
rt_ScopeSignalInfo.frameData = rt_ScopeFrameData;
rt_ScopeSignalInfo.preprocessingPtrs =
rt_ScopeSignalLoggingPreprocessingFcnPtrs;
rt_ScopeSignalInfo.labels.cptr = rt_ScopeSignalLabels;
rt_ScopeSignalInfo.titles = rt_ScopeSignalTitles;
```

```
rt_ScopeSignalInfo.titleLengths = rt_ScopeSignalTitleLengths;
rt_ScopeSignalInfo.plotStyles = rt_ScopeSignalPlotStyles;
rt_ScopeSignalInfo.blockNames.cptr = (NULL);
rt_ScopeSignalInfo.stateNames.cptr = (NULL);
rt_ScopeSignalInfo.crossMdlRef = (NULL);
rt_ScopeSignalInfo.dataTypeConvert = (NULL);
Microchannel_DW.Scope_PWORK_n.LoggedData = rt_CreateStructLogVar(
Microchannel_M->rtwLogInfo,0.0,
rtmGetTFinal(Microchannel_M),
Microchannel_M->Timing.stepSize0,
(&rtmGetErrorStatus(Microchannel_M)),
"KLaCOSB",
1,
5000,
1,
1.0E-5,
&rt_ScopeSignalInfo,
rt_ScopeBlockName);
if (Microchannel_DW.Scope_PWORK_n.LoggedData == (NULL))
return;
}

/* SetupRuntimeResources for Scope: '<S12>/Scope' */
{
RTWLogSignalInfo rt_ScopeSignalInfo;
static int_T rt_ScopeSignalWidths[] = { 1 };

static int_T rt_ScopeSignalNumDimensions[] = { 1 }; static

int_T rt_ScopeSignalDimensions[] = { 1 }; static void

*rt_ScopeCurrSigDims[] = { (NULL) }; static int_T

rt_ScopeCurrSigDimsSize[] = { 4 }; static const char_T

*rt_ScopeSignalLabels[] = { "" };

static char_T rt_ScopeSignalTitles[] = "";
static int_T rt_ScopeSignalTitleLengths[] = { 0 }; static

boolean_T rt_ScopeSignalIsVarDims[] = { 0 };static int_T

rt_ScopeSignalPlotStyles[] = { 0 }; BuiltInDTypeId

dTypes[1] = { SS_DOUBLE };

static char_T rt_ScopeBlockName[] =
"Microchannel/SBCR model/KLa H2 LB/Scope";
```

```
static int_T rt_ScopeFrameData[] = { 0 };

static RTWPreprocessingFcnPtr rt_ScopeSignalLoggingPreprocessingFcnPtrs[] =
{ (NULL)
};

rt_ScopeSignalInfo.numSignals  =  1; rt_ScopeSignalInfo.numCols =
rt_ScopeSignalWidths; rt_ScopeSignalInfo.numDims =
rt_ScopeSignalNumDimensions; rt_ScopeSignalInfo.dims =
rt_ScopeSignalDimensions; rt_ScopeSignalInfo.isVarDims =
rt_ScopeSignalIsVarDims; rt_ScopeSignalInfo.currSigDims =
rt_ScopeCurrSigDims; rt_ScopeSignalInfo.currSigDimsSize  =
rt_ScopeCurrSigDimsSize;rt_ScopeSignalInfo.dataTypes = dTypes;
rt_ScopeSignalInfo.complexSignals = (NULL);
rt_ScopeSignalInfo.frameData = rt_ScopeFrameData;
rt_ScopeSignalInfo.preprocessingPtrs =
rt_ScopeSignalLoggingPreprocessingFcnPtrs; rt_ScopeSignalInfo.labels.cptr
= rt_ScopeSignalLabels; rt_ScopeSignalInfo.titles =
rt_ScopeSignalTitles; rt_ScopeSignalInfo.titleLengths =
rt_ScopeSignalTitleLengths; rt_ScopeSignalInfo.plotStyles =
rt_ScopeSignalPlotStyles; rt_ScopeSignalInfo.blockNames.cptr = (NULL);
rt_ScopeSignalInfo.stateNames.cptr = (NULL);
rt_ScopeSignalInfo.crossMdlRef = (NULL);
rt_ScopeSignalInfo.dataTypeConvert = (NULL);
Microchannel_DW.Scope_PWORK_c.LoggedData  =  rt_CreateStructLogVar(
Microchannel_M->rtwLogInfo,0.0,
rtmGetTFinal(Microchannel_M),
Microchannel_M->Timing.stepSize0,
(&rtmGetErrorStatus(Microchannel_M)),
"KLaH2LB",
1,
0,
1,
1.0E-5,
&rt_ScopeSignalInfo,
rt_ScopeBlockName);
if  (Microchannel_DW.Scope_PWORK_c.LoggedData  ==  (NULL))
return;
}

/* SetupRuntimeResources for Scope: '<S13>/Scope' */
{
RTWLogSignalInfo  rt_ScopeSignalInfo;
static int_T rt_ScopeSignalWidths[] = { 1 };
```

```
static int_T rt_ScopeSignalNumDimensions[] = { 1 }; static

int_T rt_ScopeSignalDimensions[] = { 1 }; static void

*rt_ScopeCurrSigDims[] = { (NULL) }; static int_T

rt_ScopeCurrSigDimsSize[] = { 4 }; static const char_T

*rt_ScopeSignalLabels[] = { "" };

static char_T rt_ScopeSignalTitles[] = "";
static int_T rt_ScopeSignalTitleLengths[] = { 0 }; static

boolean_T rt_ScopeSignalIsVarDims[] = { 0 };static int_T

rt_ScopeSignalPlotStyles[] = { 1 }; BuiltInDTypeId

dTypes[1] = { SS_DOUBLE };

static char_T rt_ScopeBlockName[] =
"Microchannel/SBCR model/KLa H2 SB/Scope";
static int_T rt_ScopeFrameData[] = { 0 };

static RTWPreprocessingFcnPtr rt_ScopeSignalLoggingPreprocessingFcnPtrs[] =
{ (NULL)
};

rt_ScopeSignalInfo.numSignals = 1; rt_ScopeSignalInfo.numCols =
rt_ScopeSignalWidths; rt_ScopeSignalInfo.numDims =
rt_ScopeSignalNumDimensions; rt_ScopeSignalInfo.dims =
rt_ScopeSignalDimensions; rt_ScopeSignalInfo.isVarDims =
rt_ScopeSignalIsVarDims; rt_ScopeSignalInfo.currSigDims =
rt_ScopeCurrSigDims; rt_ScopeSignalInfo.currSigDimsSize =
rt_ScopeCurrSigDimsSize;rt_ScopeSignalInfo.dataTypes = dTypes;
rt_ScopeSignalInfo.complexSignals = (NULL);
rt_ScopeSignalInfo.frameData = rt_ScopeFrameData;
rt_ScopeSignalInfo.preprocessingPtrs =
rt_ScopeSignalLoggingPreprocessingFcnPtrs; rt_ScopeSignalInfo.labels.cptr
= rt_ScopeSignalLabels; rt_ScopeSignalInfo.titles =
rt_ScopeSignalTitles; rt_ScopeSignalInfo.titleLengths =
rt_ScopeSignalTitleLengths; rt_ScopeSignalInfo.plotStyles =
rt_ScopeSignalPlotStyles; rt_ScopeSignalInfo.blockNames.cptr = (NULL);
rt_ScopeSignalInfo.stateNames.cptr = (NULL);
rt_ScopeSignalInfo.crossMdlRef = (NULL);
rt_ScopeSignalInfo.dataTypeConvert = (NULL);
Microchannel_DW.Scope_PWORK_k.LoggedData = rt_CreateStructLogVar(
```

```
Microchannel_M->rtwLogInfo,0.0,
rtmGetTFinal(Microchannel_M),
Microchannel_M->Timing.stepSize0,
(&rtmGetErrorStatus(Microchannel_M)),
"KLaH2SB",
1,
0,
1,
1.0E-5,
&rt_ScopeSignalInfo,
rt_ScopeBlockName);
if (Microchannel_DW.Scope_PWORK_k.LoggedData == (NULL))
return;
}

/* SetupRuntimeResources for Scope: '<S14>/Scope' */
{
RTWLogSignalInfo rt_ScopeSignalInfo;
static int_T rt_ScopeSignalWidths[] = { 1 };

static int_T rt_ScopeSignalNumDimensions[] = { 1 }; static

int_T rt_ScopeSignalDimensions[] = { 1 }; static void

*rt_ScopeCurrSigDims[] = { (NULL) }; static int_T

rt_ScopeCurrSigDimsSize[] = { 4 }; static const char_T

*rt_ScopeSignalLabels[] = { "" };static char_T

rt_ScopeSignalTitles[] = "";
static int_T rt_ScopeSignalTitleLengths[] = { 0 }; static

boolean_T rt_ScopeSignalIsVarDims[] = { 0 };static int_T

rt_ScopeSignalPlotStyles[] = { 0 }; BuiltInDTypeId

dTypes[1] = { SS_DOUBLE };

static char_T rt_ScopeBlockName[] =
"Microchannel/SBCR model/LB hold-up/Scope";
static int_T rt_ScopeFrameData[] = { 0 };

static RTWPreprocessingFcnPtr rt_ScopeSignalLoggingPreprocessingFcnPtrs[] =
{ (NULL)
};
```

```
rt_ScopeSignalInfo.numSignals  =  1; rt_ScopeSignalInfo.numCols =
rt_ScopeSignalWidths; rt_ScopeSignalInfo.numDims =
rt_ScopeSignalNumDimensions; rt_ScopeSignalInfo.dims =
rt_ScopeSignalDimensions; rt_ScopeSignalInfo.isVarDims =
rt_ScopeSignalIsVarDims; rt_ScopeSignalInfo.currSigDims =
rt_ScopeCurrSigDims; rt_ScopeSignalInfo.currSigDimsSize  =
rt_ScopeCurrSigDimsSize;rt_ScopeSignalInfo.dataTypes = dTypes;
rt_ScopeSignalInfo.complexSignals = (NULL);
rt_ScopeSignalInfo.frameData = rt_ScopeFrameData;
rt_ScopeSignalInfo.preprocessingPtrs =
rt_ScopeSignalLoggingPreprocessingFcnPtrs; rt_ScopeSignalInfo.labels.cptr
= rt_ScopeSignalLabels; rt_ScopeSignalInfo.titles =
rt_ScopeSignalTitles; rt_ScopeSignalInfo.titleLengths =
rt_ScopeSignalTitleLengths; rt_ScopeSignalInfo.plotStyles =
rt_ScopeSignalPlotStyles; rt_ScopeSignalInfo.blockNames.cptr = (NULL);
rt_ScopeSignalInfo.stateNames.cptr = (NULL);
rt_ScopeSignalInfo.crossMdlRef = (NULL);
rt_ScopeSignalInfo.dataTypeConvert = (NULL);
Microchannel_DW.Scope_PWORK_cl.LoggedData  =  rt_CreateStructLogVar(
Microchannel_M->rtwLogInfo,0.0,
rtmGetTFinal(Microchannel_M),
Microchannel_M->Timing.stepSize0,
(&rtmGetErrorStatus(Microchannel_M)),
"voidLB1",
1,
5000,
1,
1.0E-5,
&rt_ScopeSignalInfo,
rt_ScopeBlockName);
if  (Microchannel_DW.Scope_PWORK_cl.LoggedData  ==  (NULL))return;
}

/* SetupRuntimeResources  for  Scope:  '<S24>/C,  CO,SB(mol//m3)8'  */
{
RTWLogSignalInfo  rt_ScopeSignalInfo;
static int_T rt_ScopeSignalWidths[] = {  1  };

static int_T rt_ScopeSignalNumDimensions[] = {  1  };static

int_T rt_ScopeSignalDimensions[] = {  1  }; static void

*rt_ScopeCurrSigDims[] = {  (NULL)  }; static int_T

rt_ScopeCurrSigDimsSize[] = {  4  };
```

```
static const char_T *rt_ScopeSignalLabels[] = {  "" };

static char_T rt_ScopeSignalTitles[] = "";
static int_T rt_ScopeSignalTitleLengths[] = { 0 }; static

boolean_T rt_ScopeSignalIsVarDims[] = { 0 };static int_T

rt_ScopeSignalPlotStyles[] = { 0 }; BuiltInDTypeId

dTypes[1] = { SS_DOUBLE };

static char_T rt_ScopeBlockName[] =
"Microchannel/SBCR model/Mass balances/CO, SB/C, CO,SB(mol//m3)8" ;static
int_T rt_ScopeFrameData[] = { 0 };

static RTWPreprocessingFcnPtr rt_ScopeSignalLoggingPreprocessingFcnPtrs[] =
{ (NULL)
};

rt_ScopeSignalInfo.numSignals  =  1; rt_ScopeSignalInfo.numCols =
rt_ScopeSignalWidths; rt_ScopeSignalInfo.numDims =
rt_ScopeSignalNumDimensions; rt_ScopeSignalInfo.dims =
rt_ScopeSignalDimensions; rt_ScopeSignalInfo.isVarDims =
rt_ScopeSignalIsVarDims; rt_ScopeSignalInfo.currSigDims =
rt_ScopeCurrSigDims; rt_ScopeSignalInfo.currSigDimsSize  =
rt_ScopeCurrSigDimsSize;rt_ScopeSignalInfo.dataTypes = dTypes;
rt_ScopeSignalInfo.complexSignals = (NULL);
rt_ScopeSignalInfo.frameData = rt_ScopeFrameData;
rt_ScopeSignalInfo.preprocessingPtrs =
rt_ScopeSignalLoggingPreprocessingFcnPtrs; rt_ScopeSignalInfo.labels.cptr =
rt_ScopeSignalLabels; rt_ScopeSignalInfo.titles = rt_ScopeSignalTitles;
rt_ScopeSignalInfo.titleLengths = rt_ScopeSignalTitleLengths;
rt_ScopeSignalInfo.plotStyles = rt_ScopeSignalPlotStyles;
rt_ScopeSignalInfo.blockNames.cptr = (NULL);
rt_ScopeSignalInfo.stateNames.cptr = (NULL); rt_ScopeSignalInfo.crossMdlRef
= (NULL); rt_ScopeSignalInfo.dataTypeConvert = (NULL);
Microchannel_DW.CCOSBmolm38_PWORK.LoggedData  =  rt_CreateStructLogVar(
Microchannel_M->rtwLogInfo,0.0,
rtmGetTFinal(Microchannel_M),
Microchannel_M->Timing.stepSize0,
(&rtmGetErrorStatus(Microchannel_M)),
"VoidL",
1,
```

```
5000,
1,
1.0E-5,
&rt_ScopeSignalInfo,
rt_ScopeBlockName);
if (Microchannel_DW.CCOSBmolm38_PWORK.LoggedData == (NULL))return;
}

/* SetupRuntimeResources for Scope: '<S29>/C, H2, L (mol//m3)' */
{
RTWLogSignalInfo rt_ScopeSignalInfo;
static int_T rt_ScopeSignalWidths[] = { 1 };

static int_T rt_ScopeSignalNumDimensions[] = { 1 }; static

int_T rt_ScopeSignalDimensions[] = { 1 }; static void

*rt_ScopeCurrSigDims[] = { (NULL) }; static int_T

rt_ScopeCurrSigDimsSize[] = { 4 }; static const char_T

*rt_ScopeSignalLabels[] = { "" };static char_T

rt_ScopeSignalTitles[] = "";
static int_T rt_ScopeSignalTitleLengths[] = { 0 }; static

boolean_T rt_ScopeSignalIsVarDims[] = { 0 };static int_T

rt_ScopeSignalPlotStyles[] = { 0 }; BuiltInDTypeId

dTypes[1] = { SS_DOUBLE };

static char_T rt_ScopeBlockName[] =
"Microchannel/SBCR model/Mass balances/H2,Liquid/C, H2, L (mol//m3)" ;static
int_T rt_ScopeFrameData[] = { 0 };

static RTWPreprocessingFcnPtr rt_ScopeSignalLoggingPreprocessingFcnPtrs[] =
{ (NULL)
};

rt_ScopeSignalInfo.numSignals = 1; rt_ScopeSignalInfo.numCols =
rt_ScopeSignalWidths; rt_ScopeSignalInfo.numDims =
rt_ScopeSignalNumDimensions; rt_ScopeSignalInfo.dims =
rt_ScopeSignalDimensions; rt_ScopeSignalInfo.isVarDims =
rt_ScopeSignalIsVarDims; rt_ScopeSignalInfo.currSigDims =
rt_ScopeCurrSigDims; rt_ScopeSignalInfo.currSigDimsSize =
rt_ScopeCurrSigDimsSize;
```

```
rt_ScopeSignalInfo.dataTypes = dTypes;
rt_ScopeSignalInfo.complexSignals = (NULL);
rt_ScopeSignalInfo.frameData = rt_ScopeFrameData;
rt_ScopeSignalInfo.preprocessingPtrs =
rt_ScopeSignalLoggingPreprocessingFcnPtrs; rt_ScopeSignalInfo.labels.cptr
= rt_ScopeSignalLabels; rt_ScopeSignalInfo.titles =
rt_ScopeSignalTitles; rt_ScopeSignalInfo.titleLengths =
rt_ScopeSignalTitleLengths; rt_ScopeSignalInfo.plotStyles =
rt_ScopeSignalPlotStyles; rt_ScopeSignalInfo.blockNames.cptr = (NULL);
rt_ScopeSignalInfo.stateNames.cptr = (NULL);
rt_ScopeSignalInfo.crossMdlRef = (NULL);
rt_ScopeSignalInfo.dataTypeConvert = (NULL);
Microchannel_DW.CH2Lmolm3_PWORK.LoggedData = rt_CreateStructLogVar(
Microchannel_M->rtwLogInfo,0.0,
rtmGetTFinal(Microchannel_M),
Microchannel_M->Timing.stepSize0,
(&rtmGetErrorStatus(Microchannel_M)),"H2L",
1,
5000,
1,
1.0E-5,
&rt_ScopeSignalInfo,
rt_ScopeBlockName);
if (Microchannel_DW.CH2Lmolm3_PWORK.LoggedData == (NULL))return;
}

/* SetupRuntimeResources for Scope: '<S19>/Scope' */
{
RTWLogSignalInfo rt_ScopeSignalInfo;
static int_T rt_ScopeSignalWidths[] = { 1 };

static int_T rt_ScopeSignalNumDimensions[] = { 1 }; static

int_T rt_ScopeSignalDimensions[] = { 1 }; static void

*rt_ScopeCurrSigDims[] = { (NULL) }; static int_T

rt_ScopeCurrSigDimsSize[] = { 4 }; static const char_T

*rt_ScopeSignalLabels[] = { "" };static char_T

rt_ScopeSignalTitles[] = "";
static int_T rt_ScopeSignalTitleLengths[] = { 0 }; static

boolean_T rt_ScopeSignalIsVarDims[] = { 0 };
```

```
static int_T rt_ScopeSignalPlotStyles[] = { 0 };

BuiltInDTypeId dTypes[1] = { SS_DOUBLE };

static char_T rt_ScopeBlockName[] =
"Microchannel/SBCR model/Ug from gas consumption/Scope" ;static
int_T rt_ScopeFrameData[] = { 0 };

static RTWPreprocessingFcnPtr rt_ScopeSignalLoggingPreprocessingFcnPtrs[] =
{ (NULL)
};

rt_ScopeSignalInfo.numSignals  =  1; rt_ScopeSignalInfo.numCols =
rt_ScopeSignalWidths; rt_ScopeSignalInfo.numDims =
rt_ScopeSignalNumDimensions; rt_ScopeSignalInfo.dims =
rt_ScopeSignalDimensions; rt_ScopeSignalInfo.isVarDims =
rt_ScopeSignalIsVarDims; rt_ScopeSignalInfo.currSigDims =
rt_ScopeCurrSigDims; rt_ScopeSignalInfo.currSigDimsSize =
rt_ScopeCurrSigDimsSize;rt_ScopeSignalInfo.dataTypes = dTypes;
rt_ScopeSignalInfo.complexSignals = (NULL);
rt_ScopeSignalInfo.frameData = rt_ScopeFrameData;
rt_ScopeSignalInfo.preprocessingPtrs =
rt_ScopeSignalLoggingPreprocessingFcnPtrs; rt_ScopeSignalInfo.labels.cptr
= rt_ScopeSignalLabels; rt_ScopeSignalInfo.titles =
rt_ScopeSignalTitles; rt_ScopeSignalInfo.titleLengths =
rt_ScopeSignalTitleLengths; rt_ScopeSignalInfo.plotStyles =
rt_ScopeSignalPlotStyles; rt_ScopeSignalInfo.blockNames.cptr = (NULL);
rt_ScopeSignalInfo.stateNames.cptr = (NULL);
rt_ScopeSignalInfo.crossMdlRef = (NULL);
rt_ScopeSignalInfo.dataTypeConvert = (NULL);
Microchannel_DW.Scope_PWORK_p.LoggedData  =  rt_CreateStructLogVar(
Microchannel_M->rtwLogInfo,0.0,
rtmGetTFinal(Microchannel_M),
Microchannel_M->Timing.stepSize0,
(&rtmGetErrorStatus(Microchannel_M)),"Ug1",
1,
5000000,
1,
1.0E-5,
&rt_ScopeSignalInfo,
rt_ScopeBlockName);
if  (Microchannel_DW.Scope_PWORK_p.LoggedData  ==  (NULL))
return;
```

```
}

/* SetupRuntimeResources for ToWorkspace: '<S1>/To Workspace1' */
{
static int_T rt_ToWksWidths[] = { 1 };

static int_T rt_ToWksNumDimensions[] = { 1 }; static

int_T rt_ToWksDimensions[] = { 1 }; static boolean_T

rt_ToWksIsVarDims[] = { 0 }; static void

*rt_ToWksCurrSigDims[] = { (NULL) };static int_T

rt_ToWksCurrSigDimsSize[] = { 4 };

static BuiltInDTypeId rt_ToWksDataTypeIds[] = { SS_DOUBLE };static

int_T rt_ToWksComplexSignals[] = { 0 };

static int_T rt_ToWksFrameData[] = { 0 };

static RTWPreprocessingFcnPtr rt_ToWksLoggingPreprocessingFcnPtrs[] = {(NULL)
};

static const char_T *rt_ToWksLabels[] = { "" };

static RTWLogSignalInfo rt_ToWksSignalInfo = {
1,
rt_ToWksWidths, rt_ToWksNumDimensions,
rt_ToWksDimensions, rt_ToWksIsVarDims,
rt_ToWksCurrSigDims,
rt_ToWksCurrSigDimsSize,
rt_ToWksDataTypeIds,
rt_ToWksComplexSignals, rt_ToWksFrameData,
rt_ToWksLoggingPreprocessingFcnPtrs,

{ rt_ToWksLabels },(NULL),
(NULL),
(NULL),

{ (NULL) },

{ (NULL) },
```

```
(NULL),(NULL)
};

static const char_T rt_ToWksBlockName[] =
"Microchannel/SBCR model/To Workspace1";
Microchannel_DW.ToWorkspace1_PWORK.LoggedData = rt_CreateStructLogVar(
Microchannel_M->rtwLogInfo,
0.0,
rtmGetTFinal(Microchannel_M),
Microchannel_M->Timing.stepSize0,
(&rtmGetErrorStatus(Microchannel_M)),"time",
1,
0,
1,
1.0E-5,
&rt_ToWksSignalInfo,
rt_ToWksBlockName);
if (Microchannel_DW.ToWorkspace1_PWORK.LoggedData == (NULL))return;
}

/* Start for Constant: '<Root>/Cco,inlet' */
Microchannel_B.Ccoinlet = Microchannel_P.Ccoinlet_Value;

/* Start for Constant: '<Root>/C,H2 inlet' */
Microchannel_B.CH2inlet = Microchannel_P.CH2inlet_Value;

/* Start for If: '<S2>/If' */
Microchannel_DW.If_ActiveSubsystem = -1;

/* Start for If: '<S3>/If' */
Microchannel_DW.If_ActiveSubsystem_o = -1;

/* InitializeConditions for Integrator: '<S24>/Integrator 2' incorporates:
    *  Integrator: '<S27>/Integrator 2'
*/
if (rtmIsFirstInitCond(Microchannel_M)) {
Microchannel_X.Integrator2_CSTATE = 218.41;
Microchannel_X.Integrator2_CSTATE_h = 436.82;
}

Microchannel_DW.Integrator2_IWORK = 1;

/* End of InitializeConditions for Integrator: '<S24>/Integrator 2' */

/* InitializeConditions for Integrator: '<S27>/Integrator 2' */
Microchannel_DW.Integrator2_IWORK_l = 1;
```

```
/* InitializeConditions for Integrator: '<S25>/Integrator1' incorporates:
    *  Integrator: '<S28>/Integrator 2'
*/
if (rtmIsFirstInitCond(Microchannel_M)) {
Microchannel_X.Integrator1_CSTATE = 218.41;
Microchannel_X.Integrator2_CSTATE_hb = 436.82;
}

Microchannel_DW.Integrator1_IWORK = 1;

/* End of InitializeConditions for Integrator: '<S25>/Integrator1' */

/* InitializeConditions for Integrator: '<S28>/Integrator 2' */
Microchannel_DW.Integrator2_IWORK_p = 1;

/* InitializeConditions for Integrator: '<S26>/Integrator 2' incorporates:
    *  Integrator: '<S19>/Integrator'
*/
if (rtmIsFirstInitCond(Microchannel_M)) {
Microchannel_X.Integrator2_CSTATE_d = 0.0;
Microchannel_X.Integrator_CSTATE = 0.0;
}

Microchannel_DW.Integrator2_IWORK_g = 1;

/* End of InitializeConditions for Integrator: '<S26>/Integrator 2' */

/* InitializeConditions for Integrator: '<S19>/Integrator' */
Microchannel_DW.Integrator_IWORK = 1;

/* InitializeConditions for Integrator: '<S29>/Integrator 2' incorporates:
    *  Integrator: '<S25>/Integrator'
*/
if (rtmIsFirstInitCond(Microchannel_M)) {
Microchannel_X.Integrator2_CSTATE_a = 0.0;
Microchannel_X.Integrator_CSTATE_n = 0.0;
}

Microchannel_DW.Integrator2_IWORK_m = 1;

/* End of InitializeConditions for Integrator: '<S29>/Integrator 2' */

/* InitializeConditions for Integrator: '<S25>/Integrator' */
Microchannel_DW.Integrator_IWORK_k = 1;

/* InitializeConditions for Integrator: '<S24>/Integrator 1' incorporates:
    *  Integrator: '<S28>/Integrator 1'
*/
```

```
if (rtmIsFirstInitCond(Microchannel_M)) {
Microchannel_X.Integrator1_CSTATE_j = 0.0;
Microchannel_X.Integrator1_CSTATE_f = 0.0;
}

Microchannel_DW.Integrator1_IWORK_o = 1;

/* End of InitializeConditions for Integrator: '<S24>/Integrator 1' */

/* InitializeConditions for Integrator: '<S28>/Integrator 1' */
Microchannel_DW.Integrator1_IWORK_f = 1;

/* InitializeConditions for Integrator: '<S27>/Integrator 1' incorporates:
    *  Integrator: '<S26>/Integrator 1'
*/
if (rtmIsFirstInitCond(Microchannel_M)) {
Microchannel_X.Integrator1_CSTATE_d = 0.0;
Microchannel_X.Integrator1_CSTATE_c = 0.0;
}

Microchannel_DW.Integrator1_IWORK_k = 1;

/* End of InitializeConditions for Integrator: '<S27>/Integrator 1' */

/* InitializeConditions for Integrator: '<S26>/Integrator 1' */
Microchannel_DW.Integrator1_IWORK_i = 1;

/* InitializeConditions for Integrator: '<S29>/Integrator
1' */if (rtmIsFirstInitCond(Microchannel_M)) {
Microchannel_X.Integrator1_CSTATE_n = 0.0;
}

Microchannel_DW.Integrator1_IWORK_a = 1;

/* End of InitializeConditions for Integrator: '<S29>/Integrator 1' */

/* set "at time zero" to false */
if
(rtmIsFirstInitCond(Microchannel_M))
{rtmSetFirstInitCond(Microchannel_M,
0);
}
}

/* Model terminate
function */ void
Microchannel_terminate(v
oid)
```

```
{
/* (no terminate code required) */
}
```